

Non-circular motions in dark matter halos



Dissertation

zur
Erlangung des Grades
„Doktor der Naturwissenschaften“
in der Fakultät für Physik und Astronomie
der Ruhr – Universität Bochum

von
Clemens Trachternach
aus
Recklinghausen

Bochum 2008

1. Gutachter: Prof. Dr. Ralf-Jürgen Dettmar
2. Gutachter: Prof. Dr. Erwin de Blok

*God does not play dice with the universe;
He plays an ineffable game of his own devising,
which might be compared,
from the perspective of any of the other players,
to being involved in an obscure and complex
version of poker in a pitch dark room,
with blank cards, for infinite stakes,
with a dealer who won't tell you the rules,
and who smiles all the time.*

Terry Pratchett

Tag der mündlichen Prüfung: 06.06.2008

Contents

1	Introduction	1
1.1	Dark matter in galaxies	1
1.1.1	The need for dark matter	1
1.1.2	Alternatives to dark matter?	2
1.1.3	Successes and problems of Λ CDM	2
1.2	This thesis	4
2	Dynamical centers and non-circular motions in THINGS galaxies	7
2.1	Introduction	7
2.2	Sample and data	9
2.3	Estimating galaxy centers	10
2.3.1	Radio continuum	11
2.3.2	<i>Spitzer</i> /IRAC 3.6 μ m image	11
2.3.3	Kinematic center	11
2.4	Harmonic decomposition	12
2.5	NGC 3198 — A case–study	14
2.5.1	Center estimates	14
2.5.2	Harmonic expansion	14
2.6	Results	16
2.6.1	Quality of the center estimates	18
2.6.2	Results of the harmonic decomposition	20
2.6.3	Comparison with predictions from simulations	22
2.6.4	Consistency Checks	25
2.6.4.1	ROTCUR vs. RESWRI: residual velocity fields	25
2.6.4.2	Making prior assumptions during the RESWRI runs	27
2.6.4.3	Hermite vs. Intensity weighted mean VF	27
2.6.4.4	Decomposition under the assumption of an incorrect center	28
2.7	Summary and Conclusions	36
2.A	Appendix: Description of individual galaxies	38
2.A.1	NGC 925	38
2.A.2	NGC 2366	38
2.A.3	NGC 2403	39
2.A.4	NGC 2841	40
2.A.5	NGC 2903	40
2.A.6	NGC 2976	41
2.A.7	NGC 3031	42
2.A.8	NGC 3198	43

2.A.9	IC 2574	43
2.A.10	NGC 3521	44
2.A.11	NGC 3621	45
2.A.12	NGC 3627	45
2.A.13	NGC 4736	46
2.A.14	DDO 154	47
2.A.15	NGC 4826	47
2.A.16	NGC 5055	48
2.A.17	NGC 6946	49
2.A.18	NGC 7331	49
2.A.19	NGC 7793	50
2.B	Appendix: The atlas	51
3	Are there any “undetected” non-circular motions?	71
3.1	Higher order harmonic decomposition	71
3.1.1	Amplitudes of the harmonic components	71
3.1.2	Residuals of the higher order decompositions	76
3.1.3	Discussion	82
3.2	Harmonic decomposition of artificial velocity fields	84
3.2.1	Creating the artificial velocity fields	84
3.2.2	Harmonic decomposition of the artificial velocity fields	87
3.3	Conclusions	90
3.A	Appendix: Velocity fields	92
4	The baryonic Tully-Fisher relation and its implication for dark matter halos	101
4.1	Introduction	101
4.2	The data	103
4.2.1	Observations	103
4.2.2	Data reduction	104
4.2.3	Post-reduction	105
4.3	Estimating the maximum rotation velocity	105
4.3.1	HI velocity profile	105
4.3.2	Major axis position-velocity diagram	105
4.3.3	Tilted-ring fit with ROTCUR	106
4.4	Comments on individual galaxies	108
4.4.1	D500-2	108
4.4.2	D500-3	109
4.4.3	D512-2	109
4.4.4	D564-8	110
4.4.5	D572-5	110
4.4.6	D575-1	111
4.4.7	D575-2	111
4.4.8	D575-5	112
4.4.9	D631-7	112
4.4.10	D640-13	113
4.4.11	D646-7	113
4.5	Analysis	114

4.5.1	The choice of the stellar mass-to-light ratio Υ_*	114
4.5.2	Line width corrections	115
4.5.3	Sources of uncertainties	116
4.5.3.1	Uncertainty of V_{\max}	116
4.5.3.2	Uncertainty of the baryonic mass	116
4.5.4	The baryonic Tully-Fisher relation	118
4.5.5	The scatter of the BTF	120
4.6	Conclusions	121
4.A	Appendix: Atlas	123
5	Summary and Conclusions	135
5.1	Summary	135
5.2	Future prospects	138
	Bibliography	141
	Acknowledgements	149
	Curriculum Vitae	151

List of Figures

2.1	Estimating the dynamical center of NGC 3198	15
2.2	Comparison of different center estimates of NGC 3198	16
2.3	Harmonic decomposition of NGC 3198: Fitted parameters	17
2.4	Harmonic decomposition of NGC 3198: Derived parameters	17
2.5	Offsets between dynamical and photometric center positions	20
2.6	Offsets between photometric centers and those from indiv. tilted-rings	20
2.7	Amplitude of the non-circular motions	22
2.8	Absolute amplitude of the non-circ. motions in the central parts: method 1	23
2.9	Absolute amplitude of the non-circ. motions in the central parts: method 2	23
2.10	Amplitudes of the non-circ. motions in the central parts w.r.t. $V(r)$: method 1	24
2.11	Amplitudes of the non-circ. motions in the central parts w.r.t. $V(r)$: method 2	24
2.12	Elongation of the potential	25
2.13	ROTCUR residuals vs. RESWRI residuals	26
2.14	ROTCUR residuals vs. amplitude of the non-circular motions	26
2.15	Constrained vs. unconstrained harmonic decomposition of NGC 3198	28
2.16	Constrained vs. unconstrained harmonic decomposition of DDO 154	29
2.17	Hermite vs. IWM VF: NGC 3198	30
2.18	Hermite vs. IWM VF: DDO 154	31
2.19	Effect of a $10''$ offset along the major axis: NGC 2366	32
2.20	Effect of a $10''$ offset along the minor axis: NGC 2366	33
2.21	Effect of a $10''$ offset along the major axis: NGC 2841	34
2.22	Effect of a $10''$ offset along the minor axis: NGC 2841	35
2.23	Summary panel for NGC 925: Center estimates and harm. decomp.	53
2.24	Summary panel for NGC 2366: Center estimates and harm. decomp.	54
2.25	Summary panel for NGC 2403: Center estimates and harm. decomp.	55
2.26	Summary panel for NGC 2841: Center estimates and harm. decomp.	56
2.27	Summary panel for NGC 2903: Center estimates and harm. decomp.	57
2.28	Summary panel for NGC 2976: Center estimates and harm. decomp.	58
2.29	Summary panel for NGC 3031: Center estimates and harm. decomp.	59
2.30	Summary panel for IC 2574: Center estimates and harm. decomp.	60
2.31	Summary panel for NGC 3521: Center estimates and harm. decomp.	61
2.32	Summary panel for NGC 3621: Center estimates and harm. decomp.	62
2.33	Summary panel for NGC 3627: Center estimates and harm. decomp.	63
2.34	Summary panel for NGC 4736: Center estimates and harm. decomp.	64
2.35	Summary panel for DDO 154: Center estimates and harm. decomp.	65
2.36	Summary panel for NGC 4826: Center estimates	66
2.37	Summary panel for NGC 5055: Center estimates and harm. decomp.	67
2.38	Summary panel for NGC 6946: Center estimates and harm. decomp.	68

2.39	Summary panel for NGC 7331: Center estimates and harm. decomp.	69
2.40	Summary panel for NGC 7793: Center estimates and harm. decomp.	70
3.1	Higher order harmonic decomposition: DDO 154	72
3.2	Higher order harmonic decomposition: NGC 925, NGC 2366, NGC 2403	77
3.3	Higher order harmonic decomposition: NGC 2841, NGC 2903, NGC 2976	78
3.4	Higher order harmonic decomposition: NGC 3031, NGC 3198, IC 2574	79
3.5	Higher order harmonic decomposition: NGC 3521, NGC 3621, NGC 3627	80
3.6	Higher order harmonic decomposition: NGC 4736, NGC 5055, NGC 6946	81
3.7	Higher order harmonic decomposition: NGC 7331, NGC 7793	82
3.8	Median amplitudes of the absolute residual velocity fields	83
3.9	Extended summary panel for DDO 154: Model VFs	85
3.10	Harmonic decomposition of the artificial velocity field of DDO 154	88
3.11	Harmonic decomposition of the artificial velocity field of NGC 3198	89
3.12	The detection efficiency of the non-circular motions	90
3.13	Summary panel for NGC 925: Model VFs	92
3.14	Summary panel for NGC 2366: Model VFs	93
3.15	Summary panel for NGC 2403: Model VFs	93
3.16	Summary panel for NGC 2841: Model VFs	94
3.17	Summary panel for NGC 2903: Model VFs	94
3.18	Summary panel for NGC 2976: Model VFs	95
3.19	Summary panel for NGC 3031: Model VFs	95
3.20	Summary panel for NGC 3198: Model VFs	96
3.21	Summary panel for IC 2574: Model VFs	96
3.22	Summary panel for NGC 3521: Model VFs	97
3.23	Summary panel for NGC 3621: Model VFs	97
3.24	Summary panel for NGC 3627: Model VFs	98
3.25	Summary panel for NGC 4736: Model VFs	98
3.26	Summary panel for NGC 5055: Model VFs	99
3.27	Summary panel for NGC 6946: Model VFs	99
3.28	Summary panel for NGC 7331: Model VFs	100
3.29	Summary panel for NGC 7793: Model VFs	100
4.1	Tilted-ring analysis of D500-2	109
4.2	Tilted-ring analysis of D512-2	110
4.3	Tilted-ring analysis of D564-8	111
4.4	Tilted-ring analysis of D575-2	112
4.5	Tilted-ring analysis of D631-7	113
4.6	Stellar Υ_* vs. (V-I) for different population synthesis models	114
4.7	How the choice of the population synthesis model affects the baryonic mass	114
4.8	The baryonic Tully-Fisher relation using different estimates for V_{\max}	117
4.9	The scatter of the baryonic Tully-Fisher relation	119
4.10	Summary panel for D500-2	123
4.11	Summary panel for D500-3	124
4.12	Summary panel for D512-2	124
4.13	Summary panel for D564-8	125
4.14	Summary panel for D572-5	125

4.15	Summary panel for D575-1	126
4.16	Summary panel for D575-2	126
4.17	Summary panel for D575-5	127
4.18	Summary panel for D631-7	127
4.19	Summary panel for D640-13	128
4.20	Summary panel for D646-7	128
4.21	Channel maps of D500-2	129
4.22	Channel maps of D500-3	130
4.23	Channel maps of D512-2	131
4.24	Channel maps of D564-8	132
4.25	Channel maps of D575-2	133
4.26	Channel maps of D631-7	134

List of Tables

2.1	Basic properties for the galaxies in the sample	10
2.2	Center positions for the galaxies in the sample.	18
2.3	Derived quantities from the harmonic decomposition.	19
3.1	Harmonic decomposition of artificial velocity fields	87
4.1	Mapping/Noise parameters	103
4.2	“Profile-width” sub-sample: derived parameters	107
4.3	“Rotation curve” sub-sample: derived parameters	107
4.4	Stellar Υ_* ratios	115

Introduction

Science is always an interplay between theory (or theoretical models) and experiments/observations. Experimentalists observe something yet unknown or not understood and as such, they need a theory to put their results in a physical context. A good theory should then not only explain the status quo, but also make testable predictions. These predictions can be — and usually are — tested again with new experiments/observations, which in turn can strengthen the theory, falsify it, or show the need for modification. The latter may be of the sort of restricting the application range of the theory (e.g., to starburst galaxies only), by revealing the necessity to include physical processes yet unaccounted for, or by showing the need to modify the handling of already implemented physical processes. Once a theory has withstood many experiments and has made several tested predictions, the confidence in the theory will grow until it is widely accepted.

1.1 Dark matter in galaxies

A theory which by now *is* widely accepted is the theory of Dark Matter (DM). This theory proposes that our Universe is dominated by matter which does not emit electro-magnetic radiation (therefore it is called “dark”), and can only be detected through its gravitational influence on the visible matter. The luminous matter that we can see, e.g., in stars and gas contributes only very little to the total energy budget of the Universe (e.g., Spergel et al. 2003, 2007).

1.1.1 The need for dark matter

The first indication for DM was given by Zwicky (1933, 1937), who measured velocity dispersions in the Coma cluster and concluded that large amounts of cold dark matter are required to bring the observations into agreement with the virial theorem. These results have been confirmed by many different authors (e.g., Abell 1977; Kent & Gunn 1982; Colless & Dunn 1996; Łokas & Mamon 2003).

Other evidence for the existence of dark matter within spiral galaxies came from the analysis of their rotation curves. In a system with a central potential, one expects a Keplerian decline of the rotation curve. However, Babcock (1939) and Oort (1940) analyzed the rotation curves of M31 and NGC 3115 and both found that the rotation velocities in the outer parts do not show a Keplerian decline, but are higher than expected from the visible stellar mass alone. This led Babcock and Oort to the speculation that the outer regions either show strong dust absorption, or have very high mass-to-light ratios.

The ultimate proof that there must be something unaccounted for (e.g., large amounts of dark matter, but see Sec. 1.1.2) came from the observation of neutral hydrogen with radio synthesis telescopes such as the Westerbork Synthesis Radio Telescope (WSRT). These telescopes provided, in contrast to previously used single-dish telescopes, both the sensitivity and the resolution to perform detailed studies of the dynamics of galaxies. Bosma (1978, 1981a,b) was the first to extensively study the kinematics and mass distribution for a larger sample of 25 spiral galaxies. His results showed that the HI rotation curves of the majority of the galaxies remain flat until the last measured point, far beyond the optical radius. If one assumes that Newton’s law of gravity is correct — and excludes the possibility that the stellar mass-to-light ratios rise to values of > 200 within the outskirts of the galaxies — these results imply large amounts of dark, unobserved matter in the outer regions of the galaxies. Many other authors have observed flat rotation curves as well (e.g., Rubin et al. 1978; Faber & Gallagher 1979; Rubin et al. 1982, 1985; van Albada et al. 1985; van Albada & Sancisi 1986; Begeman 1987), thus supporting the view that galaxies contain large amounts of dark matter and that the dynamics in the outer regions of spiral galaxies are dominated by this dark matter.

The cosmological model currently in favor is the Lambda Cold Dark Matter (Λ CDM) model. Within Λ CDM, the Universe has a cosmological constant Λ , which allows for the accelerating expansion of the Universe. The DM in the Λ CDM model is dark, cold, dissipationless, and collisionless. Although there are also other cosmological models, e.g., using hot dark matter (HDM) or warm dark matter (WDM), the CDM picture is at the moment the most promising of all models using any form of dark matter.

1.1.2 Alternatives to dark matter?

All explanations invoking dark matter assume that Newton’s law of gravity (or General Relativity on cosmological scales) is correct. However, this might be wrong. After all, for everyday purposes, a Galilei transformation is adequate to transform one inertial system of reference into another. We know, however, that for processes approaching the speed of light, the Galilei transformation breaks down and one has to use the Lorentz transformation instead. The Galilei transformation is only a special case of the Lorentz transformation for small velocities. The same might be true for the law of gravity, which lead to thoughts about alternative theories. Milgrom (1983a,b,c) propose that Newtonian gravity breaks down at low accelerations and formulated an alternative theory of gravity (MODified Newtonian Dynamics, MOND). MOND has been very successful in explaining the shapes of rotation curves without the need for unobservable, mysterious dark matter (e.g., Sanders 1996; Sanders & Verheijen 1998; McGaugh & de Blok 1998c; Sanders & McGaugh 2002). MOND also predicts the baryonic Tully-Fisher relation with a slope that is in excellent agreement with what has been found by recent studies (e.g., McGaugh et al. 2000; McGaugh 2005; Trachternach et al. 2008b, Chapter 4 of this thesis). However, MOND is — or until recently *was* — merely an empirical fitting formula without a real physical basis. Recent work by Bekenstein (2004, 2006) puts MOND on a firmer basis and also tries to include general relativity.

This thesis, however, is using the assumption of “classical” Newtonian dynamics, thus interpreting, e.g., the flat rotation curves by invoking dark matter.

1.1.3 Successes and problems of Λ CDM

Spergel et al. (2007) have used the *Wilkinson Microwave Anisotropy Probe* (WMAP) to show that we live in a Universe in which non-baryonic matter density accounts for only 22 % of the energy budget, whereas 74 % of the total energy density is in the form of a “dark energy”. Only 4 % are in the form

of baryonic matter and of that, just a small fraction can be called luminous (e.g. Walker et al. 1991; Persic & Salucci 1992).

Λ CDM has been very successful in explaining the large-scale structure of the Universe. The structure and substructure of the “cosmic web” from simulations like the Millennium Simulation (Springel et al. 2005) shows a remarkable similarity with real data from large redshift surveys like the Sloan Digital Sky Survey (SDSS, cf. Stoughton et al. 2002; Adelman-McCarthy et al. 2006). While the big successes of Λ CDM are on large scales, its challenge is on galactic scales. Two well-known problems of Λ CDM are the “missing satellites” problem and the “cusp/core” problem.

The former is based on the discrepancy between the number of observed and predicted small satellite galaxies: the N-body simulations usually predict a large number of dark matter substructures which survive over a long time. The number of observed satellite galaxies, however, is an order of magnitude smaller than what is predicted by the CDM models (e.g., Kauffmann et al. 1993; Klypin et al. 1999; Moore et al. 1999; Bullock et al. 2000; Benson et al. 2002).

This thesis focuses on the most prominent problem of CDM, the so-called cusp/core problem, which is about the slope of the inner part of galactic density profiles: Λ CDM models predict that all galaxies share a universal mass density profile. A commonly used empirical approximation to the mass density distribution in CDM halos is the so-called NFW profile by Navarro et al. (1996, 1997). The analytical form of the NFW profile is

$$\rho_{NFW}(r) = \frac{\rho_s}{(r/r_s)(1+r/r_s)^2}, \quad (1.1)$$

where r_s is the scale radius of the halo and ρ_s is related to the density of the Universe at the time of the collapse. At large radii, the NFW profile can be approximated with a power law with $\rho \sim r^{-3}$, whereas at small radii, it is described by a $\rho \sim r^{-1}$ power law; this is the so-called “cusp”. The CDM simulations show that cusps form naturally in a DM universe and that once they have been created, they will not dissolve. Therefore, if the NFW profile is the correct approximation, the Universe should be full of “cuspy” density profiles. Unfortunately, the easily accessible galaxies (i.e., the bright, high-mass spirals) are not suitable for settling this issue, as the contribution of an uncertain stellar mass-to-light ratio makes their modelled mass density profiles consistent with a broad range of density profiles (see, e.g., de Blok et al. 2008), including the cuspy NFW profile as well as “cored” profiles like the pseudo-isothermal halo:

$$\rho_{iso}(r) = \frac{\rho_0}{1+(r/r_c)^2}, \quad (1.2)$$

where ρ_0 is the central density of the halo and r_c is the core radius of the halo. The pseudo-isothermal halo profile contains no central cusp, but a so-called constant-density core.

For an unambiguous decomposition of the rotation curve into the different mass components (i.e., stars, gas, and dark halo), one would like to concentrate on galaxies with as little stars as possible, in order to minimize the effects from an uncertain stellar mass-to-light ratio. Fortunately, such galaxies do exist. We know nowadays that large numbers of low surface brightness (LSB) galaxies exist (e.g., Impey et al. 1988; de Blok et al. 1995, 1996; McGaugh 1996; Trachternach et al. 2006; Habertzettl et al. 2007). These LSB galaxies are — as well as dwarf galaxies — considered to be dark matter dominated at all radii (de Blok & McGaugh 1997; Verheijen 1997; Swaters et al. 2000), and thus should be the ideal test cases for dark matter models. However, it was noted very early that the density profiles from CDM simulations are too steep to fit the rotation curves of dwarf and LSB galaxies (e.g., Moore 1994; Flores & Primack 1994; Navarro et al. 1996; McGaugh & de Blok 1998b). Many authors have noted that the central parts of the density profiles of dwarf and LSB galaxies are better approximated by a constant-density core (e.g., de Blok et al. 2001a,b; Marchesini et al.

2002; Gentile et al. 2004; de Blok 2005; Zackrisson et al. 2006; Gentile et al. 2007; Oh et al. 2008). This is rather unexpected, because one would naturally think that (cold) dark matter models should work best for these dark matter dominated galaxies.

Therefore, several attempts have been made to explain the differences of the inferred slopes of the inner density profiles. Many of the early observational studies made use of HI observations, which — at that time — possessed only modest spatial resolution (beamsizes typically $15''$ - $30''$). It was therefore argued that these data could be affected by beam smearing, which tends to artificially flatten the slopes of the inferred density profiles (Swaters 1999; van den Bosch et al. 2000; Swaters et al. 2000). Subsequent high-resolution observations, however, showed that only a small fraction of the original HI data suffered from these effects and that HI rotation curves agree well with those from $H\alpha$ long-slit spectroscopy (e.g., McGaugh et al. 2001; de Blok et al. 2001a,b; Marchesini et al. 2002; de Blok & Bosma 2002; Gentile et al. 2004; Spekkens et al. 2005). Although beam-smearing is not an issue for $H\alpha$ long-slit spectra, Swaters et al. (2003a) argue that these data could be affected by several other systematic effects, which all lead to an underestimate of the central slope of the density profile. One of these effects is a slit offset with respect to the center of the galaxy. If the slit is not placed through the center of the galaxy, the inferred density profile will miss a potential central density cusp. However, some galaxies have been observed several times independently by different groups using data from different instruments. Given that these multiple results all point towards cored profiles suggests that (i) all observers have missed the center of the galaxy, or (ii) slit offsets do not play a significant role.

Since the advent of optical 2D velocity fields, this problem can be circumvented completely. Nevertheless, 2D velocity fields *have* been used to demonstrate that slit offsets were not responsible for the shallow density profiles (e.g., Kuzio de Naray et al. 2006). Most of the recent studies using 2D velocity fields seem to prefer *cored* profiles (e.g., Simon et al. 2003, 2005; Kuzio de Naray et al. 2006, 2008; Kuzio de Naray 2007; Spano et al. 2008), although a few are consistent with a variety of slopes ranging from *cuspy* to *cored* profiles (e.g., Swaters et al. 2003b).

Why do the density profiles from high resolution 2D velocity fields still differ from the predicted profiles? Neither low resolution, nor offsets from the centers of the galaxies are an issue for these data. Does the disagreement show the need for a radical modification of Λ CDM or are there still systematic issues which might possibly affect the observations? Currently, most theoreticians propose the latter and this thesis addresses the last remaining bastion protecting Λ CDM against a modification.

1.2 This thesis

As already mentioned by Frenk et al. (1988) and Dubinski (1994), CDM halos are not spherical, but tri-axial (see also Hayashi et al. 2004b, 2007). Therefore, it was noted (e.g., by Hayashi et al. 2004a; Hayashi & Navarro 2006) that gas moving in such an elliptical potential will not move on circular orbits, but show significant non-circular motions as well. According to these authors, the non-circular motions are largest in the centers of the galaxies (up to 15 percent of the maximum rotation velocity or 50 percent of the local rotation velocity) and therefore artificially flatten the inferred density profile, thus “hiding a cusp in a core” (direct quote from Hayashi & Navarro 2006). Large non-circular motions *can* create the illusion of a constant-density core, but one needs non-circular motions of the order of $\sim 20 \text{ km s}^{-1}$ over a large fraction of the disk in order to do so (de Blok et al. 2003).

Non-circular motions have been quantified by several groups (e.g., Schoenmakers et al. 1997; Wong et al. 2004; Gentile et al. 2005), but none of them report large enough non-circular motions to reconcile the cusp/core problem. However, most of the previous studies measuring non-circular

motions were either limited to a small sample (e.g., Gentile et al. 2005), or were based on data with moderate resolution (e.g., Schoenmakers et al. 1997). The work presented in this thesis has none of these drawbacks.

In Chapter 2, high resolution HI data from the THINGS survey (The HI Nearby Galaxy Survey, Walter et al. 2008; de Blok et al. 2008) are used to measure the non-circular motions in a sample of 19 spiral and dwarf galaxies. Before doing so, emphasis is laid on estimating the dynamical and photometric centers of the galaxies. After that, the non-circular motions are quantified by performing a harmonic decomposition of the velocity fields of the galaxies. Additionally, the elongation of the potential in the plane of the disk (i.e., the source of the predicted non-circular motions) is constrained, and a number of consistency checks to test the results against different systematic effects are presented. In Chapter 3, further tests are applied to the data in order to verify and support the previous conclusions. The analysis described in this chapter includes the decomposition of artificial velocity fields in order to test the effectiveness of the fitting-routine.

A different approach towards the cusp/core problem is presented in Chapter 4, where the scatter of the baryonic Tully-Fisher relation is used to derive firm upper limits for the ellipticity of the potential in the plane of the disk. As this ellipticity is believed to be the main source of the (large) non-circular motions (cf. Hayashi et al. 2004a; Hayashi & Navarro 2006), constraining the ellipticity constrains the non-circular motions as well. Finally, the main results of the thesis are summarized in Chapter 5.

Dynamical centers and non-circular motions in THINGS galaxies: implications for dark matter halos*

ABSTRACT

We present harmonic decompositions of the velocity fields of 19 galaxies from THINGS (The HI Nearby Galaxy Survey) which quantify the magnitude of the non-circular motions in these galaxies and yield observational estimates of the elongations of the dark matter halo potentials. Additionally, we present accurate dynamical center positions for these galaxies. We show that the positions of the kinematic and photometric centers of the large majority of the galaxies in our sample are in good agreement. The median absolute amplitude of the non-circular motions, averaged over our sample, is 6.7 km s^{-1} , with ~ 90 percent of the galaxies having median non-circular motions of less than $\sim 9 \text{ km s}^{-1}$. As a fraction of the maximum rotation velocity this translates into 4.5 percent on average. The non-circular motions in the centers of the galaxies, expressed as a fraction of the local rotation velocity, are 8 percent on average. The mean elongation of the gravitational potential, after a statistical correction for an unknown viewing angle, is 0.017 ± 0.020 , i.e., consistent with a round potential. Our derived non-circular motions and elongations are smaller than what is needed to bring Cold Dark Matter (CDM) simulations in agreement with the observations. In particular, the amplitudes of the non-circular motions are not high enough to hide the steep central mass-density profiles predicted by CDM simulations.

2.1 Introduction

Cosmological cold dark matter (CDM) simulations predict that all dark matter halos share a universal mass density profile. A well-known empirical approximation to the mass density distribution in CDM halos is the so-called NFW profile by Navarro et al. (1996, 1997). The NFW profile has the following form:

$$\rho_{NFW}(r) = \frac{\rho_s}{(r/r_s)(1+r/r_s)^2} \quad (2.1)$$

*C. Trachtenach, W.J.G. de Blok, F. Walter, E. Brinks, and R.C. Kennicutt Jr., *subm. to AJ*

At large radii, it can be approximated with a power law with $\rho \sim r^{-3}$. At small radii, it can be described with a $\rho \sim r^{-1}$ power law; this is the so-called “cusp”. This cusp has caused a lot of debate. Although it was noticed early on that CDM models produce profiles which are too steep to fit the rotation curves of dwarf and low surface brightness (LSB) galaxies (e.g., Moore 1994; Flores & Primack 1994; Navarro et al. 1996; McGaugh & de Blok 1998b), the origin of this discrepancy is still a matter of debate. As LSB galaxies are dark matter dominated at all radii (e.g., de Blok & McGaugh 1997; Verheijen 1997; Swaters et al. 2000), one would naturally think that CDM models should work best for those galaxies, as the contribution of stars is small. Many studies using either HI mapping or H α long-slit spectroscopy have concluded that the kinematics of most LSB and dwarf galaxies are inconsistent with steep mass density profiles, and instead are consistent with shallow “cored” inner profiles. These profiles are usually approximated by the pseudo-isothermal halo:

$$\rho_{iso}(r) = \frac{\rho_0}{1 + (r/r_c)^2}, \quad (2.2)$$

(see, e.g., de Blok et al. 2001a,b; Marchesini et al. 2002; de Blok & Bosma 2002; Gentile et al. 2004; de Blok 2005; Zackrisson et al. 2006; Gentile et al. 2007). However, as the original HI observations possessed only modest spatial resolution (beamsizes typically 15''- 30''), it was initially suggested that these data could be affected by beam smearing, which tends to artificially flatten the slopes of the inferred density profiles (Swaters 1999; van den Bosch et al. 2000; Swaters et al. 2000). Subsequent high-resolution observations (de Blok & Bosma 2002), however, showed that only a small fraction of the original HI data suffered from these effects. Although beam smearing is not an issue for H α long-slit spectra, they could be affected by several other systematic effects, which all lead to an underestimate of the central slope (see, e.g., Swaters et al. 2003a). One of these effects is a slit offset with respect to the galaxy center. This effect has in turn been tested using 2D optical velocity fields, and was found to play no significant role (see, e.g., Kuzio de Naray et al. 2006). It is, however, conceivable that the photometric and kinematic centers could be physically offset from each other, which would lead to a similar flattening effect if the “wrong” center is chosen as the basis for a dynamical analysis. The possible presence of such photometric and kinematic center offsets can be investigated directly with 2D velocity fields as these enable one to pinpoint the kinematic center without having to rely on optical centers.

Most of the studies using 2D velocity fields carried out in the last few years seem to prefer *cored* profiles (e.g., Simon et al. 2003, 2005; Kuzio de Naray et al. 2006; Spano et al. 2008), though a few are consistent with a variety of slopes ranging from *cuspy* to *cored* profiles (e.g., Swaters et al. 2003b).

But even if 2D velocity fields are used, systematic issues remain which potentially could affect the derived rotation curves. One which has been discussed by many authors is the effect of non-circular motions. These deviations from circular rotation could be caused by bars (Rhee et al. 2004), or a tri-axial halo (Hayashi et al. 2004a; Hayashi & Navarro 2006; Hayashi et al. 2007). Hayashi & Navarro (2006) proposed that the ellipticity of the dark matter halo induces large non-circular motions in the inner part of galaxies (up to ~ 15 percent of the maximum rotation velocity), thus making an intrinsic *cuspy* density profile appear *cored*. de Blok et al. (2003) simulated rotation curves and showed that non-circular motions of the order of $\sim 20 \text{ km s}^{-1}$ over a large fraction of the disk are needed to make them consistent with CDM halos (see also Gentile et al. 2005, who reach similar conclusions from an observational perspective).

Deviations from purely circular motions can have different causes, including chaotic non-circular motions induced for example by star formation (as investigated in detail for two THINGS dwarf galaxies in Oh et al. 2008), or systematic non-circular motions that relate to the potential (e.g., spiral arms, tri-axiality of the halo). Here, we will focus on the systematic non-circular motions. One way to

quantify these is to make a harmonic decomposition of the velocity field (VF). An extensive description of the harmonic decomposition technique is given in Schoenmakers (1999). Several groups have measured non-circular motions in disk galaxies using this technique (e.g., Schoenmakers et al. 1997; Wong et al. 2004; Gentile et al. 2005). However, none of these works report non-circular motions that are high enough to successfully “hide a cusp in a core” as proposed by Hayashi & Navarro (2006).

Choosing the correct position of the galaxy center is important not only for deriving the mass density slope of the dark matter halo, as discussed above, but also for a correct appraisal of the non-circular motions derived by performing a harmonic decomposition (cf. Schoenmakers 1999).

We will use the THINGS survey (Walter et al. 2008) to study in depth some of the aspects mentioned above. THINGS is a unique dataset to address these issues because of its high spatial and spectral resolution, and also because of its homogeneity (see the following section for more details on THINGS). The chapter is organized as follows. After a brief description of the sample in Section 2.2, we extensively discuss the various ways in which one can define the center of a galaxy in Section 2.3, and present our best determinations of the positions of the true kinematic centers of our sample galaxies. These center positions are used as inputs for our harmonic decompositions of the observed velocities, as described in Section 2.4. We illustrate the procedure and show the results for one case-study galaxy in detail in Section 2.5. Results for the rest of the sample are presented in the Appendix 2.A. Our results and several quality checks are presented and discussed in Section 2.6, and the conclusions are summarized in Section 2.7.

2.2 Sample and data

For our analysis, we used THINGS (The HI Nearby Galaxy Survey), an HI spectral line survey of 34 nearby disk galaxies obtained at the NRAO¹ VLA in B, C, and D arrays. THINGS contains a wide range of galaxy types, i.e., high and low surface brightness galaxies, grand design spirals and dwarf irregulars, barred and non-barred galaxies, all observed at high spatial ($\sim 10''$ for the natural weighted data cubes) and velocity ($\leq 5.2 \text{ km s}^{-1}$) resolution (for a detailed description of THINGS, see Walter et al. 2008). The great advantage of THINGS is that all galaxies have been observed, reduced, and analyzed in a homogeneous manner. The large range in physical properties enables one to study trends with, e.g., Hubble type. Furthermore, as THINGS was designed to overlap with the SINGS survey (Spitzer Infrared Nearby Galaxies Survey, Kennicutt et al. 2003), we can use its IRAC $3.6 \mu\text{m}$ images (which give a virtually dust-free view of the stellar disk) to directly compare photometric and kinematic centers.

In this chapter, we will study the kinematics of galaxies. We therefore use the sub-sample of THINGS for which de Blok et al. (2008) derived accurate rotation curves. This sample includes all rotationally dominated THINGS galaxies with inclinations larger than 40° , as well as NGC 6946, which, despite its lower inclination proved suitable for the derivation of a rotation curve. Basic properties of the galaxies of our sample are given in Table 2.1. For our analysis, we used the velocity fields which were created by fitting hermite polynomials to the velocity profiles from the natural weighted data cubes (as described in detail in de Blok et al. 2008). Additionally, we made use of the radio continuum maps from THINGS (Walter et al. 2008), as well as the $3.6 \mu\text{m}$ images from SINGS (Kennicutt et al. 2003).

¹The National Radio Astronomy Observatory is a facility of the National Science Foundation operated under cooperative agreement by Associated Universities, Inc.

TABLE 2.1: Basic properties for the galaxies in our sample.

Name	D	r_{25}	M_B	i	PA	V_{tot}	Δr	M_{HI}	μ_{mean}	Type
(1)	Mpc	kpc	mag	$^\circ$	$^\circ$	km s^{-1}	"	$10^8 M_\odot$	mag arcsec^{-2}	(11)
NGC 925	9.2	14.2	-20.04	66	287	115	3.0	45.8	23.3	7
NGC 2366	3.4	2.2	-17.17	64	40	55	6.0	6.5	23.9	10
NGC 2403	3.2	7.4	-19.43	63	124	135	4.0	25.8	21.6	6
NGC 2841	14.1	14.2	-21.21	74	153	260	5.0	85.8	21.4	3
NGC 2903	8.9	15.2	-20.93	65	204	190	7.0	43.5	21.4	4
NGC 2976	3.6	3.8	-17.78	65	335	80	3.5	1.4	21.9	5
NGC 3031	3.6	11.6	-20.73	59	330	200	6.0	36.4	21.2	2
NGC 3198	13.8	13.0	-20.75	72	215	150	6.0	101.7	22.6	5
IC 2574	4.0	7.5	-18.11	53	56	70	6.0	14.8	24.3	9
NGC 3521	10.7	12.9	-20.94	73	340	210	6.0	80.2	20.6	4
NGC 3621	6.6	9.4	-20.05	65	345	140	6.5	70.7	22.1	7
NGC 3627	9.3	13.9	-20.74	62	173	133	5.0	8.2	20.8	3
NGC 4736	4.7	5.3	-19.80	41	296	120	5.0	4.0	18.8	2
DDO 154	4.3	1.2	-14.23	66	230	48	6.5	3.6	24.2	10
NGC 4826	7.5	11.4	-20.63	65	121	150	5.0	5.5	20.7	2
NGC 5055	10.1	17.4	-21.12	59	102	190	5.0	91.0	21.3	4
NGC 6946	5.9	9.8	-20.61	33	243	220	3.0	41.5	23.0	6
NGC 7331	14.7	19.6	-21.67	76	168	233	3.0	91.3	21.5	3
NGC 7793	3.9	6.0	-18.79	50	290	130	6.0	8.9	22.0	7

NOTES: (1): the name of the galaxy; (2): distance as given in Walter et al. (2008); (3): radius of the major axis of the galaxy at the $\mu_B = 25 \text{ mag arcsec}^{-2}$ isophote level, taken from LEDA (LEDA.UNIV-LYON.FR); (4): absolute B -band magnitude as given in Walter et al. (2008); (5): average inclination as given in de Blok et al. (2008); (6): average position angle as given in de Blok et al. (2008); (7): total rotation velocity (used for the normalization of the non-circular motions); (8): adopted spacing of the tilted-rings; (9): HI mass as listed in Walter et al. (2008); (10): mean surface brightness from LEDA (LEDA.UNIV-LYON.FR); (11): morphological type from LEDA (LEDA.UNIV-LYON.FR).

2.3 Estimating galaxy centers

There are several ways in which one can determine the position of the center of a galaxy. As central activity in galaxies is likely to coincide with the bottom of the galaxy potential well, a central compact radio source is a good indicator of the center of a galaxy. Similarly, nuclear star clusters can be used to locate the center. One can also fit ellipses to the surface brightness distribution as well as construct a tilted-ring model using the kinematic data to obtain additional, independent estimates.

Ideally, these different determinations should all coincide. Large discrepancies can indicate strong disturbances, caused, e.g., by spiral arms or strong bars, or a genuine offset between the kinematic and photometric center. For the majority of our galaxies, multiple center estimates can be derived, namely kinematic centers derived from the velocity fields, as well as photometric centers as deduced from the 20-cm radio continuum maps taken from THINGS and from the *Spitzer* 3.6 μm images.

As will be shown in the subsequent analysis, for most galaxies the kinematic center position agrees with the position of the radio continuum source and/or the center as derived from the IRAC image within the uncertainties. In those cases where the photometric and kinematic centers agree, we have generally adopted one of the photometric centers as our best center position, given that the photometric centers usually have smaller uncertainties. Note that it is still important to evaluate any possible differences between the two types of centers, even when both are well-defined. This will enable a better understanding of possible systematic effects inherent in the method, which is important for the interpretation of the results from galaxies where the centers may not be as well-defined.

Below follows a description of the methods used to determine the various center estimates. An application of these methods is given for one “case-study” galaxy in Section 2.5. Detailed and more technical descriptions are then given for all galaxies in Appendix 2.A.

2.3.1 Radio continuum

A nuclear point source in the radio continuum is usually associated with a central compact object, which naturally should be at (or very close to) the bottom of the potential well of the galaxy. For all galaxies which show such a source in the THINGS radio continuum maps, its position was determined by fitting a Gaussian to the central source. The uncertainties for the center positions estimated in this way are all similar ($\leq 1''$) and we therefore do not show individual uncertainties for center estimates deduced from the radio continuum.

2.3.2 *Spitzer*/IRAC 3.6 μm image

We make use of the high-resolution 3.6 μm images from SINGS (Kennicutt et al. 2003)². These allow an almost dust-free view of the predominantly old stellar populations, though we note that the 3.6 μm band can also contain some trace emission from hot dust, PAHs and AGB stars.

For all galaxies in our sample, we determined the central 3.6 μm position by fitting ellipses using the GIPSY³ task ELLFIT, taking care that the ellipse fits were not affected by small scale structures. For those galaxies which also show a well-defined nuclear source in the 3.6 μm image, we additionally derived the central position by fitting a Gaussian to the central source. The two different center estimates generally agree very well. However, as the center position derived by fitting a Gaussian to the central source is usually better constrained as the center from ELLFIT, we only list the former (where available) in Table 2.2. Because of the homogeneous and consistently small positional uncertainty of less than $1''$, we do not list these here.

2.3.3 Kinematic center

In addition to the photometric centers mentioned above, we also derive kinematic centers using the GIPSY task ROTCUR. This task fits a set of tilted rings of a given width to the velocity field of a galaxy and determines their central positions, rotation and systemic velocities, inclinations and position angles. We use the best available center position (i.e., a central continuum source, if present, otherwise a nuclear source in the 3.6 μm image and as a last resort the center as derived using ELLFIT) as an initial center estimate for ROTCUR and make a fit with all parameters left free (including the

²A small number of galaxies in our sample were not part of SINGS. For these galaxies, the data were retrieved from the *Spitzer* archive.

³GIPSY, the Groningen Image Processing SYstem (van der Hulst et al. 1992)

center). By averaging the central positions over a radial range unaffected by spiral arms or other large-scale disturbances, we derive the position of the kinematic center for each galaxy.

The determination of the positions of all centers are described in Appendix 2.A, and all center estimates are summarized in Table 2.2, where our adopted best center positions are shown in bold face.

2.4 Harmonic decomposition

We perform a harmonic decomposition of the velocity fields by decomposing the velocities found along the tilted-rings into multiple terms of sine and cosine.

Following Schoenmakers (1999), we describe the line-of-sight velocity, v_{los} , as:

$$v_{\text{los}}(r) = v_{\text{sys}}(r) + \sum_{m=1}^N c_m(r) \cos m\psi + s_m(r) \sin m\psi, \quad (2.3)$$

where N is the maximum fit order used, r is the radial distance from the dynamical center, ψ is the azimuthal angle in the plane of the disk, and v_{sys} is the 0th order harmonic component, c_0 . Initial tests showed that a decomposition of the velocity fields up to third order (i.e., $N = 3$) is sufficient to capture most of the non-circular signal, as is described in Section 2.6.4.1.

The usual description of the apparent velocity, under the assumption of purely circular motion can be retrieved by only including $m = 0$ and $m = 1$ terms in Eq. 2.3, i.e.,

$$v_{\text{los}}(r) = v_{\text{sys}}(r) + c_1(r) \cos \psi + s_1(r) \sin \psi, \quad (2.4)$$

and by ignoring streaming (radial) motions (i.e., $s_1 = 0$). The circular rotation velocity corresponds therefore to c_1 . Note that the dependence on inclination is included in the c_m and s_m terms. For the following discussion it is worthwhile to repeat a few rules of thumb which apply to harmonic decompositions as given in Schoenmakers et al. (1997) and Schoenmakers (1999):

(1) A perturbation of the gravitational potential of order m will cause $m + 1$ and $m - 1$ harmonics in the velocity field (so an $m = 2$ two-armed spiral component will cause $m = 1$ and $m = 3$ harmonics in the velocity field).

(2) Perturbations in the gravitational potential are independent and can therefore be added. The same holds for velocity perturbations.

(3) The elongation of the potential ϵ_{pot} in the plane of the disk of the galaxy can be calculated at each radius as follows:

$$\epsilon_{\text{pot}} \sin 2\varphi_2 = (s_3 - s_1) \frac{1 + 2q^2 + 5q^4}{c_1(1 - q^4)}, \quad (2.5)$$

where $q = \cos i$. The only remaining unknown quantity is φ_2 , the unknown angle in the plane of the ring between the minor axis of the elongated ring and the observer.

(4) Velocities induced by a global elongation of the potential will result in a constant offset in $\epsilon_{\text{pot}} \sin 2\varphi_2$. Velocities induced by spiral arms occur on much smaller scales, and will therefore only lead to perturbations (“wiggles”) around this offset.

(5) If the fitted inclination is close to the intrinsic inclination of the disk, then $c_3 = 0$. Small offsets of a few km s^{-1} result in only small (1-2 degree) inclination offsets.

We use the GIPSY task RESWRI. This task performs a tilted-ring fit assuming circular rotation, creates a model velocity field, subtracts this from the original velocity field, and does a harmonic expansion of the residuals. RESWRI does not down-weight velocities along the minor axis as is usually

done in standard rotation curve analysis. For the width of the annuli (cf. Col (8) of Table 2.1), we chose half the beam width; neighboring rings are thus not independent.

We calculate the quadratically added amplitude (“power”) for each order of the harmonic decomposition using

$$A_1(r) = \sqrt{s_1^2(r)}, \quad (2.6)$$

for $m = 1$ (note that c_1 corresponds to the circular velocity and is not included in the calculation of the amplitude of $A_1(r)$), and

$$A_m(r) = \sqrt{c_m^2(r) + s_m^2(r)}, \quad (2.7)$$

for $m > 1$.

Additionally, we calculate the quadratically added amplitude of all (i.e., up to $N = 3$) non-circular harmonic components (“total power”):

$$A_r(r) = \sqrt{s_1^2(r) + c_2^2(r) + s_2^2(r) + c_3^2(r) + s_3^2(r)}. \quad (2.8)$$

The radial variation of $A_m(r)$ and $A_r(r)$ can be checked for coincidence with visible features in the galaxies. To quantify the power of the non-circular motions in a compact way, we also use \tilde{A}_m , the median of $A_m(r)$ defined for each value of m , and \tilde{A}_r , the median of $A_r(r)$. We derive two values for \tilde{A}_m and \tilde{A}_r , one for the entire radial range and one for the inner 1 kpc (for those galaxies where sufficiently high signal-to-noise HI is present in the inner parts). The 1 kpc choice is motivated by the fact that the distinction between a cusp and a core can be made most clearly at radii less than ~ 1 kpc (de Blok et al. 2001a; de Blok 2004), and it is therefore important to separately quantify the non-circular motions in this inner region. Note that wherever we use the term “entire radial range”, we refer to all radii over which our analysis extends. The outer radius of this “entire radial range” is usually limited by the sensitivity of the HI data. The outer regions of galaxies often show sparsely filled tilted-rings. Although these may still be used to estimate a rotation curve assuming circular motions (e.g., with ROTCUR), a harmonic decomposition has more free parameters (i.e., the c_i and s_i) and is therefore more sensitive to sparsely filled tilted-rings. We have restricted our analysis to radii for which RESWRI was able to produce reasonable and stable results (thus excluding tilted-rings showing, e.g., a rotation velocity of 1000 km s^{-1} or a harmonic component of zero amplitude, but with a 100 km s^{-1} uncertainty).

Additional to discussing the amount of non-circular motions in absolute terms, we will express the magnitude of the non-circular motions as a fraction of the local rotation velocity $V(r)$ and as a fraction of the total rotation velocity V_{tot} . The latter is defined as the rotation velocity of the flat part of the rotation curve, or as the maximum rotation velocity if the rotation curve is still rising in the outermost point.

RESWRI creates a residual velocity field which can be used as an indicator for those non-circular motions that are not captured with the harmonic decomposition (as will be shown in Section 2.6.4.1). As the residual velocity fields contain only values which scatter around a mean zero level, we use *absolute* residual velocity fields in our analysis.

Finally, as mentioned in Schoenmakers (1999), the center position should be kept fixed during the harmonic decomposition. This is because a galaxy which has real, physical c_2 and s_2 terms in its velocity field would, in the case of an unconstrained center position, appear to have a center which drifts in such a way as to minimize these terms. Moreover, rapidly varying center positions at small radii (with offsets larger than the relevant ring radii) have no physical basis.

2.5 NGC 3198 — A case–study

In this section, we present the results from our two analyses — namely the derivation of the center estimates and the harmonic decomposition — in detail for one galaxy. The purpose of this section is to explain the conventions and notations used and demonstrate our methods for one galaxy in our sample. A complete description and discussion of all galaxies from our sample is given in the Appendix 2.A.

2.5.1 Center estimates

The $3.6\ \mu\text{m}$ IRAC image of NGC 3198 shows two well-defined spiral arms, emanating from a prominent bulge. The central component has a nuclear point source embedded, which has a counterpart in the radio continuum. The IRAC and continuum centers agree to within $1''$. For ease of reference, and in order to have a compact notation for the center positions, we will in our discussion frequently refer to positions with respect to the pointing center (as listed in Walter et al. 2008). This pointing center has no physical meaning, and merely provides a convenient zero-point. We will refer to the offsets from the pointing center as δX (positive in the direction of decreasing right ascension) and δY (positive in the direction of increasing declination). Both are expressed in arcseconds. Note that we list the full coordinates of all center positions we derive in Table 2.2 (with the position used for further analysis shown in bold face).

In our determination of the kinematic center of NGC 3198, we start with an unconstrained ROTCUR fit with the position of the radio continuum center ($\delta X = -1''.4$, $\delta Y = -0''.1$) as an initial estimate. Fig. 2.1 shows the variation of the center position from the ROTCUR fit over the radial range of the galaxy, together with our best photometric center. As can be seen by the variation of δX and δY , the outer parts ($r \geq 150''$) of NGC 3198 are strongly affected by the spiral arms. For the derivation of the dynamical center, we therefore restrict the averaging of δX and δY to radii with $r \leq 100''$ (indicated in Fig. 2.1 by the vertical lines at these radii). The dynamical center derived in such a way is offset from the pointing center by $\delta X = -1''.4 \pm 1''.7$, $\delta Y = -0''.2 \pm 2''.1$ (i.e., to the south-east).

To put our estimates for the center positions in context, we show them together with the IRAC and radio continuum map (where available) overlaid on the central $150'' \times 150''$ of the HI total intensity map (cf. Fig. 2.2). Also shown are the central positions of the individual tilted-rings. As can be seen, all center positions agree well within the uncertainties and to within one natural-weighted beam (hereafter referred to as “the beam”) and we therefore adopt the center as derived from the radio continuum map as our best center position.

2.5.2 Harmonic expansion

The radial distribution of all fitted parameters from the harmonic decomposition of NGC 3198 are shown in Fig. 2.3. The PA of NGC 3198 rises swiftly within the inner $200''$, and then slowly declines. The inclination varies in the inner parts over a range of about five degrees, but shows a steady increase beyond $r \sim 450''$, indicating that the outer disk is warped. The c_3 term is small for all radii, meaning that the fitted inclination is close to the intrinsic inclination of the disk. Although there is no global offset from zero for c_2 and s_2 , they show small deviations at radii coinciding with the locations of spiral arms in the $3.6\ \mu\text{m}$ image of NGC 3198, or in the total HI map presented in Walter et al. (2008).

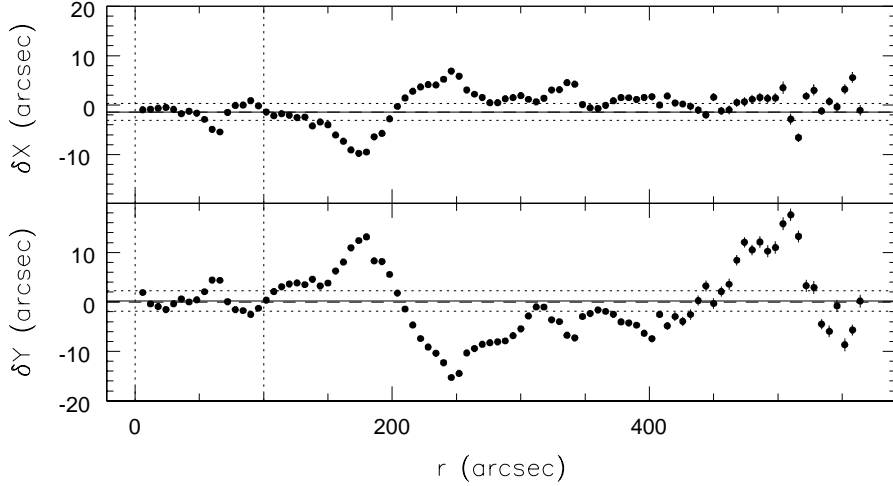


FIG. 2.1: Radial variation of the center positions of the individual tilted-rings derived in an unconstrained fit with ROTCUR. The center positions are given as an offset from the pointing center (in arcseconds). The two vertical lines at $r = 0''$ and $r = 100''$ denote the radial range over which the center positions were averaged in order to derive a kinematic center. The resulting kinematic center (together with its standard deviation) is indicated by the black solid (dotted) lines. Our best center position (in this case from the radio continuum) is indicated by the dashed horizontal line, which is however barely distinguishable from the kinematic estimate because of the good agreement between these two.

The s_1 and s_3 terms are best described as wiggles caused by spiral arms on top of a slight offset. The amplitudes of all non-circular components (c_2 , c_3 , s_1 , s_2 , s_3) are generally only a few km s^{-1} .

In Fig. 2.4, we show derived parameters which were calculated according to Eqs. 2.5-2.8. The median amplitudes of the individual harmonic components, derived following Eqs. 2.6 and 2.7, are similar in amplitude, ranging from $\tilde{A}_m \sim 2-3 \text{ km s}^{-1}$ (when averaged over the entire radial range), or ≤ 2 percent of V_{tot} . For the inner 1 kpc, the amplitudes are even smaller ($\tilde{A}_m < 1.5 \text{ km s}^{-1}$). The distribution of $A_r(r)$ (cf. Eq. 2.8) shows that the amplitude of the non-circular motions is $A_r(r) \leq 8 \text{ km s}^{-1}$ for most radii. The median amplitude is $\tilde{A}_r \sim 4.5 \text{ km s}^{-1}$ when averaged over the entire radial range, and $\tilde{A}_r \sim 1.5 \text{ km s}^{-1}$ when averaged over the inner 1 kpc only.

The elongation of the potential, $\epsilon_{\text{pot}} \sin(2\varphi_2)$, derived according to Eq. 2.5 is small over most of the radial range, but shows traces of the same spiral arms which cause the variation in, e.g., the s_3 component. Inwards of $r \sim 30''$, the elongation is rather unconstrained — mainly because of the larger uncertainty in the derived inclination, which enters into the uncertainty in ϵ_{pot} as a fourth power. The weighted mean elongation of the potential is fairly small with $\langle \epsilon_{\text{pot}} \sin(2\varphi_2) \rangle = 0.017 \pm 0.020$, and within the uncertainties consistent with zero.

As mentioned in Section 2.4, RESWRI creates residual velocity fields, which can be used to quantify the signal which was not captured in the harmonic expansion. For NGC 3198, we find a median absolute value of $\sim 2.6 \text{ km s}^{-1}$, showing that a harmonic decomposition up to third order is capable of capturing most non-circular motions. This is addressed more fully in Section 2.6.4.1.

The results from the harmonic decompositions are summarized (for all galaxies) in Table 2.3 and detailed descriptions for all galaxies are given in Appendix 2.A.

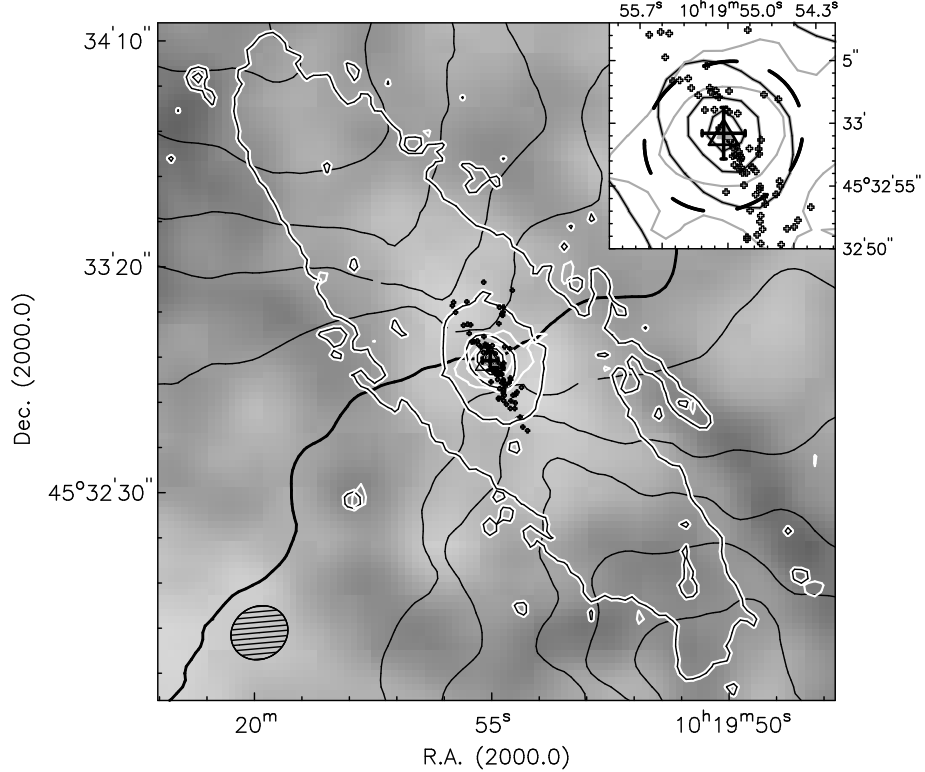


FIG. 2.2: This figure shows the inner $150'' \times 150''$ of NGC 3198. The integrated natural-weighted HI map is shown in grayscales. The beam is indicated in the bottom-left corner. The black contours show iso-velocity contours from the hermite velocity field. The thick black contour is shown at 663 km s^{-1} and represents the systemic velocity given in de Blok et al. (2008). The other velocity contours are spaced by 25 km s^{-1} . The thin black contours overlaid on the thick white contours represent the $3.6 \mu\text{m}$ IRAC image. They are drawn at 2, 5, 10, 20, and 50 percent of the maximum intensity level. The white contours represent the THINGS radio continuum map, and are drawn at 10, 20, and 50 percent of the peak intensity. The black dots indicate the individual center positions from ROTCUR and the black cross represents the derived dynamical center together with its uncertainty. The derived center from the $3.6 \mu\text{m}$ image is shown as a gray, filled triangle, whereas the one from the radio continuum is shown as a black, open triangle. **Inset:** To better highlight the different center estimates, we show an inset of the innermost $18''$ in the upper-right corner. For clarity reasons we do not show the HI grayscale and velocity field contours here. The contours from the $3.6 \mu\text{m}$ image are shown in black and are given at the same intensity levels as in the main plot. The same holds for the radio continuum contours, which are shown here in gray. The individual center estimates from ROTCUR are shown as small crosses. In the inset, the beam is indicated by the thick black dashed ellipse and is centered on our best center position.

2.6 Results

In the previous section and in the detailed notes on the individual galaxies in Appendix 2.A, we show how the center positions are derived and present the results of the harmonic decompositions. The different center estimates are summarized in Table 2.2, where our adopted positions are shown in bold face. The results from the harmonic decomposition are summarized in Table 2.3.

In this section, we will put these results in context and address some of the astrophysical questions discussed in the Introduction. Section 2.6.1 will deal with the results of the center estimates, whereas

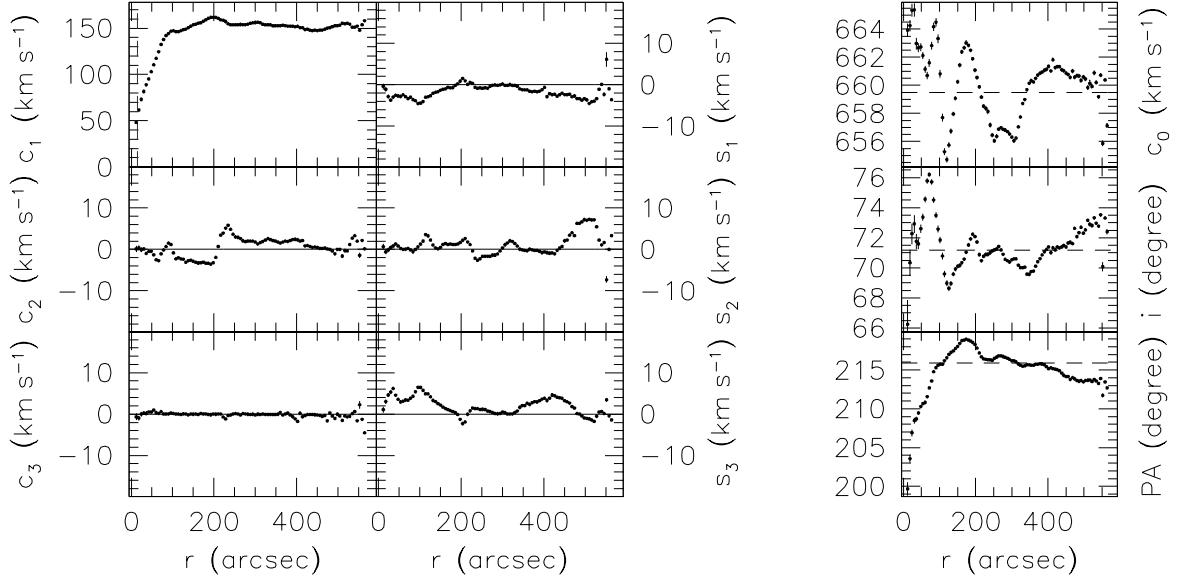


FIG. 2.3: **Left:** circular (c_1), and non-circular (c_2 , c_3 , s_1 , s_2 , s_3) harmonic components (derived according to Eq. 2.3), all corrected for inclination and plotted vs. radius. The dashed vertical line in the panel showing the distribution of c_1 indicates the radius corresponding to 1 kpc. **Right:** systemic velocity c_0 , inclination and position angle, plotted vs. radius. The dashed horizontal lines represent the error weighted means. The inclination and position angle are from the tilted-ring fit assuming circular rotation. The error bars shown in all panels of this figure are the formal uncertainties from RESWRI.

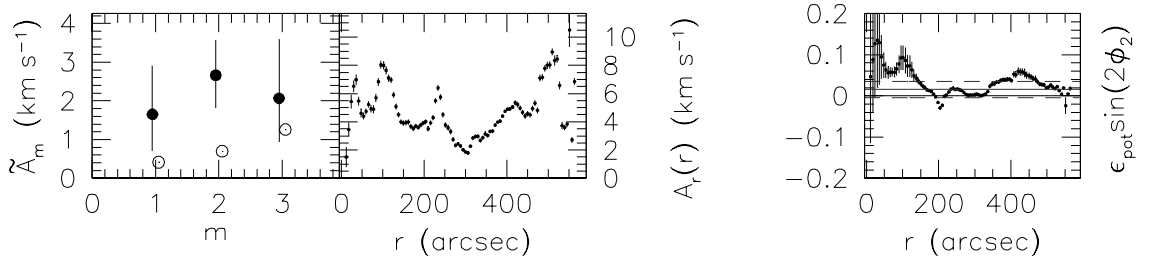


FIG. 2.4: **Left:** \tilde{A}_m , the median amplitudes of the individual harmonic components, derived following Eqs. 2.6 and 2.7, plotted vs. harmonic number m . The error bars denote the upper and lower quartile of the distribution of $A_m(r)$. We have calculated the median amplitudes twice: once for the entire radial range (filled circles), and once for the inner 1 kpc (open circles). Note that in the case of NGC 3198, the median for the inner 1 kpc has no error bars, as the inner 1 kpc contains only one data point. **Middle:** $A_r(r)$, the quadratically added amplitude of all non-circular components (derived following Eq. 2.8) vs. radius. The errors were estimated assuming Gaussian error propagation. For most radii, the amplitude is $A_r(r) \leq 8 \text{ km s}^{-1}$. **Right:** the radial distribution of the elongation of the potential, $\epsilon_{\text{pot}} \sin(2\phi_2)$, derived according to Eq. 2.5. The uncertainties are also estimated assuming Gaussian error propagation. The elongation is fairly unconstrained in the inner $\sim 30''$, mainly because of the large uncertainty in the inclination, which enters into the uncertainty of ϵ_{pot} as a fourth power. The weighted mean elongation (and its standard deviation) are represented by the horizontal dotted (and dashed) lines. The weighted mean elongation of NGC 3198 is $\langle \epsilon_{\text{pot}} \sin(2\phi_2) \rangle = 0.017 \pm 0.020$, and thus consistent with a round potential.

TABLE 2.2: Center positions for the galaxies in the sample.

Name	kinematic (ROTCUR) center		3.6 μm center		radio continuum center	
	α_{2000} (h m s)	δ_{2000} ($^{\circ}$ ' ")	α_{2000} (h m s)	δ_{2000} ($^{\circ}$ ' ")	α_{2000} (h m s)	δ_{2000} ($^{\circ}$ ' ")
NGC 925	02 27 16.5\pm0.7	+33 34 43.5\pm4.1	02 27 17.0 ^a	+33 34 42.4 ^a
NGC 2366	07 28 53.9\pm0.7	+69 12 37.4\pm7.8	07 28 53.4 ^a	+69 12 40.3 ^a
NGC 2403	07 36 51.1\pm0.9	+65 36 02.9\pm4.2	07 36 51.0 ^a	+65 36 02.1 ^a
NGC 2841	09 22 02.6 \pm 0.1	+50 58 35.3 \pm 1.0	09 22 02.7	+50 58 35.4	09 22 02.7	+50 58 35.4
NGC 2903	09 32 10.0 \pm 0.2	+21 30 02.5 \pm 2.2	09 32 10.1	+21 30 04.9	09 32 10.1	+21 30 04.3
NGC 2976	09 47 14.9 \pm 0.5	+67 55 00.8 \pm 1.4	09 47 15.3	+67 55 00.0
NGC 3031	09 55 33.5 \pm 0.6	+69 03 52.0 \pm 3.9	09 55 33.3	+69 03 54.6	09 55 33.1	+69 03 54.7
NGC 3198	10 19 55.0 \pm 0.2	+45 32 59.2 \pm 2.0	10 19 55.0	+45 32 59.1	10 19 55.0	+45 32 58.9
IC 2574 ^b	10 28 27.5\pm2.7	+68 24 58.7\pm10.4
NGC 3521	11 05 48.6 \pm 0.1	-00 02 08.4 \pm 1.4	11 05 48.6	-00 02 09.2
NGC 3621	11 18 16.6 \pm 0.2	-32 48 48.5 \pm 6.5	11 18 16.5	-32 48 50.9
NGC 3627	11 20 15.3 \pm 0.2	+12 59 22.7 \pm 4.8	11 20 15.0	+12 59 29.2	11 20 15.0	+12 59 29.6
NGC 4736	12 50 53.0 \pm 0.2	+41 07 14.2 \pm 2.0	12 50 53.1	+41 07 11.9	12 50 53.0	+41 07 13.2
DDO 154	12 54 05.9\pm0.2	+27 09 09.9\pm3.4
NGC 4826	12 56 43.6 \pm 0.1	+21 40 59.3 \pm 0.8	12 56 43.6	+21 40 59.2	12 56 43.6	+21 41 00.3
NGC 5055	13 15 49.3 \pm 0.2	+42 01 45.1 \pm 1.3	13.15 49.3	+42 01 45.5	13 15 49.2	+42 01 45.3
NGC 6946	20 34 52.4 \pm 0.6	+60 09 11.8 \pm 5.9	20 34 52.3	+60 09 14.3	20 34 52.2	+60 09 14.4
NGC 7331	22 37 04.1 \pm 0.1	+34 24 54.4 \pm 2.2	22 37 04.1	+34 24 56.5
NGC 7793	23 57 49.8 \pm 0.2	-32 35 25.2 \pm 2.1	23 57 49.7	-32 35 27.9

^aDerived by fitting ellipses with ELLFIT

^bThe center coordinates of IC2574 were derived using a bulk velocity field cleared of non-circular motions as presented in Oh et al. (2008)

NOTES: The uncertainties in the ROTCUR centers are given in units of seconds (for right ascension) and arcseconds (for declination). The center position chosen for subsequent analysis is shown in bold face.

Section 2.6.2 deals with the results of the harmonic decompositions. In Section 2.6.3, we compare the latter with predictions from CDM simulations. In Section 2.6.4, we present and discuss several consistency checks which we applied to test our methods.

2.6.1 Quality of the center estimates

In this section, we discuss the quality and reliability of our center positions. An intrinsically cuspy density profile can be mistaken for a flat, constant-density one, if possible offsets between the kinematic and the photometric center of a galaxy are ignored. Using the photometric center to derive a rotation curve or a mass model in the presence of such an offset will result in a less steep rotation curve and density profile. A potential cusp could then appear as a core-like density profile.

As we have determined the kinematic and photometric centers of the galaxies in our sample, we can directly test if such offsets exist. This is shown in Fig. 2.5, where we show the offsets between the dynamical and the best (photometric) center estimates for the 15 galaxies in our sample with well-constrained photometric centers. For 13 out of the 15 galaxies shown in Fig. 2.5, the dynamical center differs by less than the size of one beam from the best (photometric) center — and for 10 galaxies the agreement is even better than half the size of the beam. Only two galaxies (NGC 3627 and NGC 6946) show moderate offsets of between one and two beam sizes. Given that the former galaxy is extremely asymmetric and the latter has a low inclination which makes fitting tilted-rings more difficult, these

TABLE 2.3: Derived quantities from the harmonic decomposition.

Name	\tilde{A}_r km s ⁻¹	$\tilde{A}_{r,1\text{kpc}}$ km s ⁻¹	$\tilde{A}_r/V_{\text{max}}$ percent	$\langle \epsilon_{\text{pot}} \sin(2\varphi_2) \rangle$	\tilde{M}_{resid} km s ⁻¹	r_{max} "
(1)	(2)	(3)	(4)	(5)	(6)	(7)
NGC 925	6.30 ^{+1.63} _{-1.74}	9.45 ^{+0.64} _{-2.98}	5.5	0.000 ± 0.046	3.0	282
NGC 2366	2.94 ^{+1.46} _{-1.24}	1.17 ^{+0.12} _{-0.40}	5.3	0.004 ± 0.066	2.4	252
NGC 2403	4.03 ^{+1.39} _{-1.33}	2.60 ^{+0.59} _{-0.48}	3.0	-0.022 ± 0.025	2.9	950
NGC 2841	6.71 ^{+4.67} _{-3.54}	...	2.6	-0.001 ± 0.014	3.5	635
NGC 2903	6.10 ^{+3.64} _{-2.68}	13.55 ^{+2.70} _{-6.18}	3.2	0.006 ± 0.028	2.8	602
NGC 2976	2.81 ^{+0.75} _{-1.18}	2.18 ^{+0.77} _{-0.55}	3.5	-0.010 ± 0.018	2.1	147
NGC 3031	9.14 ^{+2.08} _{-3.05}	...	4.6	0.007 ± 0.045	3.0	840
NGC 3198	4.49 ^{+1.00} _{-0.91}	1.50 ^a	3.0	0.016 ± 0.020	2.6	565
IC 2574	3.75 ^{+1.78} _{-1.04}	1.36 ^{+0.49} _{-0.06}	5.4	0.012 ± 0.047	2.7	505
NGC 3521	8.80 ^{+3.45} _{-4.62}	3.12 ^{+12.67} _{-1.77}	4.2	0.017 ± 0.019	4.5	415
NGC 3621	3.36 ^{+1.00} _{-1.09}	5.52 ^{+0.94} _{-3.21}	2.4	0.002 ± 0.022	2.3	600
NGC 3627	28.49 ^{+10.91} _{-5.87}	...	14.7	-0.024 ± 0.071	3.6	165
NGC 4736	10.01 ^{+3.63} _{-2.14}	8.79 ^{+1.87} _{-1.56}	8.3	-0.055 ± 0.149	2.5	400
DDO 154	1.61 ^{+0.42} _{-0.65}	1.43 ^{+0.14} _{-0.53}	3.4	0.024 ± 0.033	1.2	325
NGC 5055	4.11 ^{+1.61} _{-0.73}	8.38 ^{+11.14} _{-2.60}	2.2	-0.003 ± 0.025	3.1	450
NGC 6946	7.28 ^{+3.12} _{-2.88}	...	3.6	0.004 ± 0.069	3.4	420
NGC 7331	5.94 ^{+1.65} _{-1.21}	...	2.6	-0.003 ± 0.017	4.2	297
NGC 7793	5.08 ^{+0.90} _{-1.677}	3.41 ^{+0.64} _{-0.48}	3.9	-0.067 ± 0.085	2.2	372
Sample mean	6.72	4.80	4.5	0.011	2.9	
Sample rms	5.91	3.99	2.9	0.013	0.8	

^aThis value has no upper or lower quartile as the inner 1 kpc of NGC 3198 contain only one data point.

NOTES: (1): the name of the galaxy; (2): \tilde{A}_r , the median of the quadratically added amplitude of the non-circular motions, averaged over the entire radial range. Error bars indicate the lower and upper quartile; (3): same as (2) but averaged over the inner 1 kpc only; (4): the percentage the non-circular motions contribute to the maximum rotation velocity; (5): the weighted mean elongation of the potential and its uncertainty; (6): the median of the absolute residual velocity field after the harmonic decomposition; (7): maximum radius for the averaging of \tilde{A}_r and ϵ_{pot} . The bottom two rows contain the mean values and their rms over the entire sample. For ϵ_{pot} , this value represents the weighted mean.

outliers can be understood and do not necessarily suggest a real offset between a dynamical and a photometric center.

The strength of the agreement we find does depend on how well-constrained the dynamical center estimates are. A tightly constrained kinematic center position which agrees with a well-determined photometric center allows one to draw strong conclusions. A weakly constrained kinematic center less so, as the increased uncertainties allow agreement with a whole range of photometric centers, as long as they are located somewhere near the kinematic center. To test the strength of our conclusions we therefore determine for each galaxy the offsets between the centers of individual tilted-rings and the best center estimate. As the outer parts of the galaxies tend to be affected by warps and asymmetries, we restrict this analysis to the data points in the inner half of each galaxy (i.e., those with $r < 0.5 r_{\max}$, where r_{\max} is the maximum radius to which our analysis extends, cf. Col (7) of Table 2.3). In Fig. 2.6, we show a histogram of the distribution of these offsets in terms of beam size for all galaxies in our sample. Approximately 50 percent of the center positions of the ~ 1000 individual tilted-rings differ less than one beam from our best center position. Another 25 percent show an offset between one and two beam sizes and only a small fraction shows large offsets. Note that the center positions of some of the tilted-rings can be affected by the presence of spiral arms and other features. Large offsets for individual rings do therefore not necessarily imply intrinsic offsets between center positions, but need to be regarded within the context of the results for the whole galaxy. The radial variation of the center positions are shown in Fig. 2.1 for NGC 3198 and in the top panels of Figs. 2.23-2.40 for the other galaxies in our sample.

Our results show that for the large majority of the galaxies studied here, the photometric and kinematic center positions agree within their uncertainties and also to within a beam. See also Section 2.6.4.4 where we evaluate the impact of a shift in center position on our results.

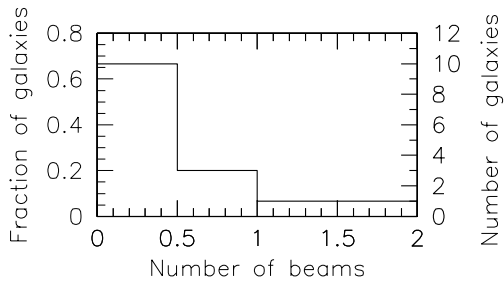


FIG. 2.5: The histogram shows the offset between the dynamical and the best (photometric) center for those 15 galaxies in our sample which have a well-constrained photometric center position. The offset is shown in terms of beam size. For 13 of the 15 galaxies, the different center estimates agree to within one beam (typical beam size: $\sim 10''$), showing that there is no indication for a genuine and general offset between kinematic and photometric centers in our sample.

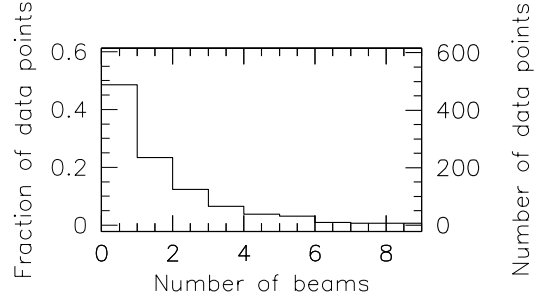


FIG. 2.6: The histogram shows (for all galaxies in our sample) the offset between the individual tilted-ring center estimates and the corresponding best center position in terms of beam size. The typical beam size is $\sim 10''$ (this corresponds to a physical size of 170 pc – 750 pc). Only tilted-rings inwards of $r = 0.5 r_{\max}$ were included. The histogram demonstrates that our dynamical center estimates are well-constrained and in good agreement with the photometric center positions.

2.6.2 Results of the harmonic decomposition

Here, we discuss the results of the harmonic decompositions in a more general way. For a description of the results for individual galaxies we refer to Appendix 2.A. Note that our sample for this part of the analysis contains only 18 and not 19 galaxies because we did not perform a harmonic decomposition for NGC 4826, because of its sparsely filled tilted-rings (cf. the velocity field shown in de Blok et al. 2008).

In the upper panels of Fig. 2.7, we show \tilde{A}_r vs. absolute magnitude and Hubble type. In all panels of Fig. 2.7, we distinguish between barred and non-barred galaxies. The Hubble types, as well as the bar classifications are based on NED. It is clear that the magnitude of the non-circular motions decreases towards lower luminosities and later Hubble types. When these motions are expressed as a fraction of V_{tot} , we see that their contribution is roughly independent of luminosity or Hubble type (Fig. 2.7, middle panel). For 16 out of the 18 galaxies, the non-circular contribution is smaller than 6 percent of V_{tot} and its mean contribution is 4.5 percent. Both in the top and in the middle panel of Fig. 2.7, barred galaxies do not stand out, except for NGC 3627. This is different if we look only at the non-circular motions in the inner 1 kpc (Fig. 2.7, bottom panel). As expected, most barred galaxies have rather high non-circular motions in the innermost region. Note that some galaxies are not shown in these diagrams, as we have no data above a detection limit of 3σ in their inner 1 kpc.

As a comparison, we also calculated the amplitude of the non-circular motions within the inner 2, 3, 4, and 5 kpc, using two different methods. The approach shown in Fig. 2.8 measures the non-circular motions by taking the median of the $A_r(r)$ values within rings of 1 kpc width, as measured over radii $0 < r < 1$ kpc, $1 < r < 2$ kpc, ..., $4 < r < 5$ kpc. Our second approach, shown in Fig. 2.9, simply increases the radial range over which the amplitudes are averaged ($0 < r < 1$ kpc, $0 < r < 2$ kpc, ..., $0 < r < 5$ kpc). In both cases, we have divided our sample into three absolute magnitude bins. It is apparent from the two figures that galaxies with low luminosity have the lowest amplitudes of non-circular motions in the inner parts, regardless of the chosen method (which is not surprising given the smaller rotation velocity of low-luminosity galaxies). Since the approach shown in Fig 2.8 measures the non-circular motions more locally than the method shown in Fig 2.9, it is also more affected by local features like effects of star formation. For instance, the two relatively high amplitudes in the $4 < r < 5$ kpc bin of the bottom panel of Fig. 2.8 belong to IC 2574 and NGC 2366. The former has a supergiant shell at those radii (see Walter et al. 1998), whereas the latter has a large star forming region in its outer parts (see Oh et al. 2008 for an in-depth analysis of the small-scale non-circular motions in these two galaxies). The only other low-luminosity galaxy in our sample which extends out to 5 kpc radius (DDO 154) is completely quiescent in contrast. In the analysis shown in Fig. 2.9, these effects have ‘‘averaged out’’, due to the larger area used for the averaging.

However, no matter how they are binned, in absolute terms the measured amplitudes of the non-circular motions are small. In order to account for the different rotation velocities, we have normalized the amplitudes shown in Figs. 2.8 and 2.9 by the local rotation velocity. The results are shown in Figs. 2.10 and 2.11, respectively. For the large majority of the galaxies in our sample, the non-circular motions in the inner few kpc contribute approximately ten percent to the local rotation velocity. Three galaxies (NGC 925, NGC 2903, and IC 2574) contain non-circular motions larger than 20 percent of the local rotation velocity. For NGC 925 and NGC 2903, it is likely that the large non-circular motions are associated with their stellar bars, especially as Figs. 2.10 and 2.11 indicate that large non-circular motions in the central parts are predominantly found in barred galaxies. For IC 2574, the large ratio between non-circular and circular motions is mainly caused by its small rotation velocity in the inner 1 kpc, which is 15 km s^{-1} at $r = 1$ kpc. The amplitudes of the non-circular motions (in the inner 1 kpc) do not exceed 2.25 km s^{-1} for any tilted-ring. However, the work of Oh et al. (2008), who use a special ‘‘bulk’’ velocity field cleared of non-circular motions shows that even after a correct appraisal of the non-circular motions in IC 2574, its density profile is cored rather than cuspy.

We will now discuss the elongation of the potential (see Fig. 2.12). The elongation of the potential shows neither a trend with absolute magnitude, nor with Hubble type. If the influence of the disk decreases with baryonic mass, and if the dark matter halos are indeed tri-axial (or more precisely, have an elliptical potential distortion in the plane of their disk, cf. Hayashi & Navarro 2006), then one would expect the measured elongations to increase with decreasing (baryonic) mass. However,

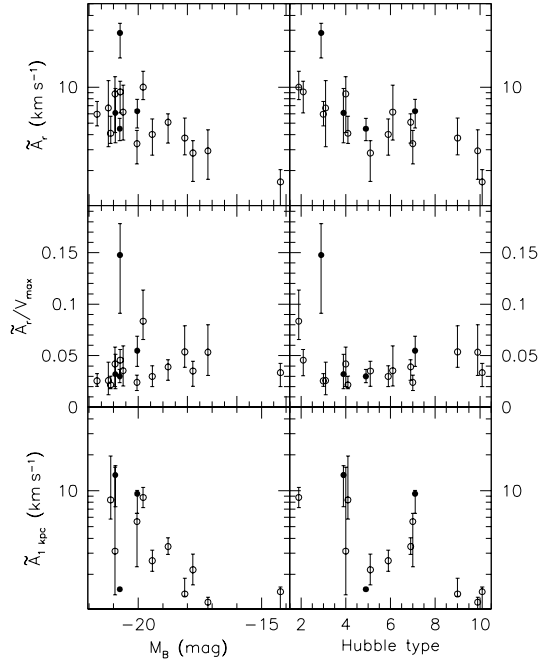


FIG. 2.7: The non-circular motions measured in different ways for our entire sample. Barred galaxies are shown as filled circles, non-barred as open circles. **Top panel:** Median amplitude of the non-circular motions (\bar{A}_r) on a logarithmic scale vs. absolute magnitude (left) and Hubble type (right). Error bars indicate the upper and lower quartile of the radial distribution of \bar{A}_r . **Middle panel:** The percentage the non-circular motions contribute to the maximum rotation velocity vs. absolute magnitude (left) and Hubble type (right). **Bottom panel:** Like top panel, but the averaging was restricted to the inner 1 kpc of the galaxies. Note that for five galaxies, the data do not show significant amounts of HI in the inner 1 kpc, and they are therefore not shown in the two bottom panels.

no such trend is seen in our data. The weighted average elongation and its standard deviation are $\langle \epsilon_{\text{pot}} \sin(2\varphi_2) \rangle = 0.011 \pm 0.013$. This elongation and the individual elongation measurements still contain an unknown viewing angle, for which one can apply a statistical correction by dividing the elongation by the expectation value of φ_2 , $2/\pi$ (middle panel of Fig. 2.12). The average, corrected elongation is $\langle \epsilon_{\text{pot}} \rangle = 0.017 \pm 0.020$, i.e., consistent with a round potential.

2.6.3 Comparison with predictions from simulations

Several authors have reported that CDM halos are triaxial objects (e.g., Frenk et al. 1988; Dubinski 1994; Hayashi et al. 2004a; Moore et al. 2004; Kasun & Evrard 2005; Hayashi & Navarro 2006; Hayashi et al. 2007). We compare our results with predictions based on cosmological Λ CDM simulations. Hayashi et al. (2004a) and Hayashi & Navarro (2006) present models where they use an elliptical distortion of the gravitational potential (mimicking a tri-axial halo) to explain the observed solid-body rotation curves of dwarfs and LSB galaxies within a CDM context. This distortion affects the orbits and thus also the rotation curve. In this picture, the major axis rotation curve depends on the viewing angle of the elliptical distortion. This viewing angle can be chosen in such a way that the major axis rotation curve in the elliptical potential looks identical to what it would have been, had the gas been on circular orbits (i.e., without elliptical distortion and without non-circular motions). It would therefore hide the presence of the disturbance due to tri-axiality and look like a solid-body rotation curve.

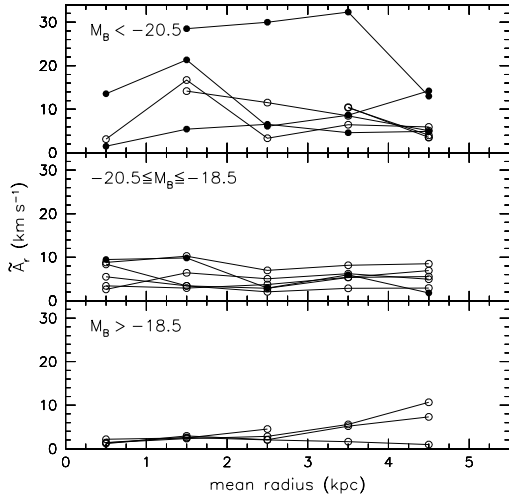


FIG. 2.8: The amplitude of the non-circular motions within rings of 1 kpc width (i.e., $0 < r < 1$ kpc, $1 < r < 2$ kpc, ..., $4 < r < 5$ kpc) for each galaxy (if data available). All measurements of a specific galaxy are connected by a line. Filled symbols correspond to barred galaxies, open symbols to non-barred galaxies. We divide the plot into three subpanels. The top panel contains all galaxies with $M_B < -20.5$, the middle panel those with $-20.5 \leq M_B \leq -18.5$ and the bottom panel all galaxies with $M_B > -18.5$.

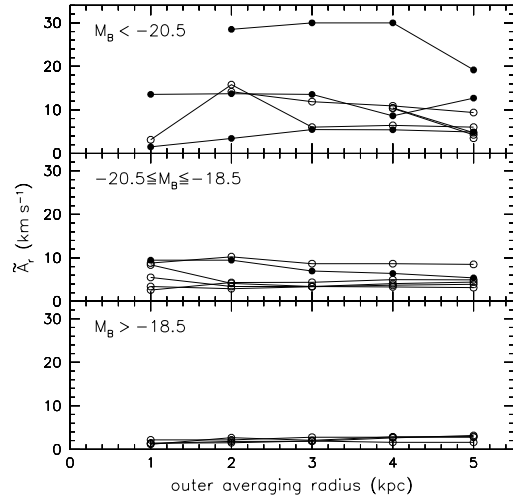


FIG. 2.9: Like Fig. 2.8, but the amplitude of the non-circular motions were averaged within rings of increasing radius (i.e., $0 < r < 1$ kpc, $0 < r < 2$ kpc, ..., $0 < r < 5$ kpc). As the region over which the non-circular motions are averaged increases outwards, the amplitudes shown are less affected by local features such as the effects of star formation.

However, even if the angle is adjusted in such a way, the minor axis rotation curve of the tri-axial case would still show large streaming motions. These can be up to 15 percent of the maximum rotation velocity. As we show in Figs. 2.7, 2.8, and 2.9, the observed non-circular motions in our sample are generally much smaller and never reach 15 percent of the total rotation (see also the minor-axis position-velocity diagrams presented in de Blok et al. 2008). We have shown that relatively high (but still small in absolute terms) non-circular motions in the inner parts of the galaxies are always found in bright and/or barred galaxies. Given that the central parts of bright galaxies are dominated by baryonic matter, this could indicate that these non-circular motions are caused by baryons rather than a tri-axial dark matter halo.

In Figs. 2.10 and 2.11, we normalize the amplitudes of the non-circular motions by the local (circular) rotation velocity. At a radius of 1 kpc, Hayashi et al. (2004a) report non-circular motions as high as 50 percent of the local rotation velocity. At smaller radii, the contribution of the non-circular motions is even larger. The results shown in Figs. 2.10 and 2.11, however, show that for the large majority of the galaxies in our sample, the non-circular motions are only as high as ten percent of the local rotation velocity. Only in one barred galaxy (NGC 925) do the non-circular motions reach an amplitude close to 50 percent of the local rotation velocity in the inner 1 kpc. The dwarf galaxies (bottom panels of Figs. 2.10 and 2.11) are of most interest here, as the cusp/core problem shows itself most clearly for them. The non-circular motions in three out of the four dwarfs in our sample (NGC 2366, NGC 2976, and DDO 154) contribute only ten percent to the local rotation velocity. Therefore, the non-circular motions in these galaxies do not significantly affect the mass models presented in de Blok et al. (2008) and Oh et al. (2008) and preclude the possibility that their cored density profiles (cf. aforementioned papers) are intrinsic cuspy profiles which have been artificially flattened by large

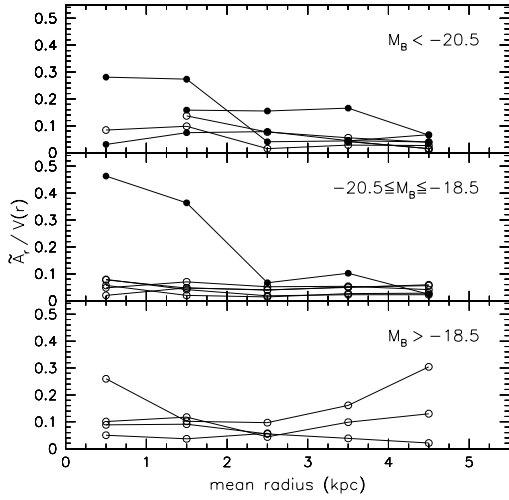


FIG. 2.10: Like Fig. 2.8, but the amplitudes of the non-circular motions are normalized by the local rotation velocity. Except for a few galaxies, the non-circular motions in the inner few kpc have an amplitude of ~ 10 percent of the local rotation velocity, irrespective of the galaxies' luminosity. Only three galaxies have non-circular motions in their centers which are larger than 20 percent of the local rotation velocity. Note also that large non-circular motions (in relative terms) are predominantly found in barred galaxies.

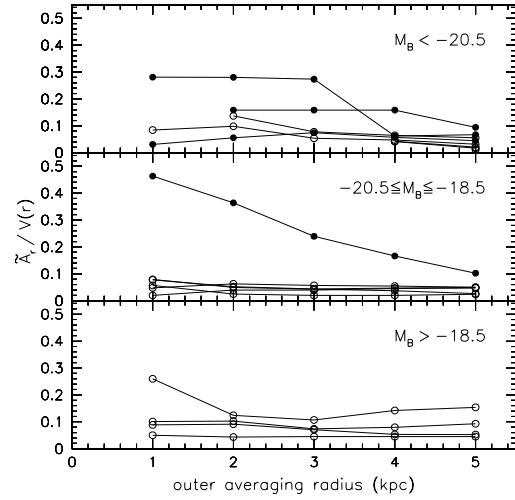


FIG. 2.11: Like Fig. 2.9, but the amplitudes of the non-circular motions are normalized by the local rotation velocity. Analogous to Fig. 2.9, the increasing region for the averaging of the non-circular motions causes the amplitudes to be somewhat less affected by local features such as the effects of star formation.

non-circular motions. The non-circular motions in IC 2574 amount to ~ 26 percent of the local rotation velocity for the inner 1 kpc. Even though this is still much smaller than what is predicted by Hayashi et al. (2004a), the unambiguous derivation of the density slope might be hindered if one assumes circular rotation. Oh et al. (2008), however, show that even after a correct appraisal of the non-circular motions in IC 2574, its density profile is still inconsistent with an NFW profile, but is better approximated with a pseudo-isothermal halo.

The gravitational potential in the simulations of Hayashi & Navarro (2006) is elongated in the inner parts as $\langle \epsilon_{\text{pot}} \rangle = 0.2 \pm 0.1$ (their Fig. 3). All but two of the individual elongation measurements presented here are systematically lower than those predictions and consistent with a round potential, although some have large enough error bars to make them marginally consistent with the lower end of the CDM predictions. The measurements for two galaxies (NGC 4736 and NGC 7793) have sufficiently large uncertainties to make them marginally consistent with the CDM predictions, though a rounder potential is preferred.

If DM halos do indeed have an elliptical distortion in their inner parts, we would expect to find higher elongations there. To test this idea, we have also determined the elongations of the potential by using only data out to $r = 0.5 r_{\text{max}}$ (bottom panel of Fig. 2.12). The individual elongation measurements do not change significantly if averaged only over the inner half of the disk. Their weighted mean ($\langle \epsilon_{\text{pot}} \rangle = 0.016 \pm 0.015$) is not significantly different from the value obtained by averaging over the entire disk ($\langle \epsilon_{\text{pot}} \rangle = 0.017 \pm 0.020$) and we therefore see no indication that the gravitational potential is more elongated towards the center of the galaxies.

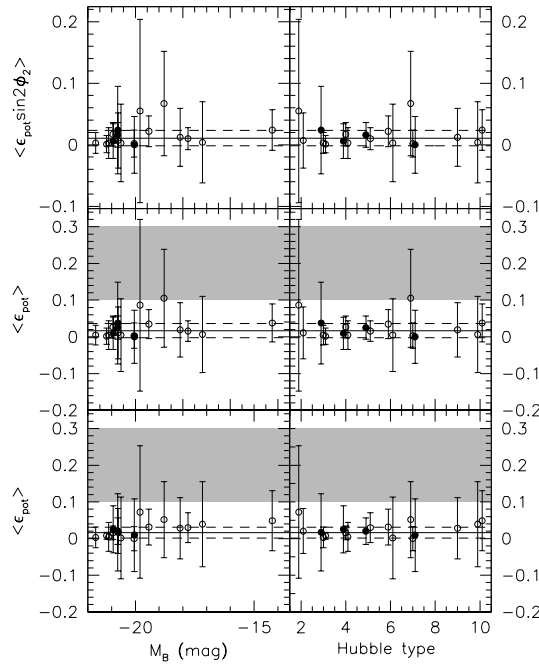


FIG. 2.12: **Top panel:** Elongation of the potential vs. absolute magnitude (left) and Hubble type (right). The horizontal lines represent the weighted mean and its standard deviation ($\langle \epsilon_{\text{pot}} \sin(2\varphi_2) \rangle = 0.011 \pm 0.013$). Barred galaxies are shown as filled circles, non-barred ones as open circles. The distribution of $\langle \epsilon_{\text{pot}} \sin(2\varphi_2) \rangle$ shows neither a trend with luminosity, nor with Hubble type. **Middle panel:** Like top panel, but a statistical correction for the unknown viewing angle was applied to the individual elongation measurements and to their mean and standard deviation. The hatched area indicates the CDM predictions by Hayashi & Navarro (2006). The elongations of the large majority of the galaxies shown here are systematically lower (rounder) than what is predicted by CDM simulations, although the measurements for some galaxies have large enough error bars to make them marginally consistent with the lower end of the CDM predictions. **Bottom panel:** Like middle panel, but we averaged the elongation of the potential not over the entire radial range, but only out to $r < 0.5 r_{\text{max}}$ (r_{max} is the maximum radius to which our analysis extends). This has generally only little effect on the individual elongation measurements. The mean value has not changed ($\langle \epsilon_{\text{pot}} \rangle = 0.017 \pm 0.020$ vs. $\langle \epsilon_{\text{pot}} \rangle = 0.016 \pm 0.015$) and we therefore do not see an indication that the elongation of the potentials increase inwards.

2.6.4 Consistency Checks

In this section, we compare the results of our harmonic decomposition with the traditional tilted-ring analysis presented in de Blok et al. (2008). Additionally, we present quality controls which show the limitations of our methods, test and validate our current results as well as indicate room for improvement.

2.6.4.1 ROTCUR vs. RESWRI: residual velocity fields

Here, we compare the residual velocity fields from the ROTCUR analysis by de Blok et al. (2008) with those from our analysis with RESWRI. As mentioned in Section 2.4, the residual velocity fields are derived by subtracting a model using the final parameter estimates from the original data. For both types of residual fields, we calculate the median and the lower and upper quartile of the *absolute* residual velocity fields. These are compared in Fig. 2.13. It is clear that all galaxies have larger residuals in the ROTCUR analysis than they have in the RESWRI analysis. This is of course to be expected, given that ROTCUR considers only circular motion, while RESWRI also takes non-circular

motions into account. Nevertheless, it is a quality test which shows that our results are behaving in the expected manner. The largest median amplitude of the residual RESWRI velocity fields is 4.5 km s^{-1} (for NGC 3521). The average value of the sample is 2.9 km s^{-1} , which clearly shows that a harmonic expansion up to third order is capable of capturing the majority of the non-circular motions in most galaxies.

Looking at Fig. 2.13, it becomes also clear that galaxies with small ROTCUR residuals also have small RESWRI residuals. Small ROTCUR residuals, however, indicate that a model assuming circular rotation already provides a good approximation. Therefore, it is to be expected that these galaxies show only small non-circular motions. This expectation is tested in Fig. 2.14, where we plot the median values of the absolute residual velocity fields from de Blok et al. (2008) vs. the median amplitudes \tilde{A}_r of the non-circular motions from our harmonic decompositions. Most galaxies are located near the line of unity, showing that our expectation is indeed correct. The only real outlier in Fig. 2.14 is NGC 3627, which is clearly offset from all other galaxies as it has — despite its large non-circular motions ($\tilde{A}_r \sim 28.5 \text{ km s}^{-1}$) — only moderate ROTCUR residuals. The results for the other galaxies, however, show that even a simple model considering only circular rotation can fit most galaxies quite well. These small residuals therefore demonstrate (independently from our RESWRI analysis) that non-circular motions are generally small.

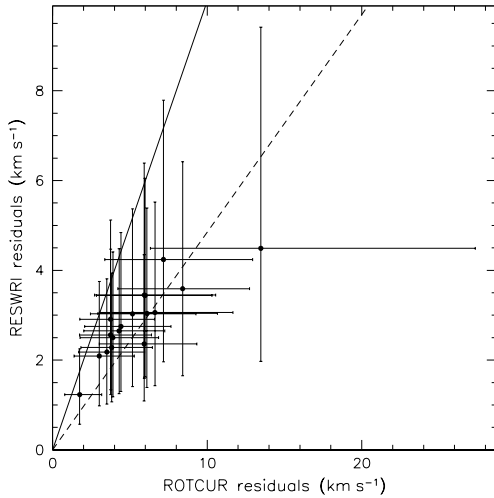


FIG. 2.13: Median of the absolute residual velocity field from the rotation curve analysis of de Blok et al. (2008) vs. the one from the harmonic decomposition presented in this chapter. The error bars indicate the lower and upper quartile, the solid line represents a one-to-one relation, and the dashed line the unweighted least square fit through the data points. The residuals in the traditional ROTCUR analysis are all larger than those from the RESWRI fits, as expected. The difference between the solid line and dashed line is due to the non-circular motions quantified in this chapter.

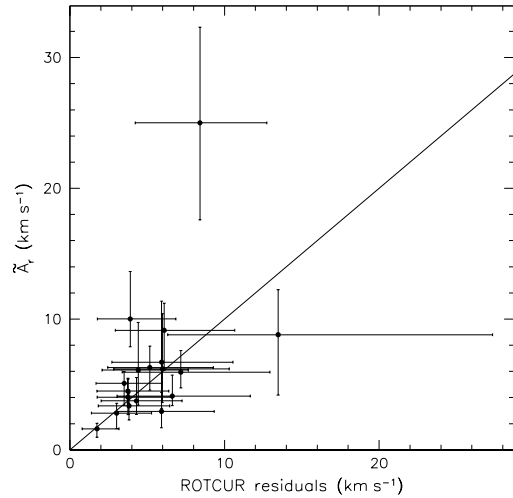


FIG. 2.14: Median of the absolute residual velocity field from the rotation curve analysis in de Blok et al. (2008) vs. \tilde{A}_r , the median of the (radially averaged) quadratically added amplitudes of the non-circular motions quantified in this chapter. The error bars indicate the lower and upper quartile. Galaxies with large residuals in the ROTCUR fits show generally also larger non-circular motions. The outlier in the upper part of the panel is NGC 3627, which shows large non-circular motions, but only moderate residuals in the ROTCUR analysis by de Blok et al. (2008).

2.6.4.2 Making prior assumptions during the RESWRI runs

The rotation curves of all galaxies in our sample were derived and discussed in detail by de Blok et al. (2008). The general procedure for the derivation of a rotation curve includes keeping some parameters fixed in the tilted-ring fits, thus reducing the number of free parameters for each individual fit with ROTCUR. In the current analysis we derive all tilted-ring parameters in a single fit with all parameters left free and do not attempt to correct for the motions induced by, e.g., star formation or spiral arms. Thus, it is expected that the tilted-ring parameters derived by us differ to some extent from the ones derived by de Blok et al. (2008). In order to check this and to estimate the impact on our results, we compare the derived values for our unconstrained harmonic decompositions with those from constrained decompositions with PA and i fixed to the final values from de Blok et al. (2008). We apply this test to two representative galaxies, NGC 3198 and DDO 154, a spiral galaxy and a dwarf irregular.

In the case of NGC 3198 (Fig. 2.15), most values agree remarkably well between the constrained and the unconstrained fit. Because de Blok et al. (2008) have assumed a constant inclination in the inner parts (in order to compensate for effects caused by spiral arms), our unconstrained values differ slightly in this region. Note though that the effect on the rotation curve is negligible. Fixing the inclination has the predictable effect that the c_3 term reaches values of a few km s^{-1} as this term tries to compensate for the effect the spiral arms have on the velocity field. The impact of this, however, is minor, as one can see in the distribution of $A_r(r)$ and \tilde{A}_m as well as in the negligible difference in the derived rotation velocity. The elongation of the potential is also largely unaffected by constraining i and PA. The only noticeable differences are the different-sized error bars. As the inclination contributes to the fourth power to the error of the elongation of the potential, the error bars are naturally smaller in the case of a fixed inclination.

For DDO 154 (Fig. 2.16), the differences between the harmonic components of the two decompositions are generally of the order of $\sim 1 \text{ km s}^{-1}$. The inclinations in the unconstrained fit differ inwards of $r \approx 80''$ from the ones in the constrained fit. This is because of the close-to solid-body rotation of DDO 154, which makes the simultaneous determination of the correct inclination difficult. The impact on the results, even in the inner $80''$, is nevertheless small. For instance, the derived rotation velocities are indistinguishable between the two decompositions.

Our tests using NGC 3198 and DDO 154 showed that fixing parameters to the final values from de Blok et al. (2008) does not change our results in a significant way. Nevertheless, in this study we prefer free parameters as opposed to fixed ones in order to avoid being unwittingly affected by any particular choices for tilted-ring parameters.

2.6.4.3 Hermite vs. Intensity weighted mean VF

Hermite velocity fields differ from intensity weighted mean (IWM) velocity fields when dealing with asymmetric (i.e., non-Gaussian) profiles. It was noted, e.g., by de Blok et al. (2008), that hermite velocity fields better reproduce the velocity of the peak intensity of the profile, as their analytical function includes an h_3 (skewness) term (see, e.g., van der Marel & Franx 1993). For a detailed overview of the different types of velocity fields we refer to the discussion in de Blok et al. (2008).

As we are using the hermite velocity fields, an investigation of how using IWM velocity fields affects our analysis, if at all, is warranted. We perform unconstrained harmonic decompositions with RESWRI using identical initial conditions on the hermite and on the IWM velocity fields of NGC 3198 and DDO 154. The results are summarized in Figs. 2.17 and 2.18, respectively. As small differences between the two decompositions are visible, it is clear that how a velocity field is created does play a role in the analysis. A close inspection of the radial variation of the various quantities shown

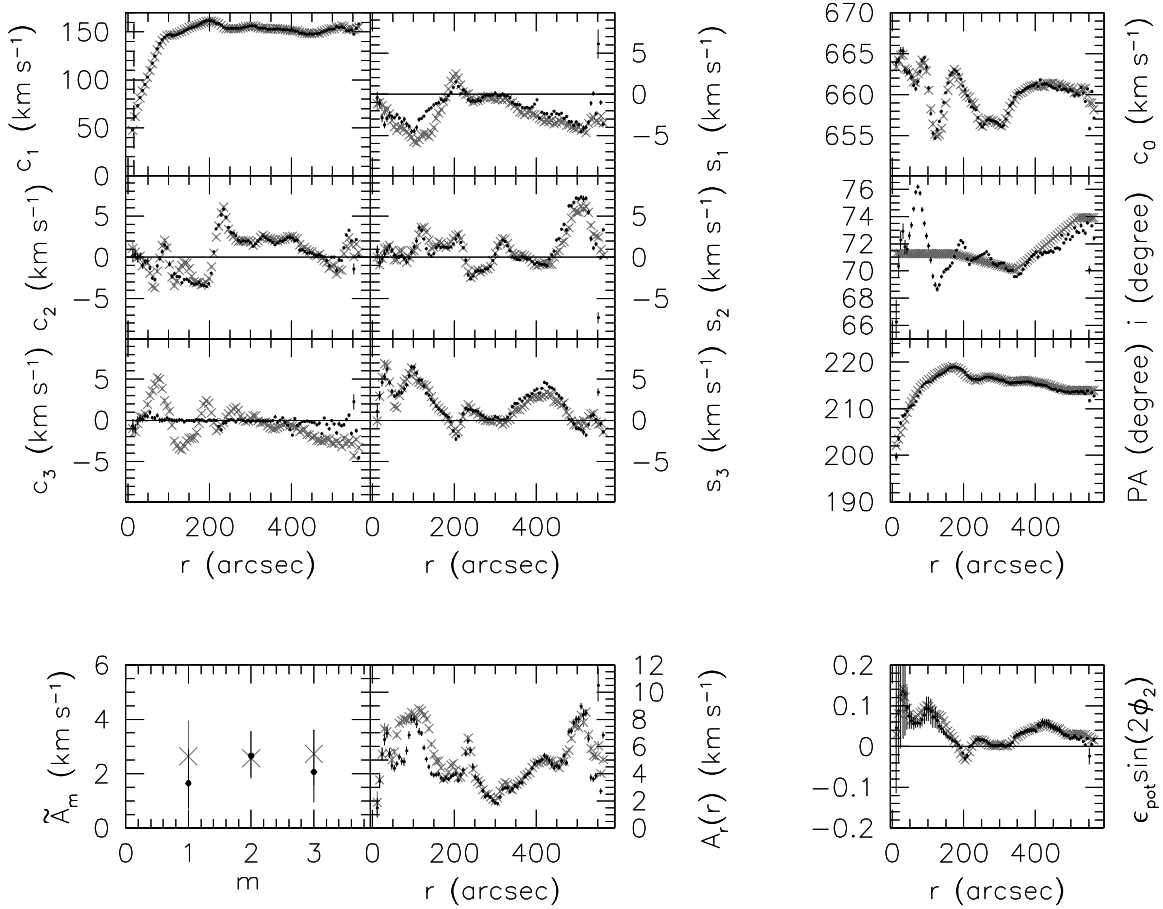


FIG. 2.15: The results of the unconstrained (black dots) and constrained (gray crosses) harmonic decomposition of NGC 3198. For the constrained fit, the inclination and position angle were fixed to the values from de Blok et al. (2008). The layout of the figure is identical to that of Figs. 2.3 and 2.4, except that we do not show any weighted means in the panels on the right-hand side. The parameters that are plotted in this figure are defined in Section 2.5. The constant inclination in the inner parts of NGC 3198 cause a non-zero c_3 term which results in slightly higher non-circular motions in the inner parts.

in both figures indicates that the radial variations are more pronounced in the case of the hermite velocity field. The choice of the velocity field construction method has, however, little impact on the derived quantities (see, e.g., bottom panels of Figs. 2.17 and 2.18), and therefore does not change our conclusions in any significant way.

2.6.4.4 Decomposition under the assumption of an incorrect center

In this section, we test the influence of an incorrect center position on our results. As test candidates, we have chosen one galaxy where the position of the center is very well-defined (NGC 2841), and one where the center is less obvious (NGC 2366). For both galaxies, we deliberately shift the center positions used in RESWRI by $2''$, $4''$, $6''$, and $10''$ along their major and minor axes. The results of the most extreme cases ($10''$ offsets, i.e., approximately the beam size) are compared with the results from our best center positions in Figs. 2.19-2.22.

For NGC 2366, the effect of an incorrectly chosen center is small, irrespective of whether the center is shifted along the major (Fig. 2.19) or along the minor (Fig. 2.20) axis. For offsets along the

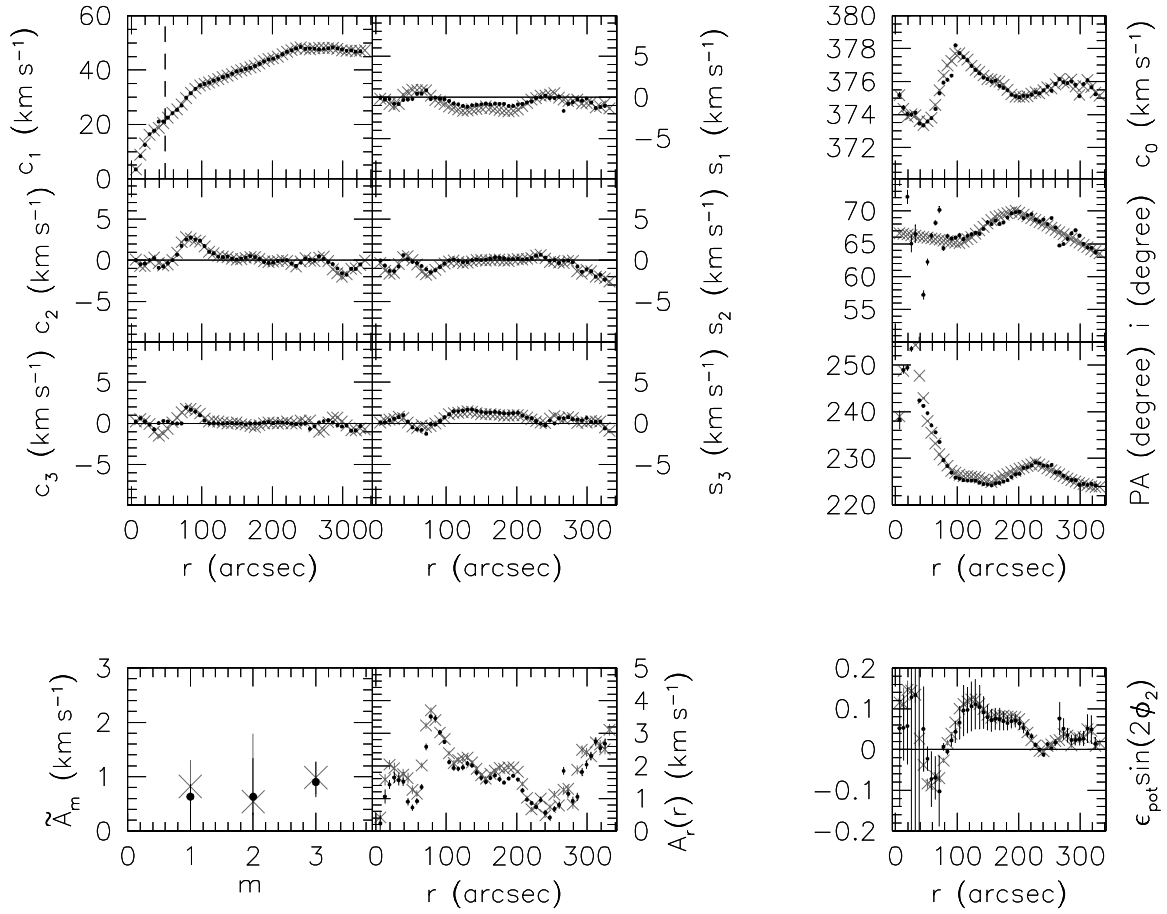


FIG. 2.16: Like Fig. 2.15 but for DDO 154. The differences between the two decompositions are mostly negligible. The close-to solid-body rotation of DDO 154 makes a determination of the inclination in the inner parts (in an unconstrained fit) more difficult. The impact of the less well-constrained i is, however, small.

major (minor) axis, the median amplitude of the non-circular motions increases from $\tilde{A}_r \sim 3 \text{ km s}^{-1}$ for our best center position to $\tilde{A}_r \sim 3.5 \text{ km s}^{-1}$ ($\tilde{A}_r \sim 4 \text{ km s}^{-1}$). Our results for the dwarf galaxy NGC 2366 are therefore unaffected by small offsets in the center position, indicating that for a rotation curve showing close-to solid-body rotation, a modest offset from the true center position is not crucial for the analysis presented here.

For NGC 2841, the situation is different. A $10''$ offset along the major axis (Fig. 2.21) already increases the median amplitude of the non-circular motions from $\tilde{A}_r \sim 7 \text{ km s}^{-1}$ to $\tilde{A}_r \sim 12 \text{ km s}^{-1}$. In the case of an offset along the minor axis (Fig. 2.21), the increment is even larger ($\tilde{A}_r \sim 25 \text{ km s}^{-1}$).

Note that the difference in the harmonic components is mostly to be found in the $m = 2$ term. This is to be expected, as a galaxy will appear kinematically lopsided if a center offset from the dynamical center is chosen for the harmonic decomposition. Also note that, as expected, it is the cosine coefficient c_2 which shows the largest amplitude in the case of an offset along the major axis, and the sine coefficient s_2 in the case of an offset along the minor axis.

For NGC 2841 — a galaxy with a steep and subsequently flat rotation curve — our results are sensitive to the chosen center position and an offset center would clearly show itself by increased non-circular motions. But this example is of course rather contrived, as for galaxies like NGC 2841,

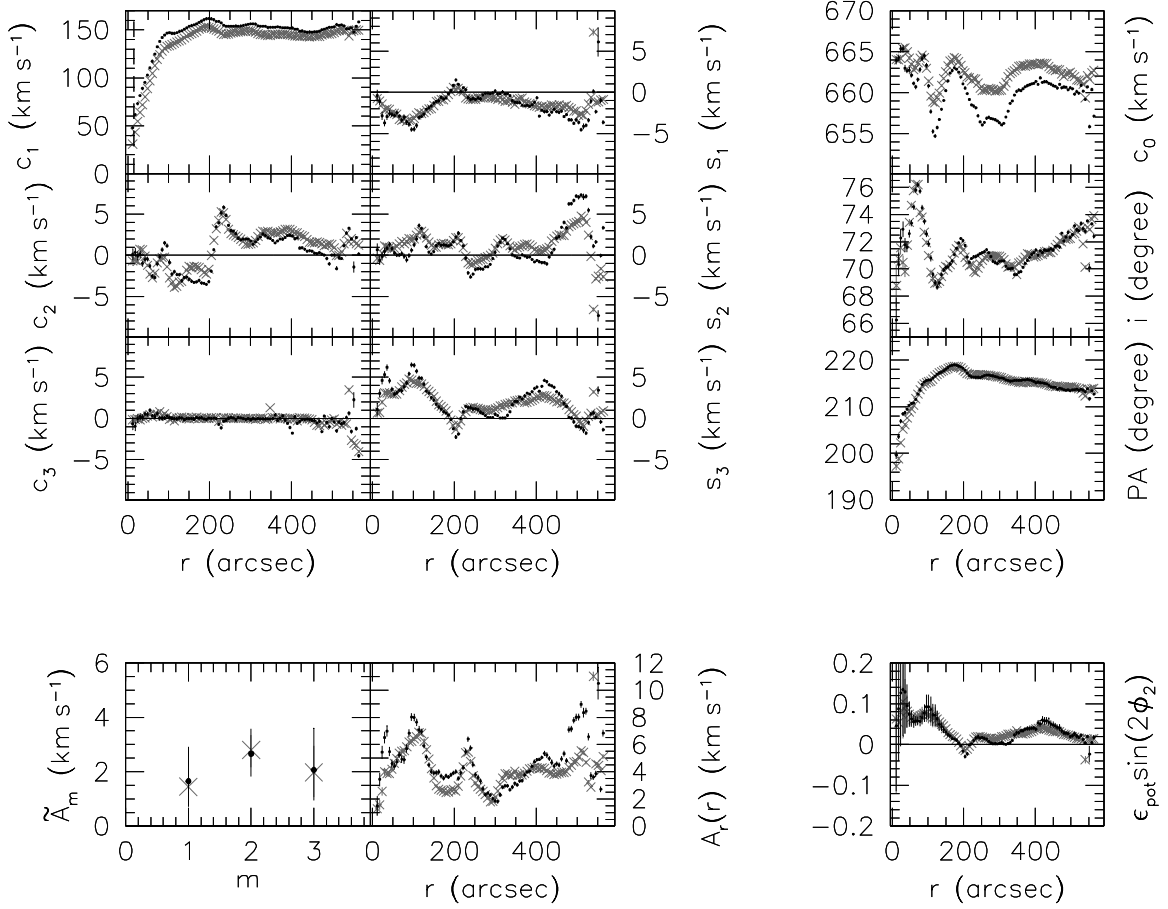


FIG. 2.17: Harmonic analysis of NGC 3198 using the hermite velocity field (black dots) and the intensity weighted mean velocity field (gray crosses). The layout of the figure is identical to that of Figs. 2.3 and 2.4, except that we do not show any weighted means in the panels on the right-hand side. The differences between the derived quantities are small. The radial variation of the harmonic components seems, however, more pronounced in the hermite velocity field.

the center is usually so well-defined that uncertainties of $10''$ as modeled here are unlikely to occur within the THINGS sample.

We have shown that the results of a harmonic decomposition of galaxies like NGC 2841 (i.e., having a steep rotation curve) are sensitive to offsets in the galaxies' center position. For NGC 2366, i.e., a dwarf galaxy showing close-to solid-body rotation, our results are mostly insensitive to small offsets in the center position. The less well-defined center for NGC 2366 does therefore not affect our results of that galaxy.

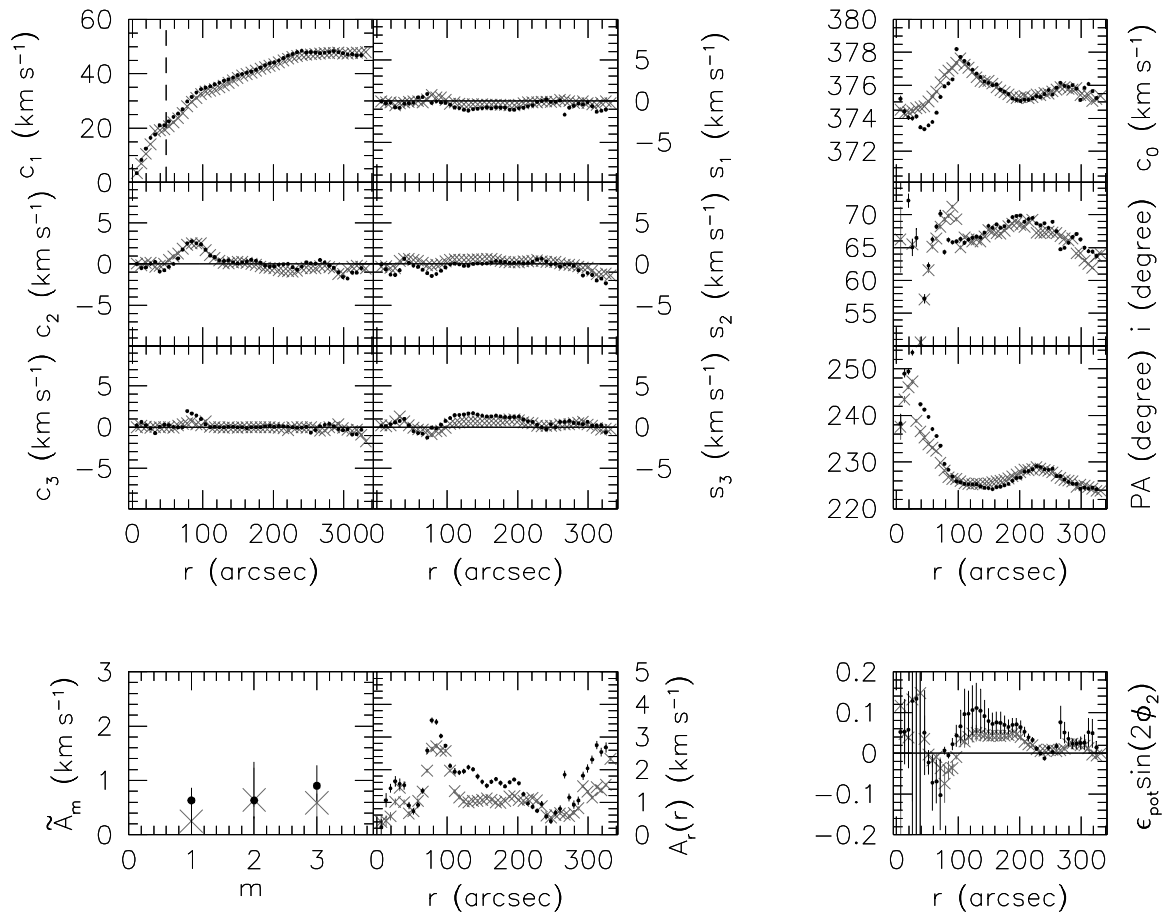


FIG. 2.18: Like Fig. 2.17 but for DDO 154.

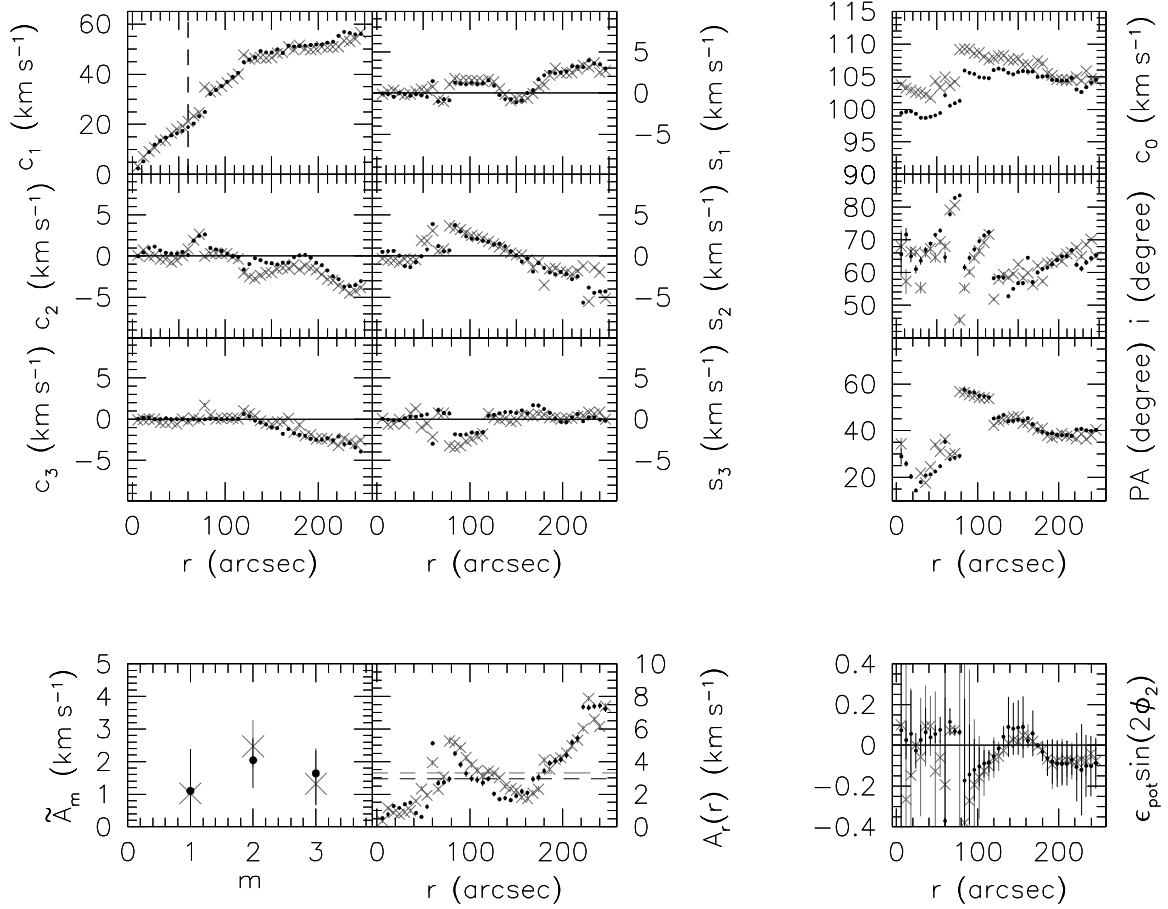


FIG. 2.19: Harmonic analysis of NGC 2366 using our best center position (black) and a center position, offset by $10''$ along the major axis (gray). The layout of the figure is identical to that of Figs. 2.3 and 2.4, except that we do not show any weighted means in the panels on the right-hand side. The difference between the two decompositions is marginal. The offset center causes the median amplitude of the non-circular motions (dashed line in the panel showing the distribution of $A_r(r)$) to increase from $\bar{A}_r \sim 3 \text{ km s}^{-1}$ to $\bar{A}_r \sim 3.5 \text{ km s}^{-1}$, showing that a small offset along the major axis has no significant effect on the derived quantities in the case of NGC 2366.

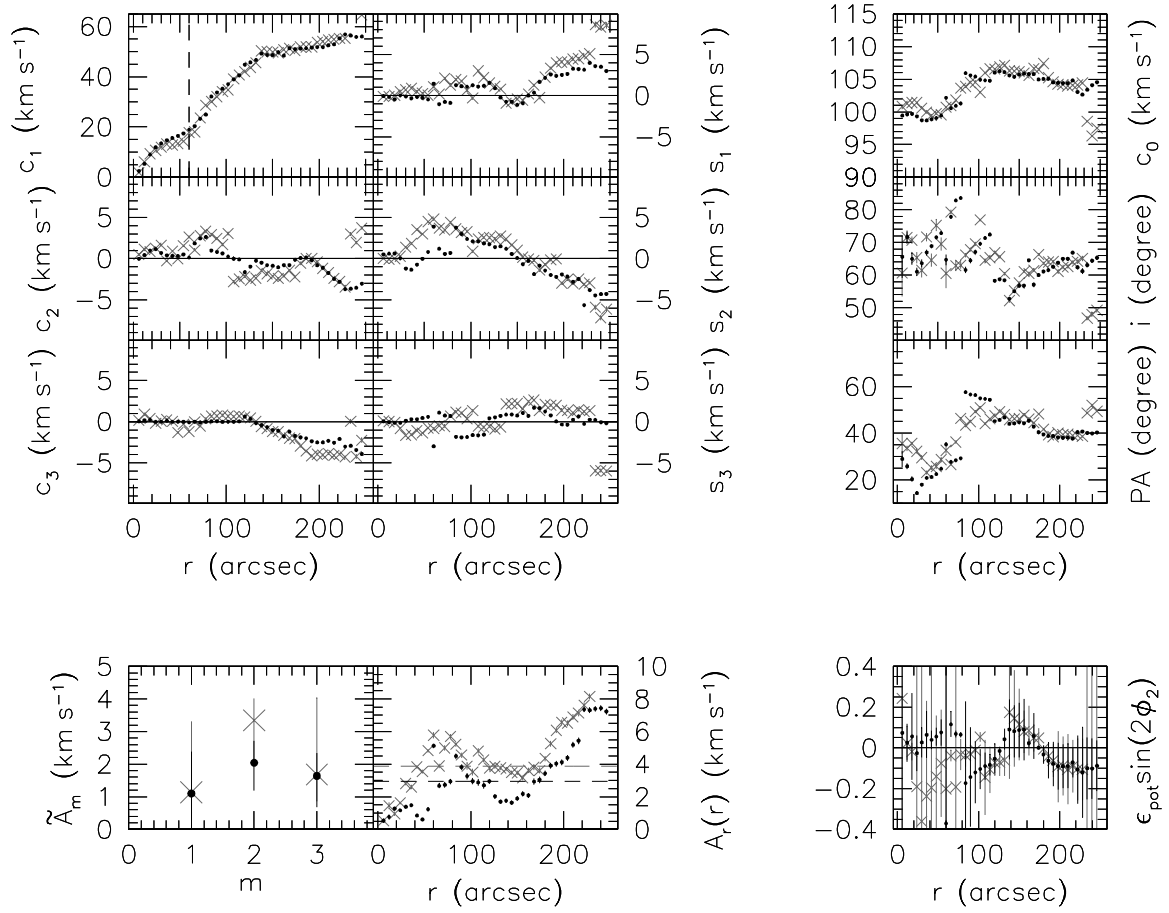


FIG. 2.20: Like Fig. 2.19, but the harmonic analysis shown in gray is using a center position offset by $10''$ along the minor axis. Although being larger than in the case of the offset along the major axis, the difference between the two decompositions is still small. The offset center causes the median amplitude of the non-circular motions (dashed line in the panel showing the distribution of $A_r(r)$) to increase from $\tilde{A}_r \sim 3 \text{ km s}^{-1}$ to $\tilde{A}_r \sim 4 \text{ km s}^{-1}$, showing that even a small offset along the minor axis does not influence the derived quantities in a significant way in the case of a dwarf galaxy like NGC 2366.

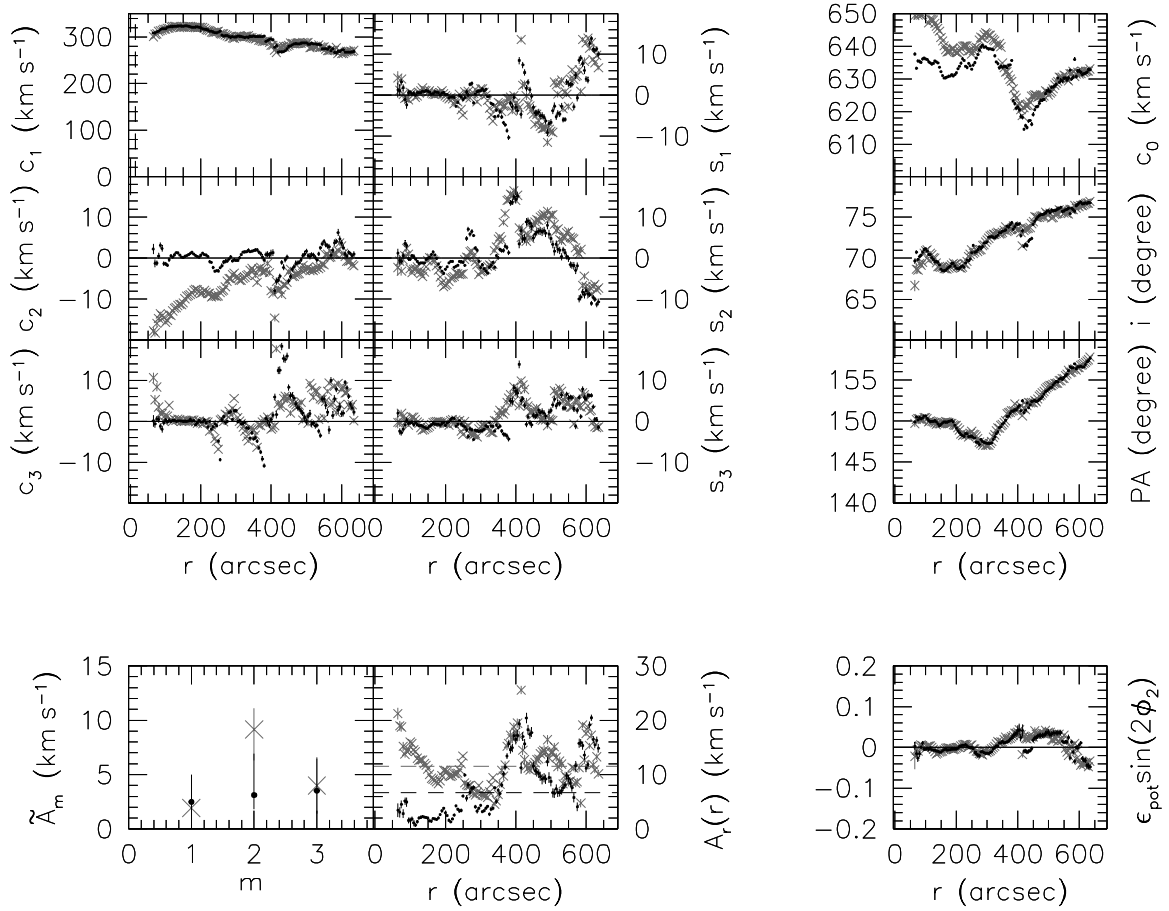


FIG. 2.21: Harmonic analysis of NGC 2841 using our best center position (black) and a center position, offset by $10''$ along the major axis (gray). The layout of the figure is identical to that of Figs. 2.3 and 2.4, except that we do not show any weighted means in the panels on the right-hand side. For NGC 2841, the amount of non-circular motions increases clearly when choosing an offset center. The largest differences are visible in the c_2 term. The median amplitude of the non-circular motions (dashed-line in the panel showing the distribution of $A_r(r)$) increases from $\tilde{A}_r \sim 7 \text{ km s}^{-1}$ to $\tilde{A}_r \sim 12 \text{ km s}^{-1}$, showing that in the case of NGC 2841, an offset along the major axis will clearly show itself as an increase in the amplitudes of the harmonic components.

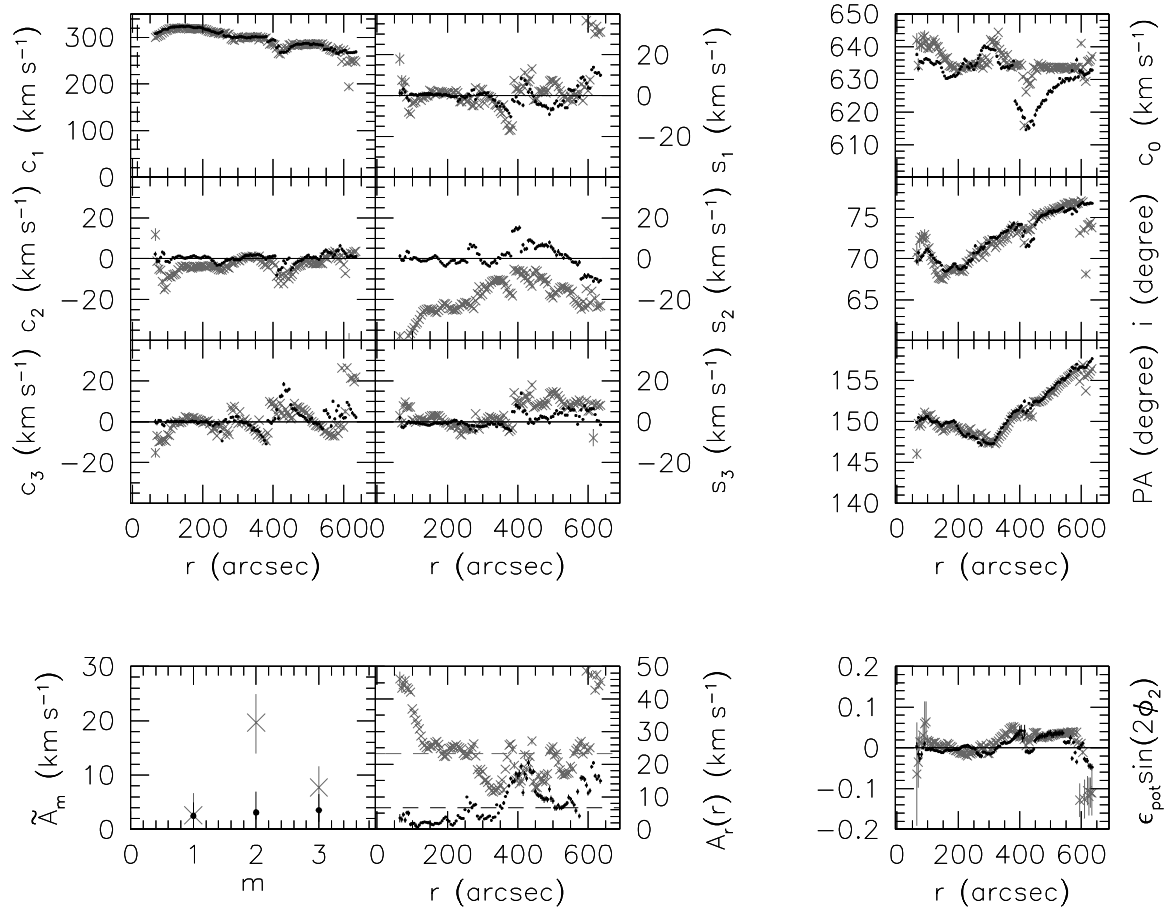


FIG. 2.22: Like Fig. 2.21, but the harmonic analysis shown in gray is using a center position offset by $10''$ along the minor axis. For NGC 2841, the amount of non-circular motions increases clearly when choosing an offset center. The largest differences are visible in the s_2 term. \bar{A}_r (dashed-line in the panel showing the distribution of $A_r(r)$) increases from $\bar{A}_r \sim 7 \text{ km s}^{-1}$ to $\bar{A}_r \sim 25 \text{ km s}^{-1}$, showing that in the case of NGC 2841, an offset along the minor axis will produce significantly different results than if the dynamical center position is chosen.

2.7 Summary and Conclusions

We have analyzed HI velocity fields of 19 THINGS disk and dwarf galaxies at the currently best available spatial and spectral resolution. The observations, data reduction and analysis of all these galaxies were done in an identical and homogeneous manner (Walter et al. 2008; de Blok et al. 2008). We have determined the center positions of these 19 galaxies by comparing the kinematic center estimates with those from the radio continuum and/or NIR data.

We have derived reliable center positions and show that most galaxies in our sample do not exhibit significant offsets between their kinematic and their optical centers. Some small offsets that were found are explainable and not relevant for the debate about the inner slope of the mass density profile. For 18 out of 19 galaxies from our sample, we have performed a harmonic decomposition of their velocity fields with the aim of quantifying the amount of non-circular motions and deriving a lower limit for the elongation of the potential.

Our results show that in the (large) majority of our sample galaxies, the effects of non-circular motions are small, irrespective of whether these non-circular motions are measured in the inner few kpc or over the entire radial range. Within our sample, the average amplitude of the non-circular motions is $\tilde{A}_r = 4.8 \pm 4.0 \text{ km s}^{-1}$ for the inner 1 kpc and $\tilde{A}_r = 6.7 \pm 5.9 \text{ km s}^{-1}$ when averaged over the entire radial range. High non-circular motions in the inner parts of the galaxies are mostly found in barred, and/or luminous galaxies. The galaxies in our sample least dominated by baryonic matter (i.e., the low luminosity galaxies) show the smallest non-circular motions in the sample, especially in the inner parts, indicating that non-circular motions might generally be associated with the baryons rather than a tri-axial dark matter halo.

The inner few kpc of the large majority of the galaxies in our sample contain non-circular motions of the order of ten percent of the local rotation velocity. Averaged over our sample, the median amplitude of the non-circular motions in the inner 1 kpc is 8 ± 3 percent of the local rotation velocity. For three out of the four dwarf galaxies in our sample — which all show a cored density profile (see de Blok et al. 2008; Oh et al. 2008) — the amplitudes of the non-circular motions amount to (at most) ten percent of the local rotation velocity.

Whether the non-circular motions are expressed in absolute terms or if they are normalized by the local rotation velocity does not affect the conclusions: the amount of non-circular motions detected in the majority of our galaxies is significantly smaller than what is expected from CDM simulations and they are far too small to successfully “hide a cusp in a core” as proposed, e.g., by Hayashi & Navarro (2006).

The average elongation of the gravitational potential and its scatter, both statistically corrected for the unknown viewing angle φ_2 , is $\langle \epsilon_{pot} \rangle = 0.017 \pm 0.020$. This is significantly lower than the predictions from cosmological simulations. The individual elongation measurements show that the large majority of the galaxies in our sample have elongation measurements which are systematically below the CDM predictions. The elongation of all galaxies in our sample is consistent with a round potential, although some galaxies have large enough uncertainties to make them also (marginally) consistent with the lower end of the predicted range for CDM halos. We therefore see no indication for a significant tri-axiality within the HI disks of the THINGS galaxies.

ACKNOWLEDGEMENTS: CT gratefully acknowledges the help and support from Ralf-Jürgen Dettmar. The work of CT is supported by the German Ministry for Education and Science (BMBF) through grant 05 AV5PDA/3. The work of WJGdB is based upon research supported by the South African Research Chairs Initiative of the Department of Science and Technology and National Research Foundation. EB gratefully acknowledges financial support through an EU Marie Curie International

Reintegration Grant (Contract No. MIRC-CT-6-2005-013556). This research has made use of the NASA/IPAC Extragalactic Database (NED) which is operated by the Jet Propulsion Laboratory, California Institute of Technology, under contract with the National Aeronautics and Space Administration.

2.A Appendix: Description of individual galaxies

In this section, we present for each galaxy in our sample a detailed description of (a) the derivation of the center position, and (b) the results of the harmonic decomposition. The galaxies are presented in order of increasing right ascension. The results are presented in graphical form in Figs. 2.23-2.40. Channel maps, optical images and moment maps for the galaxies in our sample are given in Walter et al. (2008). The hermite velocity fields are shown in Figs. 3.13-3.29 in the Appendix 3.A. The different center estimates are summarized in Table 2.2, where our adopted best center positions are shown in bold face. The results from the harmonic decomposition are summarized in Table 2.3.

2.A.1 NGC 925 (Fig. 2.23)

a) Center estimates

NGC 925 is a barred late-type spiral galaxy whose HI disk looks rather clumpy. The $3.6 \mu\text{m}$ IRAC image shows a weak central bar and two spiral arms in the outer region. NGC 925 lacks a clear center in the IRAC image as well as in the radio continuum. We used ELLFIT at varying isophote levels to derive a central position from the IRAC image. This center is offset from the pointing center by $\delta X = -0''.8$ and $\delta Y = -2''.6$ (i.e., towards the south-east) and was used as an initial estimate for a ROTCUR run with all parameters left free. Averaging the values for δX , δY over the region not too heavily affected by spiral arms and asymmetries ($r \leq 121''$, see top row of Fig. 2.23) results in a center position offset from the pointing center by $\delta X = 4''.4 \pm 8''.3$ and $\delta Y = -1''.5 \pm 4''.2$. As this position is consistent with the center from the IRAC image (see row 2 of Fig. 2.23), we adopt the former one as our best center for NGC 925.

b) Harmonic expansion

The fitted values for the inclination show a lot of scatter in the inner $100''$. This is partially caused by the near solid-body rotation in that region, which makes determining a kinematic inclination more difficult. Note that in the case of pure solid-body rotation, v_{ROT} and $\sin(i)$ are degenerate and cannot be fitted simultaneously. However, we seldom have to deal with *pure* solid-body rotation, but more usually with near solid-body rotation, which gives the algorithm some handle on the fitted values. Although the amplitudes of the individual components are not constant over the radial range, the median amplitudes of all harmonic orders are relatively small ($\tilde{A}_m \leq 5 \text{ km s}^{-1}$ when averaged over the entire galaxy). The median amplitudes are slightly higher if one averages over the inner 1 kpc only, which might be due to the stellar bar. \tilde{A}_r is $\sim 6.3 \text{ km s}^{-1}$ if averaged over the entire range and $\sim 9.5 \text{ km s}^{-1}$ if averaged over the inner 1 kpc only (see also Table 2.3). The elongation of the potential is unconstrained inwards of $r \approx 100''$, mainly because of the large uncertainties for the derived inclination (which enters into the uncertainty in ϵ_{pot} as a fourth power). Its weighted mean is consistent with a round potential ($\langle \epsilon_{\text{pot}} \sin(2\varphi_2) \rangle = 0.000 \pm 0.046$, see again Table 2.3). The median of the absolute residual velocity field is 3.0 km s^{-1} , showing that a harmonic decomposition up to third order was able to capture most non-circular motions present in NGC 925.

2.A.2 NGC 2366 (Fig. 2.24)

a) Center estimates

NGC 2366 is classified as a dwarf irregular and belongs, like NGC 2403, to the M81 group. As

for all the other dwarf galaxies in the sample presented here, the $3.6\ \mu\text{m}$ IRAC image and the radio continuum map do not show a nuclear source. We derived the center of the emission in the IRAC image by using ELLFIT at varying isophote levels. The IRAC center is offset from the pointing center by $\delta X = 7''.8 \pm 0''.6$ and $\delta Y = -18''.0 \pm 1''.8$. This center estimate was used for a ROTCUR run with all parameters left free. We averaged the derived values for δX , δY for $r \leq 200''$ (see row 1 in Fig. 2.24), but excluded the discrepant data points between $70'' \leq r \leq 100''$. The resulting dynamical center is offset from the pointing center by $\delta X = 5''.2 \pm 3''.5$ and $\delta Y = -19''.2 \pm 7''.7$, and within the uncertainties consistent with the center position derived from the IRAC image (see row 2 of Fig. 2.24). Deriving a kinematic center by averaging over all data points out to $r = 200''$ gives a consistent center estimate, though with a larger scatter ($\delta X = 2''.9 \pm 6''.5$, $\delta Y = -18''.5 \pm 7''.9$). Therefore, we adopt the former kinematic estimate as our final center position.

b) Harmonic expansion

NGC 2366 shows no clear signs of spiral structure. Its rotation curve is clearly dominated by near solid-body rotation, making it difficult to determine the rotation velocity and i simultaneously. At $r \sim 100''$, the systemic velocity c_0 rises from $\sim 100\ \text{km s}^{-1}$ to $\sim 105\ \text{km s}^{-1}$. At the same radius, the amplitude of s_2 “jumps” from $\sim 0\ \text{km s}^{-1}$ to $\sim 4\ \text{km s}^{-1}$ and decreases then to $-4\ \text{km s}^{-1}$ in the outskirts of NGC 2366. The distribution of $A_r(r)$ shows that the largest amount of non-circular motions is to be found in the outer parts of NGC 2366, and that the inner 1 kpc exhibit only minor non-circular motions. The weighted mean elongation is $\langle \epsilon_{\text{pot}} \sin(2\varphi_2) \rangle = 0.003 \pm 0.067$ and the median of the absolute residual velocity field is $2.4\ \text{km s}^{-1}$, once again showing that the galaxy has a round potential and that there are no large non-circular motions present in the $m > 3$ terms.

2.A.3 NGC 2403 (Fig. 2.25)

a) Center estimates

NGC 2403 belongs to the M81 group, and is a late-type Sc spiral. Its $3.6\ \mu\text{m}$ IRAC image shows multiple spiral arms and a bright central component. However, neither the IRAC image, nor the radio continuum map show a nuclear source. Therefore, we used $3.6\ \mu\text{m}$ isophote fits to determine center coordinates and used the resulting center position ($\delta X = -4''.7$, $\delta Y = -13''.6$) as an initial estimate for an unconstrained ROTCUR run. As can be seen in the first row of Fig. 2.25, δX and δY stay fairly constant over a large part of the galaxy. We determine the dynamical center by averaging the values for $r \leq 220''$, thus excluding the radii where δX changes considerably, probably due to the spiral arm located at that radius. The offset from the pointing center is $\delta X = -5''.2 \pm 5''.2$ to the east and $\delta Y = -12''.8 \pm 4''.1$ to the south. Averaging δX and δY over a larger part of the galaxy gives comparable results but with a larger scatter. Given the agreement between the dynamical center estimate and the center as derived using the IRAC image, we adopt the $r \leq 220''$ kinematic center estimate as our best center position.

b) Harmonic expansion

The radial variation of the inclination is only $\sim 5^\circ$, except at a few inner radii. The PA shows a steep inner rise, a flat outer part and a dip at $r \approx 200''$, which coincides with a high amplitude in the c_2 and s_2 components. Inspection of the integrated HI map shows a spiral arm crossing at this radius. The s_1 and s_3 components also show the characteristic wiggles caused by spiral arms. Additionally, s_3 has a small offset from zero, which through Eq. 2.5 can indicate a slightly elongated potential. The average

elongation of NGC 2403, however, is $\langle \epsilon_{\text{pot}} \sin(2\varphi_2) \rangle = -0.022 \pm 0.025$, and therefore consistent with a round potential. The distribution of A_m shows that the individual harmonic orders contribute only ~ 2 percent to V_{tot} , indicating that non-circular motions play a minor role in NGC 2403. The latter can also be seen in the distribution of $A_r(r)$.

2.A.4 NGC 2841 (Fig. 2.26)

a) Center estimates

NGC 2841 is an early-type spiral galaxy. Its HI distribution has a central hole and the IRAC $3.6 \mu\text{m}$ image shows a distinctive bulge and a flocculent spiral structure. The radio continuum map of NGC 2841 shows a strong nuclear source coinciding within $0''.2$ with the position of the central source in the $3.6 \mu\text{m}$ IRAC image. We used the position of the radio continuum source ($\delta X = -6''.3$, $\delta Y = 0''.5$) as input for ROTCUR and made a fit with all parameters left free. We averaged the values for δX and δY between $75'' < r < 220''$ (see first row in Fig. 2.26). The lower limit excludes the two innermost rings, as these are sparsely filled. The upper limit restricts our averaging to a region which is unaffected by spiral arms or by the warp. The dynamical center derived in such a way ($\delta X = -6''.5 \pm 0''.6$, $\delta Y = 0''.4 \pm 0''.9$) deviates by less than $0''.2$ from the other center estimates. Therefore, we choose the radio continuum center as the best center position.

b) Harmonic expansion

The inner $200''$ - $250''$ of NGC 2841 are in unperturbed circular rotation and show only small harmonic terms. For the inner 1 kpc, we have no data as the HI surface density in this region falls below the 3σ detection limit imposed on the velocity fields. Most of the parameters show a large change at $r \approx 350'' - 400''$: the systemic velocity drops by about 20 km s^{-1} , and most of the harmonic components show their highest amplitude at these radii. Looking at the total HI intensity map, one can see that this radius coincides with the location of a strong spiral arm. The dip in the fitted inclination at those radii causes a non-zero c_3 term, induced by the spiral arm. The radial variation of the PA and inclination indicates that the outer disk of NGC 2841 is warped. All harmonic components are similar in amplitude, having median amplitudes of $3 \leq \tilde{A}_m \leq 4 \text{ km s}^{-1}$, or ≤ 2 percent of V_{tot} . $A_r(r)$ is small in the inner parts, but $> 10 \text{ km s}^{-1}$ in the outer parts of NGC 2841. Its median value is $\tilde{A}_r \sim 7 \text{ km s}^{-1}$. The elongation of the potential is fairly constant over the radius and its weighted average is consistent with a round potential (see Table 2.3).

2.A.5 NGC 2903 (Fig. 2.27)

a) Center estimates

NGC 2903 is a barred galaxy with tightly wound spiral arms. Its dominant bar can be seen both in the IRAC image and in the radio continuum map. The radio continuum additionally shows a strong nuclear source, coinciding within $1''$ with the center of the bulge in the $3.6 \mu\text{m}$ image. The central position as given by the radio continuum ($\delta X = -1''.2$, $\delta Y = 2''.4$) was used to make a ROTCUR run with all parameters left free. To derive the kinematic center, we averaged the δX and δY values over the stable parts of the fit, i.e., for $100'' \leq r \leq 300''$ (see top row in Fig. 2.27). The resulting kinematic center ($\delta X = 0''.4 \pm 2''.4$, $\delta Y = 0''.6 \pm 2''.2$) agrees within the uncertainties and within one beam with both the IRAC and the radio continuum center (cf. second row in Fig. 2.27). We therefore adopt the center position as derived from the radio continuum as our final central position.

b) Harmonic expansion

NGC 2903 shows high amplitudes in all harmonic components in the inner $125''$. These non-circular motions are presumably caused by the bar in NGC 2903. The innermost 4-5 data points show the largest deviations from the general trends, most clearly visible in the distributions of the PA, inclination and c_0 .

The pronounced shape in the distribution of s_2 could be caused by an $m = 1$ or $m = 3$ term in the gravitational potential. Given that NGC 2903 is not kinematically lopsided (there is, e.g., no significant difference in the rotation curves of the approaching and receding sides), the contribution from an $m = 1$ term is likely to be small. Inspection of the total HI maps presented in Walter et al. (2008) shows that a spiral arm is located at the same radii as the pronounced variation in s_2 . The wiggles in the radial distributions of s_1 and s_3 at $r \sim 100''$ and $r \sim 350''$ also coincide with the locations of spiral arms. The median amplitudes of the individual harmonic components are small when averaged over the entire galaxy ($\tilde{A}_m \leq 4 \text{ km s}^{-1}$, or 2-3 percent of V_{tot}), but increase towards the center of the galaxy. Within the inner kpc, the $m = 2$ component of \tilde{A}_m has a median value of about 14 km s^{-1} . These high non-circular motions, which can also be seen in the distribution of $A_r(r)$, are likely to be caused by the strong bar, and the associated streaming motions. Like some of the c_i , s_i , and thus also $A_r(r)$, the elongation of the potential shows some variations with radius. Its mean value is nevertheless consistent with a round potential (see Table 2.3).

2.A.6 NGC 2976 (Fig. 2.28)

a) Center estimates

The $3.6 \mu\text{m}$ image of NGC 2976 shows no sign of a bar or spiral arms. Nevertheless, the image shows two enhanced star forming regions at either end of the disk which coincide with density enhancements in the total HI map. Additionally, the IRAC image contains a nuclear source in the central parts of the galaxy, presumably a nuclear star cluster, which has, however, no counterpart in the radio continuum. To test whether the position of this central source agrees with the dynamical center, we perform an unconstrained ROTCUR run and use the position of the nuclear star cluster ($\delta X = 0''.2$, $\delta Y = 0''.1$) as an initial center estimate. By averaging δX , δY over $r < 50''$ (see Fig. 2.28, top row), we derive a dynamical center which is offset from the pointing center by $\delta X = 2''.2 \pm 3''.0$ and $\delta Y = 0''.8 \pm 1''.4$ towards the north-west. Averaging over the entire galaxy gives consistent results ($\delta X = 2''.5 \pm 3''.0$, $\delta Y = 1''.6 \pm 3''.9$). As the dynamical center and the position of the nuclear star cluster agree within the uncertainties and to within one beam (cf. second row in Fig. 2.28), we adopt the position of the nuclear star cluster as the best center position of NGC 2976.

b) Harmonic expansion

The harmonic components of the velocity field of NGC 2976 show a regular behavior. Both s_1 and s_3 scatter within $\sim 1 \text{ km s}^{-1}$ around zero, indicating that the elongation of the gravitational potential is very small. Its weighted mean is consistent with zero ($\langle \epsilon_{\text{pot}} \sin(2\varphi_2) \rangle = -0.010 \pm 0.018$).

The c_2 component is slightly offset from zero and shows sine-like variations with radius, especially for $r > 80''$, where the two HI density enhancements are located. According to Schoenmakers (1999), a non-zero $m = 2$ harmonic component in the velocity field can be caused by an $m = 1$ or $m = 3$ term in the potential. NGC 2976 does not seem to be kinematically lopsided (cf. the negligible differences in the rotation curves of the approaching and receding sides in de Blok et al. 2008). Therefore, there is most likely only a small contribution of an $m = 1$ term in the potential to the $m = 2$ harmonic

term in the velocity field, and the significant contribution should come from an $m = 3$ term in the potential.

Beyond $r \approx 80''$, the PA stays constant. The median amplitudes of all harmonic component are small ($\tilde{A}_m \leq 3$ percent V_{tot}), irrespective of whether one averages over the entire galaxy or only over the inner 1 kpc. The distribution of $A_r(r)$ is also small for most radii. Only a few data points at extreme radii show large amplitudes, but these are associated with large uncertainties. The mean elongation of the potential is, despite being unconstrained in the inner $30''$, again consistent with a round potential (see Table 2.3).

2.A.7 NGC 3031 (Fig. 2.29)

a) Center estimates

NGC 3031 (better known as M 81) is a grand design spiral. Its two well-defined spiral arms are easily visible in the IRAC $3.6 \mu\text{m}$ image as well as in the HI intensity map. NGC 3031 contains a strong central radio source. The $3.6 \mu\text{m}$ image also shows a well-defined central component with a central minimum which coincides with the position of the central radio-continuum source ($\delta X = -202.''7$, $\delta Y = -371.''9$). We used the position of the radio continuum source as input for a ROTCUR run with all parameters left free. As can be seen in the top row of Fig. 2.29, δX and δY show a clear break at $r \sim 400''$, probably because of the prominent spiral arm which is located at approximately that radius. We therefore estimated the dynamical center by averaging δX and δY over $200'' \leq r \leq 385''$, thus omitting the innermost data points whose tilted-rings are only sparsely filled and have correspondingly large uncertainties. The resulting dynamical center ($\delta X = -205.''1 \pm 3.''1$, $\delta Y = -374.''6 \pm 3.''9$) coincides within the uncertainties and within less than one beam with the other center estimates (second row of Fig. 2.29) and we therefore adopt the position of the radio continuum source as the best center position of M 81.

b) Harmonic expansion

The PA, c_0 , and the inclination of M 81 rise steadily beyond $r \approx 400''$, indicating that the outer disk is warped or disturbed, which is not unexpected given that M 81 interacts with M 82 and NGC 3077. The radii with the highest gradient in s_1 and s_3 ($r \approx 350'' - 400''$) correspond with the location of a prominent spiral arm. Between $400'' \leq r \leq 700''$, c_2 and s_2 change from values around $+5 \text{ km s}^{-1}$ to $< -10 \text{ km s}^{-1}$. Note that if we were to perform a harmonic decomposition with an unconstrained center position, the center would vary at those radii in order to minimize the c_2 and s_2 term, thus underestimating the amount of non-circular motions present in M 81. However, as we keep the center position fixed, we are able to quantify and detect these non-circular motions. The median amplitudes \tilde{A}_m of the $m = 2$ and $m = 3$ component are roughly equally high ($\sim 5 \text{ km s}^{-1}$), whereas that of the $m = 1$ component is slightly smaller ($\sim 2 \text{ km s}^{-1}$). As M81 has a central HI minimum, we have no data for the inner 1 kpc. The radial distribution of the non-circular motions varies between $3 \leq A_r(r) \leq 15 \text{ km s}^{-1}$ and has a median of $\tilde{A}_r \sim 9 \text{ km s}^{-1}$ (< 5 percent of V_{tot}), making the amount of non-circular motions quite small, despite the prominent spiral arms. The elongation of the potential shows distinct radial variation which is due to the spiral arms. Its weighted average is again consistent with zero (see Table 2.3).

2.A.8 NGC 3198 (Figs. 2.1-2.4)

a) Center estimates

NGC 3198 is classified as a SBc spiral. Its $3.6 \mu\text{m}$ IRAC image shows two well-defined spiral arms, emanating from a prominent bulge. The central component has a nuclear point source embedded, which has a counterpart in the radio continuum. The center estimates from the IRAC image and the continuum map agree to within $1''$. We make a ROTCUR run with the position of the radio continuum center ($\delta X = -1''.4$, $\delta Y = -0''.1$) as an initial estimate. The variation of the center positions in Fig. 2.1 show that the outer parts ($r \geq 150''$) of NGC 3198 are strongly affected by the spiral arms. For the derivation of the dynamical center, we therefore restrict the averaging of δX and δY to radii with $r \leq 100''$. The derived dynamical center ($\delta X = -1''.4 \pm 1''.7$, $\delta Y = -0''.2 \pm 2''.1$) agrees well with the other estimates (see Fig. 2.2). We therefore adopt the position of the continuum source as the best center position for NGC 3198.

b) Harmonic expansion

The PA of NGC 3198 shows a steep increase within the inner $200''$, and then declines slowly. The inclination varies in the inner parts in a range of about five degrees, but shows a steady increase beyond $r \sim 450''$, indicating that the outer disk is warped. The c_3 term is small, meaning that the fitted inclination is close to the intrinsic inclination of the disk. Although there is no global offset from zero for c_2 and s_2 , they show small deviations from zero for some radii which are coinciding with the locations of spiral arms in the $3.6 \mu\text{m}$ image or the total HI map presented in Walter et al. (2008). The distributions of s_1 and s_3 are best described as wiggles caused by spiral arms on top of a small offset. The global elongation of the potential is with $\langle \epsilon_{\text{pot}} \sin(2\varphi_2) \rangle = 0.017 \pm 0.020$ consistent with zero.

The median amplitudes of the individual harmonic components are similar in amplitude, and of order $\tilde{A}_m \sim 2-3 \text{ km s}^{-1}$, or ≤ 2 percent of V_{tot} . The distribution of $A_r(r)$ shows that the amplitude of the non-circular motions is $\leq 8 \text{ km s}^{-1}$ for most radii. Its median is $\tilde{A}_r \sim 4.5 \text{ km s}^{-1}$ when averaged over the entire radial range, and $\tilde{A}_r \sim 1.5 \text{ km s}^{-1}$ for the inner 1 kpc. The median value of the absolute residual velocity field is $\sim 2.6 \text{ km s}^{-1}$, showing that a harmonic decomposition up to third order was capable of capturing most non-circular motions.

2.A.9 IC 2574 (Fig. 2.30)

a) Center estimates

IC 2574 has neither a central radio continuum source, nor a clear nuclear source in the $3.6 \mu\text{m}$ IRAC image. The dynamics of this galaxy show clear evidence of random non-circular motions, showing themselves as kinks in the iso-velocity contours. For the center determination, we make use of a velocity field where most non-circular features were removed (as presented in Oh et al. 2008). We make a ROTCUR run with all parameters free, using the center position derived by Oh et al. (2008) as an initial center estimate. The results of the ROTCUR fit are shown in row 1 of Fig. 2.30. It can be seen that the values for δX and δY do not change much over a large part of the galaxy. Averaging δX , δY over $r \leq 400''$ results in a dynamical center which is offset by $\delta X = 8''.7 \pm 14''.9$ and $\delta Y = 18''.6 \pm 10''.4$ towards the north-west of the pointing center. This corresponds to $\alpha_{2000} = 10^{\text{h}}28^{\text{m}}27.5^{\text{s}}$, $\delta_{2000} = +68^{\circ}24'58''.7$ and is in excellent agreement with the estimate derived by Oh et al. (2008) ($\alpha_{2000} = 10^{\text{h}}28^{\text{m}}27.7^{\text{s}}$, $\delta_{2000} = +68^{\circ}24'59''.4$).

b) Harmonic expansion

Although we made use of the bulk velocity field from Oh et al. (2008) for the center estimate, we use the hermite velocity field for the harmonic decomposition, as we aim to quantify non-circular motions. The results of the harmonic decomposition of the hermite velocity field of IC 2574 are shown in the third row of Fig. 2.30.

At a radius of $r \sim 250''$, the PA and inclination drop significantly, and the harmonic components jump to more extreme values. The distribution of $A_r(r)$ has its maximum at this radius, and c_1 also shows a clear break. The feature which is most likely responsible for the major non-circular motions is the supergiant shell in the north-east of IC 2574 (see Walter et al. 1998). Looking only at the inner 1 kpc, the amplitudes of the individual harmonic components are all $\leq 1 \text{ km s}^{-1}$. If one measures the amplitudes over the entire radial range of the galaxy, the $m=2$ component is the dominant one, mainly because of the large amplitudes in c_2 and s_2 at $r \sim 250''$.

The median amplitude of the quadratically added non-circular motions is $\tilde{A}_r \sim 3.8 \text{ km s}^{-1}$ when averaged over the entire radial range, and $\tilde{A}_r \sim 1.4 \text{ km s}^{-1}$ for the inner 1 kpc. This shows that although IC 2574 contain a significant amount of *chaotic* non-circular motions (see Oh et al. 2008), the effect of *systematic* (potential induced) non-circular motions is small. For some parts of the galaxy, the elongation of the potential is unconstrained. Its weighted mean is consistent with a round potential, although it has a large uncertainty associated ($\langle \epsilon_{\text{pot}} \sin(2\varphi_2) \rangle = 0.015 \pm 0.045$).

2.A.10 NGC 3521 (Fig. 2.31)

a) Center estimates

NGC 3521 appears in the $3.6 \mu\text{m}$ IRAC image as well as in the HI map as a multi-armed, flocculent spiral galaxy. The IRAC image shows an inner disk, in which a strong nuclear point source (without a counterpart in the radio continuum) is embedded. We use the position of the nuclear point source ($\delta X = -8.''8$, $\delta Y = 5.''7$) as input for a ROTCUR fit with all parameters left free. The top row of Fig. 2.31 shows that the values of δX and δY stay constant for radii smaller than $220''$. Beyond that radius, the rotation curves for the approaching and receding sides start to differ (see de Blok et al. 2008) and this most likely also affects the derived central positions. In order to derive a dynamical center, we average δX and δY for $r \leq 220''$. The resulting center ($\delta X = -8.''9 \pm 0.''8$, $\delta Y = 6.''6 \pm 1.''4$) agrees with the central position found in the IRAC image (see second row of Fig. 2.31) and we adopt the IRAC position as the best center estimate.

b) Harmonic expansion

As can be seen, e.g., in the radial distribution of PA, i , and $A_r(r)$, the inner few data points clearly deviate from the rest. Note that the c_3 component is higher for these points, meaning that their inclination could not be fitted correctly in an unconstrained fit. Some of these inner data points show large non-circular motions, while others (e.g., the inner two points) do not. This becomes even clearer if one looks at the distribution of \tilde{A}_m . Although the median of the $m=3$ component in the inner 1 kpc is small, its upper quartile is rather large, as the inner 1 kpc contain only three data points, one of which has a large amplitude. The s_1 and s_3 components are both slightly offset from zero and superimposed on a wiggle at $r \approx 200''$. The wiggle coincides with a density enhancement in the total HI intensity map (in this case a spiral arm). However, as s_1 is offset to negative values, and s_3 to positive ones, their offsets almost cancel out for the derivation of the elongation of the potential (cf. Eq. 2.5), whose weighted mean is within the uncertainties consistent with zero ($\langle \epsilon_{\text{pot}} \sin(2\varphi_2) \rangle = 0.017 \pm 0.019$).

The effect of the spiral arms is clearly visible in the c_2 and s_2 components. NGC 3521 has the highest median value in the absolute residual velocity field of our sample (4.5 km s^{-1}).

2.A.11 NGC 3621 (Fig. 2.32)

a) Center estimates

The $3.6 \mu\text{m}$ IRAC image of NGC 3621 is dominated by a flocculent spiral structure, which contains a central point source. The prominent star forming region in the south-west is connected to the center of the galaxy by a spiral arm which is clearly visible in the total HI map and the IRAC image. While this star forming region has a counterpart in the radio continuum, the IRAC nuclear point source has not. We use the coordinates of the nuclear point source in the IRAC image ($\delta X = -4.''2$, $\delta Y = -1.''1$) as an initial estimate for a ROTCUR fit with all parameters left free. The results (top row of Fig. 2.32) show that the derived central positions are fairly constant for radii smaller than $450''$ and we therefore derive the dynamical center by averaging over all points with $r < 450''$, with the additional exclusion of the innermost data point. The resulting dynamical center ($\delta X = -6.''0 \pm 2.''0$, $\delta Y = 1.''4 \pm 6.''5$) coincides with the coordinates of the point source both within the uncertainties and the size of the beam (Fig. 2.32, second row). Therefore, we adopt the position of the central point source as our best center estimate for NGC 3621.

b) Harmonic expansion

The data points beyond $r = 600''$ are not used for our analysis due to their sparsely filled tilted-rings. The PA of NGC 3621 is, except for the innermost two data points, constant to within a few degrees. Apart from a few data points at extreme radii, the amplitude of s_1 is almost negligible. c_3 is close to zero, except for $r \approx 300''$. This position also coincides with the radius of the highest amplitude in c_2 , and s_2 . Inspection of the total HI intensity map shows that there is a ring-like HI density enhancement at which a spiral arm emerges in the south-east. The s_3 component shows clear wiggles, indicating spiral arms, and a steep rise beyond $r \approx 500''$, where the tilted-rings are less filled. The elongation of the potential again shows the kinematic signature of the spiral arms. Its weighted average is consistent with zero (see Table 2.3). The median amplitudes for each individual harmonic component are fairly small ($\tilde{A}_m < 3 \text{ km s}^{-1}$, or ≤ 2 percent of V_{tot}). The distribution of $A_r(r)$ is $\leq 5 \text{ km s}^{-1}$ for the majority of radii and has a median value of $\tilde{A}_r \sim 3.4 \text{ km s}^{-1}$.

2.A.12 NGC 3627 (Fig. 2.33)

a) Center estimates

The $3.6 \mu\text{m}$ IRAC image shows that NGC 3627 is a barred galaxy with two asymmetric spiral arms, which are also clearly visible in the total HI map. The central parts of NGC 3627 contain a nuclear point source which is visible in the IRAC image as well as in the radio continuum. Using the position of the point source ($\delta X = 0.''1$, $\delta Y = 0.''1$) as input for an unconstrained ROTCUR fit results in a slightly different center estimate (see row 1 and 2 of Fig. 2.33). We exclude some data points at extreme radii because of their large uncertainties, and average δX , δY for $45'' \leq r \leq 160''$, resulting in a dynamical center which is offset from the pointing center by $\delta X = -4.''5 \pm 3.''1$ and $\delta Y = -6.''8 \pm 4.''8$. These values deviate from the radio continuum source by approximately 1.5σ . Given the asymmetric appearance of NGC 3627, it is to be expected that the results from ROTCUR are somehow affected by it. However, the difference between the kinematic center and the center from the radio continuum is only one beam.

We therefore use the coordinates of the central radio continuum source as the best center position for NGC 3627.

b) Harmonic expansion

NGC 3627 has a central hole in the HI distribution. Therefore, we see only the flat part of the rotation curve and have no data within the inner kpc. The systemic velocity changes from $\sim 730 \text{ km s}^{-1}$ at $r \leq 60''$ to $\sim 705 \text{ km s}^{-1}$ for $r \geq 90''$. All harmonic components (c_2 , c_3 , s_1 , s_2 , s_3) show high amplitudes. The galaxy is kinematically and morphologically lopsided (cf., de Blok et al. 2008), which is also indicated by the non-zero values for c_2 and s_2 . Both the s_1 and the s_3 component show a “dip” at $r \approx 70''$, followed by a steep rise beyond that radius. In the case of s_3 , the rise is followed by a second decline. The radius of that first “dip” coincides with the location of the large arm which extends to the south of NGC 3627. The median amplitudes of the individual harmonic components are the highest in our sample, reaching from $\tilde{A}_m \sim 10 \text{ km s}^{-1}$ for $m = 3$ to $\tilde{A}_m \sim 17 \text{ km s}^{-1}$ for $m = 2$. The distribution of $A_r(r)$ shows that the amplitude of non-circular motions is large at all radii. The median amplitude is $\tilde{A}_r \sim 28.5 \text{ km s}^{-1}$, or up to 14.7 percent of V_{tot} . Given the morphology of NGC 3627, this is not unexpected. Despite the high non-circular motions present here, the weighted mean elongation of the potential is still small, and within its uncertainty consistent with a round potential (cf. Table 2.3), although there are large errors associated with the data points in the outer parts and in the region at $r \approx 70''$.

2.A.13 NGC 4736 (Fig. 2.34)

a) Center estimates

The $3.6 \mu\text{m}$ IRAC image of NGC 4736 is dominated by a ring of star formation which is also prominently visible in the radio continuum and the total HI map. The center is well-defined both in the $3.6 \mu\text{m}$ image and in the radio continuum. The former shows a small central *minimum* in the flux which coincides within $1.''3$ with the central radio-continuum *maximum*. We use the position of the radio continuum source ($\delta X = 0.''2$, $\delta Y = -0.''4$) for a ROTCUR run with all parameters left free. The fitted center positions are stable within the inner $100''$, but have an increasingly large scatter towards the outer parts, most likely due to the marginally filled tilted-rings beyond $r \sim 100''$, and also because of the low inclination of NGC 4736. We therefore average the estimates for δX and δY over the inner $100''$, resulting in a dynamical center ($\delta X = 0.''5 \pm 1.''8$, $\delta Y = 0.''6 \pm 2.''0$) whose deviation from the other center estimates slightly exceeds the uncertainties (1.2σ deviation for δY). Though, to put things into perspective, this is far smaller than one beam (see second row of Fig. 2.34). Thus, we will use the position of the radio continuum source as the best center estimate for NGC 4736.

b) Harmonic expansion

The star forming ring at $r \sim 80''$ causes a lot of confusion in the inner parts of NGC 4736. Here the unconstrained fit by RESWRI produces an apparent rotation velocity which rises to twice the value in the outer parts. The other harmonic components also show high amplitudes. The median amplitudes of each harmonic component (averaged over the inner 1 kpc) are negligible for the $m = 1$ and $m = 3$ component ($\tilde{A}_m \sim 1 \text{ km s}^{-1}$), but much higher for the $m = 2$ component ($\tilde{A}_m \sim 7 \text{ km s}^{-1}$). The amplitude of the quadratically added non-circular motions, $A_r(r)$, is $\sim 10 \text{ km s}^{-1}$ for most radii.

NGC 4736 is both kinematically and morphologically lopsided, which can be seen not only in the differences between the rotation curves of the approaching and receding sides (see de Blok et al.

2008), but also in the high amplitudes in the c_2 and s_2 terms of our harmonic expansion. The highest amplitudes in the harmonic terms are found for radii between $r \approx 200''$ and $r \approx 300''$, i.e., those radii where the large northern spiral arm is located. The weighted average of the elongation of the potential is $\langle \epsilon_{\text{pot}} \sin(2\varphi_2) \rangle = -0.055 \pm 0.149$.

2.A.14 DDO 154 (Fig. 2.35)

a) Center estimates

DDO 154 is a quiescent, gas-rich dwarf galaxy with a warp in the outer parts. It does not have a compact, well-defined center in the $3.6 \mu\text{m}$ IRAC image, or in the radio continuum. We attempted to derive a center position by fitting ellipses at a few representative intensity levels to the IRAC image, and the total HI map. The resulting central positions showed a variation of up to $15''$, demonstrating that deriving an unambiguous *photometric* center for DDO 154 is not straightforward. We used the center which was derived using the total HI map as a initial estimate for a ROTCUR fit with all parameters left free. The central positions as derived by ROTCUR are fairly stable over the radial range of the galaxy and the kinematic center was derived by averaging the δX , δY values over $100'' \leq r \leq 260''$, thus omitting the slightly more unstable inner and outer regions. The resulting center position is given in Table 2.2. Including the inner data points gives a similar center position, but with two times larger scatter. We therefore adopt the dynamical center as averaged over $100'' \leq r \leq 260''$ as the best center position of DDO 154.

b) Harmonic expansion

The c_3 term is close to zero for the entire radial range, normally indicating that the inclination could be well-determined. However, due to the nearly solid-body rotation in the innermost parts of DDO 154, the inclination is not very well-constrained in this region, as can be seen in the large scatter of the individual data points for $r \leq 70''$. This is studied in more detail in Section 2.6.4. The c_2 component shows a maximum at around $r \approx 80''$ which coincides with a minimum in the s_2 component and a change in the systemic velocity c_0 , providing evidence for a small kinematic lopsidedness as supported by the variation of the center position at these radii and the differences between the approaching and receding sides of the rotation curve (see de Blok et al. 2008). However, the effects described above are small. Despite the small-scale structure present in the velocity field, the amplitudes of all harmonic components — both for the entire galaxy and for the innermost 1 kpc — are $\leq 1 \text{ km s}^{-1}$, or ~ 2 percent of V_{tot} . The distribution of $A_r(r)$ shows that the amplitudes of non-circular motions in DDO 154 are small for all radii. The mean elongation of the potential is small, $\langle \epsilon_{\text{pot}} \sin(2\varphi_2) \rangle = 0.024 \pm 0.033$, and consistent with zero. The median of the absolute residual velocity field is 1.2 km s^{-1} (the smallest in our sample).

2.A.15 NGC 4826 (Fig. 2.36)

a) Center estimates

NGC 4826 shows no sign of spiral structure in the $3.6 \mu\text{m}$ IRAC image, but has two counter-rotating gas disks (Braun et al. 1994). The center of NGC 4826 is well-defined by the central, compact source visible in the radio continuum, and the IRAC $3.6 \mu\text{m}$ image, whose coordinates agree to within $1''$. We use the position of the radio continuum source ($\delta X = 2''.4$, $\delta Y = 8''.5$) as an initial estimate for an unconstrained ROTCUR fit. We derive the dynamical center by averaging the δX , δY values inwards

of $60''$, i.e., over the radial range of the inner disk. The kinematic center derived in such a way ($\delta X = 2.''2 \pm 1.''6$, $\delta Y = 7.''5 \pm 0.''8$) agrees well with the other center estimates and we therefore assume the position of the radio continuum source to be the best center for NGC 4826.

b) Harmonic expansion

Because of the sparsely filled tilted-rings, and the additional complication of the two counter-rotating disks, we have not attempted to derive a harmonic decomposition for this galaxy.

2.A.16 NGC 5055 (Fig. 2.37)

a) Center estimates

NGC 5055 is classified as an Sbc galaxy and has a flocculent structure in the $3.6 \mu\text{m}$ IRAC image. The IRAC image shows a compact nucleus with a well-defined center, whose position coincides to within $1''$ with a faint central radio continuum source. We use the position of the latter ($\delta X = 8.''8$, $\delta Y = 0.''4$) as the input center for a ROTCUR run with all parameter left free.

We derive the dynamical center by averaging the δX , δY values for radii smaller than $450''$ to exclude the parts with sparsely filled tilted-rings beyond $r \sim 450''$. This center ($\delta X = 8.''2 \pm 4.''8$, $\delta Y = 0.''4 \pm 2.''0$) coincides within the uncertainties and to within a beam size with the other center estimates. We therefore adopt the position of the radio continuum source as the best estimate for the central position of NGC 5055.

The HI distribution and kinematics of NGC 5055 were recently analyzed by Battaglia et al. (2006). They define a dynamical center coinciding with their optical center at $\alpha_{2000} = 13^{\text{h}}15^{\text{m}}49.25^{\text{s}}$, $\delta_{2000} = +42^{\circ}01'49.''3$, which is $4''$ to the north of our choice. As our choice was also guided by the position of the central source in the $3.6 \mu\text{m}$ image, this would imply that the respective photometric centers must be shifted by $4''$ with respect to each other. The optical center position listed in Battaglia et al. (2006) is ultimately based on a listing in Maoz et al. (1996) of the position of the central UV source in NGC 5055 determined using an HST FOC image. On examination of the relevant image in the Hubble Space Telescope archive, we find the central source to be located at $\alpha_{2000} = 13^{\text{h}}15^{\text{m}}49.3^{\text{s}}$, $\delta_{2000} = +42^{\circ}01'46.''2$, which is in much closer agreement ($0.''8$) with our position.

b) Harmonic expansion

For the harmonic analysis of NGC 5055, a distinction between the inner and the outer parts has to be made. NGC 5055 has a well-defined HI disk which extends to about $450''$. Beyond that radius, the HI column density is lower and generally falls below the 3σ column density limit which we imposed during the construction of the velocity fields (see de Blok et al. 2008). Therefore, the uncertainties increase rapidly and we considered only data points with radii $r < 450''$ for the radial averaging of the parameters. The median amplitudes of the individual harmonic components (averaged over $r < 450''$) are all fairly low ($\tilde{A}_m < 3 \text{ km s}^{-1}$ or ~ 2 percent of V_{tot}). The median amplitudes averaged over the inner 1 kpc contain only three data points and are also low for the $m = 1$ and $m = 3$ components, but quite high ($\sim 8 \text{ km s}^{-1}$) for the $m = 2$ component. The latter has a large scatter associated with it, mainly because of the innermost data point which shows high non-circular motions, but is derived from an only partially filled tilted-ring. The global elongation of the potential is well-constrained in the inner part of NGC 5055. The weighted mean elongation within $450''$ is again consistent with a round potential (see Table 2.3).

2.A.17 NGC 6946 (Fig. 2.38)

a) Center estimates

NGC 6946 is a late-type spiral galaxy with well-defined multiple spiral arms. The IRAC $3.6\ \mu\text{m}$ image shows a point source in the center of the galaxy which coincides to better than $1''$ with the central radio continuum source. We use the position of the latter ($\delta X = -1''.8$, $\delta Y = 14''.5$) as input for a ROTCUR fit with all parameters left free and determine the dynamical center by averaging the δX , δY values for $22'' \leq r \leq 290''$, thus excluding the two innermost points which are affected by sparsely filled tilted-rings. The resulting dynamical center ($\delta X = -3''.3 \pm 4''.4$, $\delta Y = 11''.8 \pm 5''.8$) coincides within the uncertainties and to within one beam with the other center estimates (see Fig. 2.38, row 2). The large uncertainties in the kinematic estimate are caused by the relatively low inclination of NGC 6946, which makes an unconstrained tilted-ring fit of the velocity field more difficult. We adopt the position of the central radio continuum source as the best center for NGC 6946.

b) Harmonic expansion

NGC 6946 is the galaxy in our sample with the lowest inclination. This introduces larger uncertainties in the rotation curve and the harmonic decomposition. For our analysis of the median amplitudes, and for the derivation of the average elongation, we regard only the inner $420''$, i.e., the region where the unconstrained apparent circular velocity c_1 does not rise to a value two times that in the flat part. This radius also coincides with the location from which, when moving outwards, the approaching and receding sides of the velocity field start to differ substantially (see de Blok et al. 2008). The median amplitudes averaged over $r < 420''$ are small for each harmonic component ($\tilde{A}_m \leq 5\ \text{km s}^{-1}$). Due to the deficiency of HI in the center of NGC 6946, we can not study the kinematics within the inner 1 kpc. Again averaging only over $r < 420''$, the median of the quadratically added amplitudes of all non-circular components is $\tilde{A}_r \approx 7\ \text{km s}^{-1}$. The steep rise in s_2 and s_3 at $r \approx 120''$ is probably caused by the spiral arm which crosses at that radius. Due to the low inclination of NGC 6946, and the associated large error in the derivation of the fitted parameters, the elongation of the potential is not well-constrained for $r \leq 150''$ and $r \geq 420''$. Its weighted mean (again averaged over $r \leq 420''$), however, is consistent with a round potential.

2.A.18 NGC 7331 (Fig. 2.39)

a) Center estimates

The $3.6\ \mu\text{m}$ IRAC image of NGC 7331 shows prominent spiral arms, and a well-defined nucleus which has no counterpart in the radio continuum. We use the center from the $3.6\ \mu\text{m}$ image ($\delta X = 0''.1$, $\delta Y = 0''.3$) as input for an unconstrained fit with ROTCUR. Ignoring the two innermost points as their tilted-rings are only sparsely filled, we average the values for δX and δY over the stable region with $r \leq 185''$. This results in a dynamical center of $\delta X = 0''.0 \pm 0''.6$, $\delta Y = -1''.8 \pm 2''.2$, which agrees within the uncertainties and to within one beam with the IRAC center. Therefore, we adopt the IRAC center as our best center position for NGC 7331.

b) Harmonic expansion

Although PA and inclination do not change much over the radial range (~ 4 -6 degrees), they both increase outwards, indicating a warping of the disk. The small c_3 values denote that the inclination could be well-determined for most radii. The s_1 and s_3 values both show a wiggle at $r \approx 150''$,

coinciding with the location of a spiral arm visible in the total intensity HI map and in the IRAC 3.6 μm image. The variation of c_0 , c_2 , and s_2 shows that NGC 7331 is kinematically lopsided, as shown by the differences in the rotation curves of the receding and approaching sides of the velocity field (cf., de Blok et al. 2008). The median amplitudes of the individual harmonic components are all small ($\tilde{A}_m < 5 \text{ km s}^{-1}$). Because of the central HI deficiency of NGC 7331, there is no kinematic data for the inner 1 kpc. The distribution of $A_r(r)$ varies between $A_r(r) \sim 2 \text{ km s}^{-1}$ and $A_r(r) \sim 10 \text{ km s}^{-1}$ and has a median of $\tilde{A}_r \sim 6 \text{ km s}^{-1}$. The elongation of the potential is well-determined and close to zero for most radii. The wiggle at $r \approx 150''$ is again an indication of the aforementioned spiral arm. The weighted mean elongation is $\langle \epsilon_{\text{pot}} \sin(2\varphi_2) \rangle = -0.003 \pm 0.017$, and therefore consistent with a round potential.

2.A.19 NGC 7793 (Fig. 2.40)

a) Center estimates

NGC 7793 is a flocculent spiral whose 3.6 μm IRAC image shows a well-defined central source without a counterpart in the radio continuum. We adopt the position of this source ($\delta X = -9''.1$, $\delta Y = -0''.9$) as the initial estimate for an unconstrained ROTCUR fit, and average the δX , δY values over the stable part of the galaxy ($r \leq 180''$). The resulting kinematic center ($\delta X = -9''.9 \pm 2''.6$, $\delta Y = 1''.8 \pm 2''.1$) agrees reasonably well with the IRAC center (1.5σ deviation). However, the deviation between these two center estimates is ~ 6 times smaller than the size of one beam and we therefore use the IRAC center as our best center position.

b) Harmonic expansion

The PA and the inclination vary continuously with radius, indicating that the disk of NGC 7793 might be warped. The systemic velocity, c_0 , stays fairly constant over radius. The offset from zero in the s_2 component might indicate a slight kinematic lopsidedness, which is also visible in the difference between the receding and approaching sides of the rotation curve in de Blok et al. (2008). The s_3 term is significantly larger than the s_1 term, which is typical for galaxies with low inclination (Schoenmakers 1999). In fact, the s_3 component seems to be offset from zero, indicating through Eq. 2.5 an elongation of the potential. The weighted mean elongation is $\langle \epsilon_{\text{pot}} \sin(2\varphi_2) \rangle = -0.067 \pm 0.085$, which is the largest elongation we have measured in our sample. It is due to its large uncertainty consistent with both the CDM predictions by Hayashi et al. (2007) and with a round potential. The large uncertainty for the elongation arises from the relatively large error bars of the inclination values, which enter into the uncertainty in ϵ_{pot} as a fourth power (cf. Eq. 2.5). The median amplitude of each harmonic component is fairly low ($A_m < 4 \text{ km s}^{-1}$), both for the entire galaxy and for the inner 1 kpc. The distribution of $A_r(r)$ shows that the amplitude of non-circular motions is small, especially in the inner parts of NGC 7793. Its median value (averaged over the entire galaxy) is $\tilde{A}_r \sim 5 \text{ km s}^{-1}$. The median of the absolute residual velocity field is 2.2 km s^{-1} , again showing that a harmonic expansion up to third order did cover most of the non-circular motions.

2.B Appendix: The atlas

The center estimates and the harmonic decompositions are shown in Figs. 2.23-2.40. Following is a description of the content and layout of the figures: Each figure consists of four rows. From top to bottom, they contain:

Row 1: The radial variation of the center position. Shown is the offset from the pointing center in arcsecond. The top panel shows the offsets in the X (or right ascension) direction, with positive δX to the west; the bottom panel those in the Y (declination) direction, with positive δY to the north. The filled circles represent the individual center positions derived using ROTCUR, and the error bars indicate the formal uncertainties derived by ROTCUR. The two dotted, vertical lines indicate the radial range over which the positions were averaged in order to derive a kinematic center. The kinematic center is indicated by the solid horizontal line, and the 1σ standard deviation by the dotted, horizontal lines. For those cases where the kinematic center was not used as our best center position, we additionally show the best estimate with a dashed, horizontal line.

Row 2: The inner $150'' \times 150''$ of the galaxy. The total intensity HI map is shown in grayscales, and the beam size is indicated in the bottom-left corner. The black contours are drawn from the velocity field which was used for the estimate of the dynamical center (bulk velocity field from Oh et al. 2008 for IC 2574, hermite velocity field from de Blok et al. 2008 for the other galaxies). The thick line represents the systemic velocity as derived in de Blok et al. (2008). The thin black contours overlaid on the thick white contours belong to the $3.6\ \mu\text{m}$ IRAC image and are usually given at a 2, 5, 10, 20, and 50 percent level of the maximum flux in the image. The white contours are taken from the THINGS radio continuum maps and are usually given at a 10, 20, and 50 percent level of the maximum flux. The black, filled circles indicate the individual center positions from ROTCUR and the black cross represents the chosen dynamical center and its uncertainty. The derived center from the $3.6\ \mu\text{m}$ image is shown as a gray, filled triangle, and the one from the radio continuum as a black, open triangle.

Inset: To better highlight the different center estimates, we additionally show in the upper-right corner an inset with only the central few arcseconds. For clarity, we omit the total HI map and the velocity field contours in the inset. The contours from the $3.6\ \mu\text{m}$ image are shown in black and are given at the same intensity levels as in the main plot. The same holds for the radio continuum contours, which are shown here in gray. The individual center estimates from ROTCUR are shown as small crosses. In the inset, the beam size is indicated by the thick dashed ellipse, which is centered on our best center position.

Row 3: The error bars of all plots in this row are the formal uncertainties as derived by RESWRI. *Left panel:* This panel consists of six sub-panels, all of which are plotted against radius in arcsecond. The upper-left sub-panel shows c_1 , the amplitude of the circular velocity. The other five sub-panels show the amplitudes of the non-circular components, namely the second and third order component of the cosine term (c_2, c_3) and the first, second, and third order component of the sine term (s_1, s_2, s_3). The axis scale of these five sub-panels is generally -20 to $+20\ \text{km s}^{-1}$. The solid, vertical line in the panel containing c_1 indicates the radius corresponding to 1 kpc. All quantities shown in Row 3 are corrected for inclination effects.

Right panel: From top to bottom: systemic velocity c_0 ; inclination angle i ; and position angle PA, all plotted against radius in arcsecond. The dashed, horizontal line in all three sub-panels indicates the weighted mean, using the inverse square of the uncertainties as weight.

Row 4: *Left panel:* This panel consists of two sub-panels. The left sub-panel shows \tilde{A}_m , the median amplitudes for each harmonic order m . The values are calculated by radially averaging the quadratically added amplitudes as described by Eqs. 2.6 and 2.7. We show the median as determined

for the entire extent of the galaxy (filled circles) as well as using only the inner 1 kpc (open circles). The error bars indicate the lower and upper quartile respectively. The right sub-panel shows $A_r(r)$, the radial distribution of the amplitude of all non-circular motions derived following Eq. 2.8. The error bars of $A_r(r)$ are derived with formal error propagation assuming a Gaussian error distribution. Both \tilde{A}_m and $A_r(r)$ are corrected for inclination effects.

Right panel: This panel contains the elongation of the potential $\langle \epsilon_{\text{pot}} \sin(2\varphi_2) \rangle$ (cf., Eq. 2.5) vs. radius. The elongation is also corrected for inclination. The solid, black line indicates the zero level, the dotted gray one represents the weighted mean elongation, and the dashed, gray ones its standard deviation. The error bars shown here are derived using a formal error propagation assuming a Gaussian error distribution.

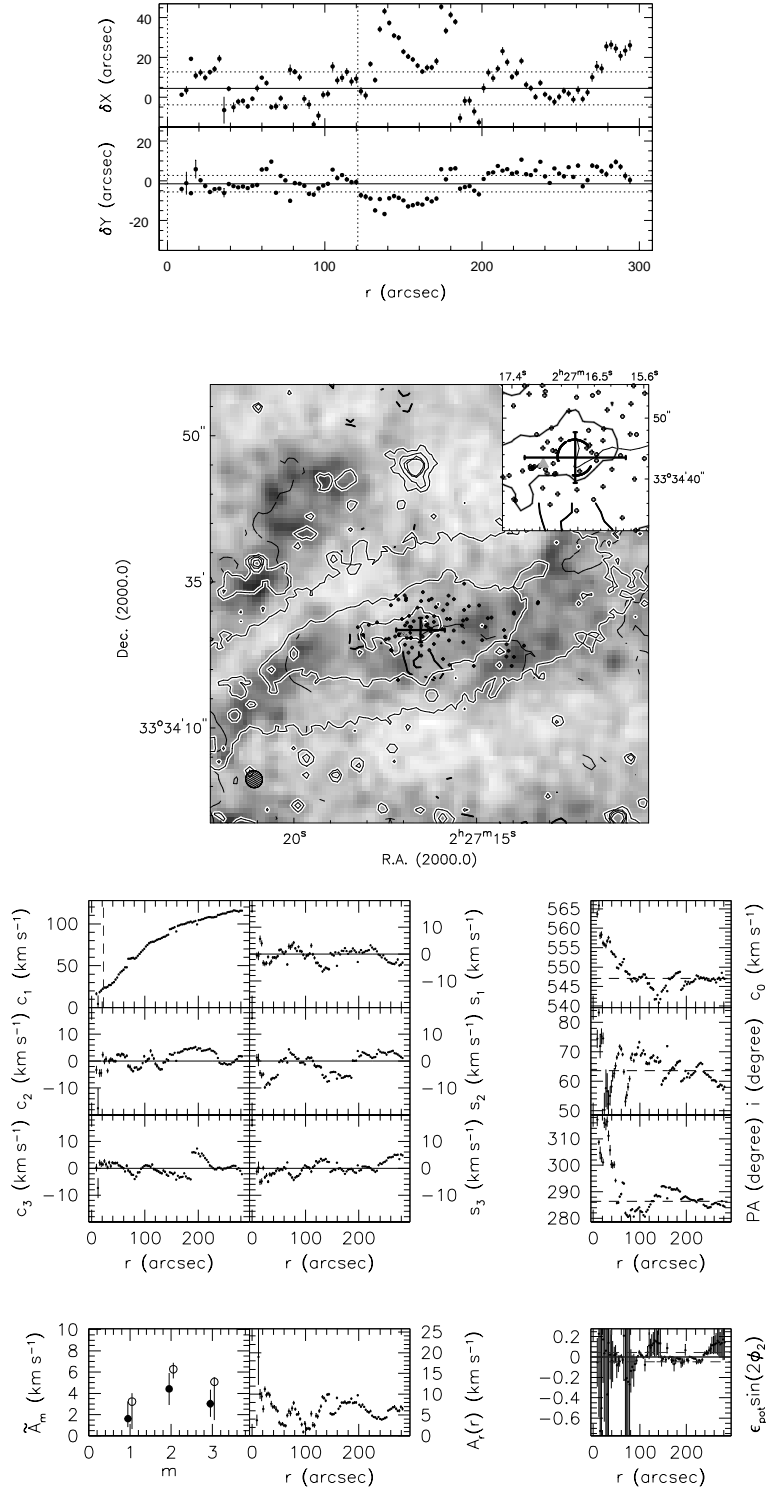


FIG. 2.23: Summary panel for NGC 925. Lines and symbols are described in the text, Appendix 2.B. The IRAC center shown was derived using ELLFIT. We omitted the IRAC contours at the 2% and 5% levels for clarity reasons. See Appendix 2.A.1 for a discussion of this galaxy.

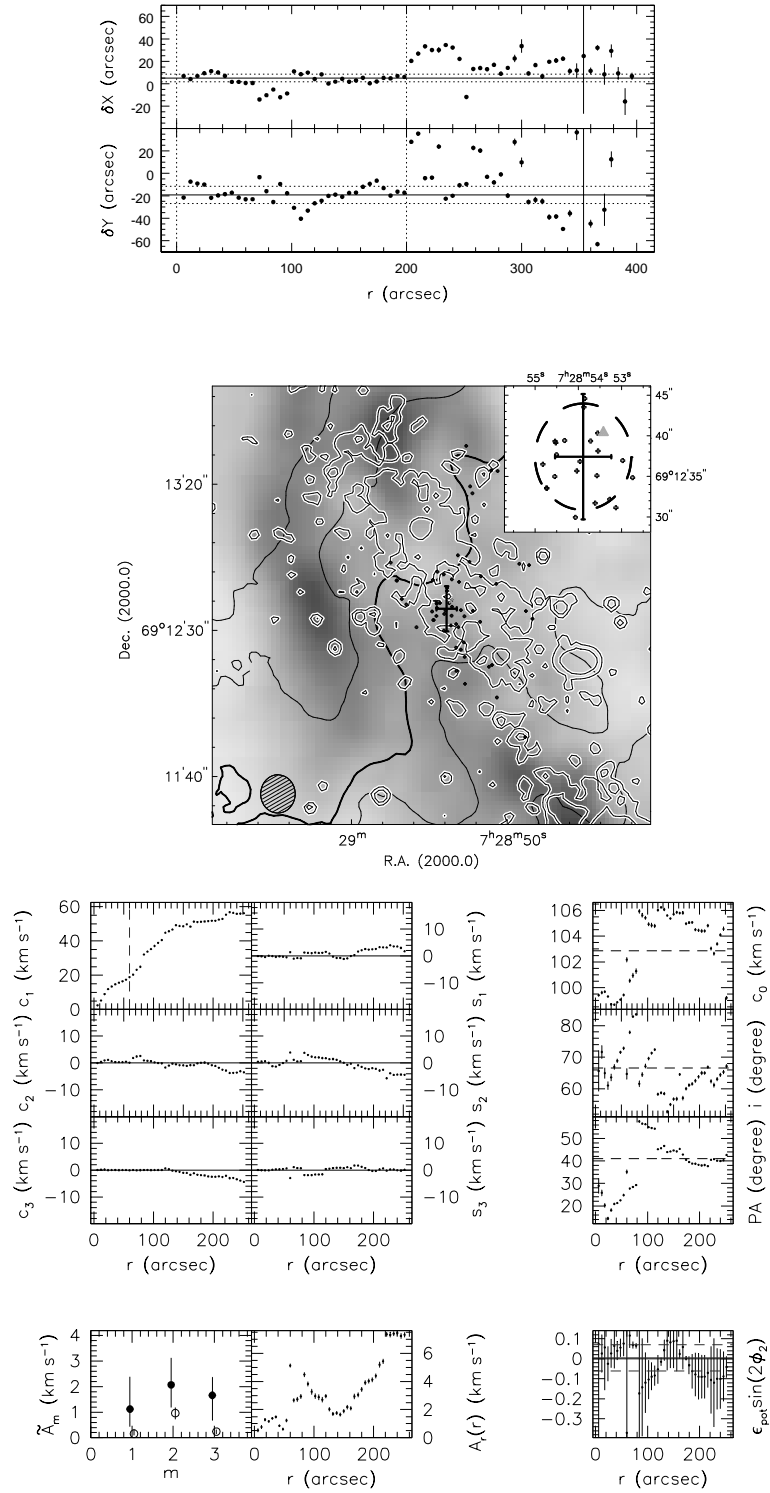


FIG. 2.24: Summary panel for NGC 2366. Lines and symbols are described in the text, Appendix 2.B. The IRAC center shown was derived using ELLFIT. See Appendix 2.A.2 for a discussion of this galaxy.

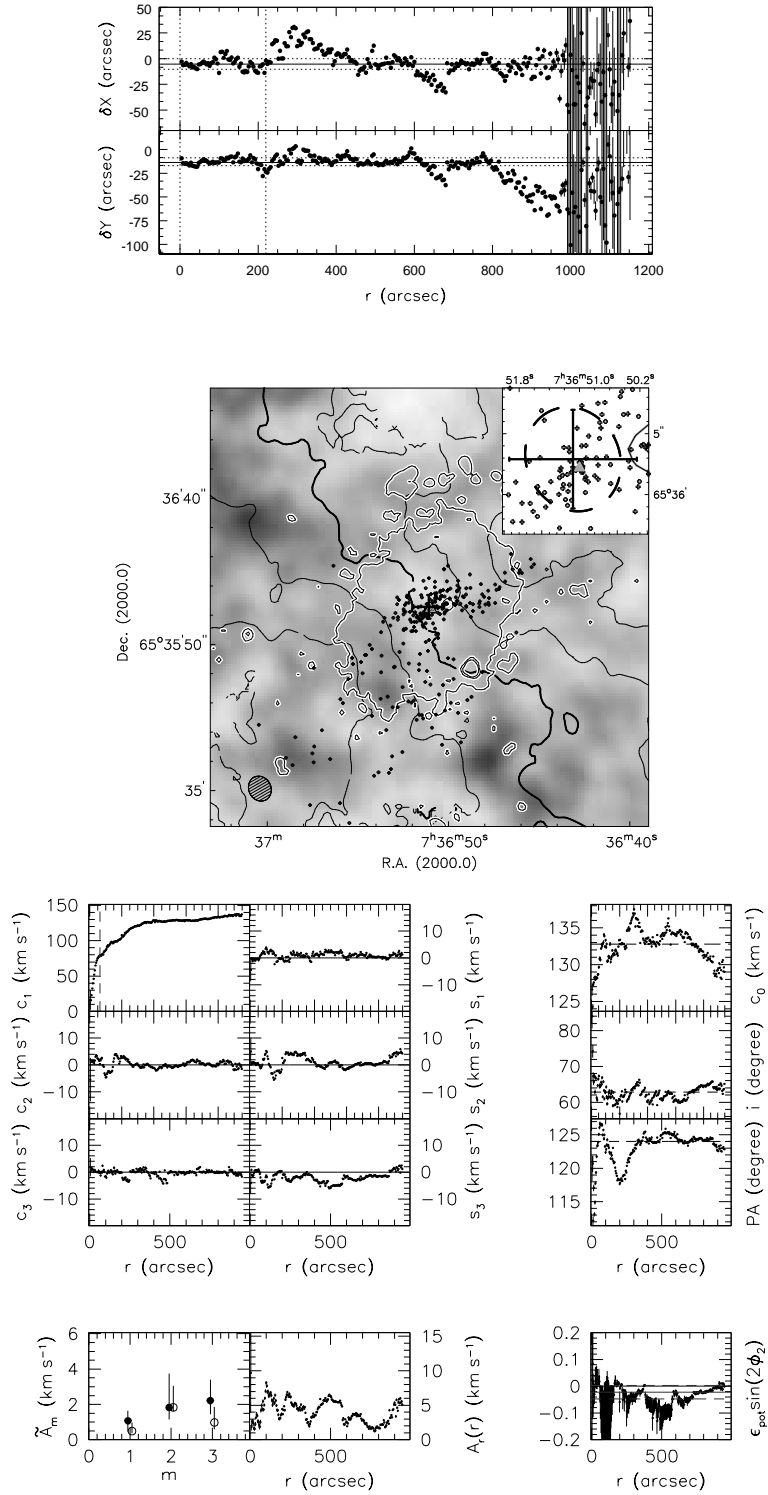


FIG. 2.25: Summary panel for NGC 2403. Lines and symbols are described in the text, Appendix 2.B. The 2, 5, and 10% IRAC contours were omitted for clarity reasons. See Appendix 2.A.3 for a discussion of this galaxy.

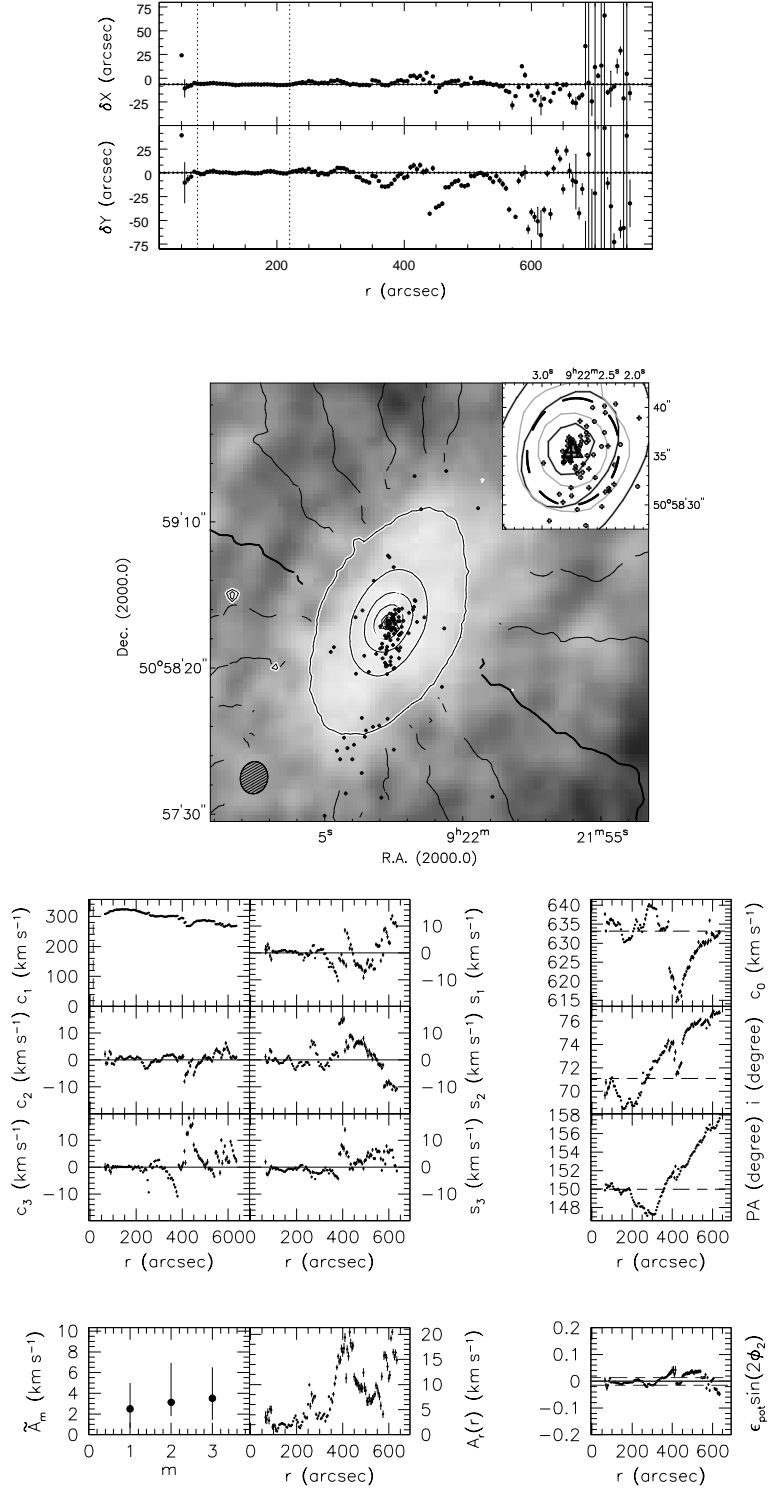


FIG. 2.26: Summary panel for NGC 2841. Lines and symbols are described in the text, Appendix 2.B. See Appendix 2.A.4 for a discussion of this galaxy.

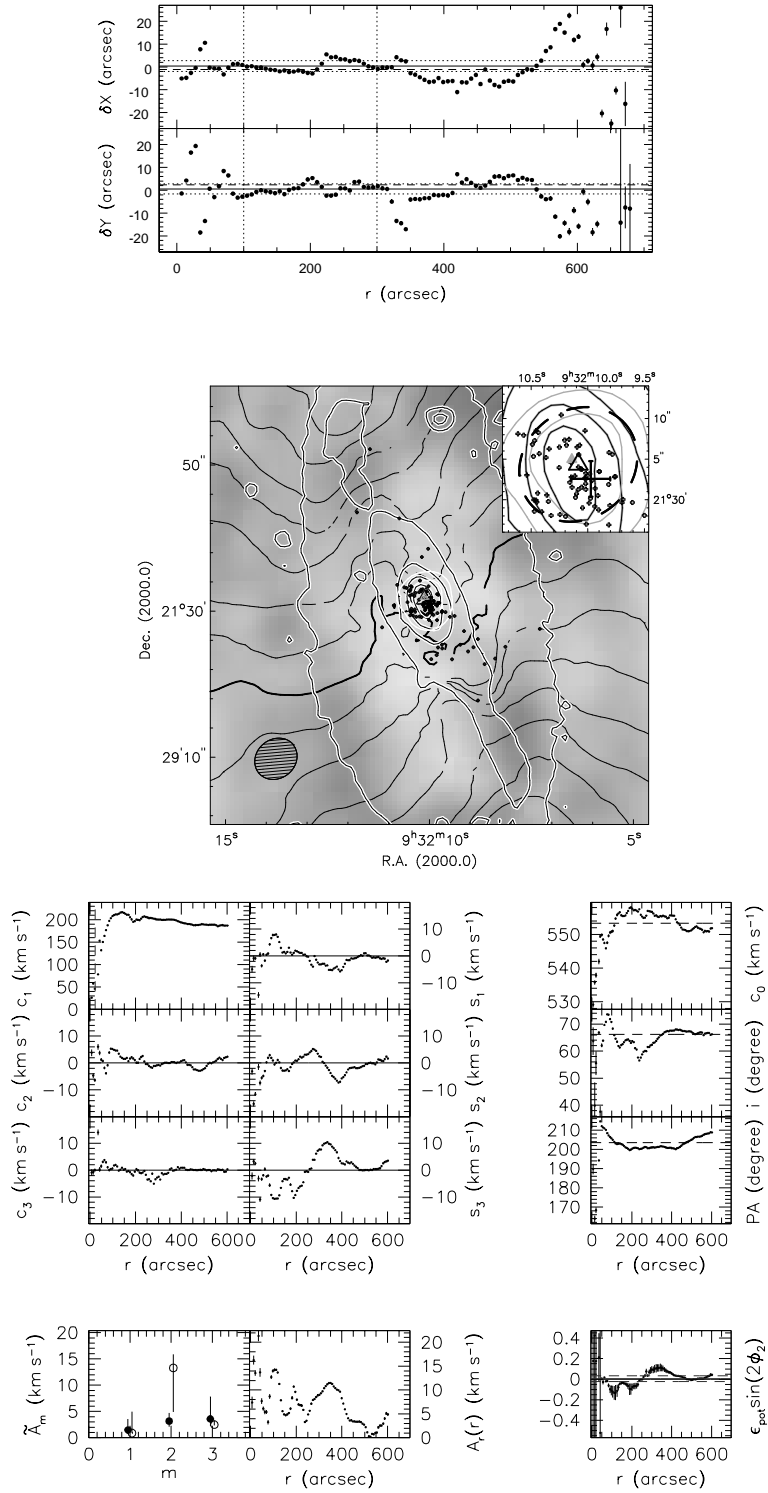


FIG. 2.27: Summary panel for NGC 2903. Lines and symbols are described in the text, Appendix 2.B. See Appendix 2.A.5 for a discussion of this galaxy.

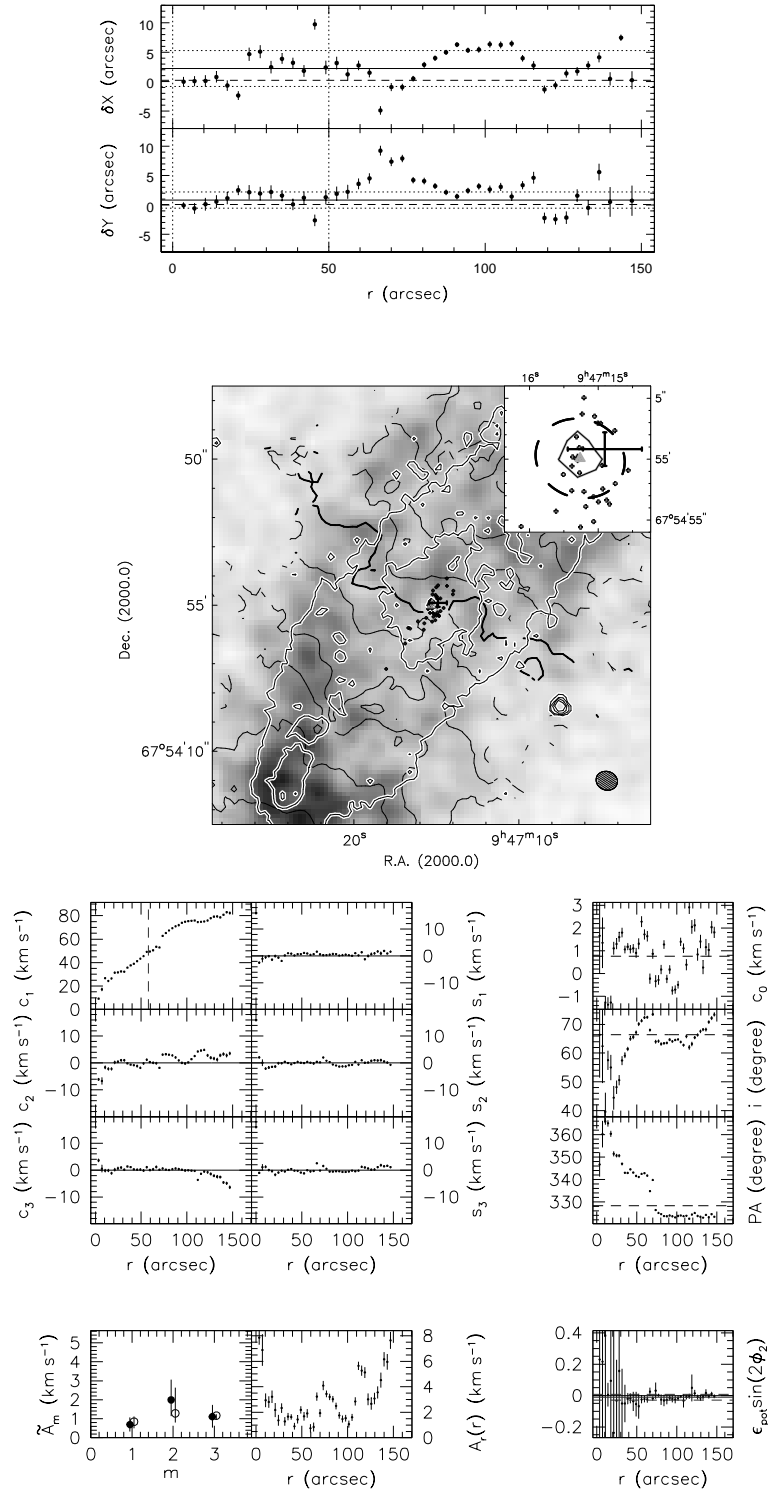


FIG. 2.28: Summary panel for NGC 2976. Lines and symbols are described in the text, Appendix 2.B. The 2% and 5% IRAC contours were omitted for clarity reasons. See Appendix 2.A.6 for a discussion of this galaxy.

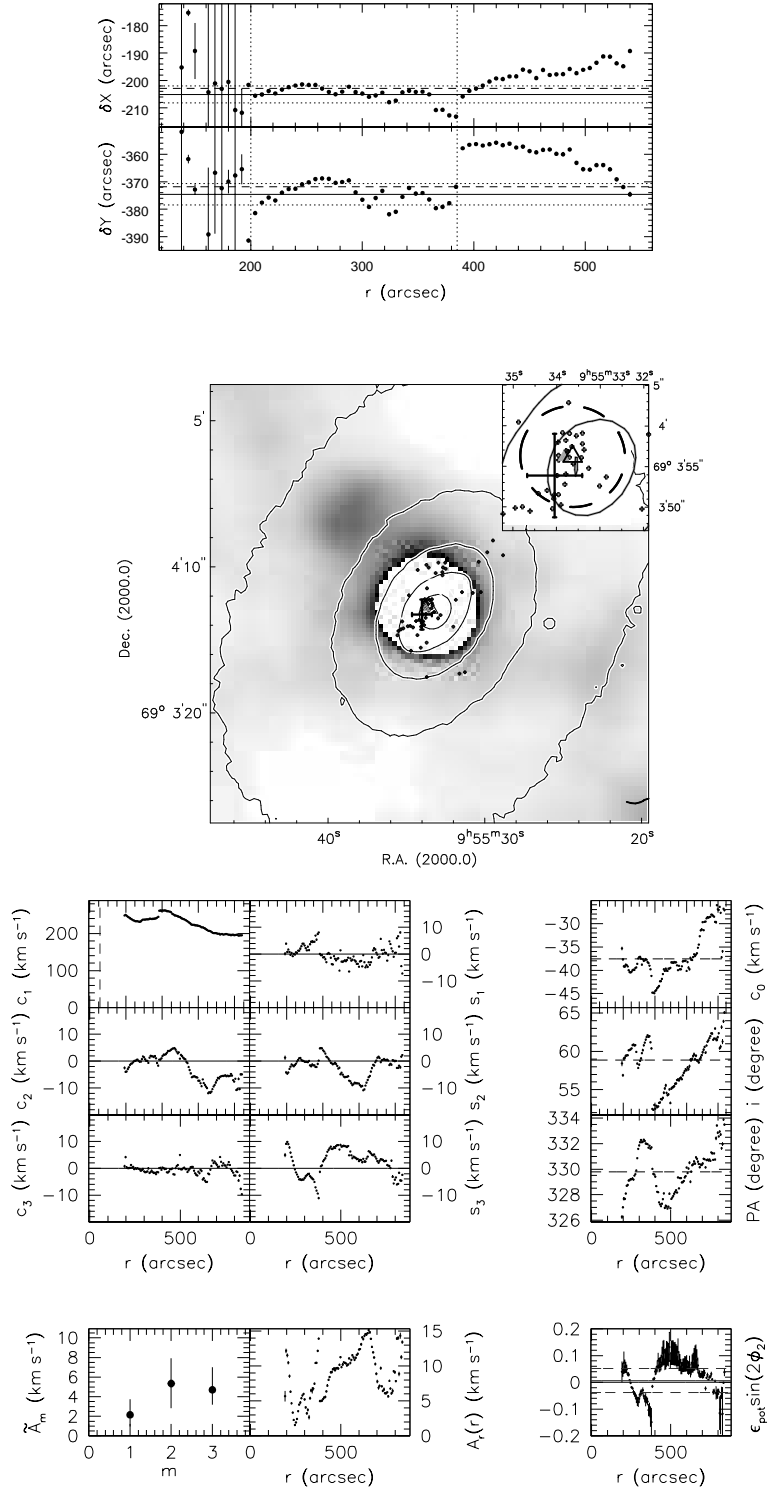


FIG. 2.29: Summary panel for NGC 3031. Lines and symbols are described in the text, Appendix 2.B. The bright radio continuum source which is still visible in the total intensity HI map was blanked out for clarity reasons. Due to the central HI deficiency, no velocity contours are visible. See Appendix 2.A.7 for a discussion of this galaxy.

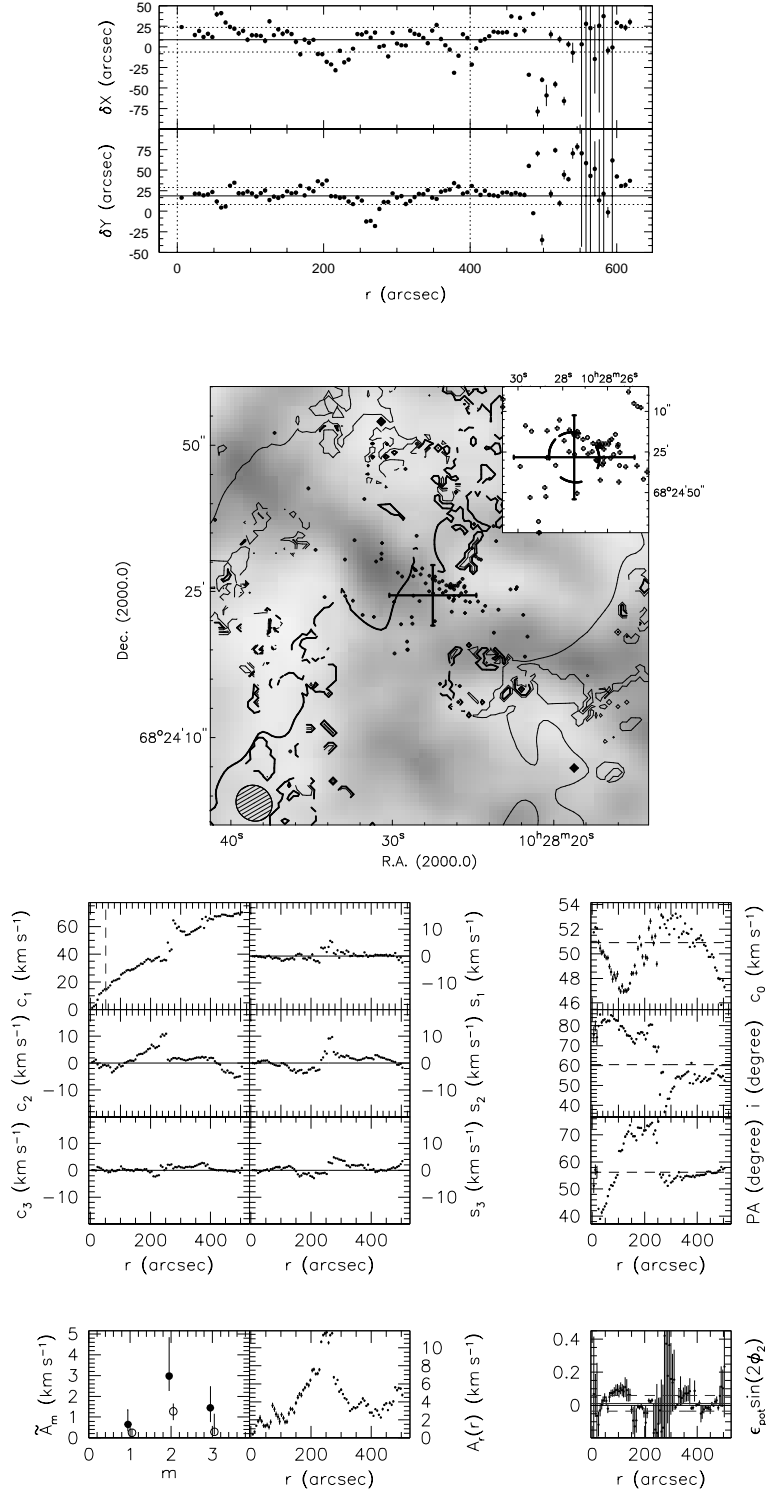


FIG. 2.30: Summary panel for IC 2574. Lines and symbols are described in the text, Appendix 2.B. No estimate could be derived from the IRAC and radio continuum images, and their respective contours are therefore not shown. See Appendix 2.A.9 for a discussion of this galaxy.

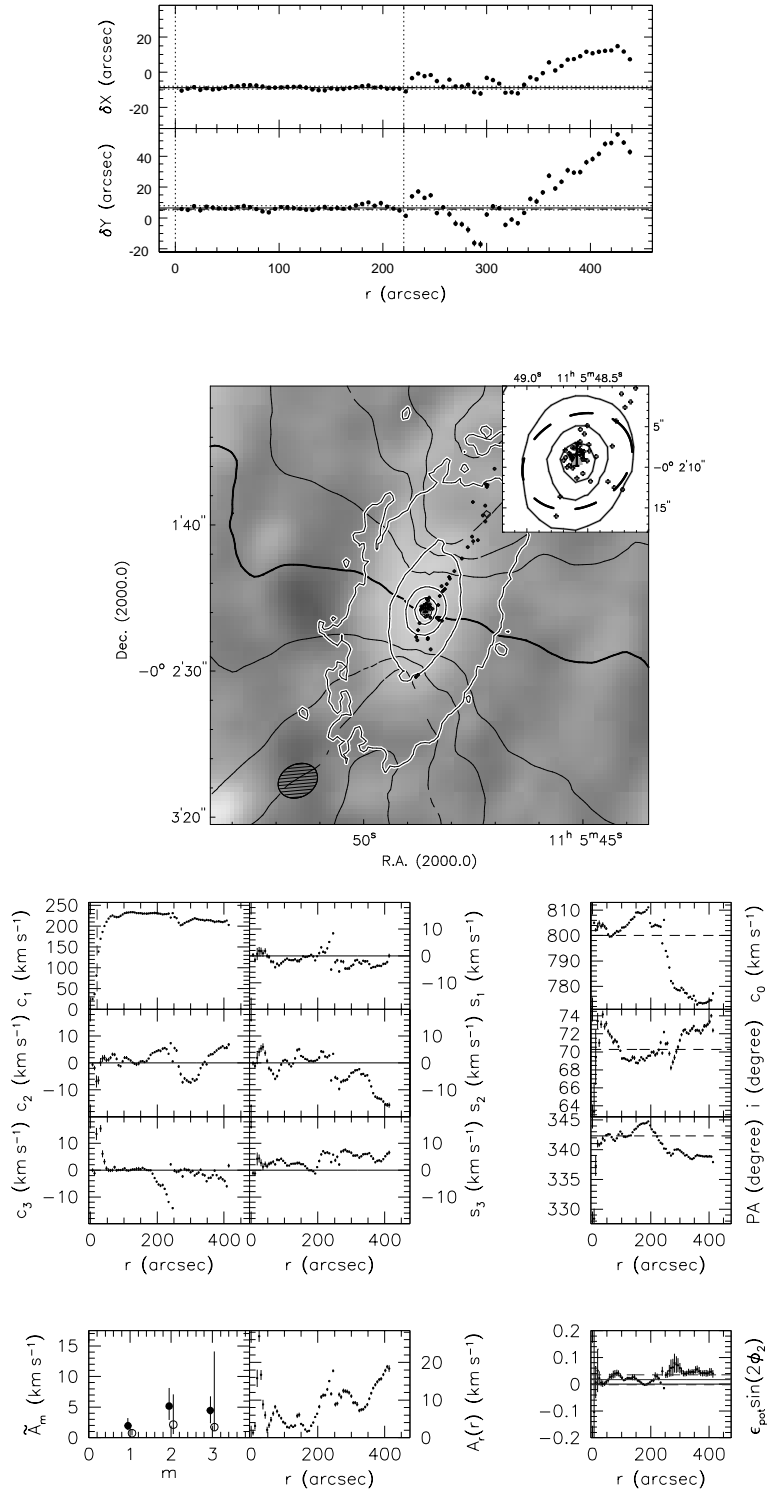


FIG. 2.31: Summary panel for NGC 3521. Lines and symbols are described in the text, Appendix 2.B. See Appendix 2.A.10 for a discussion of this galaxy.

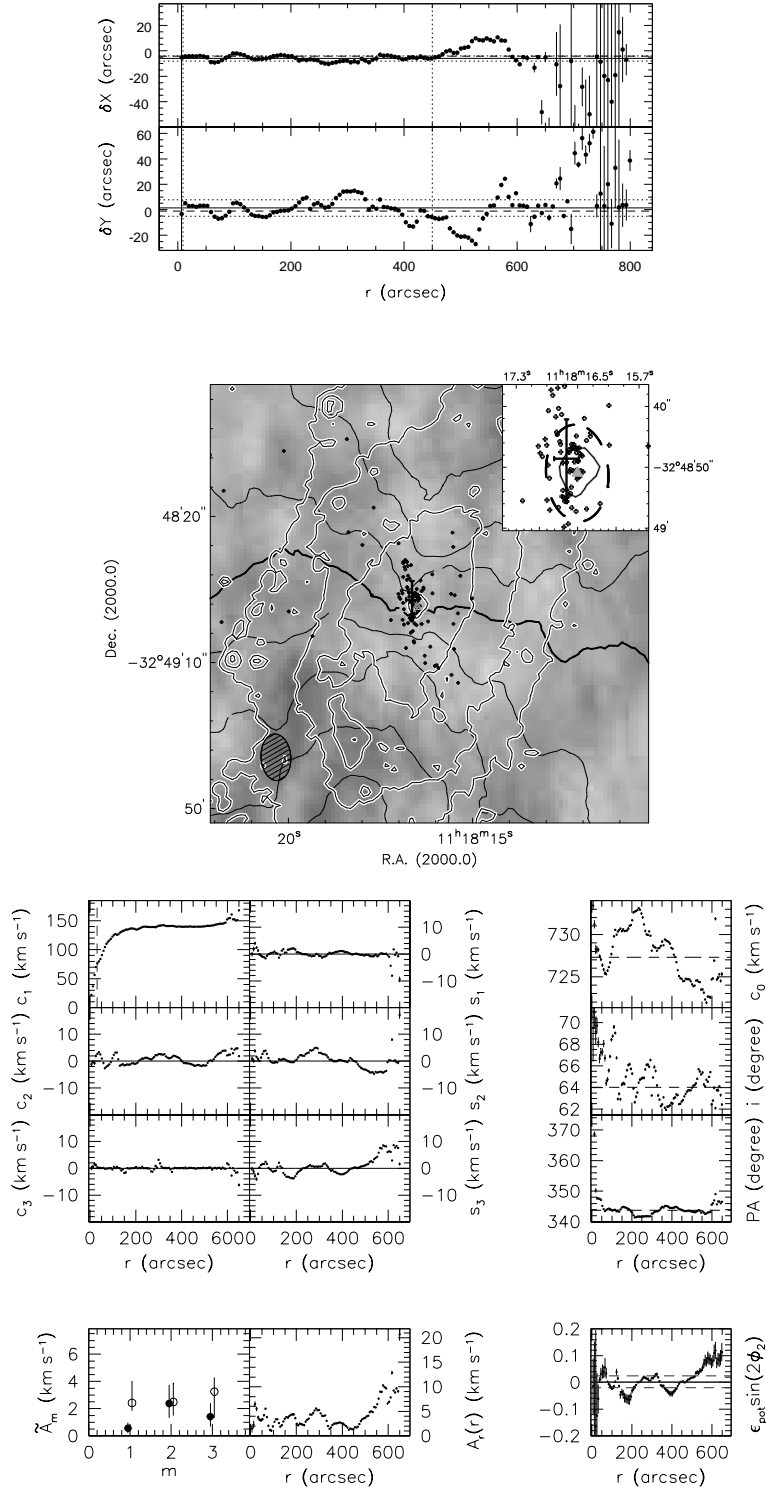


FIG. 2.32: Summary panel for NGC 3621. Lines and symbols are described in the text, Appendix 2.B. The 2% level in the IRAC contours was omitted for clarity reasons. Only data with $r \leq 600''$ was used for radial averaging of \tilde{A}_m or ϵ_{pot} . See Appendix 2.A.11 for a discussion of this galaxy.

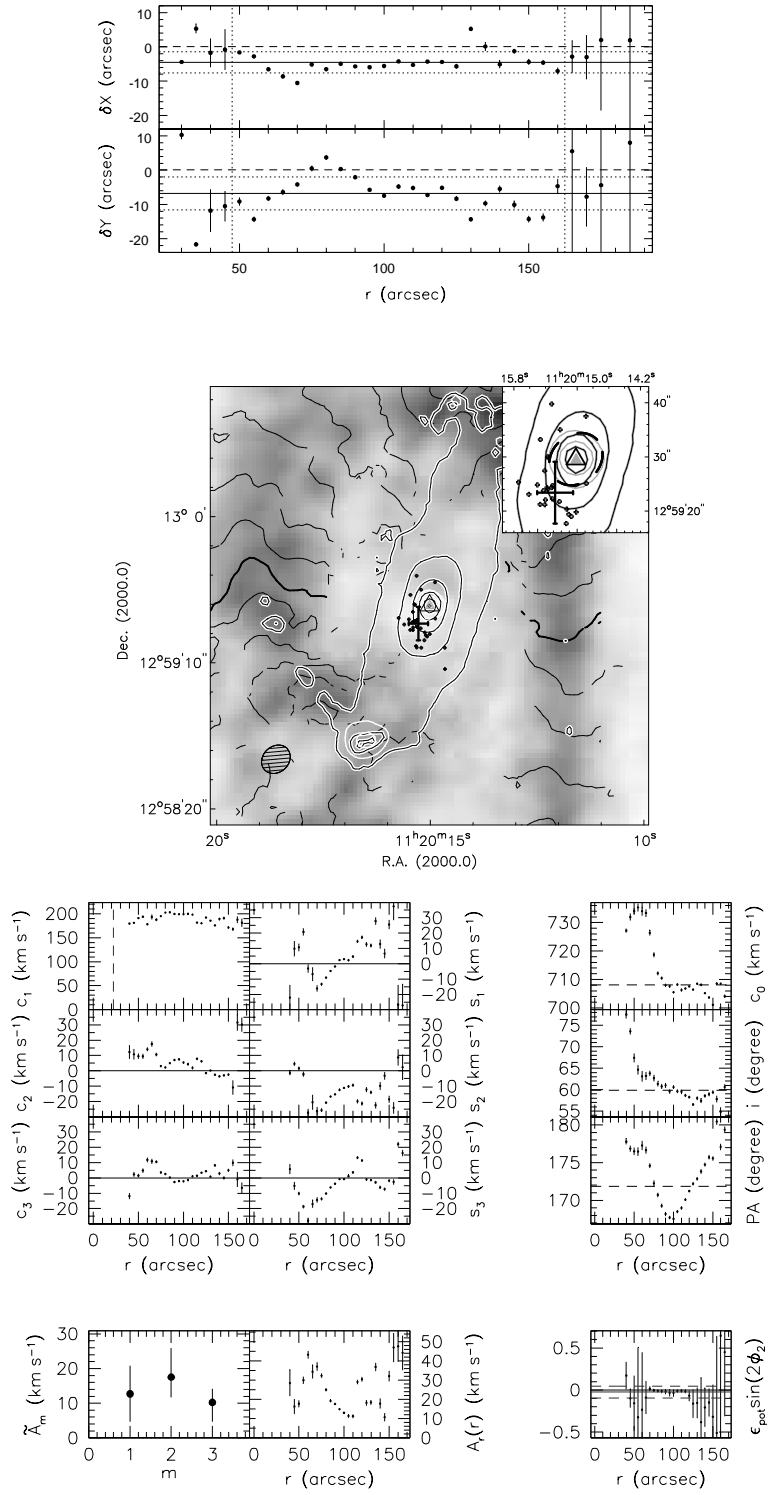


FIG. 2.33: Summary panel for NGC 3627. Lines and symbols are described in the text, Appendix 2.B. The axis scale on the panels showing the non-circular components runs from -30 to 40 km s⁻¹. See Appendix 2.A.12 for a discussion of this galaxy.

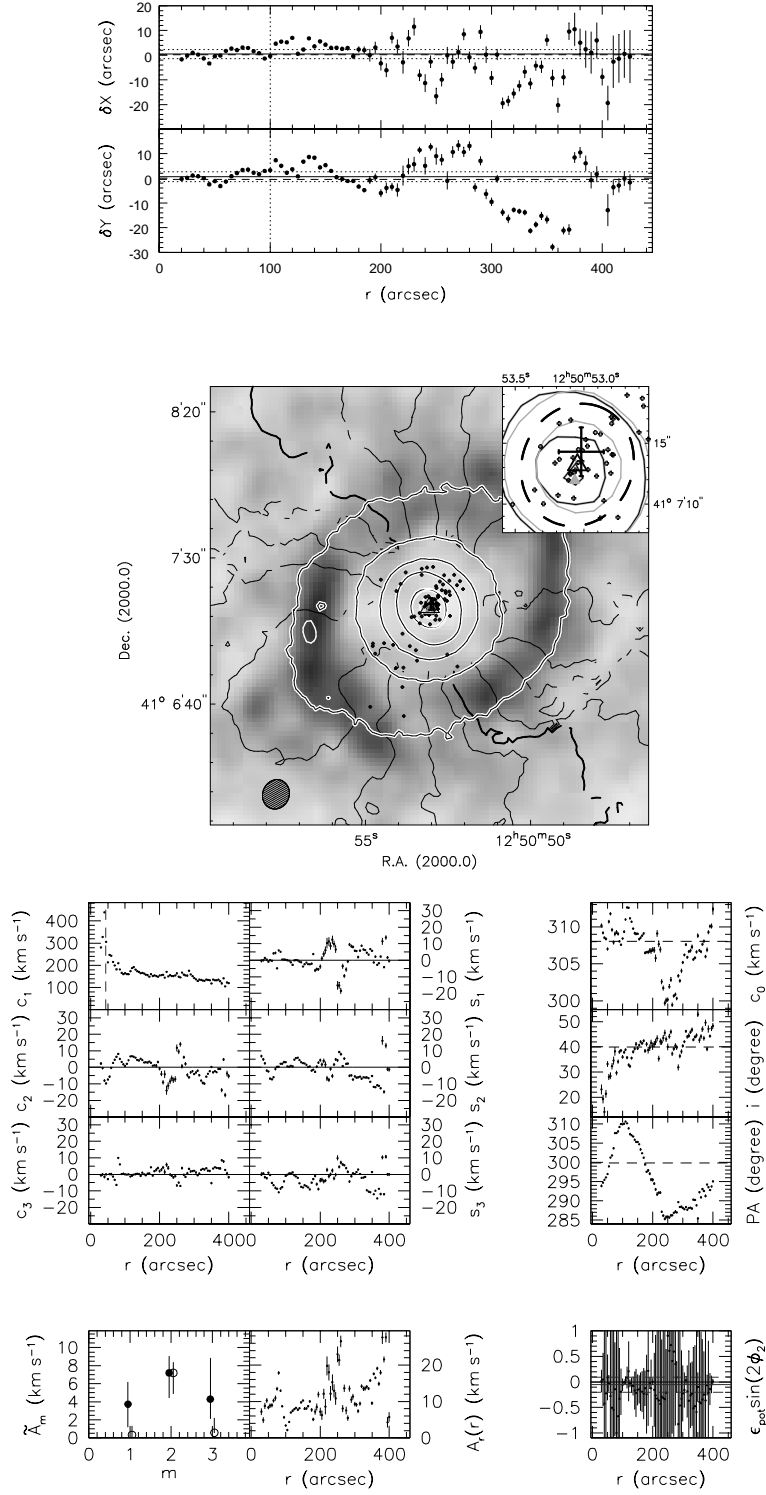


FIG. 2.34: Summary panel for NGC 4736. Lines and symbols are described in the text, Appendix 2.B. The axis scale on the panels showing the non-circular components runs from -30 to 35 km s $^{-1}$. See Appendix 2.A.13 for a discussion of this galaxy.

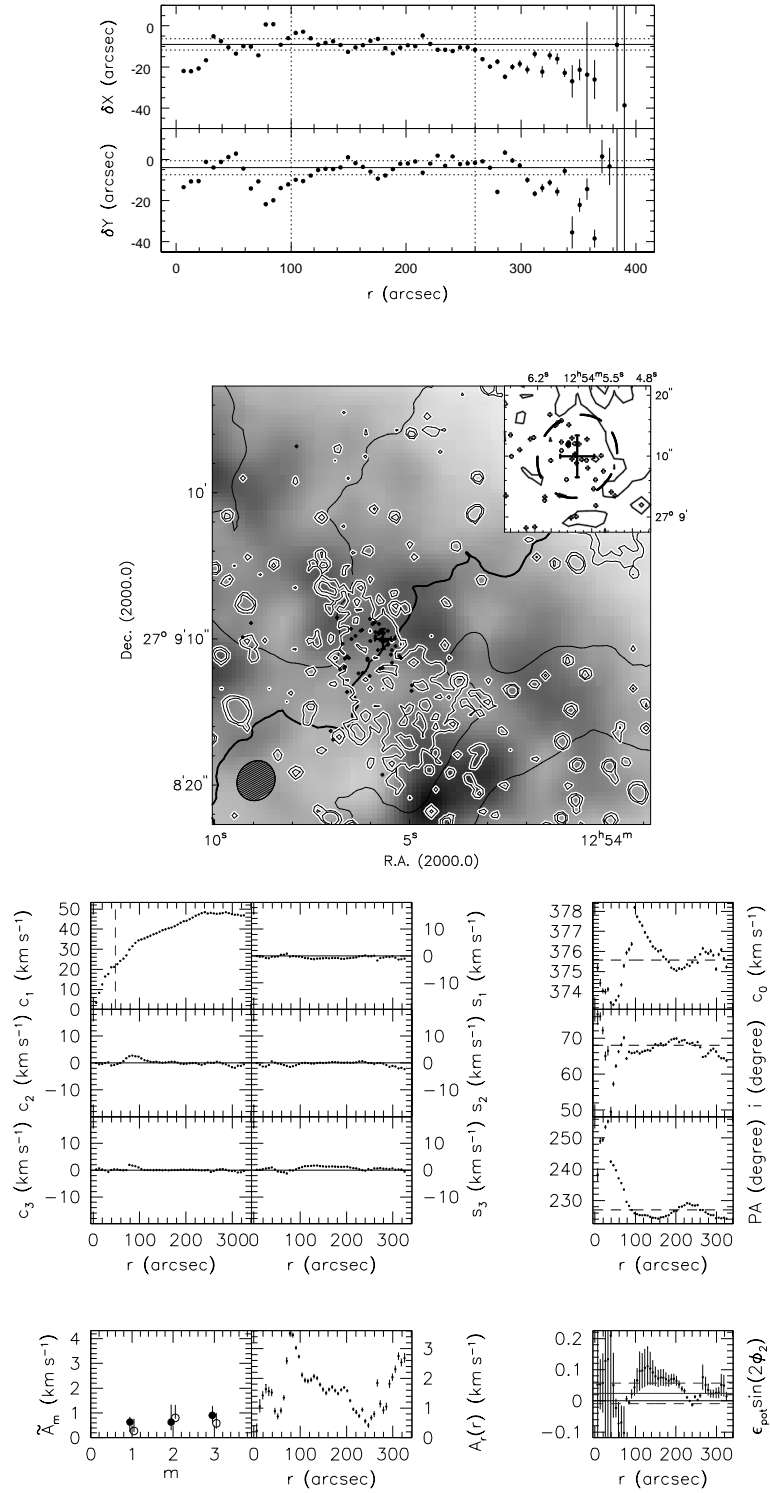


FIG. 2.35: Summary panel for DDO 154. Lines and symbols are described in the text, Appendix 2.B. The IRAC contours show that there is no well-constrained photometric center. See Appendix 2.A.14 for a discussion of this galaxy.

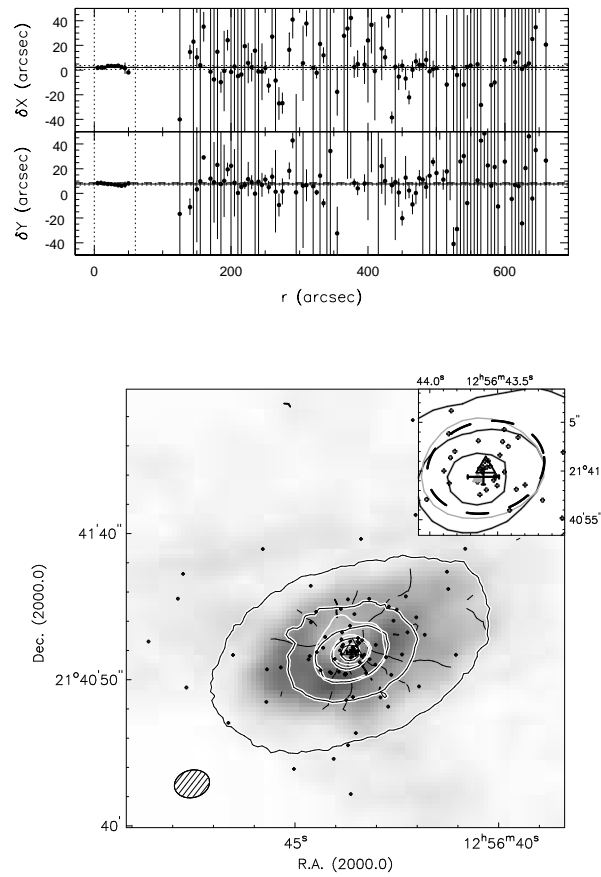


FIG. 2.36: Summary panel for NGC 4826. Lines and symbols are described in the text, Appendix 2.B. The lower panel is missing given that we were not able to derive a meaningful harmonic decomposition of the velocity field. See Appendix 2.A.15 for a discussion of this galaxy.

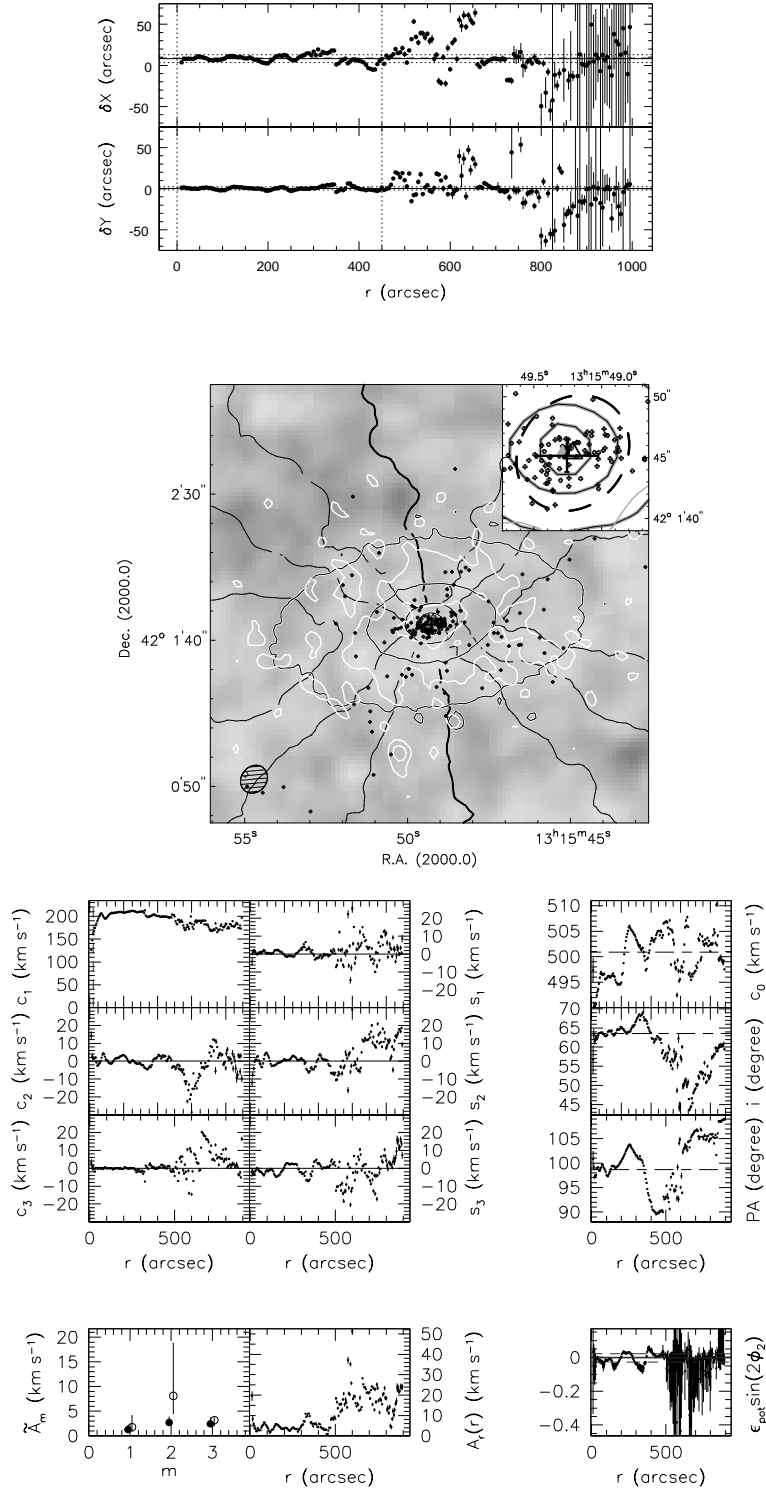


FIG. 2.37: Summary panel for NGC 5055. Lines and symbols are described in the text, Appendix 2.B. The axis scale on the panels showing the non-circular components runs from -30 to 30 km s^{-1} . Only data with $r \leq 450''$ was used for radial averaging of \tilde{A}_m or ϵ_{pot} . See Appendix 2.A.16 for a discussion of this galaxy.

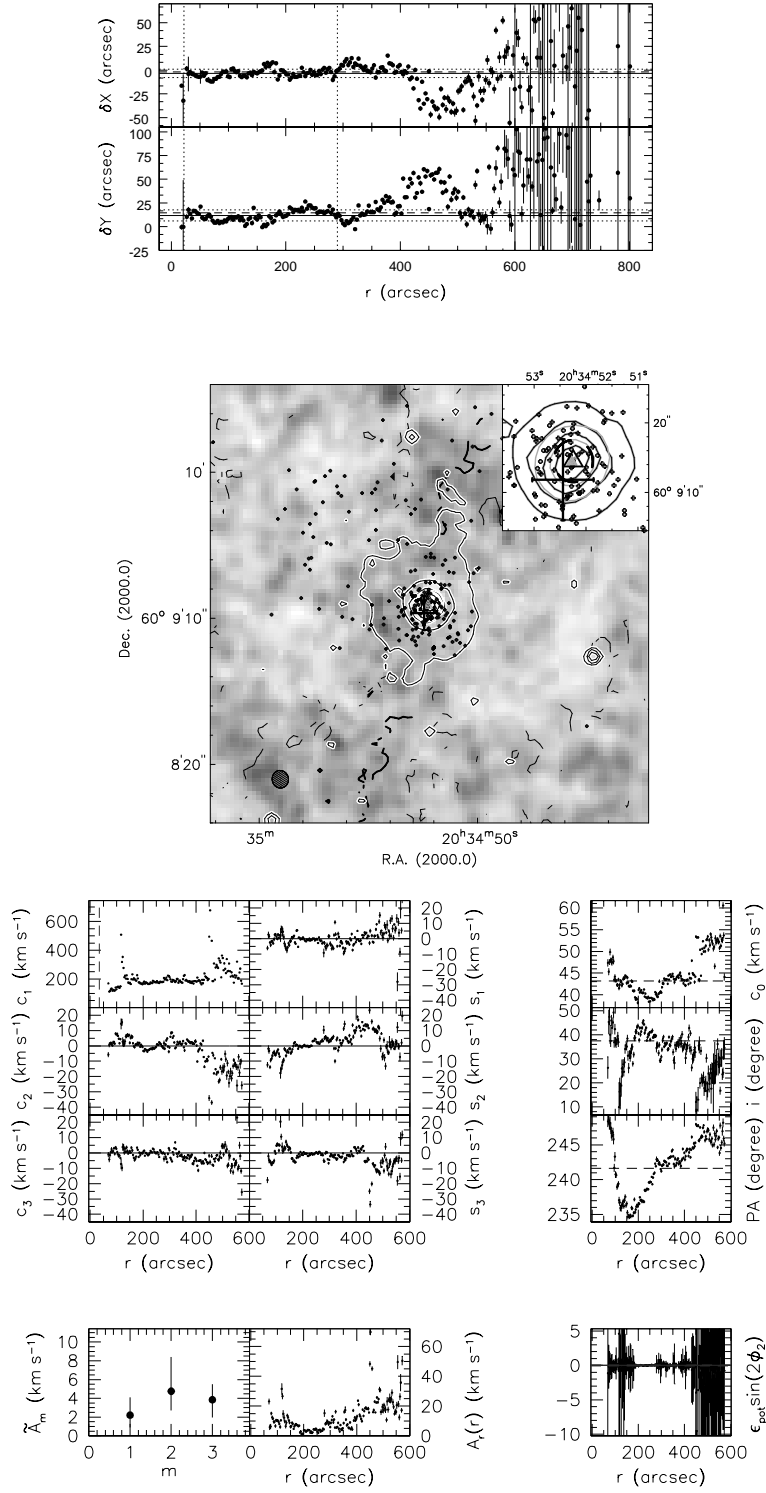


FIG. 2.38: Summary panel for NGC 6946. Lines and symbols are described in the text, Appendix 2.B. The axis scale on the panels showing the non-circular components runs from -45 to 25 km s⁻¹. Only data with $r \leq 420''$ was used for radial averaging of \tilde{A}_m or ϵ_{pot} . See Appendix 2.A.17 for a discussion of this galaxy.

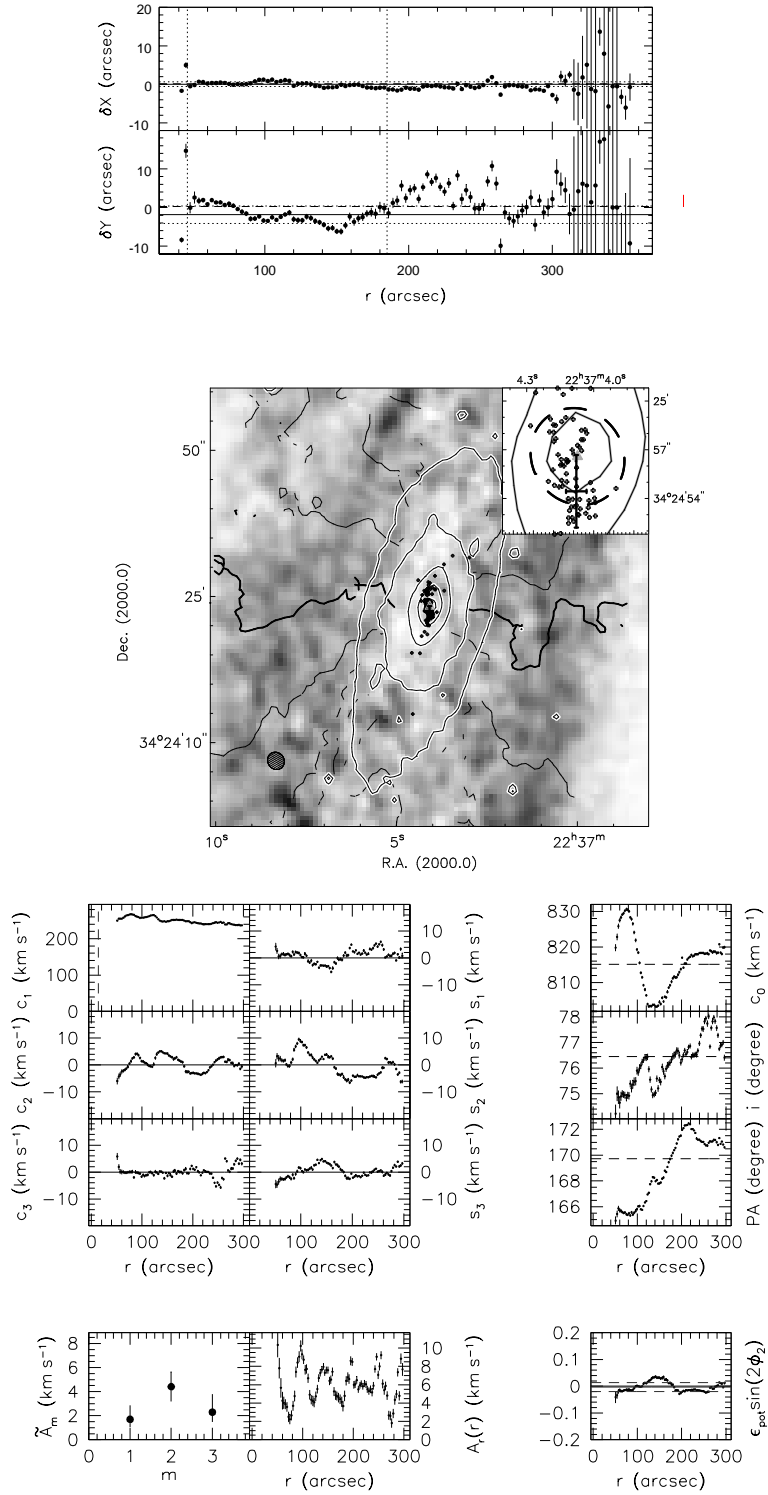


FIG. 2.39: Summary panel for NGC 7331. Lines and symbols are described in the text, Appendix 2.B. See Appendix 2.A.18 for a discussion of this galaxy.

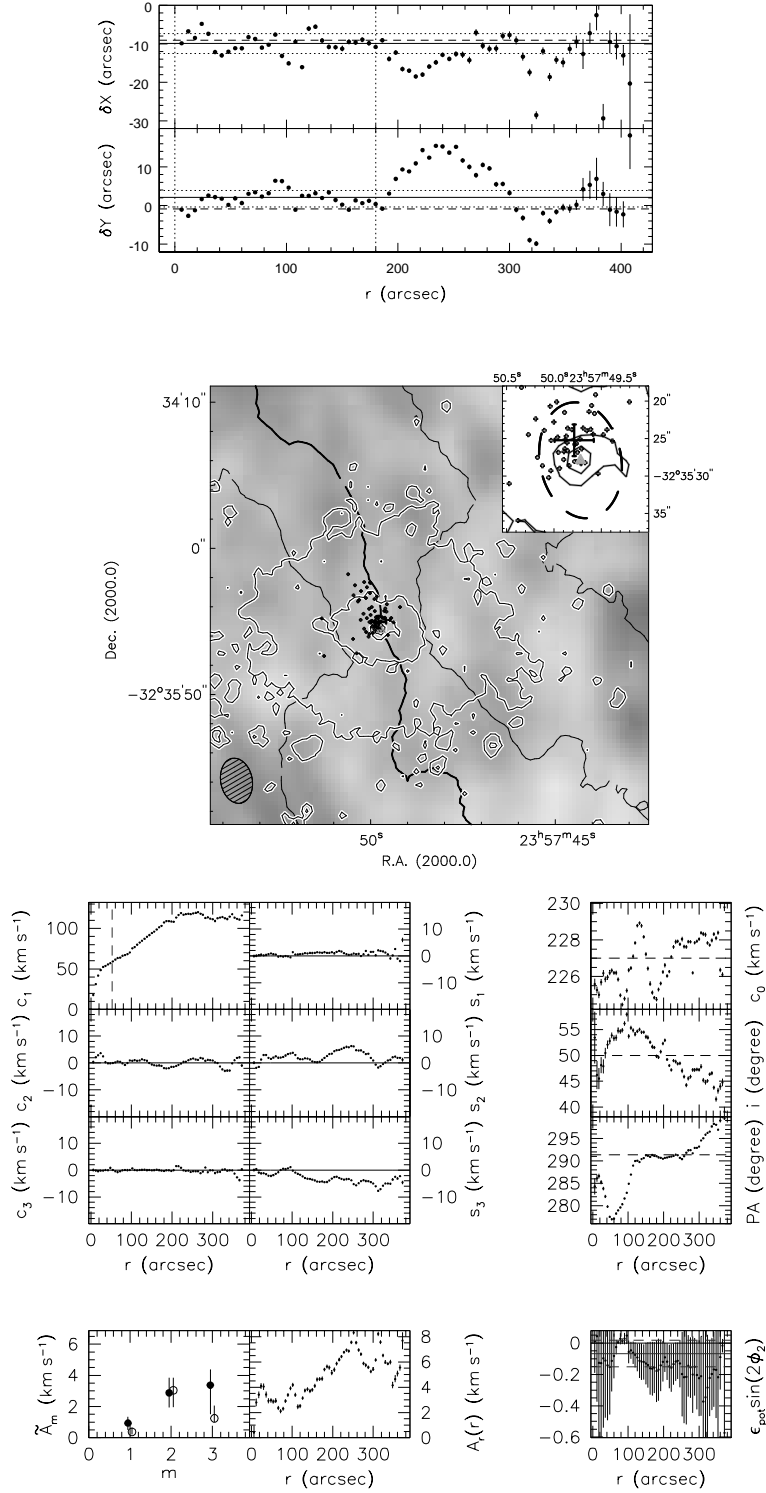


FIG. 2.40: Summary panel for NGC 7793. Lines and symbols are described in the text, Appendix 2.B. The 2% IRAC contour was omitted for clarity reasons. See Appendix 2.A.19 for a discussion of this galaxy.

Are there any “undetected” non-circular motions?

It was shown in Chapter 2 that the detected non-circular motions are by far not high enough to reconcile the density slopes from CDM simulations with those from observations. In this chapter, I will probe the existence and potential influence of any non-circular motions not quantified by the analysis presented in the previous chapter.

3.1 Higher order harmonic decomposition

The harmonic decompositions presented in Chapter 2 were restricted to the third order. Therefore, non-circular motions of higher harmonic order would have been missed by that analysis. The consistency checks presented in Section 2.6.4.1, however, suggested that the impact of the higher orders is relatively small. Here, I will quantify the higher-order non-circular motions by decomposing the velocity fields of the galaxies in the sample up to fifth, ninth, and fifteenth order. The line-of-sight velocity is described as given in Eq. 2.3, but N , the maximum fit order, is increased from $N = 3$ to $N = 5, 9, 15$.

3.1.1 Amplitudes of the harmonic components

Rather than showing and discussing the radial distributions of the individual harmonic components (in total ~ 1200 for the entire sample), emphasis is placed on \tilde{A}_m and $A_r(r)$. The former represents the “power” of the non-circular motions for a given harmonic order m , whereas the latter, the so-called “total power” represents the quadratically added amplitude of all harmonic components. See Section 2.4 and Eqs. 2.6 - 2.8 for an analytical description of \tilde{A}_m and $A_r(r)$.

The results for one galaxy are discussed in detail, whereas for the other galaxies, only deviations and peculiarities are mentioned. As it is for dwarf galaxies that the slopes of the inner parts of the density profiles differ most prominently, it is obvious to use one of them for a detailed discussion. Therefore, DDO 154 will be discussed in detail, although any of the other dwarf galaxies would have been equally well suited. The results of the individual galaxies are discussed in a more general way in Section 3.1.3.

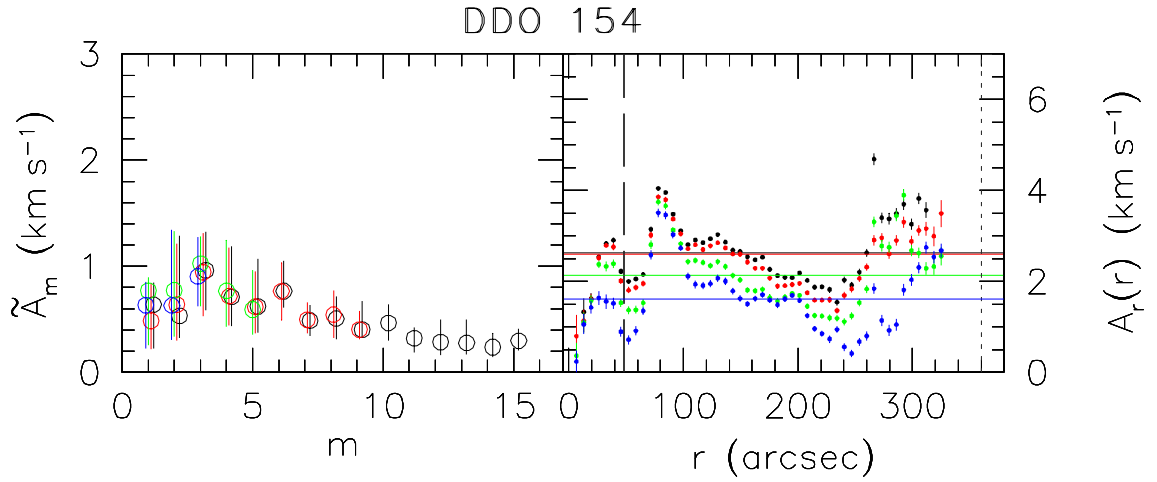


FIG. 3.1: Third (blue), fifth (green), ninth (red), and fifteenth (black) order harmonic decomposition of the velocity field of DDO 154. The left panel shows \tilde{A}_m , the median value of $A_m(r)$, derived following Eqs. 2.6 and 2.7 vs. the harmonic number m . The error bars denote the upper and lower quartile of the distribution of \tilde{A}_m . The right panel shows $A_r(r)$, the so-called “total power” of the non-circular motions, derived following Eq. 2.8. The colored horizontal lines indicate \tilde{A}_r , the median value of $A_r(r)$. The vertical short-dashed line indicates the maximum radius used for the averaging of \tilde{A}_r and also for \tilde{A}_m in the left panel (DDO 154: all data points are used). The long-dashed line at $r \sim 45''$ indicates the radius corresponding to a physical size of 1 kpc.

DDO 154

The results for DDO 154 are shown in Fig. 3.1, where the different harmonic decompositions are color-coded. The third order harmonic decomposition (i.e., $N = 3$), which was presented in Chapter 2 is shown in blue and is plotted on top of the one with $N = 5$ in green, which in turn is on top of the harmonic decomposition with $N = 9$ (red). The bottom layer contains the harmonic decomposition with $N = 15$, which is shown in black. As, e.g., the $m = 3$ component of the third order decomposition agrees quite well with the $m = 3$ component of the higher-order decompositions, the data points generally overlap with each other and only the topmost layer is clearly visible (cf. left panel of Fig. 3.1).

The distribution of \tilde{A}_m can be used for two purposes. Firstly, one can estimate which harmonic order contains the largest amount of non-circular motions. Secondly, one can investigate the influence of the higher orders in order to quantify the missed non-circular motions if a harmonic decomposition of low order has been used previously. In the case of DDO 154, the distribution of \tilde{A}_m shows that no harmonic component is strongly favored and that the amplitudes of all harmonic components are small ($\leq 1 \text{ km s}^{-1}$). Analogous to the analysis presented in Chapter 2, the errorbars shown here do not represent a real uncertainty, but indicate the upper and lower quartile of the radial distribution of $A_m(r)$.

The right panel of Fig. 3.1 shows $A_r(r)$, i.e., the radial variation of the quadratically added amplitudes of all harmonic components. Its median (\tilde{A}_r) is indicated for each harmonic decomposition by a solid horizontal line. Using $A_r(r)$ allows to check *where* the non-circular motions are, e.g., to compare them with the locations of spiral arms, star forming regions etc., whereas its median value (\tilde{A}_r) can be used as an indicator for the global amount of the non-circular motions. The amount by which \tilde{A}_r changes from an $N = 3$ harmonic decomposition to, e.g., a $N = 9$ harmonic decomposition shows how the inclusion of higher order harmonic terms would influence the results presented in Chapter 2. In the case of DDO 154, non-circular motions play a minor role over the entire radial range, but even

more so in the inner 1 kpc (the radius corresponding to 1 kpc is indicated in the right panel of Fig. 3.1 by the long-dashed line).

Beside the obvious advantage of covering more non-circular motions, harmonic decompositions of higher order also come with the drawback of an increased number of free parameters. This is a problem for those regions of a galaxy where the tilted-rings are only sparsely filled, as the fitting algorithm has too few data points to fit many free parameters simultaneously. For most galaxies, this is only a problem in the outer regions. Therefore, a maximum radius for the averaging of the \tilde{A}_m and \tilde{A}_r is introduced, which is indicated by the vertical short-dashed line in the right panel of Fig. 3.1. In the case of DDO 154, which has a very regular velocity field which allowed a stable $N = 15$ harmonic decomposition even in its outer regions, it was not necessary to introduce a maximum radius for the averaging. For these cases, the maximum radius is artificially set to a value larger than the last modelled radius. For DDO 154, \tilde{A}_r increases from $\tilde{A}_r \sim 1.6 \text{ km s}^{-1}$ for $N = 3$ over $\tilde{A}_r \sim 2.1 \text{ km s}^{-1}$ for $N = 5$ to $\tilde{A}_r \sim 2.6 \text{ km s}^{-1}$ for $N = 9$ and $N = 15$. Note that \tilde{A}_r does not change significantly if one increases the fitting order from $N = 9$ to $N = 15$.

NGC 925

The results for NGC 925 are shown in the top panels of Fig. 3.2. The distribution of $A_r(r)$ shows that the $N = 3$ (blue) and the $N = 5$ (green) decompositions produce similar results with smooth radial variations and median amplitudes of $\tilde{A}_r \sim 6 - 8 \text{ km s}^{-1}$. The radial distributions of $A_r(r)$ for the ninth and fifteenth order harmonic decomposition, however, show clear breaks and jumps over a large fraction of the radial range. This is mainly caused by sparsely filled tilted-rings (cf. the velocity field of NGC 925 in Fig. 3.13). Therefore, RESWRI has only relatively few data points to simultaneously fit many free parameters. For the harmonic decompositions with $N = 9$ and $N = 15$, the number of free parameters is simply too large to allow for a stable fit. This hypothesis is supported by the distribution of \tilde{A}_m . It is directly apparent that the amplitude of, e.g., the $m = 1$ component as obtained from a third order harmonic decomposition differs from that of the $N = 15$ harmonic decomposition. The same is true for other harmonic orders m as well. However, increasing the maximum fitting order should not affect the amplitude of the low-order harmonic terms. If it does, as it is the case here, and if the radial distribution of $A_r(r)$ shows such large variations (and uncertainties) from one tilted-ring to the next, then this strongly indicates that the results of the higher order harmonic decomposition are not reliable for this particular galaxy.

NGC 2366

The results for NGC 2366 (middle panels of Fig. 3.2) show that the highest non-circular motions are found in the $m = 4$ component, followed by those from the $m = 2$ and $m = 3$ component. All other components have amplitudes of about 1 km s^{-1} or less, and contribute therefore only little to $A_r(r)$. Including higher order harmonic terms increases the median amplitude of the non-circular motions from $\tilde{A}_r \sim 3 \text{ km s}^{-1}$ for $N = 3$ to $\tilde{A}_r \sim 5.5 \text{ km s}^{-1}$ for $N = 9$. However, these non-circular motions of higher harmonic order are mainly found at large radii. In the inner 1 kpc of NGC 2366, the amount of non-circular motions is small, irrespective of the fit order of the harmonic decomposition.

NGC 2403

In the outer parts of NGC 2403, the sparsely filled tilted-rings cause an increase in the measured non-circular motions and their associated uncertainties (cf. bottom panels of Fig. 3.2). Therefore, only

data points inwards of $r = 800''$ have been used for the averaging of \tilde{A}_m and \tilde{A}_r . The distribution of \tilde{A}_m shows that although the second-to-fifth orders contain the largest amount of non-circular motions, no single order is strongly preferred. The median amplitude of the non-circular motions increases by about 3.5 km s^{-1} if one increases the maximum fit order from $N = 3$ to $N = 15$. The central region again shows the lowest amount of non-circular motions, regardless of the maximum fit order.

NGC 2841

The different harmonic decompositions of the velocity field of NGC 2841 are shown in the top panels of Fig. 3.3. As the scatter in the amplitudes of the non-circular motions increases significantly for larger radii, the maximum radius for the averaging of \tilde{A}_m and \tilde{A}_r is set to $r = 325''$. The highest amplitude of the non-circular motions is found in the $m = 4$ and $m = 5$ component. Therefore, a fifth order harmonic decomposition is already capable of capturing most non-circular motions.

NGC 2903

The different harmonic decompositions of NGC 2903 (middle panels of Fig. 3.3) show a similar behavior for most radii. The results differ only for the inner few tilted-rings and for those at radii between $r = 175''$ and $r = 225''$. While the former might be due to large streaming motions associated with the bar of NGC 2903, the latter is likely to be caused by the sparsely filled tilted-rings at those radii (cf. Fig. 3.17). The highest amplitude of the non-circular motions is found for the $m = 3$ component, whose median value and upper and lower quartile is $\hat{A}_3 \approx 4_{-2}^{+5} \text{ km s}^{-1}$.

NGC 2976

For NGC 2976, the radial averaging of \tilde{A}_m and \tilde{A}_r was restricted to $r \leq 110''$ (cf. bottom panels of Fig. 3.3). When changing N from $N = 3$ to $N = 15$, the median amplitude of the non-circular motions is increased from $\tilde{A}_r \sim 2 \text{ km s}^{-1}$ to $\tilde{A}_r \sim 5 \text{ km s}^{-1}$. The inner two data points show relatively large non-circular motions, which might be attributed to the bar of NGC 2976 (cf. Spekkens & Sellwood 2007). The distribution of \tilde{A}_m shows that no harmonic component is strongly favored, although the second and fourth order show somewhat larger amplitudes than the others.

NGC 3031

For NGC 3031 (top panels of Fig. 3.4), the radial averaging of \tilde{A}_m and \tilde{A}_r is restricted to $r \leq 800''$. Additionally, the data points at radii between $300''$ and $370''$ of the fifteenth order harmonic decomposition had to be removed manually, as these are heavily affected by sparsely filled tilted-rings (cf. Fig. 3.19). The distribution of \tilde{A}_m shows that the first five harmonic orders contain the largest amount of non-circular motions; higher harmonic orders ($m > 5$) contribute only very little to the total amount of the non-circular motions.

NGC 3198

The results for NGC 3198 (middle panels of Fig. 3.4) show that for radii smaller than $450''$, all harmonic decompositions show well-defined radial trends. The median amplitude of the non-circular motions increases from $\tilde{A}_r \sim 4 \text{ km s}^{-1}$ to $\tilde{A}_r \sim 6 \text{ km s}^{-1}$, if one increases the maximum fit order from $N = 3$ to $N = 9$ (or $N = 15$). The panel containing \tilde{A}_m shows that the largest non-circular motions are found in the first five harmonic orders.

IC 2574

For IC 2574 (bottom panels of Fig. 3.4), the $m = 2$ component is clearly the dominant one. As already discussed in the previous chapter, $A_r(r)$ shows a clear maximum at $r \sim 250''$, which is probably caused by the supergiant shell in the north-east of IC 2574 (Walter et al. 1998). It is again striking that the inner 1 kpc contain only very small non-circular motions, regardless of whether one performs a third or a fifteenth order harmonic decomposition.

NGC 3521

For NGC 3521, the radial averaging is confined to radii with $r \leq 350''$. The results are shown in the top panels of Fig. 3.5 and show that the largest non-circular motions are found in the second-to-fifth order. The radial trends in the distribution of $A_r(r)$ can be traced in all decompositions, although for radii larger than $200''$, the results of the different harmonic decompositions start to diverge slightly.

NGC 3621

In NGC 3621 (middle panels of Fig. 3.5), most harmonic components show similarly small amplitudes. The radial trends seen in the distribution of $A_r(r)$ are visible for all harmonic decompositions, with a steady increase in amplitude as one includes higher and higher orders. The radial averaging is restricted to $r \leq 500''$, thus excluding the outer deviant data points.

NGC 3627

The harmonic decompositions of NGC 3627 (bottom panels of Fig. 3.5) are heavily affected by its asymmetry and its bar. As shown in the previous chapter, NGC 3627 contains the highest non-circular motions in the sample. It was not possible to decompose the velocity field up to the fifteenth order and even the harmonic decompositions with $N = 5$ and $N = 9$ show unrealistic large values for some radii (much larger than the rotation velocity), indicating that a harmonic decomposition up to third order is already at the limit of what makes sense. Given these problems, NGC 3627 is disregarded in the subsequent analysis.

NGC 4736

NGC 4736 has an inner and an outer disk. The latter is only sparsely filled (cf. the velocity field shown in Fig. 3.25), which results in a large scatter of the derived amplitudes of the non-circular motions (see top panels of Fig. 3.6). While the third order harmonic decomposition can still somewhat cope with these sparsely filled tilted-rings, the higher order decompositions can not. Therefore, the values of \tilde{A}_m and \tilde{A}_r are averaged over $r \leq 175''$ only. For this inner disk, the radial trends of the different distributions of $A_r(r)$ are all similar in shape. The highest amount of non-circular motions is found in the $m = 2$ and $m = 3$ component.

NGC 5055

Like NGC 4736, NGC 5055 also shows sparsely filled outer regions (cf. Fig. 3.26) and the averaging of \tilde{A}_m and \tilde{A}_r is therefore restricted to $r \leq 450''$. Within this radial range, the different harmonic decompositions (see middle panels of Fig. 3.6) show similar radial trends and differ only in amplitude. The distribution of \tilde{A}_m shows that no harmonic component is preferred.

NGC 6946

The results for NGC 6946 (bottom panels of Fig. 3.6) are affected not only by sparsely filled tilted-rings (cf. velocity field in Fig. 3.27), but also by its low inclination, which on the one hand results in large correction terms, and on the other hand makes it more difficult to unambiguously separate the rotational signal from turbulent motions. Due to these problems, it was not possible to perform a fifteenth order harmonic decomposition of the velocity field of NGC 6946. Because of the large uncertainties and scatter at large radii, only tilted-rings with $r \leq 250''$ are considered for the averaging of \tilde{A}_m and \tilde{A}_r . Most harmonic orders show similar amplitudes of about 3 - 4 km s^{-1} . The differences between the amplitudes of the $m = 1$ component for the 3rd and 5th order harmonic decompositions on the one hand, and the 9th order decomposition on the other hand, suggests that the latter is already at the edge of what is feasible.

NGC 7331

The results for NGC 7331 in the top panels of Fig. 3.7 show that the second harmonic order contains the largest amount of non-circular motions and that only very small power is in the $m = 1$ and $m = 3$ terms. The amplitudes of the fourth-to-sixth harmonic orders are approximately 3 km s^{-1} . Increasing the maximum fit order N has therefore a noticeable effect on \tilde{A}_r , which is almost doubled when changing N from $N = 3$ to $N = 15$. The values of \tilde{A}_m and \tilde{A}_r are averaged over tilted-rings with $r \leq 240''$.

NGC 7793

In NGC 7793 (bottom panels of Fig. 3.7), the largest amount of non-circular motions is found in the second and third harmonic order. All other orders contain only small non-circular motions. This is also apparent in the value of \tilde{A}_r , which changes by only 2 km s^{-1} when increasing the maximum fit order from $N = 3$ to $N = 15$. It is again noticeable that the lowest amount of non-circular motions is found in the inner parts of the galaxy.

3.1.2 Residuals of the higher order decompositions

Residual velocity fields are created by subtracting a model from the original data. In the previous chapter, an analysis of the residual velocity fields of the third order harmonic decompositions has been presented (cf. Section 2.6.4.1). Here, I will apply the same method to the residual velocity fields based on higher order harmonic decompositions. In particular, this means creating *absolute* residual velocity fields and using their median values for the subsequent analysis. The result is shown in Fig. 3.8, where the median amplitudes are plotted vs. the maximum fit order of the harmonic decomposition. The data points of each galaxy are connected by a line. The (dwarf) galaxies with absolute magnitudes of $M_B > -18.5$ mag are shown in gray, more luminous galaxies in black. Two things are directly apparent: firstly, dwarf galaxies generally show the smallest residuals, regardless of the maximum fit order. Secondly, even though the median amplitude of the residuals decreases if one performs a higher order harmonic decomposition, the gain is usually only of the order of 1 km s^{-1} . Even for the third order harmonic decomposition, the median values of most absolute residual velocity fields are below the velocity resolution of the data (for 14 out of 18 galaxies). For the ninth order decompositions, the same holds for all galaxies but NGC 6946, which is the only galaxy in the sample with a velocity resolution of 1.3 km s^{-1} . Only for very few galaxies do the residuals change significantly if N is increased from $N = 3$ to $N = 15$. One of these galaxies is NGC 3521, which

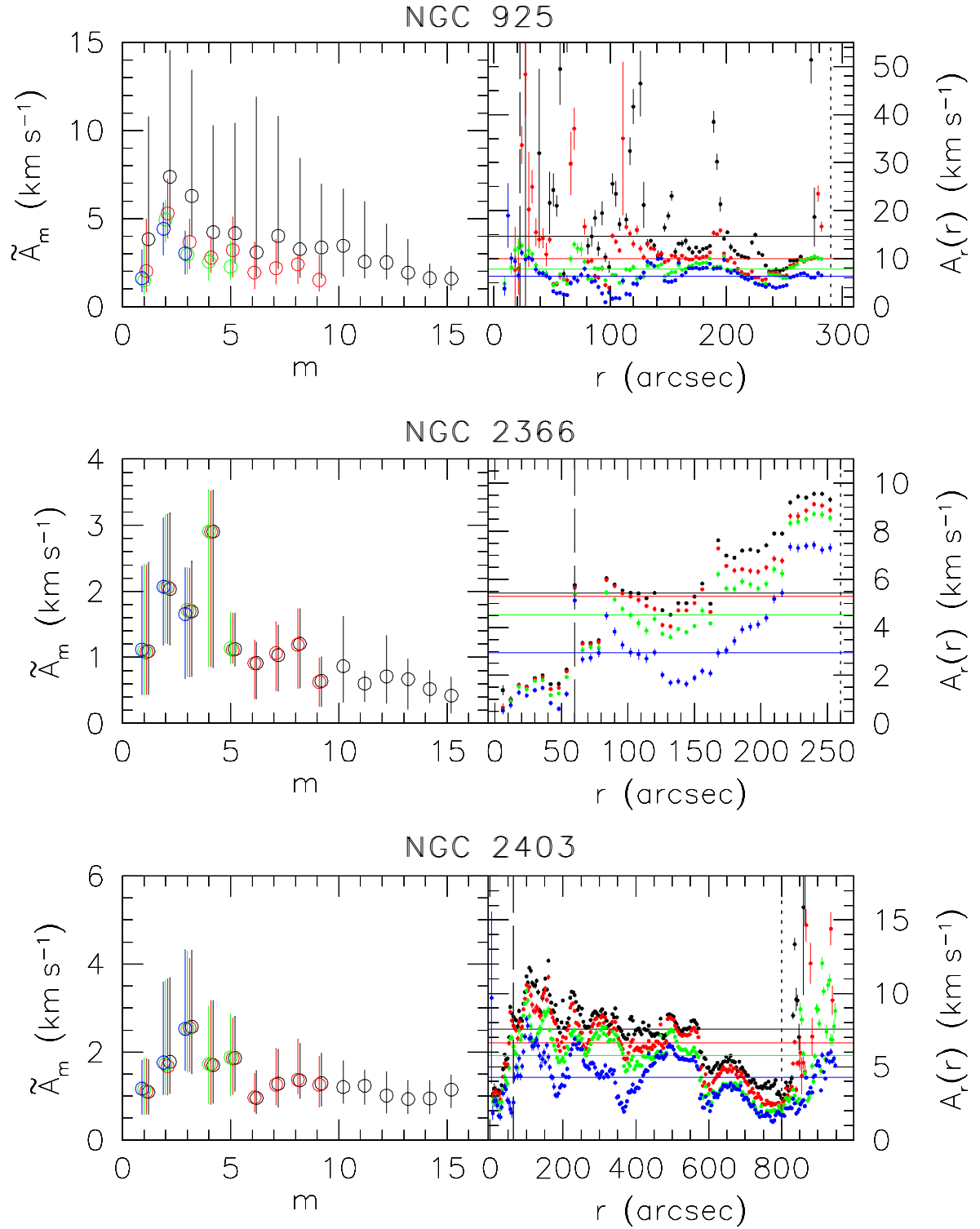


FIG. 3.2: Different order harmonic decomposition of NGC 925 (top), NGC 2366 (middle), and NGC 2403 (bottom). The layout of the panels is identical to Fig. 3.1. See text for more information about the galaxies shown here.

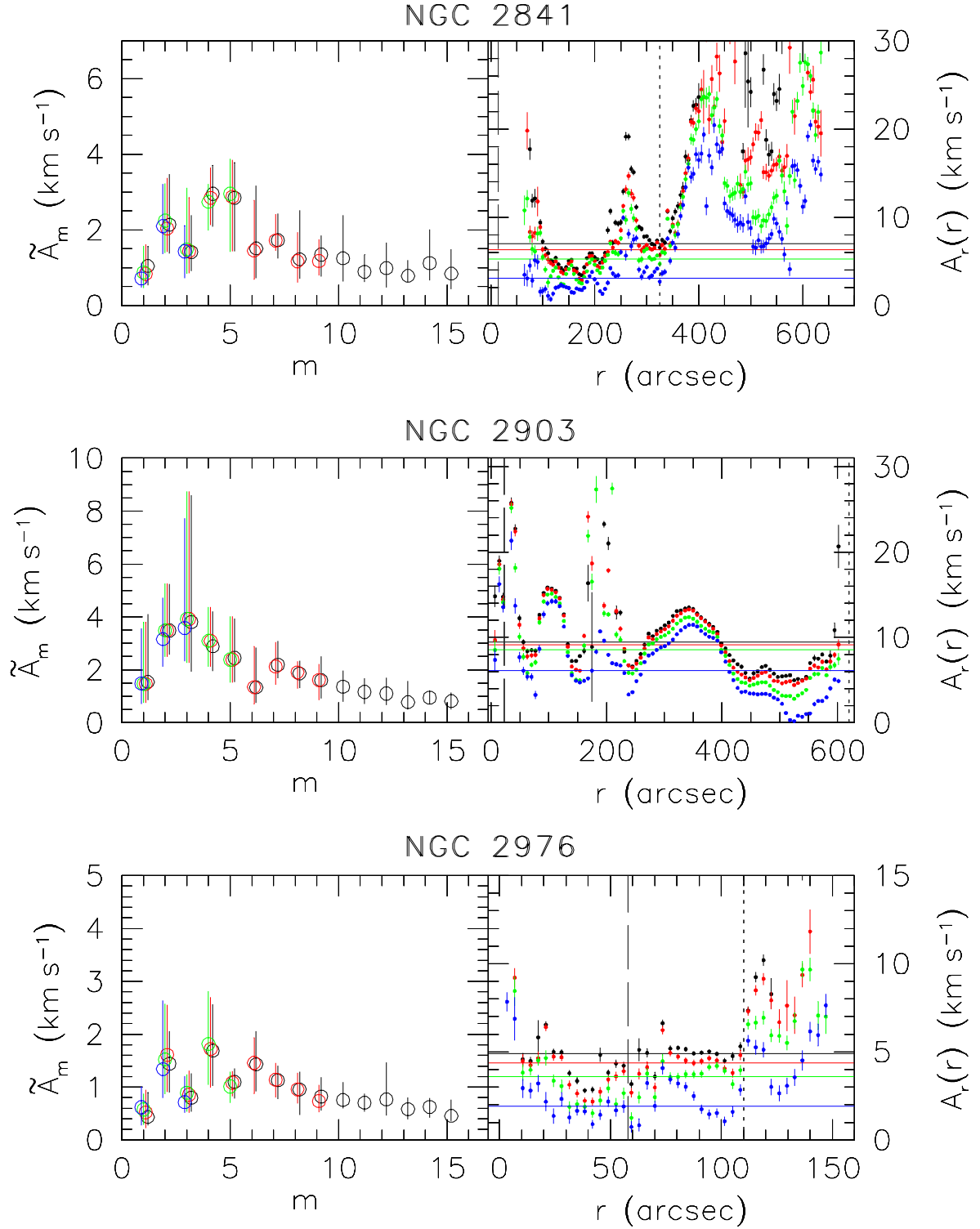


FIG. 3.3: Different order harmonic decomposition of NGC 2841 (top), NGC 2903 (middle), and NGC 2976 (bottom). The layout of the panels is identical to Fig. 3.1. See text for more information about the galaxies shown here.

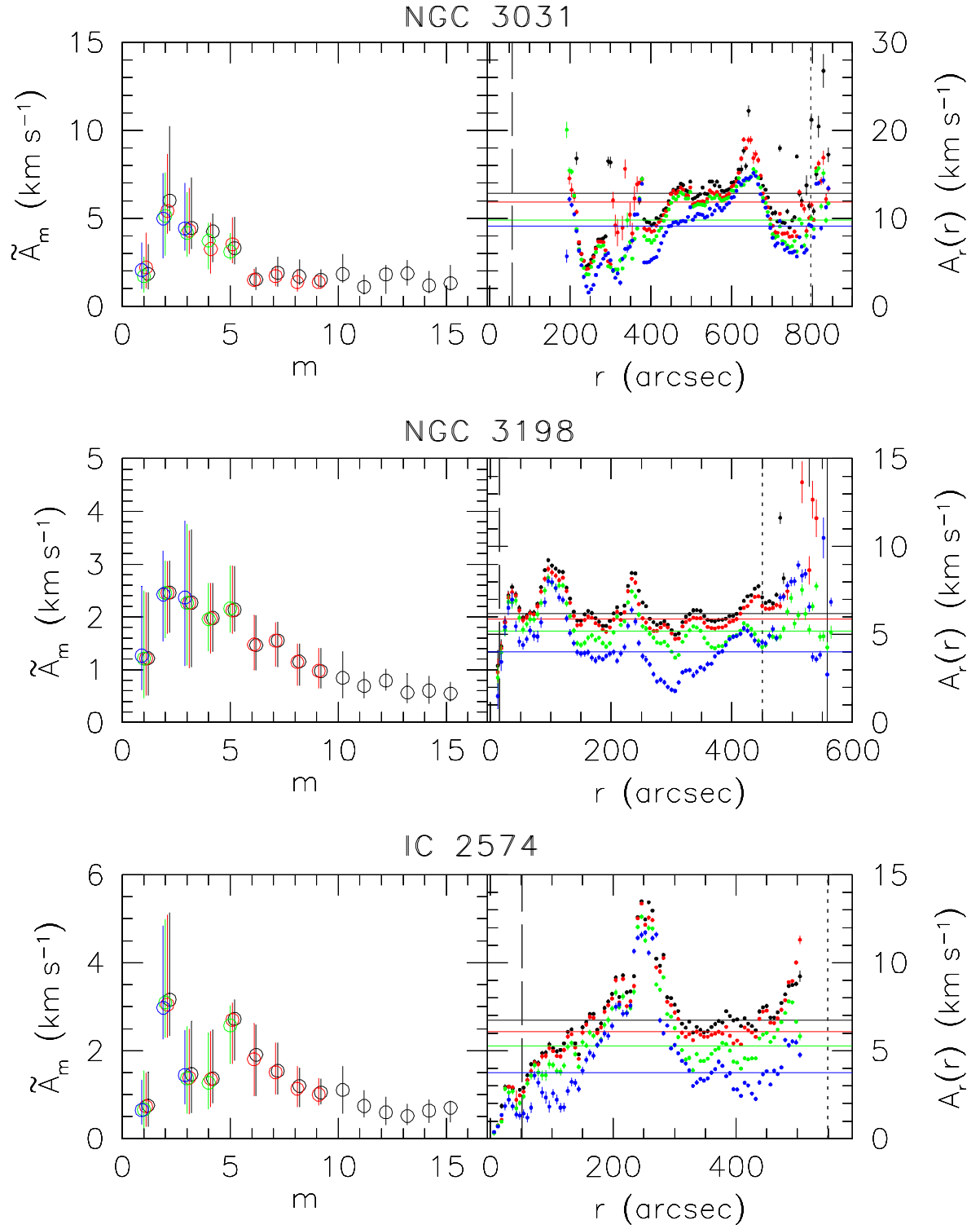


FIG. 3.4: Different order harmonic decomposition of NGC 3031 (top), NGC 3198 (middle), and IC 2574 (bottom). The layout of the panels is identical to Fig. 3.1. See text for more information about the galaxies shown here.

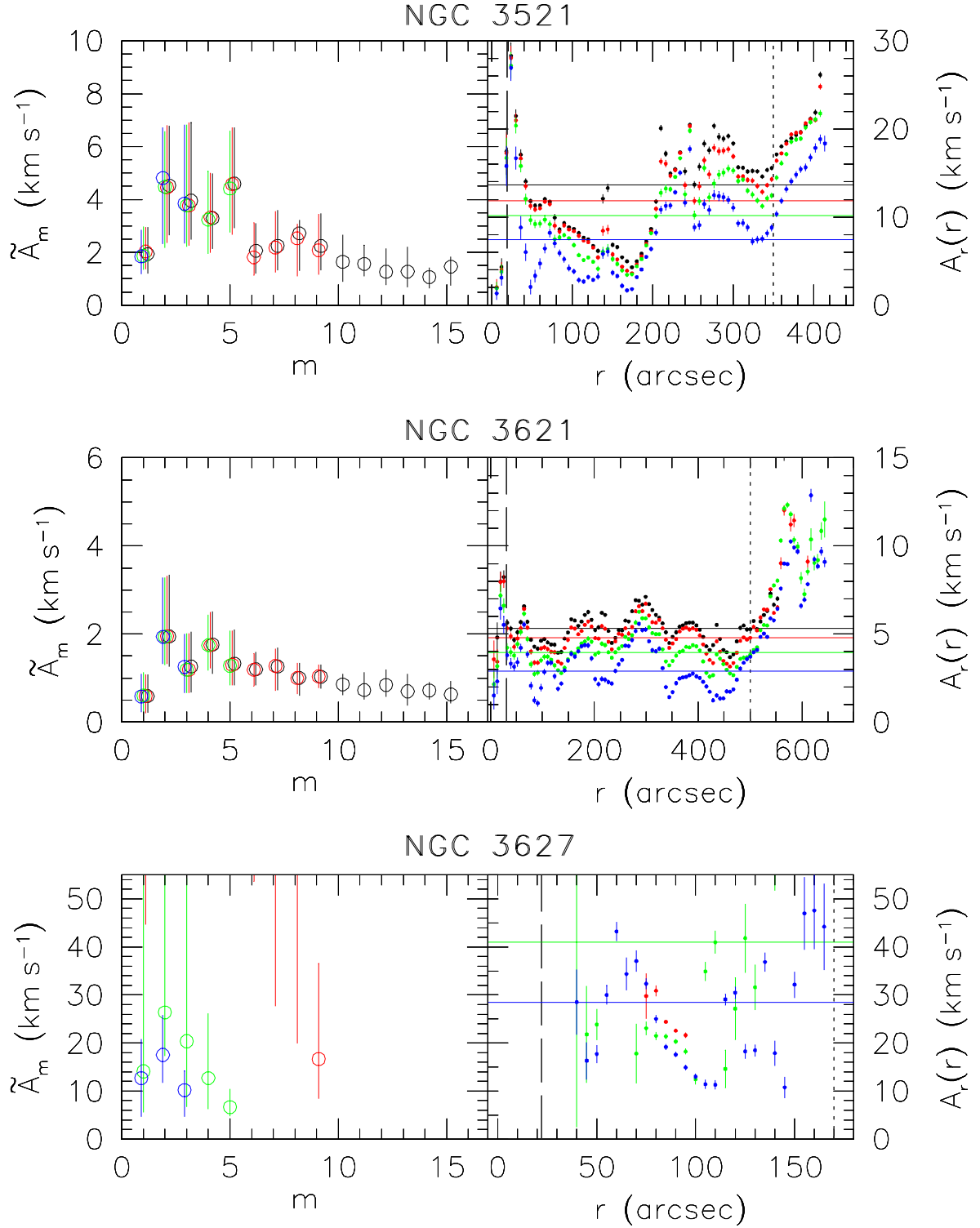


FIG. 3.5: Different order harmonic decomposition of NGC 3521 (top), NGC 3621 (middle), and NGC 3627 (bottom). The layout of the panels is identical to Fig. 3.1. See text for more information about the galaxies shown here.

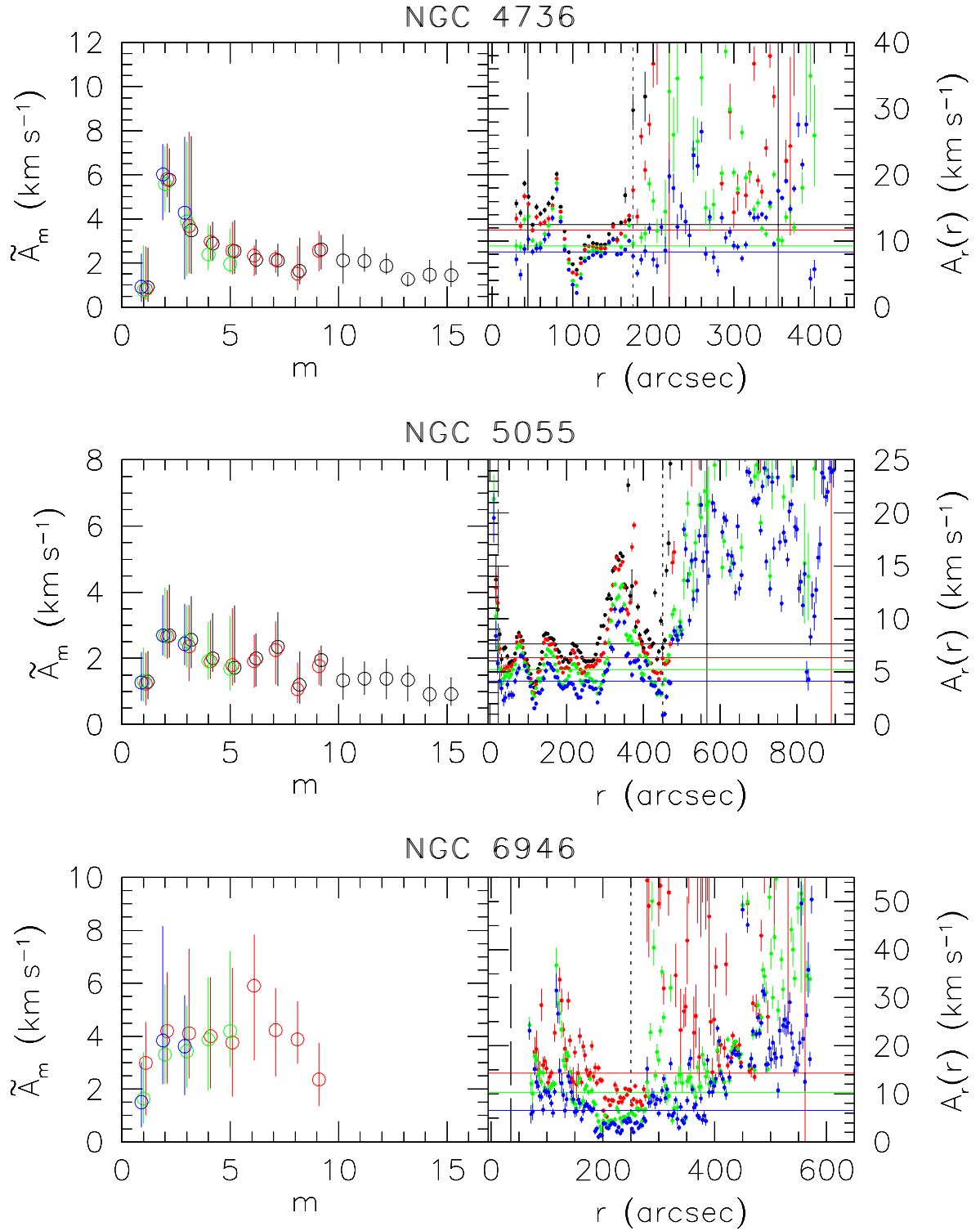


FIG. 3.6: Different order harmonic decomposition of NGC 4736 (top), NGC 5055 (middle), and NGC 6946 (bottom). The layout of the panels is identical to Fig. 3.1. See text for more information about the galaxies shown here.

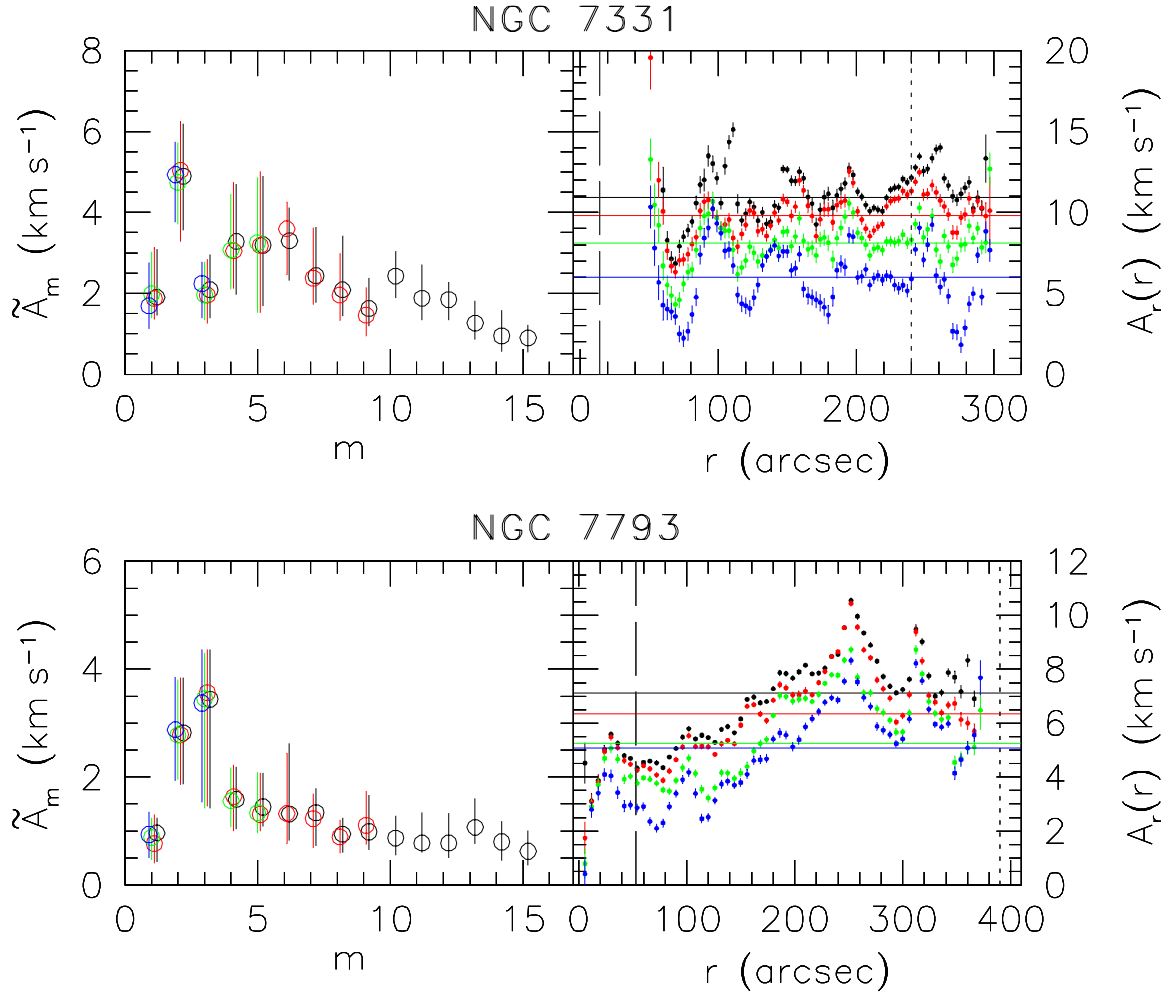


FIG. 3.7: Different order harmonic decomposition of NGC 7331 (top) and NGC 7793 (bottom). The layout of the panels is identical to Fig. 3.1. See text for more information about the galaxies shown here.

shows the highest residuals of the sample for $N = 3$, but only average residuals for $N = 15$. This is because NGC 3521 contains relatively large fourth and fifth order harmonic components (cf. Fig. 3.5). However, for the majority of the galaxies presented here, a third order harmonic decomposition is able to quantify most of the non-circular motions.

3.1.3 Discussion

The results presented in Section 3.1.1 all show that increasing the maximum fit order N does result in somewhat larger non-circular motions. However, due to the increased number of free parameters, the number of galaxies suitable for this kind of analysis decreases. A harmonic decomposition of high order precludes the analysis of regions with sparsely filled tilted-rings. Galaxies showing a patchy velocity field with many HI holes and sparsely filled tilted-rings (like NGC 925, NGC 5055, and NGC 6946) prove largely unsuitable for high (i.e., $N = 9$ or $N = 15$) order harmonic decompositions. Nevertheless, for the galaxies where, e.g., the ninth order harmonic decomposition shows results of satisfying accuracy, one can still ask: does the inclusion of non-circular motions of higher harmonic order change the conclusions from Chapter 2?

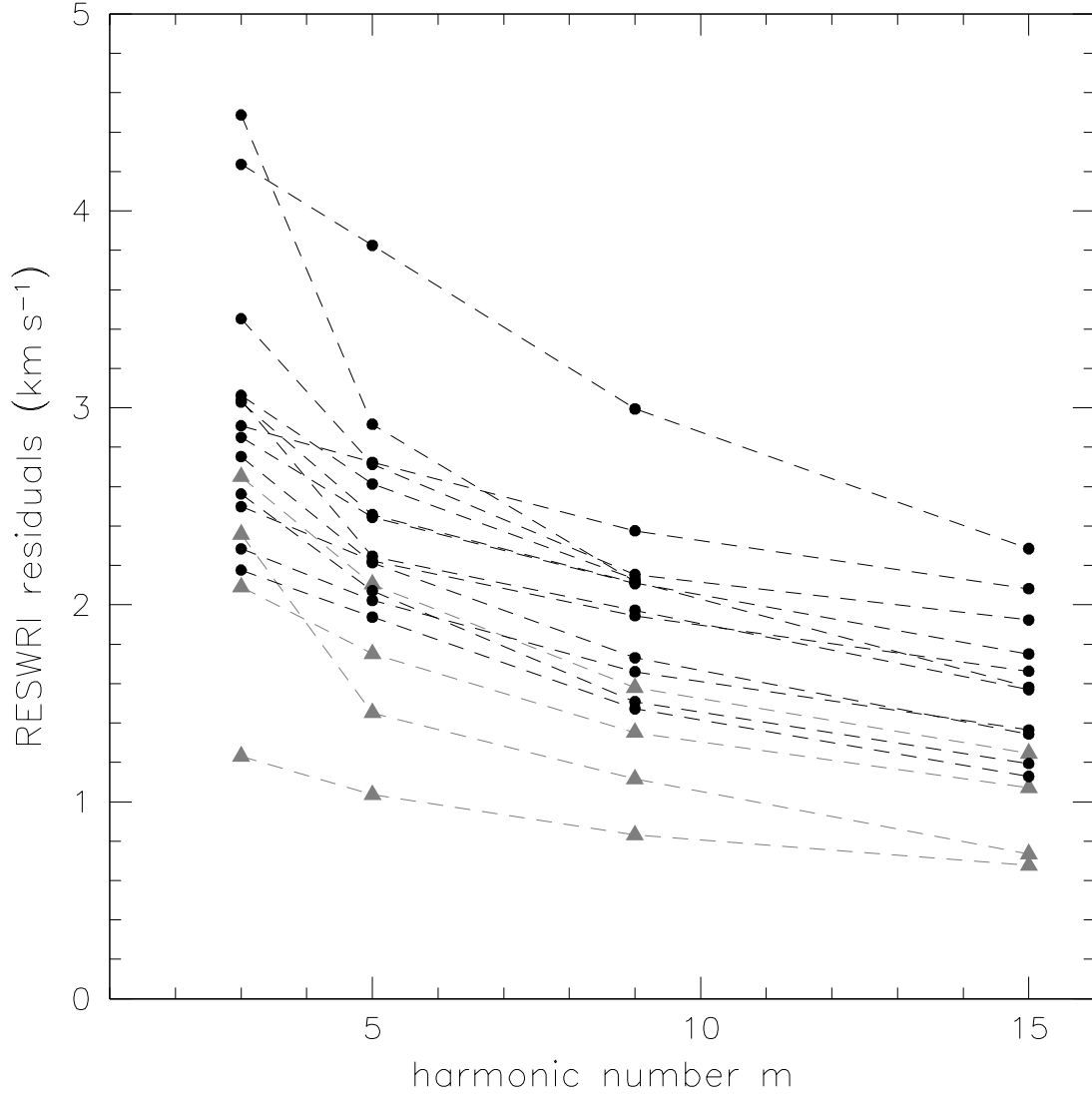


FIG. 3.8: Median value of the absolute residual velocity fields for harmonic decompositions of different order. Dwarfs ($M_B > -18.5$ mag) are shown in gray, all other galaxies in black.

To address this question, emphasis is placed again on the four dwarf galaxies with $M_B > -18.5$ mag (NGC 2366, NGC 2976, IC 2574, and DDO 154), as all of these are inconsistent with an NFW profile but are better approximated with a cored profile (de Blok et al. 2008; Oh et al. 2008). Including only third order harmonic terms, the four galaxies show non-circular motions with median amplitudes of $\tilde{A}_r \sim 1.2\text{--}2.2$ km s $^{-1}$ in their inner 1 kpc, with an average value of 1.6 km s $^{-1}$. Including higher order harmonic terms (e.g., up to $N = 9$) increases the median values to $\tilde{A}_r \sim 1.6\text{--}4.5$ km s $^{-1}$ with an average of 2.9 km s $^{-1}$. These non-circular motions are significantly smaller than the 15-20 km s $^{-1}$ which are needed in order to reconcile the different density slopes (see de Blok et al. 2003; Hayashi & Navarro 2006; Kuzio de Naray et al. 2008).

However, one might argue that the absolute amplitudes of the non-circular motions are not very meaningful, but that they have to be normalized by the local rotation velocity. This has been done for the third order harmonic decompositions in Figs. 2.10 and 2.11 in Chapter 2. It has been shown (in Section 2.6.2), that for three out of the four dwarfs in the sample, the non-circular motions in the inner 1 kpc contribute less than ten percent to the local rotation velocity. Only IC 2574 shows larger non-circular motions of about 26 percent. Including non-circular motions of higher harmonic order increases the contribution of the non-circular motions (relative to the local rotation velocity) by 3.4 percent on average. This means that even with the inclusion of high order non-circular motions, these contributions are much smaller than the > 50 percent which Hayashi et al. (2004a) need to invoke in order to explain the differences between the theoretical predictions and the observations.

This clearly shows that the quantification of non-circular motions of higher harmonic order does not change the conclusions from Chapter 2.

3.2 Harmonic decomposition of artificial velocity fields

The results of the previous section show that taking non-circular motions of higher harmonic order into account does not change the conclusions from Chapter 2. In this section, I test the effectiveness of the harmonic decomposition by analyzing artificial velocity fields. In particular, this means creating artificial velocity fields with a certain (and most importantly *known*) amount of non-circular motions, adding noise and other “disturbances” to the artificial VFs, and finally performing a harmonic decomposition of them. By comparing the detected non-circular motions with the inserted ones, one can estimate the efficiency of the fitting-routine.

3.2.1 Creating the artificial velocity fields

For the creation of the artificial velocity fields, a modified version of the GIPSY task VELFI has been used. VELFI can create model velocity fields with circular motions and is therefore often used to visualize the results from a tilted-ring fit with ROTCUR. In order to create model velocity fields which include non-circular motions, I had to modify the existing task VELFI by changing the line-of-sight velocity from one based on circular motions (Eq. 2.4) to one including non-circular motions as well (cf. Eq. 2.3 on page 12). This modified version of VELFI (hereafter called NONCIRC) accepts harmonic terms up to ninth order. Allowing for the inclusion of higher order harmonic terms would have been possible, but is generally unnecessary (cf. analysis in Section 3.1).

For testing the effectiveness of the RESWRI routine, it does not matter which radial variation of what assortment of harmonic components is used for the creation of the artificial velocity field — as long as the values make sense. It is important that one creates model velocity fields which are comparable to real velocity fields, meaning that the model velocity fields should also contain, e.g., the wiggles which are typically associated with spiral arms. The best resemblance with a real galaxy is in the genuine galaxy itself. Therefore, the results of the harmonic decompositions presented in Chapter 2 are used to create model velocity fields which contain non-circular motions of the first, second, and third harmonic order. These model velocity fields are shown for all galaxies in the sample in the top-right panels of Figs. 3.13 - 3.29 in the Appendix 3.A. The small amplitudes in the residual velocity fields (bottom-right panels of Figs. 3.13 - 3.29), which are created by subtracting the model velocity fields from the original data show that these models are a good approximation to the real velocity fields (top-left panels of Figs. 3.13 - 3.29).

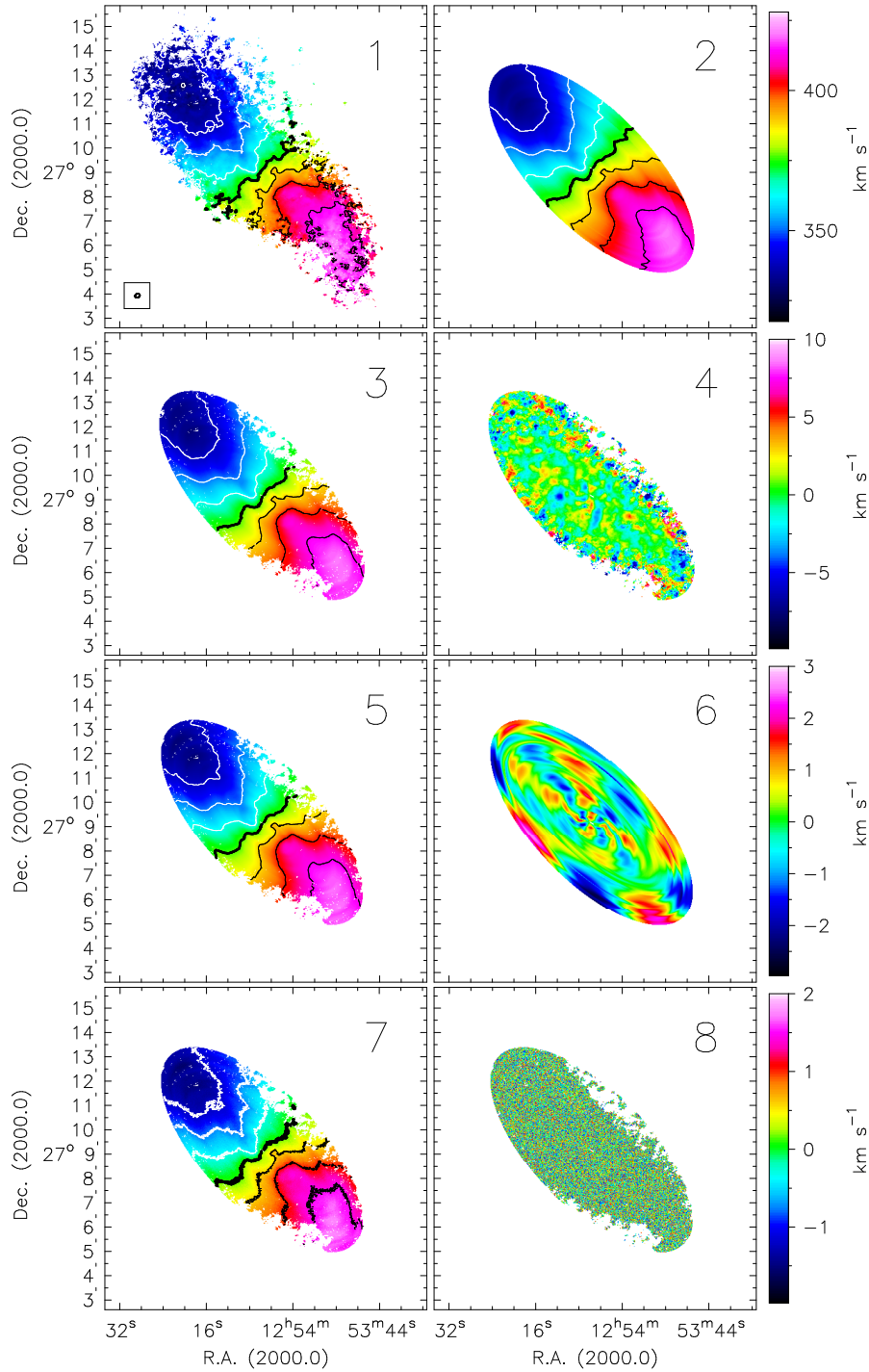


FIG. 3.9: Extended summary panel for DDO 154. The velocity fields in the first (i.e., top) row and in the entire left column (i.e., panels 1, 2, 3, 5, and 7) share the same color bar, shown rightwards of the first row. The contour levels are also identical: the thick black contour represents the systemic velocity at $V_{\text{sys}} = 375.9 \text{ km s}^{-1}$ and the velocity contours are spaced by 12.5 km s^{-1} with white contours marking the approaching side and black contours the receding side, respectively. The individual panels contain the following maps: **(1)**: Original hermite velocity field; the beam is indicated in the bottom left corner; **(2)**: Model velocity field of the third order harmonic decomposition; **(3)**: Clipped version of the model velocity field in panel (2), derived by using the original velocity field in panel (1) as a mask; **(4)**: Residual velocity field, derived by subtracting the model velocity field in panel (2) from the original data in panel (1). The color bar is indicated to the right of the panel; **(5)**: Model velocity field which is the sum of the velocity fields in panels (3) and (6), i.e., containing non-circular motions up to ninth order; **(6)**: Velocity field showing only the fourth-to-ninth harmonic components (quantified in Section 3.1.1). The color bar is indicated rightwards of the panel; **(7)**: Model velocity which is the sum of panels (5) and (8), i.e., containing non-circular motions up ninth order as well as noise; **(8)**: The noise which was added to create the velocity field in panel (7). The noise assumed here follows a uniform noise distribution with values of $-\frac{1}{2}V_{\text{disp}} \leq x \leq +\frac{1}{2}V_{\text{disp}}$, where V_{disp} is the average velocity dispersion along the tilted-rings (derived during the harmonic decomposition).

However, it is oversimplifying to directly use these models for a harmonic decomposition. The model velocity fields consist solely of harmonic components, without any noise or turbulence or deviations, as one might expect in a real galaxy. Therefore, several steps in order to create suitable model velocity fields for the testing of the fitting routine have been undertaken. These are described here for one galaxy (DDO 154) in detail. The first (i.e., top) row of Fig. 3.9 show the original hermite velocity field (left) and the model velocity field from the third order harmonic decomposition (right). One characteristic of the model velocity field is that its tilted-rings are all fully filled. This is not necessarily the case for real galaxies. Therefore, the model contains signal at positions where there is no information in the original velocity field. For DDO 154, this applies mostly to the outer regions only, but, e.g., for NGC 6946, the situation is different (see Fig. 3.27). Therefore, the model velocity fields are clipped with the GIPSY task `CONDIT`, using the original data as a mask. The result of this is shown in panel 3 of Fig. 3.9 for DDO 154, and in the bottom-left panels of Figs. 3.13-3.29 for all other galaxies in the sample.

The results of Chapter 2 and Section 3.1 show that in most cases, a third order harmonic decomposition approximates the velocity field well. Nevertheless, a real velocity field will not agree perfectly with any kind of model. Even for DDO 154, the galaxy with the smallest non-circular motions and residuals in the sample, the residual velocity field (panel 4 of Fig. 3.9) still shows some small-scale residuals for which the third order harmonic decomposition could not account for. Therefore, a model velocity field used for testing the efficiency of the fitting routine should also contain some signal which the algorithm can not fit. In order to do so, I used the ninth order harmonic decompositions presented in Section 3.1 (see the red data points in Fig. 3.1 for DDO 154) and created a map containing harmonic components of fourth-to-ninth order only (panel 6 of Fig. 3.9). By adding this map to the model velocity field from the third order harmonic decomposition (panel 3), a new model velocity field with non-circular motions up to ninth order is created (cf. panel 5 of Fig. 3.9).

However, these additions are of systematic nature only. Real data will also contain some noise and random deviations from harmonic components. Within the tilted-ring analysis, `RESWRI` also measures the velocity dispersion along each tilted-ring. This velocity dispersion, V_{disp} , can be used as an indicator for the uncertainty of the derived rotation velocity. Here, it is used to create noise maps. I determine the radial average of the velocity dispersion for each galaxy (cf. Col. (7) of Table 3.1) and create a map containing uniform noise of amplitudes x with $-\frac{1}{2}V_{\text{disp}} \leq x \leq +\frac{1}{2}V_{\text{disp}}$. The noise map for DDO 154 is shown in panel 8 of Fig. 3.9. Adding this noise to the velocity field from panel 5 results in the model velocity field used for the further analysis (panel 7 of Fig. 3.9).

This procedure has also been applied to the other galaxies of the sample, with a few modifications as described in the following. Firstly, while DDO 154 has a very regular velocity field which allows a ninth order harmonic decomposition even in its outer parts (cf. Fig. 3.1), other galaxies have not. A ninth order harmonic decomposition comes with an increased number of free parameters (compared to a third order decomposition). Therefore, the former is much more affected by sparsely filled tilted-rings in the outskirts of galaxies. For example, the amplitudes of the ninth order decomposition of NGC 2403 (red data points in the bottom panels of Fig. 3.2) deviate from the ones of the third order decomposition (blue data points) for radii larger than $800''$. As the amplitudes of the ninth order harmonic decomposition are used as a “disturbance term” in the artificial velocity fields, the results should not be affected by these deviant data points. Therefore, the harmonic decomposition of the artificial velocity fields is restricted to a maximum radius, which is identical to the maximum radius used in Section 3.1 for the averaging of \tilde{A}_m and \tilde{A}_r . This is fully appropriate, providing that one restricts the analysis of the original velocity field (i.e., the inserted non-circular motions) to the same radius. This way, one compares the amplitudes of the non-circular motions detected in an artificial

TABLE 3.1: Harmonic decomposition of artificial velocity fields

Name	$\tilde{A}_r^{\text{Orig}}$ km s ⁻¹	$\tilde{A}_r^{\text{Model}}$ km s ⁻¹	$\frac{\tilde{A}_r^{\text{Model}}}{\tilde{A}_r^{\text{Orig}}}$	$\tilde{A}_r^{\text{Model}} - \tilde{A}_r^{\text{Orig}}$ km s ⁻¹	R_{max} "	V_{disp} km s ⁻¹
(1)	(2)	(3)	(4)	(5)	(6)	(7)
NGC 2366	2.67	2.08	0.78	-0.58	...	3.9
NGC 2403	4.27	3.84	0.90	-0.43	800	5.5
NGC 2841	3.08	2.88	0.93	-0.20	325	10.3
NGC 2976	1.93	1.85	0.95	-0.09	110	3.9
NGC 3031	9.11	9.97	1.09	0.86	800	7.6
NGC 3198	4.01	3.97	0.99	-0.03	450	5.1
IC 2574	3.75	3.47	0.92	-0.28	...	4.6
NGC 3521	7.45	7.40	0.99	-0.05	350	11.0
NGC 3621	2.90	2.72	0.94	-0.18	500	4.2
NGC 4736	8.36	8.23	0.98	-0.13	175	5.6
DDO 154	1.59	1.53	0.96	-0.06	...	2.1
NGC 5055	4.11	4.09	1.00	-0.02	450	6.0
NGC 6946	6.53	7.27	1.11	0.73	250	5.5
NGC 7331	5.99	5.66	0.94	-0.33	240	9.1
NGC 7793	4.67	4.89	1.05	0.22	...	4.1

NOTES: (1): the name of the galaxy; (2): the median amplitude of the non-circular motions inserted into the artificial velocity field ($\tilde{A}_r^{\text{Orig}}$); (3): the median amplitude of the non-circular motions detected in the artificial velocity field ($\tilde{A}_r^{\text{Model}}$); (4): recovery-rate, i.e., $\tilde{A}_r^{\text{Model}}$ divided by $\tilde{A}_r^{\text{Orig}}$; (5): difference between the detected and inserted non-circular motions (i.e., $\tilde{A}_r^{\text{Model}} - \tilde{A}_r^{\text{Orig}}$); (6): the maximum radius used for averaging $\tilde{A}_r^{\text{Orig}}$ and $\tilde{A}_r^{\text{Model}}$; (7): average velocity dispersion of the tilted-ring analysis. The noise which was added to the model velocity fields has amplitudes x of $-\frac{1}{2}V_{\text{disp}} \leq x \leq +\frac{1}{2}V_{\text{disp}}$.

velocity field with the inserted ones (initially detected in a real velocity field) *within the same radial range*.

For the individual galaxies, the maximum radius is listed in Col. (6) of Table 3.1 and is also indicated by the dotted lines in the right panels of Figs. 3.1-3.7. Note that if no maximum radius is given in Table 3.1, the harmonic analysis extends to the entire radial range (i.e., the range as plotted in Figs. 3.1-3.7).

Additional to the aforementioned restriction, three galaxies (NGC 925, NGC 2903, and NGC 3627) are excluded entirely from this analysis, as none of them shows a maximum radius inwards of which the ninth order harmonic decomposition produces results of acceptable quality. NGC 925 for example shows unrealistic high (and uncertain) amplitudes throughout a large part of its disk. It would of course be possible to refrain from including higher order harmonic terms into the velocity fields of these three galaxies, but for the sake of consistency, this possibility is not approved.

Therefore, the subsequent analysis is restricted to 15 galaxies which are all listed in Table 3.1.

3.2.2 Harmonic decomposition of the artificial velocity fields

The harmonic decomposition of the artificial velocity fields is done using the same initial estimates as for the decomposition of the original velocity fields, whose analysis has been presented in Chapter 2.

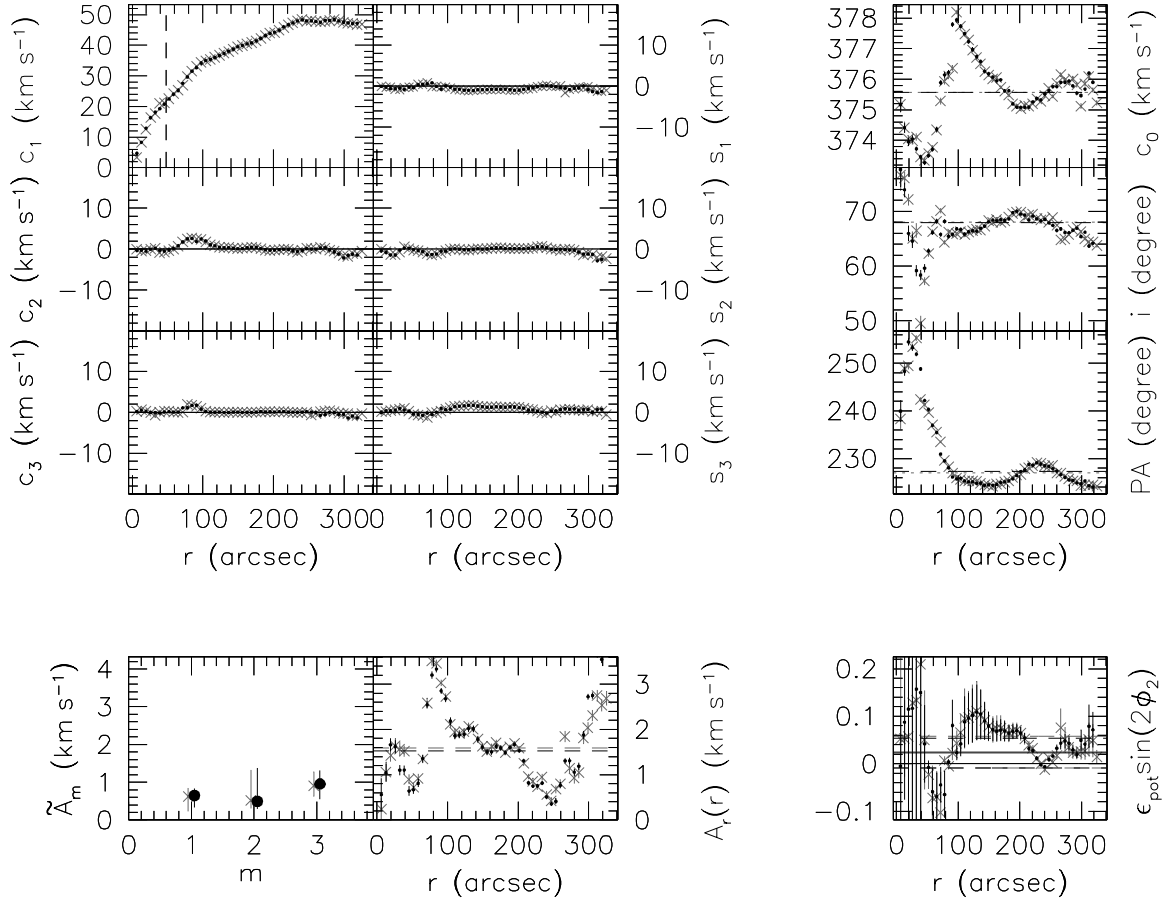


FIG. 3.10: Results from the harmonic decomposition of the artificial velocity field of DDO 154 (black dots) together with those from the original velocity field (gray crosses). The agreement between the inserted (gray) and detected (black) non-circular motions is excellent.

Analogous to the analysis presented in the previous chapter, the center position is kept fixed at the position listed in Table 2.2 and the artificial velocity fields are decomposed up to the third order. For DDO 154, the results of this harmonic decomposition are shown in Fig. 3.10, where the gray data points are based on the original velocity field (i.e., these non-circular motions were *inserted* into the artificial VF) and the black data points are based on the artificial velocity field (i.e., these non-circular motions were *detected* in the artificial VF). The agreement between the inserted (gray) and the detected (black) non-circular motions is very good. The difference of the radially averaged “total power” of the non-circular motions (i.e., \tilde{A}_r) is less than 0.1 km s^{-1} . As DDO 154 shows the smallest non-circular motions of the entire sample, one might argue that the good agreement is just a coincidence. That it is not is demonstrated by Fig. 3.11, which shows the harmonic decomposition of NGC 3198. This galaxy has non-zero harmonic components which show distinct radial variations. Nevertheless, the amplitudes of the harmonic decomposition of the artificial velocity field (black) trace the inserted non-circular motions (gray) extremely well, except for the outermost two or three data points. The discrepancy for the data points at the largest radii has a simple reason. The artificial velocity field is somewhat less extended than the original velocity field, which results in boundary

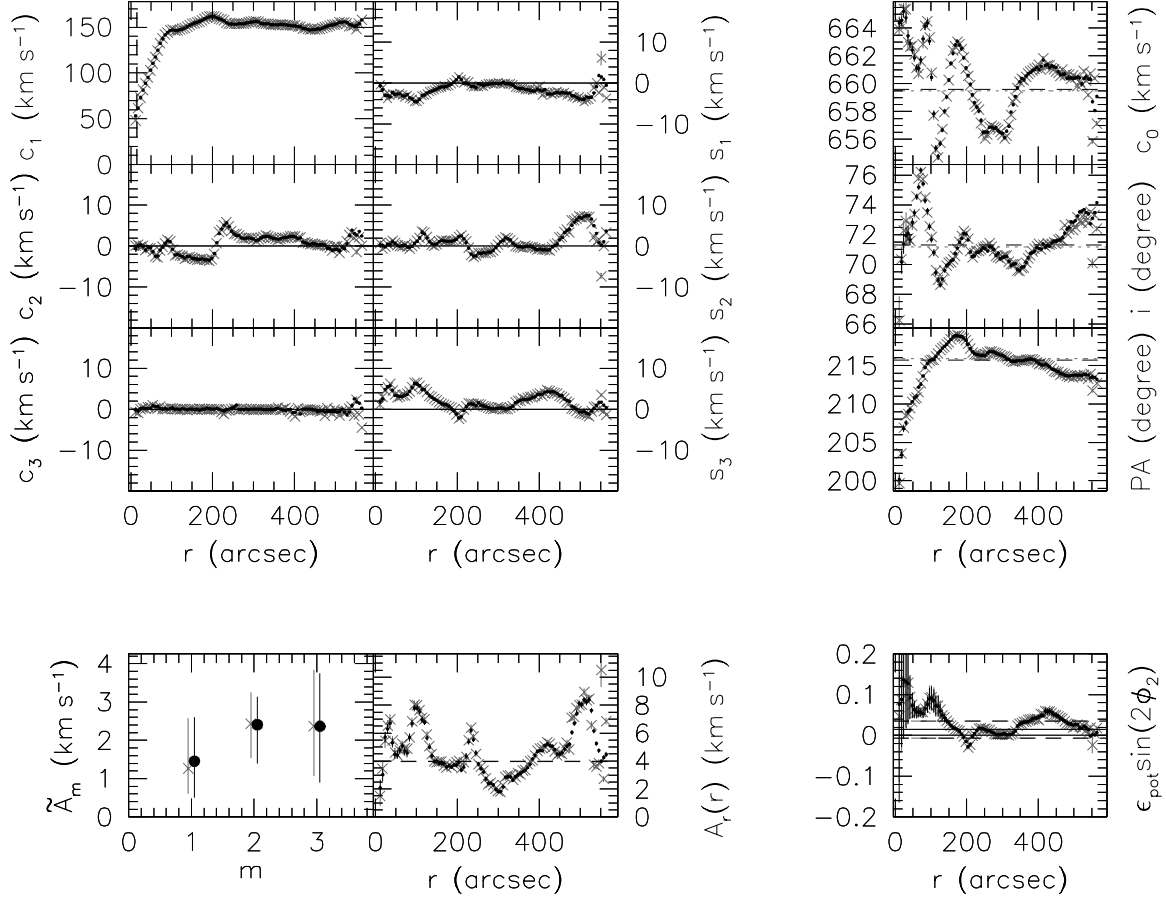


FIG. 3.11: Results from the harmonic decomposition of the artificial velocity field of NGC 3198 (black dots) together with those from the original velocity field (gray crosses). The detected (black) non-circular motions trace the radial trends of the inserted (gray) non-circular motions very well.

problems when decomposing the very outer parts of the artificial velocity field. Therefore, and also due to the problems discussed in the previous section, the radial averaging of $A_r(r)$ — both for the inserted non-circular motions as well as for the detected ones — is restricted to radii smaller than a maximum radius (450'' for NGC 3198, cf. Col. (6) in Table 3.1).

Rather than showing detailed plots like Figs. 3.10 or 3.11 for all 15 galaxies, the results of the harmonic decomposition of the artificial velocity fields are discussed in a more general way. The median amplitudes of the *inserted* non-circular motions (i.e., those that were initially detected in the original velocity field) are referred to as $\tilde{A}_r^{\text{Orig}}$ and are listed in Col. (2) of Table 3.1. The median amplitudes of the *recovered* non-circular motions (i.e., those that were detected in the model velocity field) are referred to as $\tilde{A}_r^{\text{Model}}$ and are given in Col. (3) of Table 3.1. The left panel of Fig. 3.12 shows a histogram of the so-called “recovery-rate”, i.e., $\tilde{A}_r^{\text{Model}}$ divided by $\tilde{A}_r^{\text{Orig}}$ (cf. Col. (4) of Table 3.1). For twelve out of the fifteen galaxies (i.e., 80 percent), the median amplitudes of the recovered non-circular motions differ by less than ten percent from the inserted non-circular motions. For one galaxy (NGC 6946), the recovered non-circular motions are 1.11 times as large as the inserted ones, and for two galaxies (NGC 2366 and NGC 2403), the recovery rates are below 90 percent. Although

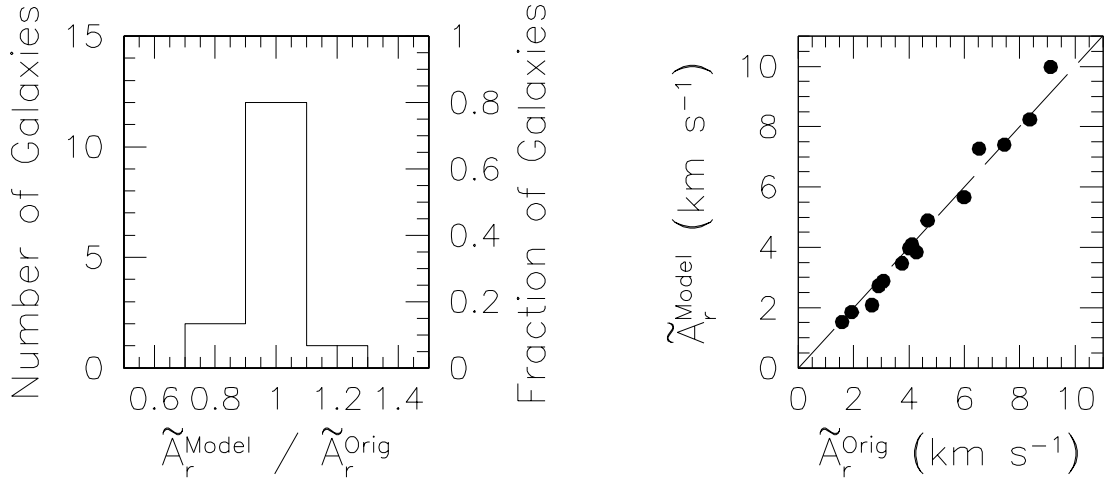


FIG. 3.12: **Left:** Histogram of the recovery-rate of the harmonic decomposition of the artificial velocity fields. In 12 out of 15 galaxies, the non-circular motions detected in the artificial velocity fields are within ten percent of the ones inserted into the artificial velocity fields (i.e., those that have been previously detected in the original data). Only three galaxies show larger deviations. **Right:** Detected amplitudes of the non-circular motions ($\tilde{A}_r^{\text{Model}}$) vs. inserted amplitudes ($\tilde{A}_r^{\text{Orig}}$). The dashed line indicates the line of unity. The deviations from a one-to-one relation are small ($< 1 \text{ km s}^{-1}$ for all galaxies).

a deviation of more than ten percent sounds quite high at first glance, one has to keep in mind the absolute numbers as well. In the right panel of Fig. 3.12, $\tilde{A}_r^{\text{Model}}$ is plotted vs. $\tilde{A}_r^{\text{Orig}}$. The dashed line indicates a one-to-one correlation (i.e., a recovery-rate of 1.00). The individual data points are all very close to the line of unity, showing that the difference between the amplitudes is small on absolute scales. As can be seen in Col. (5) of Table 3.1, the difference is below 1 km s^{-1} for all galaxies in the sample, and thus smaller than the velocity resolution of the data.

The average recovery-rate is 0.97 ± 0.08 , i.e., on average, only three percent of the non-circular motions within the model velocity fields were not re-detected. This value is, however, somewhat affected by those galaxies for which RESWRI detected larger non-circular motions than have been inserted. Being conservative and excluding these galaxies from the calculation of the mean results in an average recovery-rate of 0.94 ± 0.06 . Doing the same with the difference between $\tilde{A}_r^{\text{Model}}$ and $\tilde{A}_r^{\text{Orig}}$ (Col. (5) of Table 3.1) results in an average difference of $-0.04 \pm 0.39 \text{ km s}^{-1}$ when including all galaxies or $-0.20 \pm 0.18 \text{ km s}^{-1}$ when excluding those galaxies where the detected non-circular motions exceed the inserted ones. Whether one approaches this analysis in a statistical way, or on a case-by-case basis, the results are unchanged. The harmonic decomposition of the artificial velocity fields is able to detect most of the non-circular motions previously inserted into said velocity fields. The differences are of the order of five percent, or 0.2 km s^{-1} . This large recovery-rate strongly indicates that the harmonic decomposition with RESWRI is able to detect most non-circular motions within a galaxy.

3.3 Conclusions

This chapter was dedicated to probe whether the velocity fields of the galaxies in the sample contain any non-circular motions which have been missed by the analysis in Chapter 2. Special emphasis has

been laid on the influence of non-circular motions of higher harmonic orders — which would have been undetected in the previous analysis — and on the detection efficiency of the RESWRI routine.

The work presented in Section 3.1 showed that increasing the maximum fit order N from $N = 3$ up to $N = 15$ does result in a modest increase of the detected non-circular motions. Only few galaxies contain significant terms of higher ($m > 3$) harmonic order and harmonic components with $m > 5$ are usually negligible in all galaxies. Focussing on the dwarf galaxies, i.e., the galaxies where the cusp/core problem is most apparent, it has been shown that including non-circular motions up to ninth order does not alter the conclusion from the previous chapter: the non-circular motions in the centers of the galaxies are too small to reconcile cuspy DM density profiles with non-circular motions. Given these results, it seems sufficient to decompose the velocity fields up to third order, because if one increases the maximum fit order, one also increases the number of free parameters and thus enhances the problems when dealing with galaxies having sparsely filled tilted-rings like, e.g., NGC 925 or NGC 6946.

In Section 3.2, artificial velocity fields have been created and analyzed. These artificial velocity fields contain the same amount of first-to-third order non-circular motions as initially quantified in Chapter 2. Additionally, uniform noise and fourth-to-ninth order harmonic terms were added to the velocity fields. The velocity fields were then decomposed up to third order and the detected non-circular motions have been compared with the inserted ones. The results show that the recovered non-circular motions deviate on average by 0.2 km s^{-1} from the inserted ones. In relative terms, the average difference is about 5 percent. Therefore, I conclude that RESWRI is able to quantify almost all non-circular motions in the velocity field of a galaxy. I have demonstrated that the velocity fields of the galaxies in this sample do not contain large non-circular motions which have been undetected by the analysis in Chapter 2. Therefore, the work presented in this chapter strengthens the results from the previous one. Non-circular motions are small, especially in the centers of dwarf galaxies and can not explain why observers fail to see the cuspy density profiles characteristic for CDM halos.

3.A Appendix: Velocity fields

In this section, the summary panels for all galaxies of the sample are presented, except for DDO 154, whose summary panel is shown in Fig. 3.9. Each of the summary panels contains four sub-panels, whose content and layout is identical to panels 1 - 4 of Fig. 3.9: **(1)** the original hermite velocity field (top left), **(2)** the model velocity field (top right), **(3)** the clipped model velocity field where the original hermite velocity field was used as a mask (bottom left), and **(4)** the residual velocity field (bottom right), derived by subtracting the clipped model velocity field from the original data. Sub-panels (1) - (3) share the same color bar, indicated rightwards of sub-panel (2). The residual velocity field is shown on a different color scale indicated by the color bar rightwards of sub-panel (4).

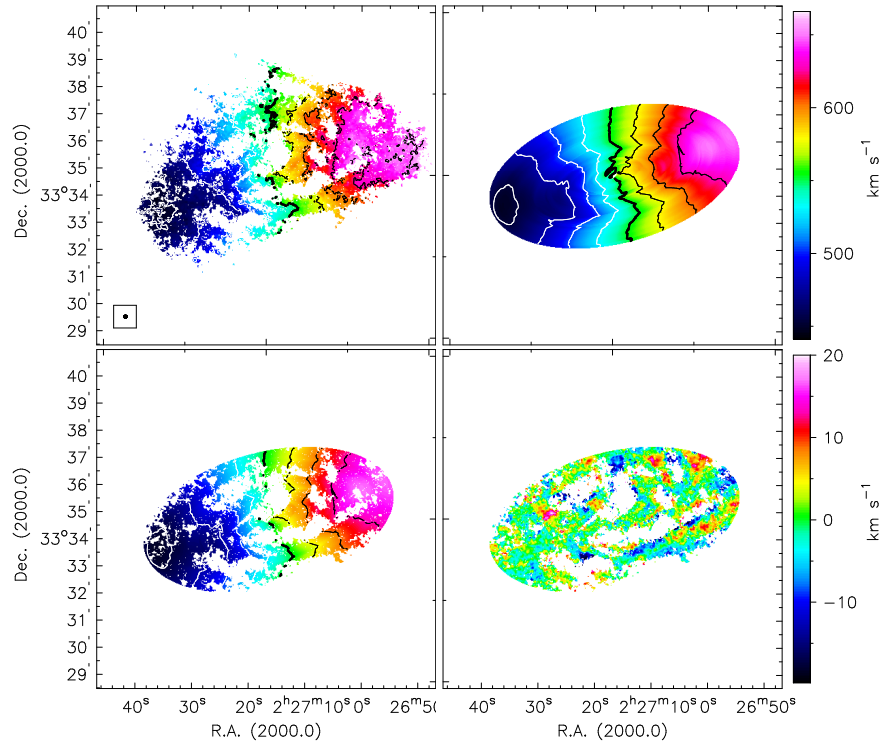


FIG. 3.13: Summary panel for NGC 925. The velocity contours are spaced by 25 km s^{-1} and the thick black contour indicates the systemic velocity at $V_{\text{sys}} = 552.5 \text{ km s}^{-1}$. See text for further details.

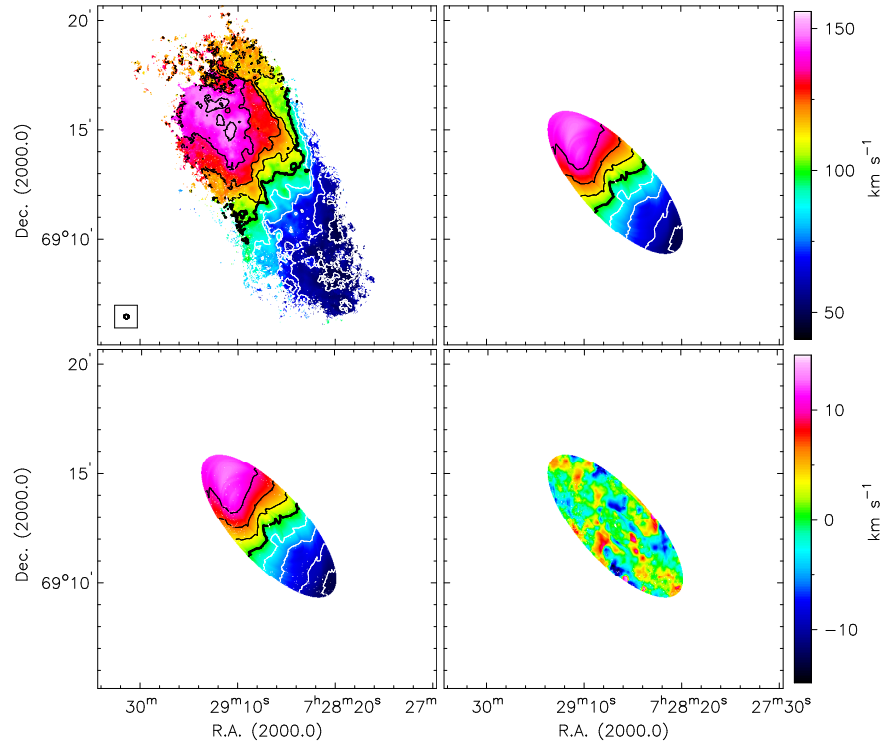


FIG. 3.14: Summary panel for NGC 2366. The velocity contours are spaced by 12.5 km s^{-1} and the thick black contour indicates the systemic velocity at $V_{\text{sys}} = 100.0 \text{ km s}^{-1}$. See text for further details.

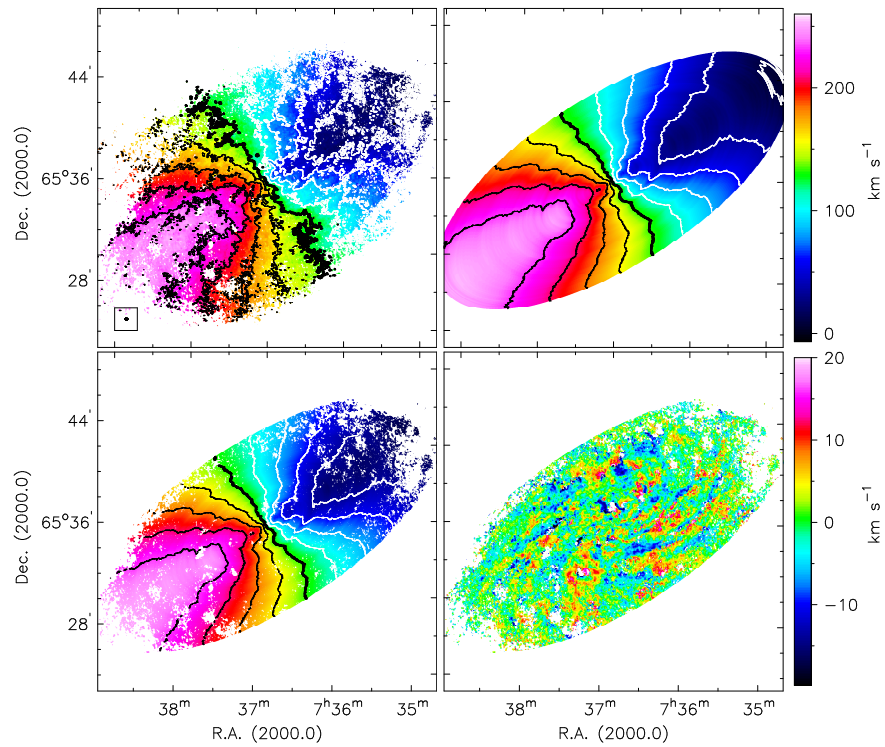


FIG. 3.15: Summary panel for NGC 2403. The velocity contours are spaced by 25 km s^{-1} and the thick black contour indicates the systemic velocity at $V_{\text{sys}} = 133.1 \text{ km s}^{-1}$. See text for further details.

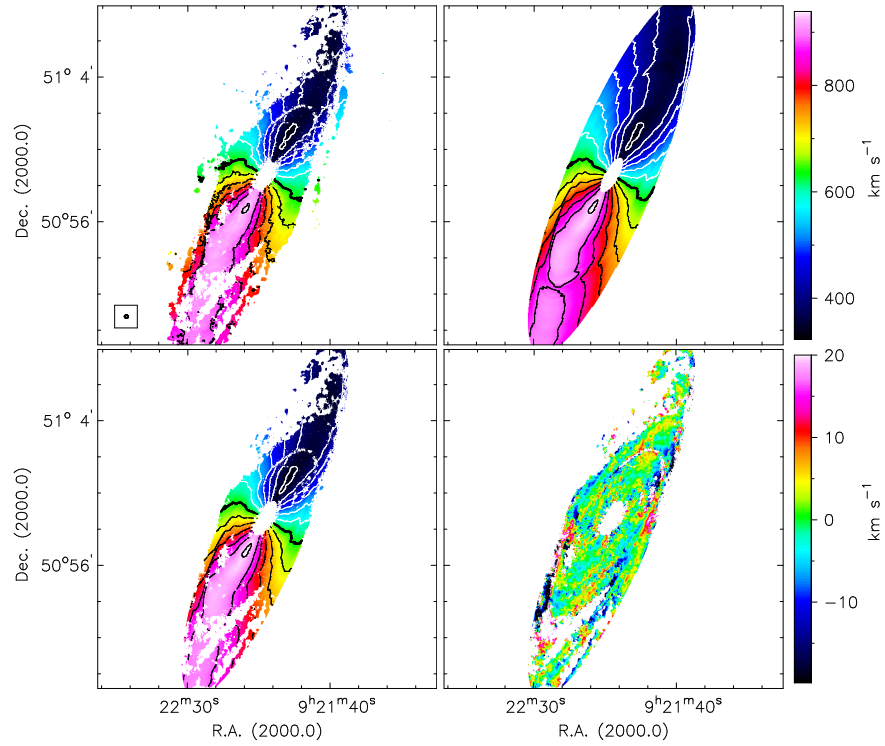


FIG. 3.16: Summary panel for NGC 2841. The velocity contours are spaced by 50 km s^{-1} and the thick black contour indicates the systemic velocity at $V_{\text{sys}} = 635.2 \text{ km s}^{-1}$. See text for further details.

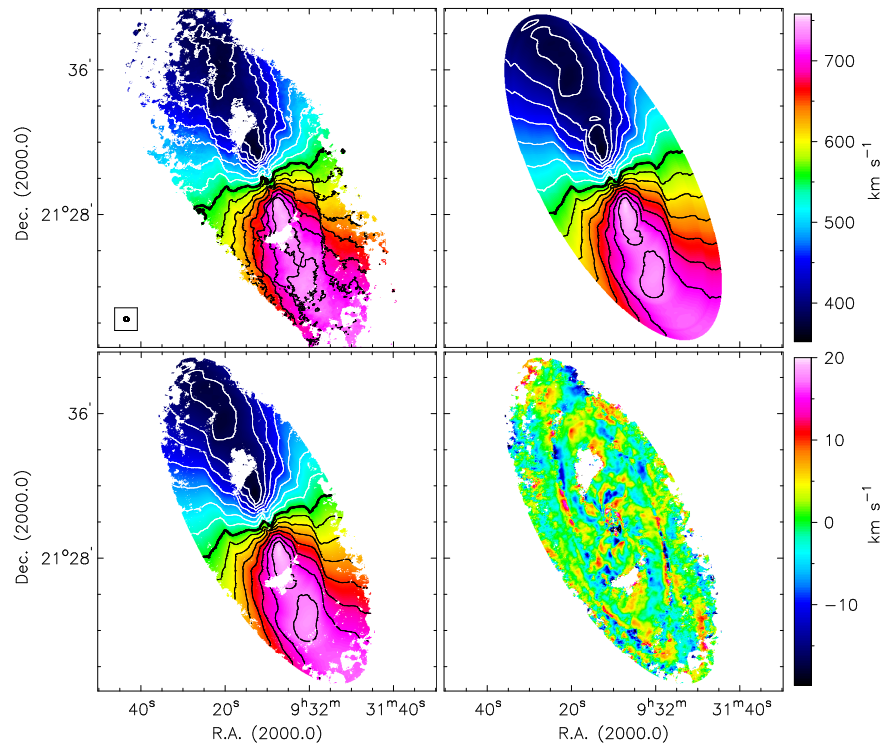


FIG. 3.17: Summary panel for NGC 2903. The velocity contours are spaced by 25 km s^{-1} and the thick black contour indicates the systemic velocity at $V_{\text{sys}} = 555.6 \text{ km s}^{-1}$. See text for further details.

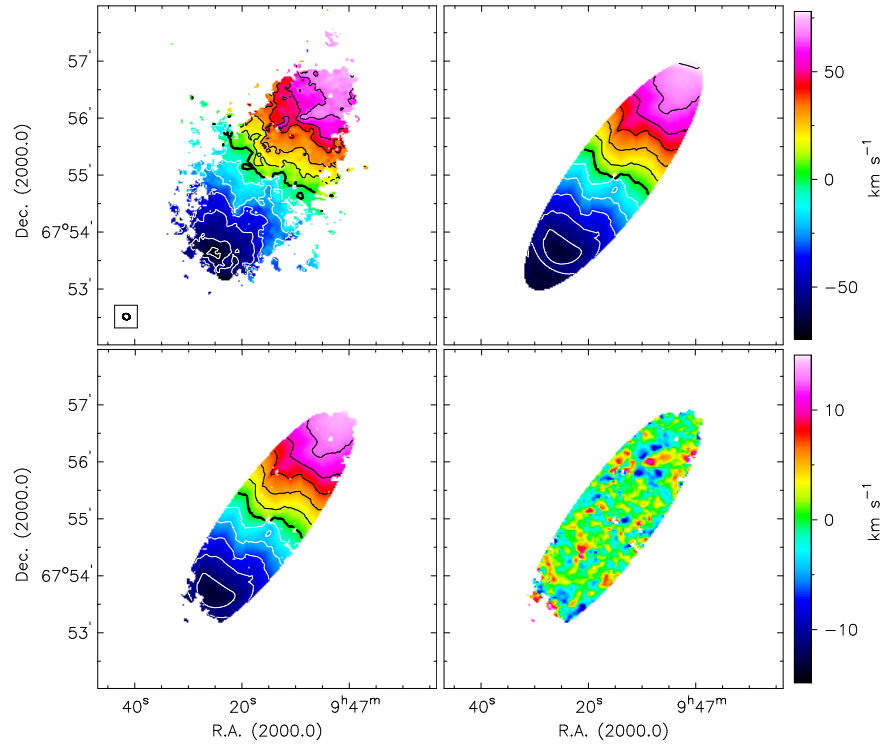


FIG. 3.18: Summary panel for NGC 2976. The velocity contours are spaced by 12.5 km s^{-1} and the thick black contour indicates the systemic velocity at $V_{\text{sys}} = 2.6 \text{ km s}^{-1}$. See text for further details.

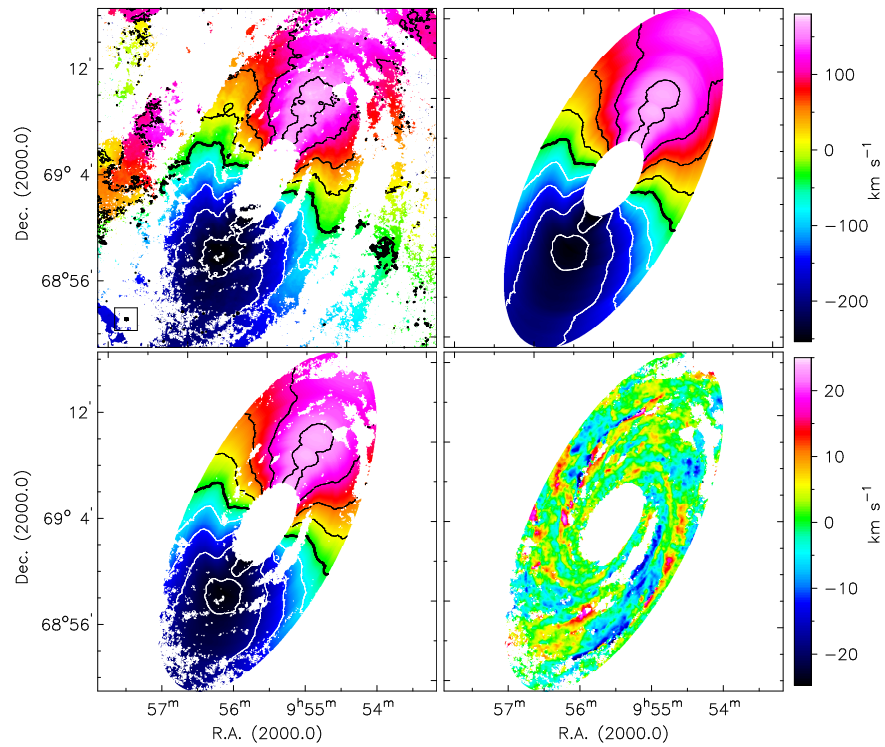


FIG. 3.19: Summary panel for NGC 3031. The velocity contours are spaced by 50 km s^{-1} and the thick black contour indicates the systemic velocity at $V_{\text{sys}} = -39.8 \text{ km s}^{-1}$. See text for further details.

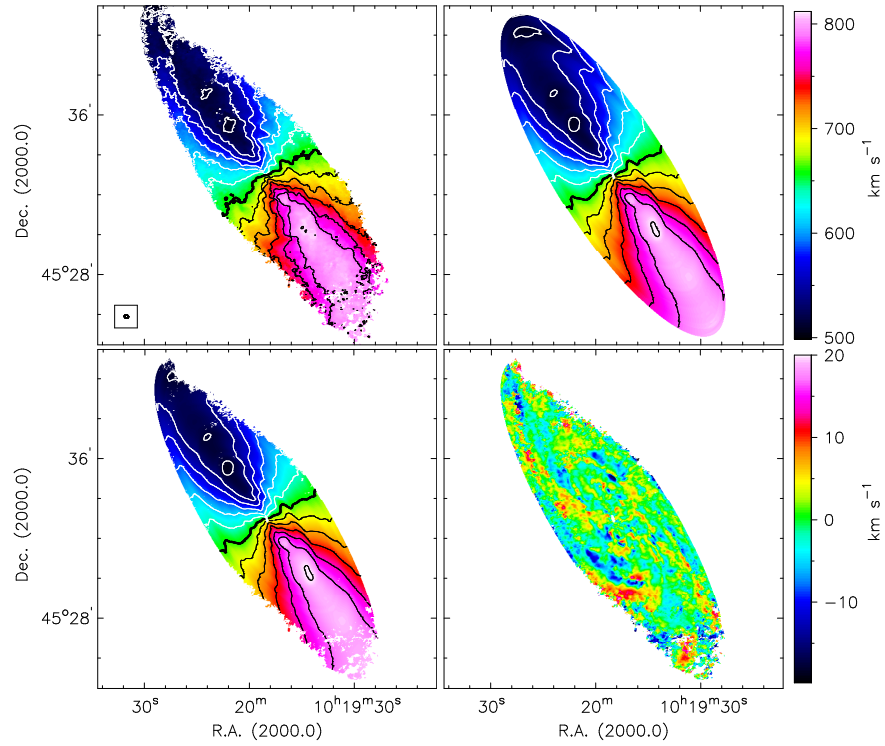


FIG. 3.20: Summary panel for NGC 3198. The velocity contours are spaced by 25 km s^{-1} and the thick black contour indicates the systemic velocity at $V_{\text{sys}} = 661.2 \text{ km s}^{-1}$. See text for further details.

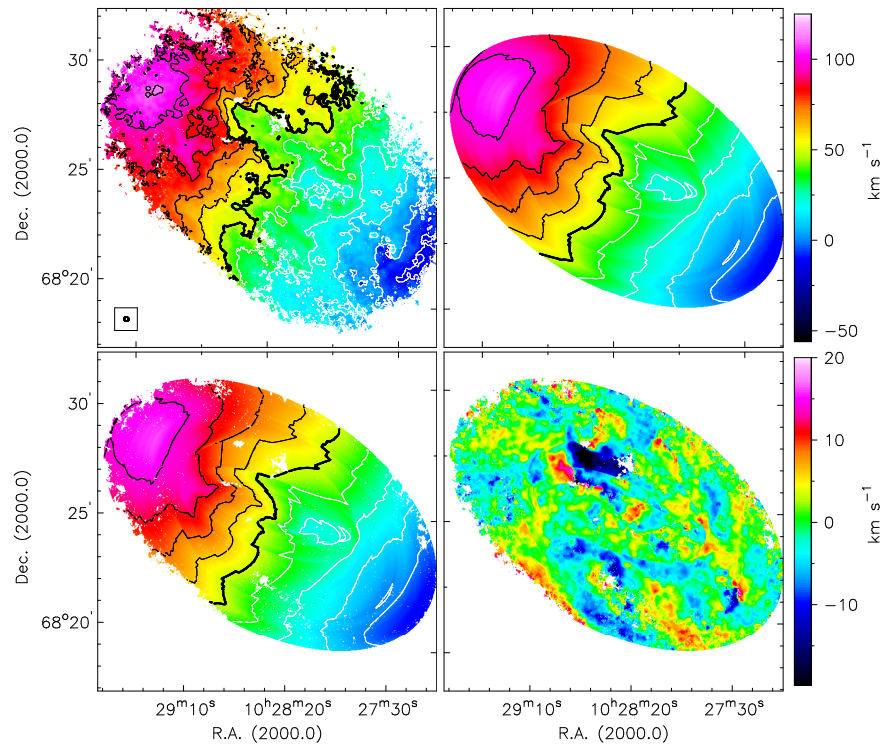


FIG. 3.21: Summary panel for IC 2574. The velocity contours are spaced by 12.5 km s^{-1} and the thick black contour indicates the systemic velocity at $V_{\text{sys}} = 48.6 \text{ km s}^{-1}$. See text for further details.

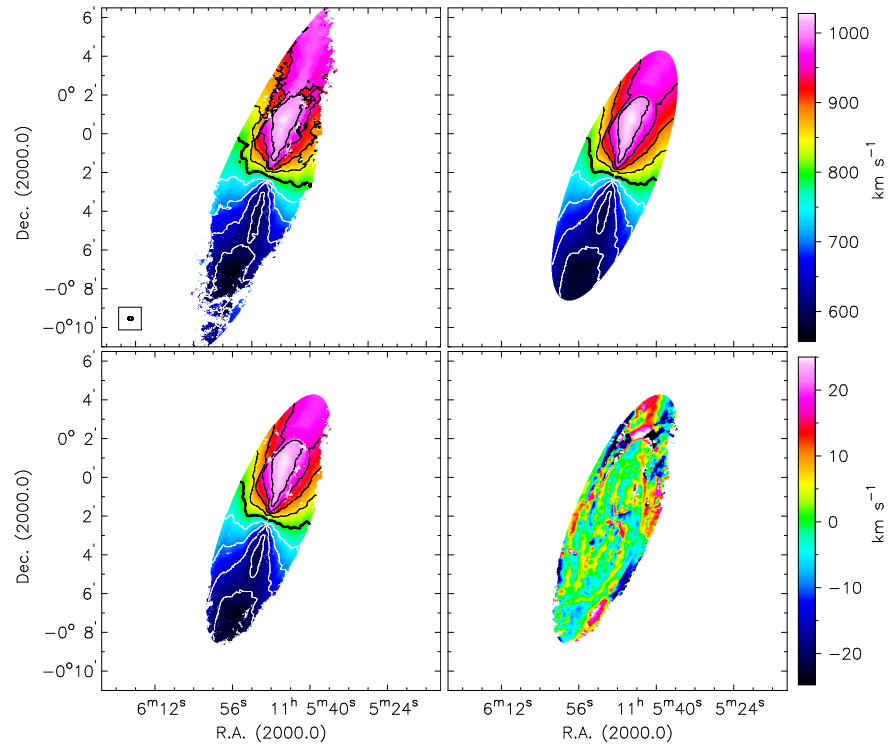


FIG. 3.22: Summary panel for NGC 3521. The velocity contours are spaced by 50 km s^{-1} and the thick black contour indicates the systemic velocity at $V_{\text{sys}} = 798.2 \text{ km s}^{-1}$. See text for further details.

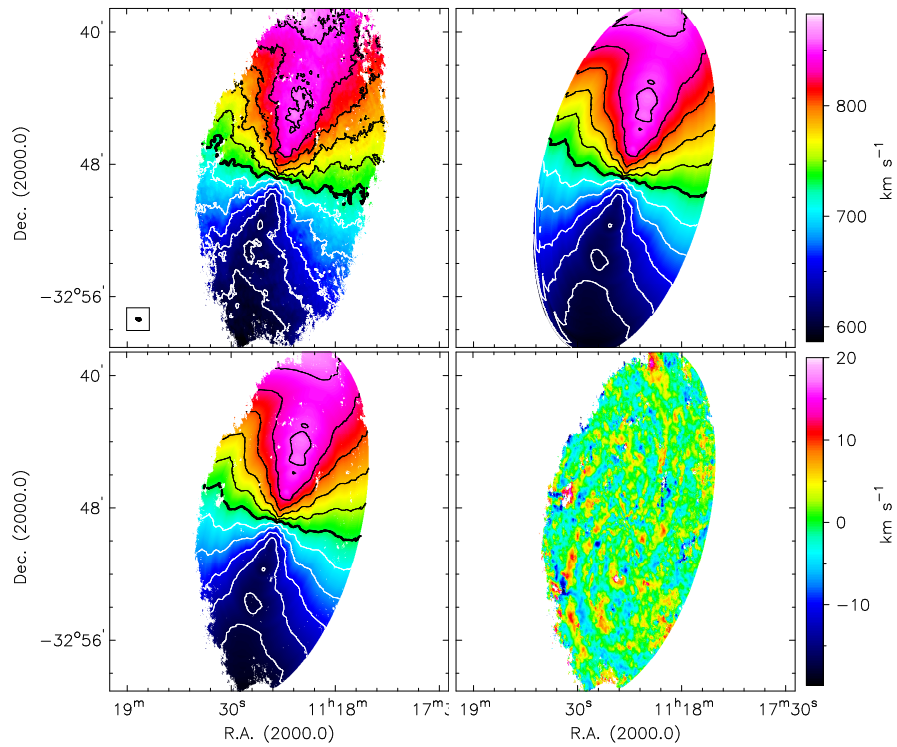


FIG. 3.23: Summary panel for NGC 3621. The velocity contours are spaced by 25 km s^{-1} and the thick black contour indicates the systemic velocity at $V_{\text{sys}} = 730.1 \text{ km s}^{-1}$. See text for further details.

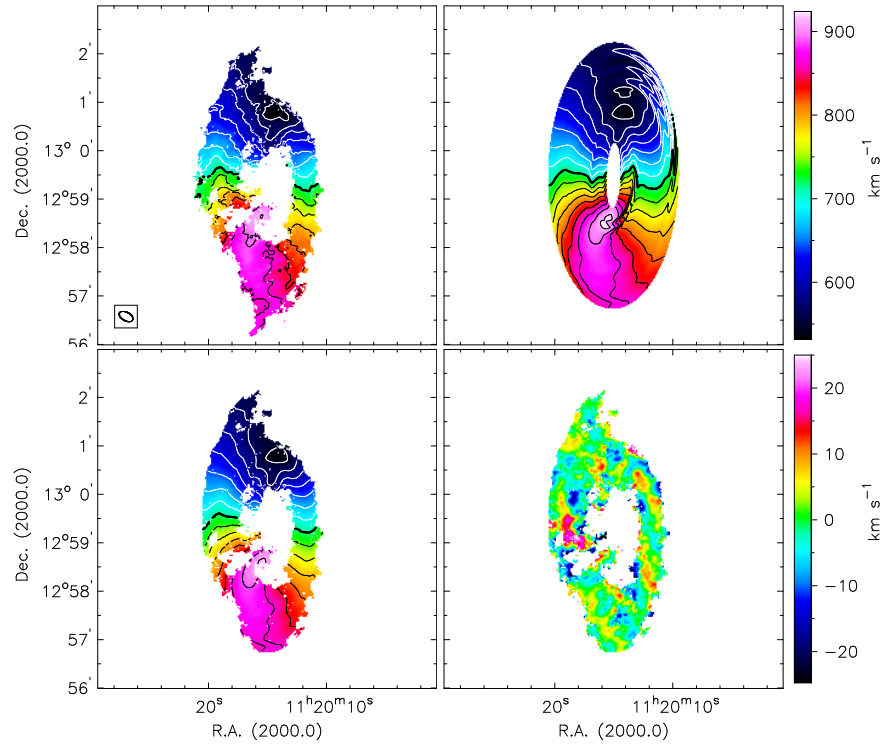


FIG. 3.24: Summary panel for NGC 3627. The velocity contours are spaced by 25 km s^{-1} and the thick black contour indicates the systemic velocity at $V_{\text{sys}} = 717.3 \text{ km s}^{-1}$. See text for further details.

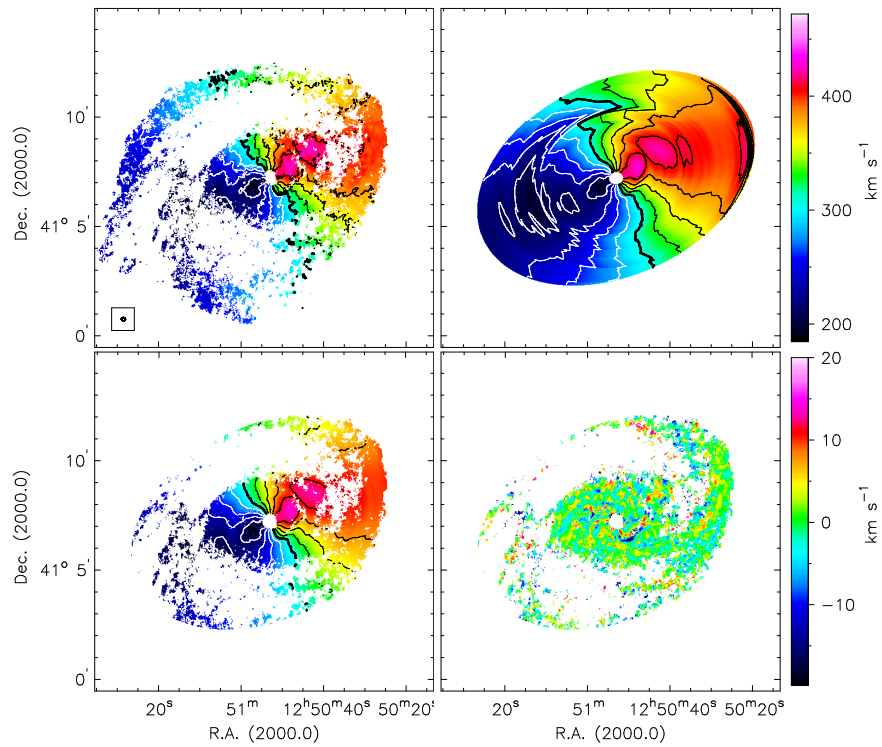


FIG. 3.25: Summary panel for NGC 4736. The velocity contours are spaced by 25 km s^{-1} and the thick black contour indicates the systemic velocity at $V_{\text{sys}} = 307.6 \text{ km s}^{-1}$. See text for further details.

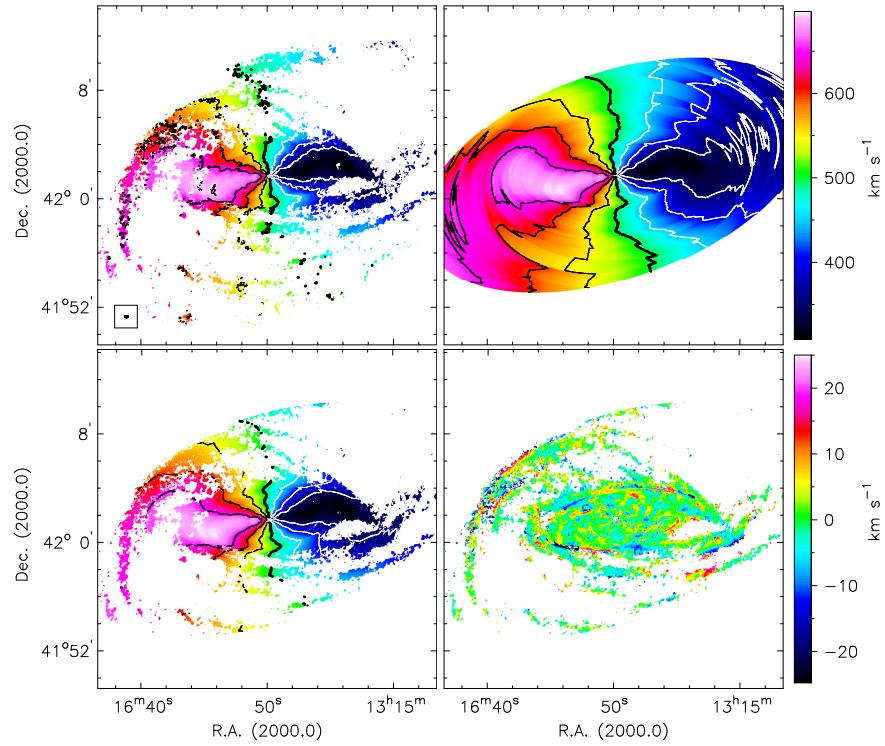


FIG. 3.26: Summary panel for NGC 5055. The velocity contours are spaced by 50 km s^{-1} and the thick black contour indicates the systemic velocity at $V_{\text{sys}} = 499.3 \text{ km s}^{-1}$. See text for further details.

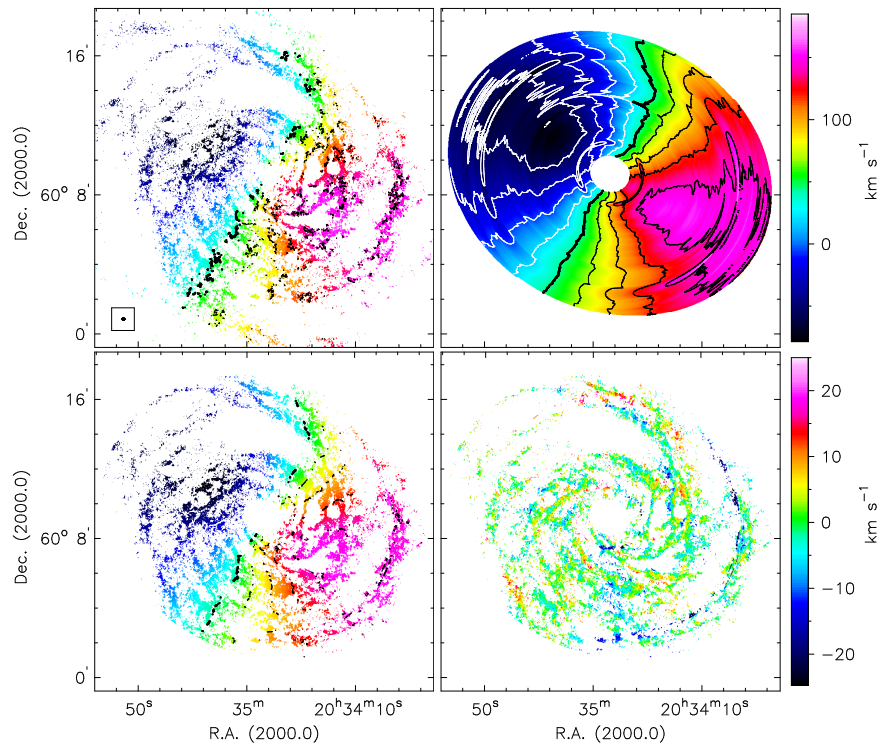


FIG. 3.27: Summary panel for NGC 6946. The velocity contours are spaced by 25 km s^{-1} and the thick black contour indicates the systemic velocity at $V_{\text{sys}} = 43.5 \text{ km s}^{-1}$. See text for further details.

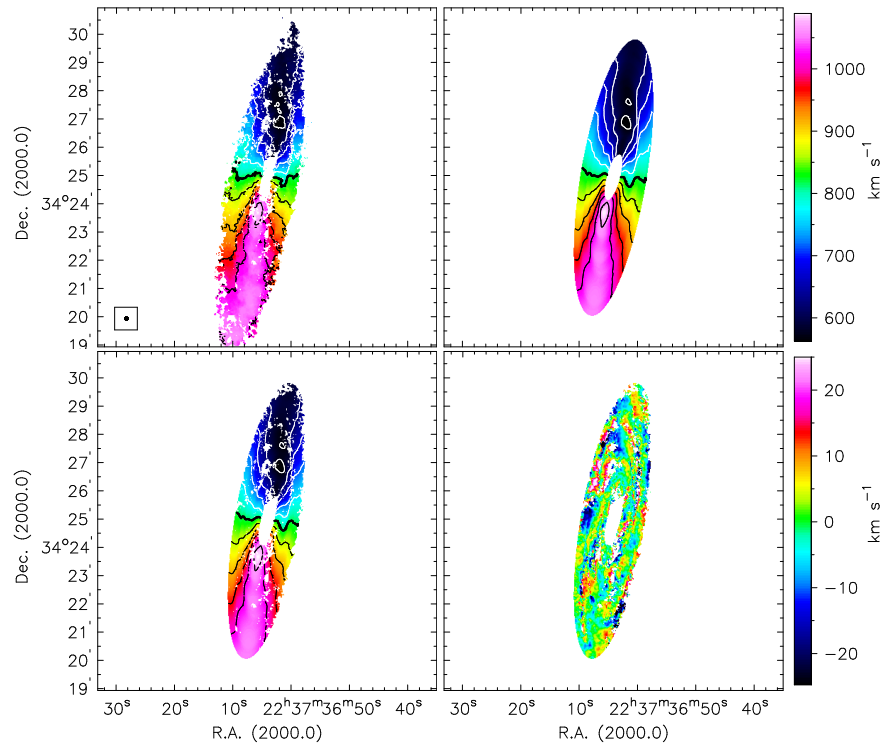


FIG. 3.28: Summary panel for NGC 7331. The velocity contours are spaced by 50 km s^{-1} and the thick black contour indicates the systemic velocity at $V_{\text{sys}} = 815.6 \text{ km s}^{-1}$. See text for further details.

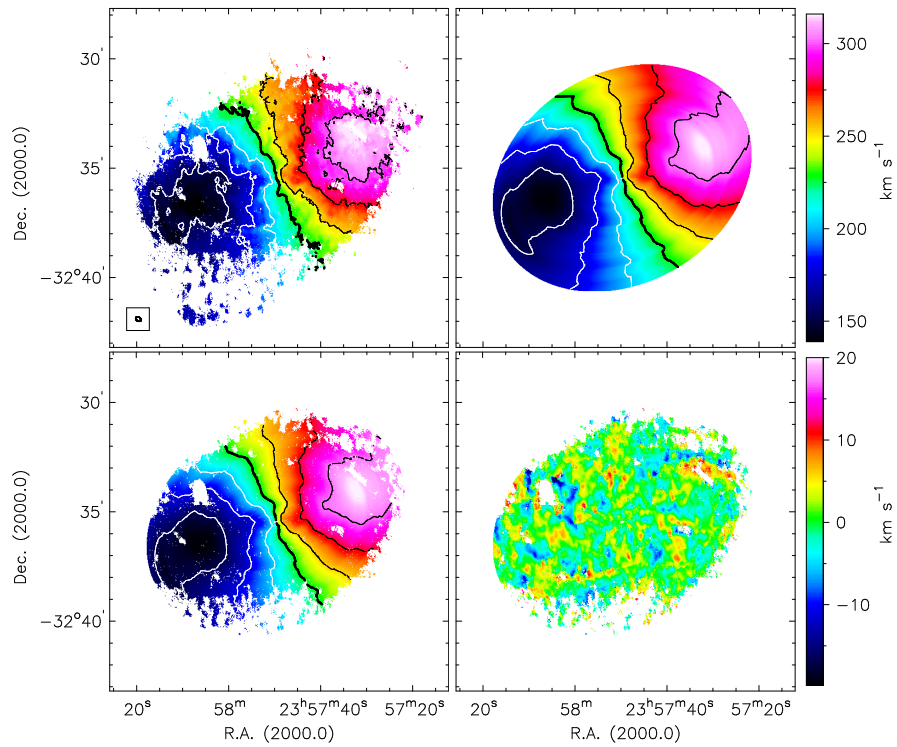


FIG. 3.29: Summary panel for NGC 7793. The velocity contours are spaced by 25 km s^{-1} and the thick black contour indicates the systemic velocity at $V_{\text{sys}} = 227.2 \text{ km s}^{-1}$. See text for further details.

The baryonic Tully-Fisher relation and its implication for dark matter halos*

ABSTRACT

The remarkably small scatter of the baryonic Tully-Fisher relation (BTF) places strong constraints on the tri-axiality of cold dark matter (CDM) halos. Recent attempts to solve the cusp/core problem (i.e., to reconcile the inferred density slopes from CDM simulations and observations) include the effect a tri-axial halo has on the motion of the gas. As the cusp/core problem is most apparent for dwarf galaxies, we test if extremely low-mass dwarf galaxies follow the same (tight) BTF relation as high-mass galaxies. We obtained HI synthesis data of 11 dwarf galaxies and derived several independent estimates for the maximum rotation velocity. Constructing a BTF relation using data from the literature for the high-mass end, and the highest-quality galaxies from our sample for the low-mass end results in a BTF with a scatter of 0.28 mag. This scatter constrains the ellipticities of the potentials in the plane of the disks of the galaxies to an upper limit of 0-0.06, making it unlikely that tri-axiality can fully address some of the current small-scale problems of Cold Dark Matter.

4.1 Introduction

The Tully-Fisher (TF) relation (Tully & Fisher 1977), the relation between the luminosity and rotation velocity of a galaxy, has been extensively used to estimate extragalactic distances (e.g., Pierce & Tully 1988; Sakai et al. 2000; Tully & Pierce 2000). In the usual “classical” interpretation, luminosity is a proxy for the stellar mass, which in turn depends on the total (visible and dark) mass and through it on the rotation velocity. The slope and zero point of this classical TF relation do not depend on the central surface brightness of galaxies (Zwaan et al. 1995), though for very low mass dwarf galaxies, the slope tends to steepen (e.g., Matthews et al. 1998; McGaugh et al. 2000). Low-mass dwarf galaxies are apparently underluminous given their rotation velocity and therefore fall below the TF relation as defined by the high mass galaxies. A single linear relation can be restored if one replaces the luminosity (or stellar mass) with the baryonic disk mass, thus including the gas mass as well (McGaugh et al. 1999, 2000). This relation is called the baryonic Tully-Fisher (BTF) relation and has been studied by

*C. Trachternach, W.J.G. de Blok, S.S. McGaugh, J.M. van der Hulst, and R.-J. Dettmar, *subm. to A & A*

many authors in the last few years (e.g., Bell & de Jong 2001; Verheijen 2001; Gurovich et al. 2004; McGaugh 2004, 2005; Geha et al. 2006; De Rijcke et al. 2007; Noordermeer & Verheijen 2007).

The baryonic Tully-Fisher relation seems to be a universal and remarkably tight relation. This places severe constraints on galaxy formation and evolution theories (cf. Eisenstein & Loeb 1996; McGaugh & de Blok 1998a,b; Mo et al. 1998; Steinmetz & Navarro 1999; Blanton et al. 2007). Franx & de Zeeuw (1992) for instance note that the observed scatter of the TF relation places an upper limit on the elongation of the dark matter halos. Note that they investigated the TF relation, not the BTF relation, but since the BTF is an even tighter correlation than the stellar TF relation (e.g., McGaugh 2005), their reasoning is valid for the BTF as well. From the scatter of the TF relation, Franx & de Zeeuw (1992) argue that the ellipticity of the potential in the plane of the disk is most likely between 0 and 0.06. This is in good agreement with what (Trachternach et al. 2008a, Chapter 2 of this thesis) found observationally for a sample of 18 dwarf and spiral galaxies from the THINGS survey (Walter et al. 2008; de Blok et al. 2008), but in disagreement with results from theoretical CDM simulations which predict more elongated potentials (e.g., Frenk et al. 1988; Hayashi & Navarro 2006).

This discrepancy contains important implications for the so-called “cusp/core” debate. The cusp/core debate is about the density profiles of dwarf and low surface brightness galaxies, whose innermost parts of their rotation curves generally do not show the steep central “cusp”, characteristic for CDM-consistent density profiles like the NFW profile (Navarro et al. 1996, 1997), but are better approximated by a constant-density “core”, as deduced from a pseudo-isothermal halo profile (cf. McGaugh & de Blok 1998b; de Blok et al. 2001a,b; Marchesini et al. 2002; de Blok & Bosma 2002; Gentile et al. 2004; de Blok 2005; Kuzio de Naray et al. 2008). A recent, well-motivated explanation for the discrepancy of the inferred slopes of the density profiles has been given by Hayashi & Navarro (2006) and Hayashi et al. (2007), who argue that CDM halos are tri-axial and that this tri-axiality induces large non-circular motions, which makes it impossible to distinguish an intrinsic “cusp” from a constant-density “core”. Reconciling the different slopes in the density profiles needs non-circular motions of about 15 - 20 km s⁻¹ over a large part of the disk (de Blok et al. 2003; Hayashi et al. 2004a; Kuzio de Naray et al. 2008). However, extensive non-circular motions of this order have not been observed, yet (cf. Schoenmakers et al. 1997; Gentile et al. 2004; Trachternach et al. 2008a). We refer, e.g., to Hayashi & Navarro (2006), de Blok et al. (2008), and Trachternach et al. (2008a) for a more extensive discussion of this topic.

In this context, it is important to check whether the BTF relation holds and remains tight even for extreme dwarf galaxies, because then the conclusions of Franx & de Zeeuw (1992) — which were largely based on observations of high-mass galaxies — would also apply to low-mass galaxies, and thus constrain the range of ellipticities of the potentials of *dwarf* galaxies, too.

The low mass end of the BTF relation has also been studied by Geha et al. (2006) and Kovac (2007). They measure line widths and after correcting these for broadening due to turbulent motion of the HI gas, they find that the extreme dwarf galaxies of their sample follow the same BTF relation as the high mass galaxies, albeit with a larger scatter. This increased scatter, however, is most likely a result of their use of the W_{20} profile. Verheijen (1997) already pointed out that using the maximum rotation velocity from a resolved rotation curve significantly decreases the scatter in the (B)TF relation as compared to one using line width measurements.

In this chapter, we therefore attempt to determine several independent estimates for the maximum rotation velocity (V_{max}) for a sample of extremely low-mass dwarf galaxies. Doing this, we can check whether these galaxies follow the same tight correlation between baryonic disk mass and rotation velocity as their high mass counterparts. As a reference, we use the sample of McGaugh (2005), for

TABLE 4.1: Mapping/Noise parameters for the entire sample.

ID	Date of Obs.	length of Obs.	B_{maj} "	B_{min} "	BPA °	noise/channel mJy b^{-1}	pixel size "	channel width km s^{-1}
(1)	(2)	(3)	(4)	(5)	(6)	(7)	(8)	(9)
D500-2	01-05-2002	12h	25.0	10.6	0.0	1.0	5	4.12
D500-3	03-05-2002	12h	33.0	12.3	0.0	0.6	5	4.12
D512-2	16-05-2004	12h	28.9	13.4	0.6	0.9	4	2.10
D564-8	08-05-2002	12h	36.4	12.8	0.0	0.6	5	4.12
D572-5	10-05-2004	12h	86.6	24.0	-0.2	1.2	4	2.10
D575-1 ^a	07-05-2004	12h	48.2	18.4	0.2	0.9	4	2.10
...	12-05-2004	12h
D575-2 ^b	09-05-2004	12h	45.6	14.0	-3.5	0.6	4	2.10
...	13-05-2004	10h
...	17-10-2004	7h
D575-5	05-05-2004	12h	37.5	11.3	-0.1	1.1	4	2.10
D631-7	04-11-2004	12h	57.7	12.0	0.2	1.1	4	2.10
D640-13	10-11-2004	12h	70.8	11.5	-0.1	1.1	4	2.10
D646-7	11-05-2004	12h	133.8	20.6	0.6	1.4	4	2.10

^aThe data for D575-1 is combined from two individual observations

^bThe data for D575-2 is combined from three individual observations

NOTES: (1): galaxy identifier; (2): Date of observations; (3): length of observations; (4, 5) major (minor) axis diameter of the robust weighted beam in arcsec; (6): position angle of the beam (in degree), measured counter-clockwise from the north; (7): noise per channel in mJy beam^{-1} ; (8): pixel size in arcsec; (9): velocity resolution in km s^{-1}

which well-determined estimates for V_{max} exist. For a thorough description of the comparison sample, the reader is referred to McGaugh (2005) and references therein.

The chapter is organized as follows: in Section 4.2 we describe the observations and the data reduction, which is followed by a description of the different methods in estimating V_{max} in Section 4.3. We comment the individual galaxies in Section 4.4, and present further analysis and our results in Section 4.5. We summarize our results and give our conclusions in Section 4.6. The Appendix 4.A contains moment maps, position-velocity diagrams and channel maps of our sample galaxies.

4.2 The data

In this section, we describe the observational set-up, the basic data reduction from the raw data to the data cubes, and the moment map creation and other “post-reduction” steps.

Our sample was selected from the larger sample of Schombert et al. (1997), which is one of the largest samples of extreme field dwarf galaxies for which both line width measurements and HI masses (Eder & Schombert 2000), as well as optical photometry (Pildis et al. 1997) exist. The galaxies were chosen to be relatively nearby ($v_{\text{hel}} < 1400 \text{ km s}^{-1}$), have suitable optical inclinations ($45 \leq i_{\text{opt}} \leq 75$), and to have V- and I-band photometry available.

4.2.1 Observations

Observations were carried out at the Westerbork Synthesis Radio Telescope (WSRT) in maxi-short configuration, in the 21-cm line of neutral hydrogen. We use both polarizations and sample 1024

channels with a bandwidth of 10 MHz or 20 MHz (corresponding to velocity resolutions of 2.10 or 4.12 km s⁻¹). The sample integration time was set to 60 seconds. Further observational details are summarized in Table 4.1.

4.2.2 Data reduction

Here, we describe the steps used to obtain the data cubes from the raw *uv*-data. The calibration and data reduction of the data is performed using standard routines in MIRIAD¹. We use the task UVFLAG to flag data affected by shadowing of the dishes and inspect the *uv*-data by eye to remove data points showing any kind of interference (task TVFLAG). The data are calibrated using one of the standard primary calibrators used at the WSRT (3C48, 3C147, 3C286, J2052+362). The primary calibrators are also used for the bandpass and gain corrections (tasks MFCAL, GPCOPY).

After determining the line-free channels in the data sets (i.e., the channels containing only continuum emission), we fit the continuum with second order polynomials using the task UVLIN and average the continuum into one 2D map (the so-called *channel0* map). This map is then self-calibrated. The self-calibration consists of four steps:

1. Firstly, the task INVERT is used to create a dirty continuum map of the *uv*-data. We set the sidelobe suppression area to the size of the field being mapped (i.e., to uniform weighting).
2. This dirty map is cleaned with the task CLEAN.
3. Using the task RESTOR, we check if the cleaned map looks satisfactory.
4. Finally, we perform the self-calibration of the phases with the task SELFCAL, initially using a calibration interval of five minutes, but decreasing this down to the original data interval of one minute for the last iterations.

These four tasks are called iteratively, in order to improve the gain solutions, always using the result from the previous iteration as a starting point for the next iteration. The stop condition for the CLEAN task has to be adjusted between the iterations. Running CLEAN for the first time, we stop cleaning when the first negative component is encountered. During the next few major iterations (i.e., cycles through steps Nos. 1 - 4), we slowly increase the number of minor iterations (i.e., the iteration within CLEAN) from 1 000 to 10 000. Once this is done, we run a few more major iterations, gradually decreasing the cutoff condition from three times the noise to one time the noise. After the map is sufficiently cleaned, we go once more through steps 1 - 4, this time performing both a phase and an amplitude self-calibration with SELFCAL.

The gain solutions are then copied to the line data using the task GPCOPY. Afterwards, we subtract the continuum emission from the line data, again using UVLIN with second order polynomials. Having done this, we create the image cube using the task INVERT. We use the robust weighting scheme (Briggs 1995) with a robust parameter of *robust=0* for all galaxies. In a last step, the tasks CLEAN and RESTOR are used to clean and restore the image cube, using a cutoff level of $\sim 1\sigma$ for the CLEAN task. For a list of the beam sizes and noise levels, see Table 4.1.

We additionally created Hanning smoothed data cubes, which were used for the creation of the HI profiles and the derivation of the velocity widths.

¹Multichannel Image Reconstruction, Image Analysis and Display (Sault et al. 1995)

4.2.3 Post-reduction

In this section, the steps undertaken to create moment maps from the data cubes are described.

Using the GIPSY² task MOMENTS, we create 0th, 1st, and 2nd moment maps of all galaxies (i.e., the HI total intensity map, the velocity field, and a map of the velocity dispersion). In order to isolate significant signal, we smoothed the data cubes to twice the original resolution and only retain pixels with values > 2.5 times the (smoothed) rms. Spurious pixels were then blotted by hand. This smoothed and blotted data cube was used as a mask for the original data cube. Once this is done, we determine the number of channels with significant emission for each pixel of the unsmoothed data cube and create a map containing the signal-to-noise (S/N) of each pixel. Using this map, we determine which average flux in the 0th moment map corresponds to a S/N = 3, and clip all moment maps using this flux limit. Channel maps and moment maps are presented in the Appendix 4.A.

4.3 Estimating the maximum rotation velocity

In order to construct a (baryonic) Tully-Fisher relation, one needs to estimate the maximum rotation velocity (V_{\max}) of a galaxy. There are several ways in which this can be done, which are described below in increasing order of preference.

4.3.1 HI velocity profile

The simplest way is to use the width of the HI velocity profile at the 20 (50) percent level of the maximum intensity, the so-called W_{20} (W_{50}). The advantage in using the profile width is that it is easy to measure and can be derived even using low resolution data. The drawback is that one can not distinguish rotation and turbulence. This uncertainty matters little for the overall rotation of large, fast rotating spiral galaxies. However, as one goes to smaller and more slowly rotating galaxies, turbulent motions will result in a significant broadening of the HI profiles (cf. Verheijen 1997). In our analysis, we use the velocity profiles from the Hanning smoothed data cubes and correct them for instrumental broadening and turbulent motion. The corrections applied are addressed and discussed more fully in Section 4.5.2.

4.3.2 Major axis position-velocity diagram

A more sophisticated way to derive V_{\max} is to make use of the major axis position-velocity (pV) diagram. For a galaxy with a flat rotation curve, the major axis pV -diagram has a pronounced s-shape (see, e.g., Fig. 4.10 in the Appendix 4.A). Using the GIPSY task XGAUPROF, we fit Gaussians to the velocity profiles at the flat parts of the rotation curve. The maximum rotation velocity is then calculated by subtracting the line-of-sight velocity of the approaching side from the one of the receding side, dividing it by two, and correcting for inclination:

$$V_{pv} = \frac{V_{\text{receding}} - V_{\text{approaching}}}{2 \sin(i)} \quad (4.1)$$

As the use of the pV -diagram gives a better approximation to the maximum rotation velocity than the W_{20}, W_{50} values do (Verheijen 2001), we will prefer the former where possible.

²GIPSY, the Groningen Image Processing SYstem (van der Hulst et al. 1992)

4.3.3 Tilted-ring fit with ROTCUR

The most sophisticated method presented in this chapter is the tilted-ring fit, in which the kinematics of a galaxy are described using a set of concentric rings of a width Δr . Each of these rings can have its own center position (x_0, y_0) , systemic velocity v_{SYS} , rotation velocity v_{ROT} , inclination i , and position angle PA. However, the galaxy has to have a convenient inclination of $i \gtrsim 40^\circ$ (Begeman 1987, 1989), and a well-resolved velocity field. For the galaxies in our sample which meet these two criteria, we derive rotation curves using the GIPSY task ROTCUR. This algorithm assumes that the gas moves on circular orbits. The line-of-sight velocity can then be expressed as

$$V(x, y) = V_{\text{sys}} + V_{\text{rot}}(r) \sin(i) \cos(\theta). \quad (4.2)$$

Here, θ is the azimuthal distance from the major axis in the plane of the galaxy and is linked to the position angle of the galaxy by

$$\cos(\theta) = \frac{-(x - x_0) \sin(\text{PA}) + (y - y_0) \cos(\text{PA})}{r} \quad (4.3)$$

and

$$\sin(\theta) = \frac{-(x - x_0) \cos(\text{PA}) - (y - y_0) \sin(\text{PA})}{r \cos(i)}. \quad (4.4)$$

The PA is measured counter-clockwise from the north to the major axis of the receding side of the galaxy.

As positions along the major axis of a galaxy carry more rotational information as positions near the minor axis, we weight the individual data points by $|\cos(\theta)|$. The derivation of a rotation curve is generally an iterative process involving the consecutive fixing of parameters. Following is a general description of the procedure applied here. In order to get good initial estimates for i , PA, and the center position, we fit isophotes at varying intensity levels to the HI total intensity maps with the GIPSY task ELLFIT, taking care that the results are not affected by small-scale structures. As initial estimates for v_{SYS} and v_{ROT} , we use the central velocity of the W_{50} profile and $\frac{1}{2} W_{50}$, respectively.

In a first ROTCUR run, we determine the systemic velocity by keeping all parameters except v_{SYS} (and v_{ROT}) fixed. In a second fit with ROTCUR, we derive the position of the dynamical center leaving only x_0 and y_0 unconstrained. In a third fit, we determine the position angle by running ROTCUR with PA and i as free parameters. As we sample the rotation curves in most cases with relatively few tilted-rings (~ 10), we approximate the fitted values either by a constant or linearly changing PA. Once the PA is modeled in such a way, we run ROTCUR once again with only i as free parameter and derive the inclination of the galaxy. We do not model any radial trends for the inclination. In a last fit with ROTCUR, we determine the rotation curve by keeping all parameters except v_{ROT} fixed to their best determined values. The maximum rotation velocity, derived in such a way, will be referred to as V_{vf} hereafter.

TABLE 4.2: Derived parameters for the profile width sub-sample, i.e., the galaxies having neither a V_{pv} , nor a V_{vf} , but only W_{20} and W_{50} .

ID	α_{2000} (h m s)	δ_{2000} ($^{\circ}$ ' ")	V_{sys} km s^{-1}	D Mpc	M_V mag	(V-I)	M_{HI} $10^7 M_{\odot}$	W_{20} km s^{-1}	W_{50} km s^{-1}	$W_{20, \text{turb}}$ km s^{-1}	$W_{50, \text{turb}}$ km s^{-1}	i $^{\circ}$
(1)	(2)	(3)	(4)	(5)	(6)	(7)	(8)	(9)	(10)	(11)	(12)	(13)
D572-5	11 48 16.4	+18 38 33	994	14.6	-14.56	0.52	8.55	77	62	68	55	50 ^a
D575-1	12 51 46.1	+21 44 07	600	10.0	-14.22	0.70	3.76	38	24	30	18	53
D575-5	12 55 41.4	+19 12 34	437	7.7	-13.21	0.44	4.27	28	19	16	10	50
D640-13	10 56 13.9	+12 00 41	958	13.4	-14.36	0.55	4.53	38	25	30	18	48 ^a
D646-7	12 58 40.4	+14 13 03	233	2.1 ^b	-12.52	0.84	0.37	35	23	26	16	55 ^a

^aoptical inclination from Pildis et al. (1997)^bdistance as given in Karachentsev et al. (2003)

NOTES: (1): galaxy identifier; (2, 3): central position taken from NED; (4): systemic velocity derived from the central velocity of the W_{50} profile; (5): distance in Mpc. If no reference is given, the distance is based on V_{sys} (column 4) and a Hubble flow using $H_0 = 75 \text{ km s}^{-1} \text{ Mpc}^{-1}$, including the correction for Virgo-centric infall (Mould et al. 2000); (6): absolute V-band magnitude as given in Pildis et al. (1997), corrected to our distance estimates; (7): V-I color from Pildis et al. (1997); (8): total HI mass (in units of $10^7 M_{\odot}$); (9): uncorrected width of the HI profile at the 20 percent level of the maximum intensity. The values listed here for W_{20} are derived using the Hanning smoothed data cube; (10): like column 9, but for the W_{50} profile; (11): width of the W_{20} profile, corrected for the finite velocity resolution, and turbulent motion of the HI gas; (12): as column 11, but for the W_{50} profile; (13): adopted inclination angle. The velocity widths in Cols. (9) - (12) are not corrected for inclination effects.

TABLE 4.3: Derived parameters for the rotation curve sub-sample, i.e., the galaxies having not only the velocity width as estimate of V_{max} , but at least one additional, independent estimate (i.e., V_{pv} or V_{vf}).

ID	α_{2000} (h m s)	δ_{2000} ($^{\circ}$ ' ")	V_{sys} km s^{-1}	D Mpc	M_V mag	(V-I)	M_{HI} $10^7 M_{\odot}$	W_{20} km s^{-1}	W_{50} km s^{-1}	$W_{20, \text{turb}}$ km s^{-1}	$W_{50, \text{turb}}$ km s^{-1}	i $^{\circ}$	$\langle PA \rangle$ $^{\circ}$	V_{vf} km s^{-1}	V_{pv} km s^{-1}
(1)	(2)	(3)	(4)	(5)	(6)	(7)	(8)	(9)	(10)	(11)	(12)	(13)	(14)	(15)	(16)
D500-2*	10 31 43.0	+25 18 33	1259	17.9	-16.38	0.42	87.08	135	120	119	105	57 ± 6	345	68	68
D500-3	10 05 59.5	+23 52 04	1327	18.5	-15.74	0.31	6.58	96	83	84	72	$55^a \pm 6$	45
D512-2	14 33 20.2	+26 59 54	840	14.1	-15.22	0.80	6.96	88	74	78	65	56 ± 10	40	35	37
D564-8*	09 02 54.0	+20 04 28	478	6.5	-12.64	0.93	1.58	62	48	54	42	63 ± 7	13	25	29
D575-2*	12 52 21.9	+21 37 46	774	12.2	-15.15	0.78	31.51	146	119	129	104	57 ± 5	220	74	...
D631-7*	07 57 01.8	+14 23 27	311	5.5 ^b	-14.50	0.55	14.68	113	89	100	78	59 ± 3	324	58	53

^aoptical inclination from Pildis et al. (1997)^bdistance as given in Karachentsev et al. (2003)

NOTES: Cols. (1) to (12) contain mostly the same information as the ones in Table 4.2, with the only exception that for the starred galaxies, the center position and V_{sys} were derived kinematically; (13) inclination angle (optical inclination for D500-3, kinematic inclination otherwise). The uncertainties given for the kinematic inclination angles represent the scatter of the values of the individual tilted-rings. For D500-3, the given uncertainty is the average uncertainty of the kinematic inclination estimates; (14) average position angle of the rotation curve analysis, measured counter-clockwise from north to the receding side of the galaxy; (15) maximum rotation velocity from the tilted-ring analysis of the velocity field, corrected for inclination effects; (16) maximum rotation velocity from the position-velocity diagram, corrected for inclination effects.

4.4 Comments on individual galaxies

In this section, we present our results for the individual galaxies. Unless mentioned otherwise, the distances given in the following sections are calculated by correcting the systemic velocities of the galaxies for Virgo infall (following the formalism presented in Mould et al. 2000), and assuming a Hubble flow with a Hubble constant of $H_0 = 75 \text{ km s}^{-1} \text{ Mpc}^{-1}$.

We split our sample into two sub-samples (the ‘‘profile width’’ sub-sample and the ‘‘rotation curve’’ sub-sample). The profile width sub-sample contains the galaxies for which we have to rely on the profile width as an indicator for V_{max} as it was impossible to derive a maximum rotation velocity from either the tilted-ring analysis (i.e., V_{vf}) or from the position-velocity diagram (i.e., V_{pv}). Their properties are summarized in Table 4.2. The rotation curve sub-sample contains the galaxies, for which we were able to derive V_{vf} and/or V_{pv} (in addition to W_{20} and W_{50}). Their properties are given in Table 4.3. In the Appendix 4.A, we show for all galaxies presented in this chapter a summary panel consisting of moment maps, major and minor axis position-velocity diagrams and the global HI profile. We additionally show channel maps for the galaxies of the rotation curve sub-sample.

We also observed D565-5. The WSRT observations do not detect any emission at the position of D565-5. We do, however, see strong emission from the nearby galaxy NGC 2903 at the edge of the primary beam. The agreement of the apparent velocity of this emission with that of the Schombert et al. (1997) detection suggests that the latter detection was simply NGC 2903 emission that was picked up with the larger single-dish beam.

4.4.1 D500-2 (Data presented in Figs. 4.10 and 4.21)

D500-2 is also known as UGC 05716 and is classified as an Sm galaxy for which we assume a distance of 17.9 Mpc. The global HI profile of D500-2 (cf. Fig. 4.10) shows the double-horned profile typical for spiral galaxies, and its velocity field indicates that D500-2 is clearly dominated by rotation. We fit ellipses at a few representative intensity levels using the GIPSY task ELLFIT. The inclination of the HI disk, as obtained with ELLFIT and corrected for the beam, is $i_{HI} \sim 57^\circ$. The parameters from our ellipse-isophote fits are used as initial estimates for the tilted-ring analysis with ROTCUR. The spacing of the tilted-rings is set to $11''$. The systemic velocity is derived in the first fit with ROTCUR and shows only small radial variation. Its mean value is $V_{\text{sys}} \approx 1259 \text{ km s}^{-1}$, and is in excellent agreement with the central velocity of the W_{50} profile (1258.6 km s^{-1}). Fixing the systemic velocity, we derive the dynamical center in a new ROTCUR fit by averaging the x_0, y_0 values over the entire radial range. The resulting central position (cf. Table 4.3) is in good agreement with the optical center from NED and with that from our ellipse fits with ELLFIT. Keeping the center position fixed for the subsequent ROTCUR runs, we derive the PA and inclination angle. The position angle shows a linear decrease from 350° in the center to 340° in the outer parts.

The inclination is then determined in an additional ROTCUR fit by averaging the inclination values for $r \geq 35''$, i.e., by excluding the three deviant data points in the inner part of D500-2. The resulting kinematic inclination is $i_{\text{kin}} \sim 57^\circ \pm 6^\circ$, which agrees very well with the (beam corrected) inclination of the HI disk. In a last fit with ROTCUR, we derive the rotation velocity by keeping all parameters except VROT fixed to their previously derived values. After a gentle inner rise, the rotation curve of D500-2 reaches a flat part at a rotation velocity of $V_{vf} \sim 68 \text{ km s}^{-1}$. The rotation curve, as well as the radial distributions for PA and i_{kin} are shown in Fig. 4.1. The maximum rotation velocity from the pV -diagram is $V_{pv} \sim 68 \text{ km s}^{-1}$.

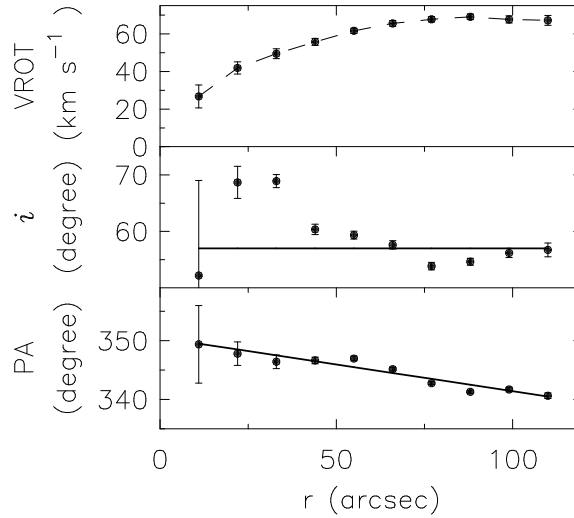


FIG. 4.1: Tilted-ring analysis of D500-2. From top to bottom, the radial distributions of the rotation velocity, the inclination angle, and the position angle are shown. The data points in the center and bottom panel indicate the values derived for i and PA as free parameters. The solid lines indicate the values adopted to derive the rotation curve shown in the top panel.

4.4.2 D500-3 (Data presented in Figs. 4.11 and 4.22)

D500-3 is a dwarf irregular (dI) at a distance of 18.5 Mpc. Its velocity field (cf. Fig. 4.11) indicates solid-body rotation throughout the entire disk, and the major axis pV -diagram also shows only a linearly rising rotation curve. We fit isophotes to different intensity levels to derive, e.g., the inclination of the HI disk ($i_{HI} \sim 42^\circ$). This value is somewhat smaller than the optical inclination of $i_{opt} \sim 55^\circ$ as given in Pildis et al. (1997). Due to the large beam size, we consider the optical inclination superior to the HI inclination and use it in our further analysis. Because of the solid-body rotation, and also due to the few resolution elements, it is not possible to derive a well-determined rotation curve with ROTCUR. We are, however, able to get an estimate for the maximum rotation velocity by using the position-velocity diagram ($V_{pv} \sim 45 \text{ km s}^{-1}$).

4.4.3 D512-2 (Data presented in Figs. 4.12 and 4.23)

D512-2 is a galaxy of Hubble type Sm and we assume a distance of 14.1 Mpc. The HI profile has a fairly low signal-to-noise. The velocity field of D512-2 shows signs of solid-body rotation in its inner parts. We use ELLFIT to fit ellipses at a few representative intensity levels and derive an inclination of the HI disk of $i_{HI} \sim 48^\circ$ (corrected for the beam size). Because the apparent size of D512-2 is small, we do not fit the center position or the systemic velocity with ROTCUR. For the former, we adopt the center estimate from ELLFIT, which is in good agreement with the optical center from NED. For the latter, we use the central velocity of the W_{50} profile. Keeping the center and the systemic velocity fixed, we derive the position angle of D512-2 by averaging the values for all tilted-rings with $r > 0''$, while choosing the width of the tilted-rings to be $13''$. The resulting PA (40°) is then kept fixed for a subsequent ROTCUR fit to estimate i . Averaging the inclination values over all tilted-rings results in a kinematic inclination of $i_{kin} \sim 56^\circ \pm 10^\circ$, which is consistent with the values discussed above. Using the kinematic inclination, we determine the rotation curve in a last ROTCUR run leaving only VROT unconstrained. The rotation curve (cf. Fig. 4.2) confirms what was already suggested by the velocity field: a solid-body rotation in the inner parts and a flat part in the outer regions. The rotation velocity

of the flat part of the rotation curve is $V_{vf} \sim 35 \text{ km s}^{-1}$. Although the pV -diagram shows no plateaus, we estimate the (inclination corrected) maximum rotation velocity to be $V_{pv} \sim 37 \text{ km s}^{-1}$.

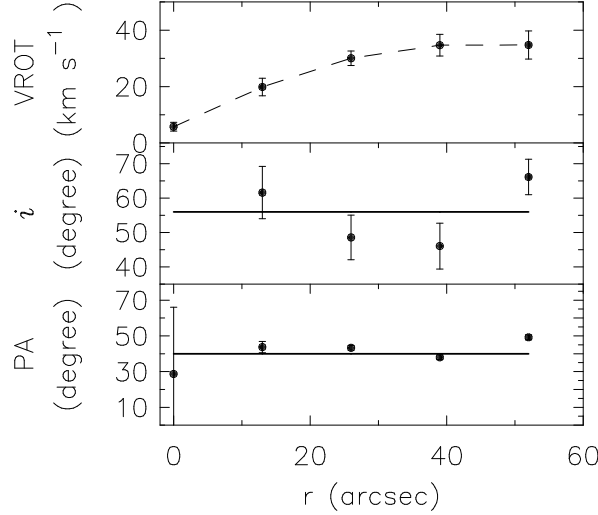


FIG. 4.2: Tilted-ring analysis of D512-2. The layout is identical to that of Fig. 4.1.

4.4.4 D564-8 (Data presented in Figs. 4.13 and 4.24)

For the dwarf irregular D564-8, we assume a distance of 6.5 Mpc. The global HI profile of D564-8 is asymmetric with its peak shifted to the receding side of the galaxy. The asymmetry of the global HI profile can be traced also in the pV -diagram. The pV -diagram of D564-8 represents a mixture between the s-shape typical for spiral galaxies having a flat rotation curve and the linearly increasing position-velocity diagram usually seen for dwarf galaxies. The maximum rotation velocity, obtained from the pV -diagram is, $V_{pv} \sim 29 \text{ km s}^{-1}$. Analogous to the other galaxies, we use ELLFIT to derive initial estimates for our tilted-ring fit with ROTCUR. For the rotation curve analysis, we set the width of the tilted-rings to $12''$. In the first ROTCUR fit, we derive the systemic velocity to $V_{\text{sys}} \approx 478 \text{ km s}^{-1}$, which coincides very well with the central velocity of the W_{50} profile. In a subsequent fit, we derive the dynamical center by averaging the values for x_0 and y_0 over the entire radial range. The resulting center (cf. Table 4.3) agrees to within a few arcseconds with the optical center from NED. In two consecutive fits with ROTCUR, we derive the PA and inclination by averaging the individual measurements over the radial range, while excluding the innermost (deviant) data point. The resulting inclination ($i_{\text{kin}} \sim 63^\circ \pm 7^\circ$) is larger than both the one from the HI disk ($i_{\text{HI}} \sim 50^\circ$), and the optical inclination ($i_{\text{opt}} \sim 35^\circ$, Pildis et al. 1997). However, an inclination of 50° , or even 35° can be ruled out by our kinematic data. Keeping all parameters except the rotation velocity fixed to their best estimates, we derive the rotation curve of D564-8. The maximum rotation velocity is $V_{vf} \sim 25 \text{ km s}^{-1}$ (see Fig. 4.3).

4.4.5 D572-5 (Data presented in Fig. 4.14)

D572-5 is an irregular galaxy at an assumed distance of 14.6 Mpc. Our HI data of this galaxy is barely resolved (see, e.g., the moment maps in Fig. 4.14), which severely affects the apparent value of the HI inclination. For comparison, the optical inclination as given by Pildis et al. (1997) is $i_{\text{opt}} \sim 50^\circ$, whereas the one of the HI disk is $i_{\text{HI}} \sim 65^\circ$ (uncorrected) or $i_{\text{HI}} \sim 61^\circ$ (corrected for the size of the beam). Therefore, we use the optical inclination for the further analysis. The low resolution causes the

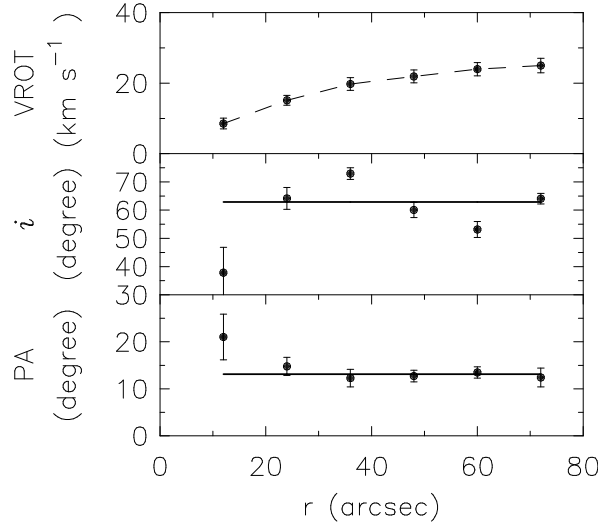


FIG. 4.3: Tilted-ring analysis of D564-8. The layout is identical to that of Fig. 4.1.

large velocity range in the minor axis pV -diagram. Given these problems, we refrain from deriving a rotation curve or a V_{pv} from the major axis position-velocity diagram. The only usable indicators for the maximum rotation velocity are W_{20} and W_{50} .

4.4.6 D575-1 (Data presented in Fig. 4.15)

D575-1, also known as IC 3810, is classified as an Sm/Irr galaxy. We assume a distance of 10.0 Mpc. Its global HI profile is well described by a Gaussian. The 1st moment map and the position-velocity diagrams show only a small velocity range and it was not possible to estimate either V_{vf} or V_{pv} . The inclination of the HI disk (derived using ELLFIT and corrected for the beam size) is $i_{HI} \sim 53^\circ$ and in reasonable agreement with the optical inclination ($i_{opt} \sim 61^\circ$) from Pildis et al. (1997).

4.4.7 D575-2 (Data presented in Figs. 4.16 and 4.25)

D575-2, or UGC 8011, is a galaxy of the Hubble type Im, for whose distance we assume 12.2 Mpc. It was not possible to estimate V_{pv} from the position-velocity diagram. Although the iso-velocity contours in the first moment map indicate a flat rotation curve in the outer parts, the global HI profile of D575-2 lacks the double-horned profile often seen for such galaxies. The galaxy is kinematically lopsided, which can be seen in the differences in the velocity contours between the approaching and receding side. We determine the inclination of the HI disk with ELLFIT to be $i_{HI} \sim 52^\circ$, which is somewhat less inclined than what Pildis et al. (1997) found optically ($i_{opt} \sim 63^\circ$). Using the results from our isophote fits with ELLFIT as initial estimates for a tilted-ring analysis and a width of the tilted-rings of $14''$, we determine the systemic velocity ($V_{sys} \sim 774 \text{ km s}^{-1}$). This agrees to within 2 km s^{-1} with the center of the W_{50} profile. Fixing the systemic velocity again, we estimate the dynamical center of D575-2 to the position listed in Table 4.3, which is in excellent agreement with the optical center as given by NED. Leaving PA and i unconstrained, we find a gradual decrease of the position angle from $\sim 230^\circ$ in the inner parts to $\sim 210^\circ$ in the outskirts of D575-2. Fixing the PA to these values, we derive the inclination by averaging over all data points with $r > 0''$. The resulting inclination ($i_{kin} \sim 57^\circ \pm 5^\circ$) is halfway between the optical inclination and the one from the HI disk. Keeping the inclination fixed

to the kinematic estimate, we derive the rotation curve of D575-2 (see Fig. 4.4). After a linear increase in the inner parts of the galaxy, the rotation velocity reaches a flat part at around 74 km s^{-1} .

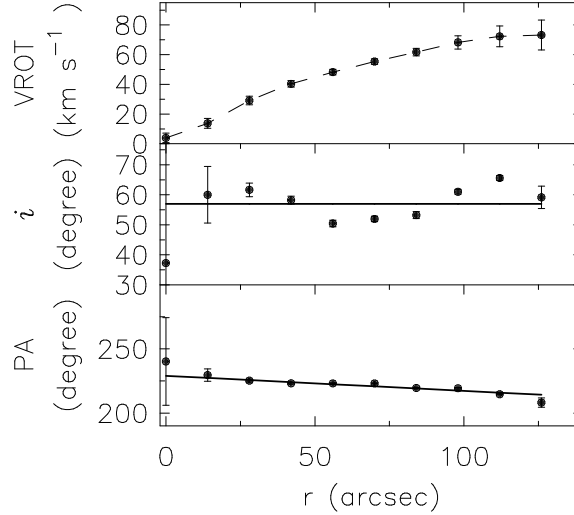


FIG. 4.4: Tilted-ring analysis of D575-2. The layout is identical to that of Fig. 4.1.

4.4.8 D575-5 (Data presented in Fig. 4.17)

D575-5 is classified as a dwarf irregular at an assumed distance of 7.7 Mpc. Its global HI profile has a Gaussian shape and its W_{50} is the smallest of our sample ($W_{50} \sim 19 \text{ km s}^{-1}$ for the Hanning smoothed data cube). Pildis et al. (1997) estimated the optical inclination to $i_{\text{opt}} \sim 66^\circ$, which is somewhat higher than the (beam corrected) inclination of the HI disk, which we derive to $i_{\text{HI}} \sim 50^\circ$. An inclination of that order is usually considered as being optimal for a dynamical analysis. However, neither the 1st moment map, nor the major axis pV -diagram show clear signs of rotation. The minor axis pV -diagram shows even more emission than the major axis one. It was therefore not possible to estimate a maximum rotation velocity from either the velocity field, or from the major-axis position-velocity diagram. The 2nd moment map shows velocity dispersions of 6-8 km s^{-1} throughout the entire disk. Given all these indications, we can only assume that D575-5 is rather face-on and that a relatively large fraction of the profile width is caused by turbulence. For the inclination-correction of the W_{20} and W_{50} , we use the inclination of the HI disk as the appearance of D575-5 excludes the optical inclination of $i_{\text{opt}} \sim 66^\circ$.

4.4.9 D631-7 (Data presented in Figs. 4.18 and 4.26)

D631-7 is also known as UGC 4115 and is classified as a dwarf irregular. Karachentsev et al. (2003) estimated its distance to 5.5 Mpc using the luminosity of the tip of the red giant branch stars. The global HI profile of D631-7 is single-peaked and its velocity field is well-resolved and shows clear signs of rotation. The major axis pV -diagram shows the indication of a flat rotation curve in the outer parts of the galaxy, and it is possible to estimate a maximum rotation velocity ($V_{pv} \sim 53 \text{ km s}^{-1}$) using XGAUPROF. The inclination of the HI disk is obtained with ELLFIT ($i_{\text{HI}} \sim 57^\circ$) and the ELLFIT results are used as initial estimates for the rotation curve derivation with ROTCUR. The width of the tilted-rings in our analysis with ROTCUR is set to $12''$. In the first tilted-ring fit, we derive the systemic velocity to $V_{\text{sys}} \sim 311 \text{ km s}^{-1}$, which agrees very well with the center of the W_{50} profile. The

dynamical center is fitted in the second run with ROTCUR. The resulting center position is given in Table 4.3, and agrees to within $1''$ with the optical center as given by NED. The PA of D631-7 is obtained in a subsequent fit with ROTCUR and shows a gradual increase from $\sim 318^\circ$ in the inner parts to $\sim 330^\circ$ in the outer parts. Fixing the PA to these values, we derive the kinematic inclination of D631-7 to $i_{\text{kin}} \sim 59^\circ \pm 3^\circ$ by averaging the individual tilted-ring values for $50'' \leq r \leq 150''$. This is in good agreement with the inclination of the HI disk ($i_{\text{HI}} \sim 57^\circ$), and still in reasonable agreement with the optical inclination ($i_{\text{opt}} \sim 66^\circ$, derived by Pildis et al. 1997). Keeping all parameters except VROT fixed, we determine the rotation curve of D631-7 (see Fig. 4.5). It shows the typical solid-body rotation in the inner parts, but reaches a flat part at $V_{\text{vf}} \sim 58 \text{ km s}^{-1}$.

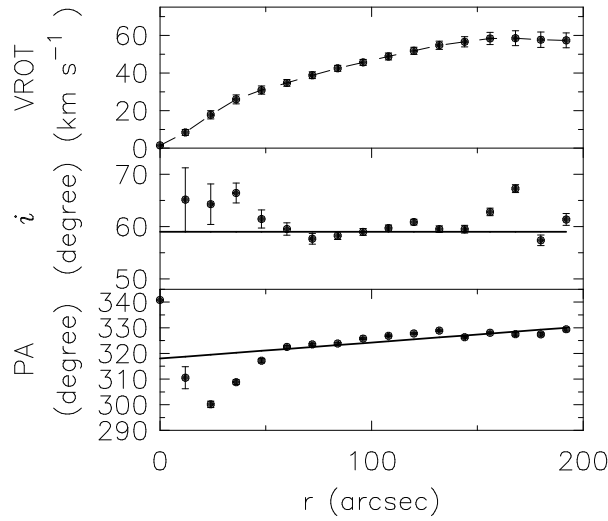


FIG. 4.5: Tilted-ring analysis of D631-7. The layout is identical to that of Fig. 4.1.

4.4.10 D640-13 (Data presented in Fig. 4.19)

D640-13 is an Im/Sm type galaxy for whose distance we adopt 13.4 Mpc. Its global HI profile has a Gaussian shape. Comparing the size and the shape of the beam with that of the moment maps of the galaxy shows that D640-13 is barely resolved. This heavily affects the inclination of the HI disk ($i_{\text{HI}} \sim 71^\circ$) which is much higher than the optical inclination ($i_{\text{opt}} \sim 48^\circ$) by Pildis et al. (1997). We therefore use the optical inclination for the further analysis. As neither the position-velocity diagrams, nor the first moment map show a clear sign of rotation, only the widths of the W_{20} and W_{50} profiles remain as a proxy for the maximum rotation velocity, which we correct using the optical inclination.

4.4.11 D646-7 (Data presented in Fig. 4.20)

D646-7 (or UGC 8091) is classified as an irregular dwarf galaxy for which Karachentsev et al. (2003) estimated a distance of 2.1 Mpc, using the tip of the red giant branch. The global HI profile of D646-7 has a clear Gaussian shape. The galaxy lacks clear signs of rotation, either in the first moment map, or in the major-axis position-velocity diagram. Thus, only W_{20} and W_{50} remain as indicators for the maximum rotation velocity. The optical inclination of D646-7, derived by Pildis et al. (1997), is $i_{\text{opt}} \sim 55^\circ$, which is in good agreement with the (uncorrected) inclination of the HI disk ($i_{\text{HI}} \sim 51^\circ$). However, given that the galaxy is not well resolved, we use the optical inclination for the subsequent analysis.

4.5 Analysis

In the previous section, we have derived several estimates for the maximum rotation velocities of the galaxies in our sample. Before using them to construct a BTF, we discuss our choices for the stellar mass-to-light ratios (Υ_*), describe the corrections applied to the line width measurements and estimate the uncertainties of our observables. After that, we present and discuss the baryonic Tully-Fisher relation for our sample.

4.5.1 The choice of the stellar mass-to-light ratio Υ_*

One of the largest contributors to the vertical scatter in the (baryonic) Tully-Fisher relation is the assumed stellar mass-to-light ratio (Υ_*) and its uncertainty. Fortunately, the effect of the chosen Υ_* becomes less important when dealing with low-mass galaxies, as their stellar mass generally contributes less to the total baryonic mass than the gas mass does. The Υ_* values used here are derived on the basis of two different population synthesis models using two different Initial Mass Functions (IMFs). The first model is from Bell & de Jong (2001) and uses a scaled Salpeter IMF (Salpeter 1955). The second population synthesis model discussed here uses a Kroupa IMF (Kroupa 1998) and is taken from Portinari et al. (2004). Figure 4.6 shows the derived stellar (*I*-band) mass-to-light ratios for the two population models.

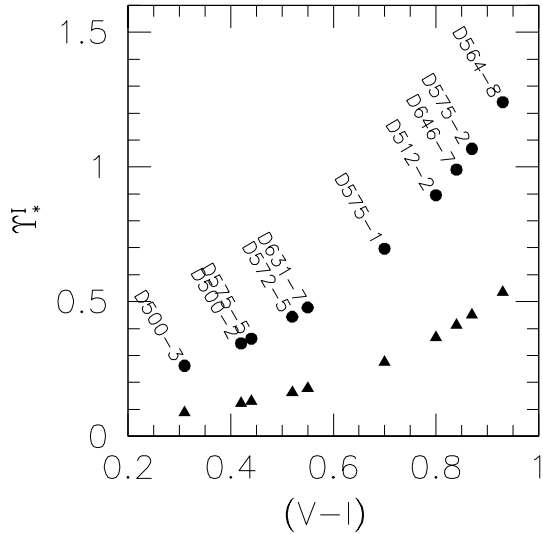


FIG. 4.6: Stellar *I*-band mass-to-light ratio (Υ_*) vs. $(V-I)$ color for two different population synthesis models. The circles are based on the models from Bell & de Jong (2001) with a scaled Salpeter IMF, the triangles on Portinari et al. (2004) models with a Kroupa IMF. Note that D631-7 and D640-7 have the same color, and their values for Υ_* are thus identical; therefore, we do not show the data point (and label) of D640-13 for clarity reasons.

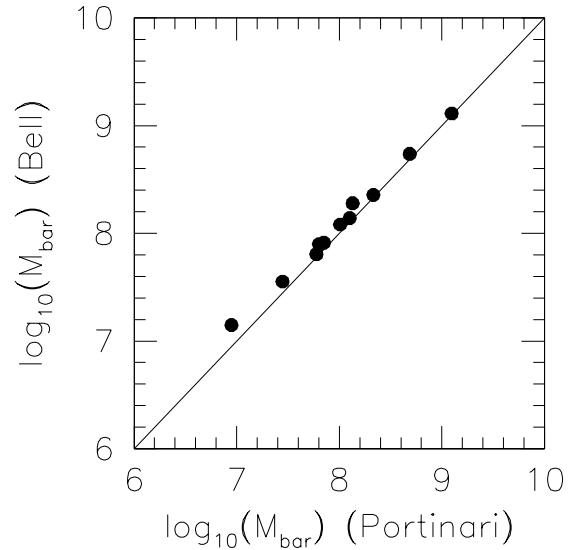


FIG. 4.7: The baryonic mass where Υ_* from the models of Bell & de Jong (2001) was used to determine the stellar mass vs. the baryonic mass where Υ_* from the models of Portinari et al. (2004) has been used. The solid line indicates the line of unity.

It is immediately apparent that the Υ_* from Bell & de Jong (2001) are consistently larger than the ones from Portinari et al. (2004). Although this difference can amount to a factor close to three, the impact on the baryonic mass (i.e., the sum of the stellar mass and the gas mass) is rather small, as

TABLE 4.4: Stellar Υ_* assuming different stellar population synthesis models.

ID	Υ_*^I (Bell)	Υ_*^I (Portinari)	$\langle \Upsilon_*^I \rangle$
(1)	(2)	(3)	(4)
D500-2	0.35	0.12	0.24 ± 0.12
D500-3	0.26	0.09	0.18 ± 0.09
D512-2	0.90	0.37	0.64 ± 0.27
D564-8	1.24	0.54	0.89 ± 0.35
D572-5	0.44	0.16	0.30 ± 0.14
D575-1	0.70	0.28	0.49 ± 0.21
D575-2	1.07	0.45	0.76 ± 0.31
D575-5	0.36	0.13	0.25 ± 0.12
D631-7	0.48	0.18	0.33 ± 0.15
D640-13	0.48	0.18	0.33 ± 0.15
D646-7	0.99	0.41	0.70 ± 0.29

NOTES: (1): galaxy identifier; (2): stellar I -band mass-to-light ratio based on Bell & de Jong (2001); (3): stellar I -band mass-to-light ratio based on Portinari et al. (2004); (4): average (I -band) Υ_* between columns (2) and (3). The subsequent analysis is based on these mass-to-light ratios. For the uncertainty of Υ_* , we assume half the difference between the mass-to-light ratios of the two population models.

can be seen in Fig. 4.7, where we plot the baryonic mass based on Υ_* from the Bell & de Jong (2001) models *vs.* the baryonic mass derived using the Portinari et al. (2004) models. The data points are usually very close to the line of unity. In the subsequent analysis we will adopt the average values of the two models. The mass-to-light ratios are listed in Table 4.4.

4.5.2 Line width corrections

The V_{\max} estimates from either the major-axis pV -diagram (V_{pv}) or from the tilted-ring analysis of the velocity field (V_{vf}) only need to be corrected for inclination effects. The estimates derived using the profile widths W_{20} , W_{50} , however, need additional corrections. To correct for the instrumental resolution, which results in a broadening of the measured profiles, we use the approach of Verheijen (1997), who assumes a turbulent motion of the gas with a velocity dispersion of 10 km s^{-1} :

$$W_x = W_x^{\text{obs}} - C_x \cdot \left[\sqrt{1 + \left(\frac{R}{23.5} \right)^2} - 1 \right], \quad (4.5)$$

where the subscript x refers to the chosen profile width (i.e., $x = 20$ for W_{20} and $x = 50$ for W_{50}), R is the instrumental resolution in km s^{-1} (cf. Col. (9) in Table 4.1), and C_x is a constant factor, which is $C_{20} = 35.8$ for the W_{20} profile and $C_{50} = 23.5$ for the W_{50} profile. The superscript *obs* in W_x^{obs} denotes the observed profile width (given in Cols. (9) and (10) of Tables 4.2 and 4.3).

Additionally to the broadening due to finite resolution, we correct the velocity widths for broadening due to turbulent motion of the neutral gas. Following Tully & Fouque (1985), we use

$$W_{x,\text{turb}}^2 = W_x^2 + W_{t,x}^2 \left[1 - 2e^{-\left(\frac{W_x}{W_{c,x}} \right)^2} \right] - 2W_x W_{t,x} \left[1 - e^{-\left(\frac{W_x}{W_{c,x}} \right)^2} \right]. \quad (4.6)$$

The subscript x again denotes the profile width at 20 or 50 percent of the peak flux. The W_x used here is the W_{20} (or W_{50}) which was corrected for instrumental resolution according to Eq. 4.5. The $W_{c,x}$ represent the velocity widths where the shapes of the velocity profiles change from boxy to Gaussian profiles and the values of $W_{t,x}$ indicate the amount by which turbulent motion of the neutral gas broadens the HI profile. For the choice of $W_{c,x}$ and $W_{t,x}$, we follow Verheijen (1997) and use his best values of $W_{t,20} = 22 \text{ km s}^{-1}$ and $W_{t,50} = 5 \text{ km s}^{-1}$, as well as the commonly adopted values of $W_{c,20} = 120 \text{ km s}^{-1}$ and $W_{c,50} = 100 \text{ km s}^{-1}$ (see Chapter 5 of Verheijen (1997) for an extensive discussion of these correction terms). The resulting corrected profile widths are given in Cols. (11) and (12) of Tables 4.2 and 4.3. Note that the profile widths listed in Tables 4.2 and 4.3 are not corrected for inclination.

4.5.3 Sources of uncertainties

Here we discuss the uncertainties of the individual quantities and their contribution to the total uncertainty in the two parameters for the BTF — maximum rotation velocity and baryonic mass.

4.5.3.1 Uncertainty of V_{max}

The uncertainty of V_{max} depends on two individual uncertainties. Firstly, on the uncertainty in the velocity estimate (i.e., width of the velocity profile, fit with ROTCUR, etc.) and secondly on the error of the derived inclination. Given that profile widths can be measured quite accurately and because our estimates of V_{vf} are usually based on the rotation velocities of several tilted-rings, we assume a uniform uncertainty of 4 km s^{-1} (of order of the velocity resolution) for the uncertainty of V_{max} . For the uncertainty in the derived inclination angle, we distinguish between galaxies with a kinematically derived inclination, and those where we used the optical inclination or that of the HI disk. For the former, i.e., the five galaxies with a full ROTCUR analysis, we calculate the scatter of the inclination values of the individual tilted-rings (see middle panels in Figs. 4.1-4.5) and use this scatter as the uncertainty in the derived inclination (see Col. (13) of Table 4.3). For the other six galaxies (D500-3, D572-5, D575-1, D575-5, D640-13, D646-7), we use the mean uncertainty of the kinematically derived inclinations (i.e., 6°) as a global uncertainty of their inclination angles. The absolute uncertainty of the (inclination-corrected) maximum rotation velocity is then calculated assuming Gaussian error propagation.

4.5.3.2 Uncertainty of the baryonic mass

The baryonic mass is the sum of the stellar mass and the gas mass:

$$M_{\text{bar}} = M_{\text{stars}} + M_{\text{gas}}. \quad (4.7)$$

The stellar mass is calculated through

$$M_{\text{stars}} = \Upsilon_*^I 10^{-0.4[M_V - (V - I) - 4.02]}, \quad (4.8)$$

where Υ_*^I is the stellar mass-to-light ratio in the I -band, $M_I = M_V - (V - I)$ is the absolute I -band magnitude, and 4.02 is the magnitude of the Sun in the I -band. The absolute magnitude of a galaxy depends through the distance modulus on its apparent magnitude and its distance. Thus, the stellar mass depends on three quantities: stellar mass-to-light ratio, distance, and apparent magnitude. For the uncertainty of the mass-to-light ratio, we use the difference between the two stellar population models which were discussed in Section 4.5.1. For the uncertainty of the distances, we distinguish between

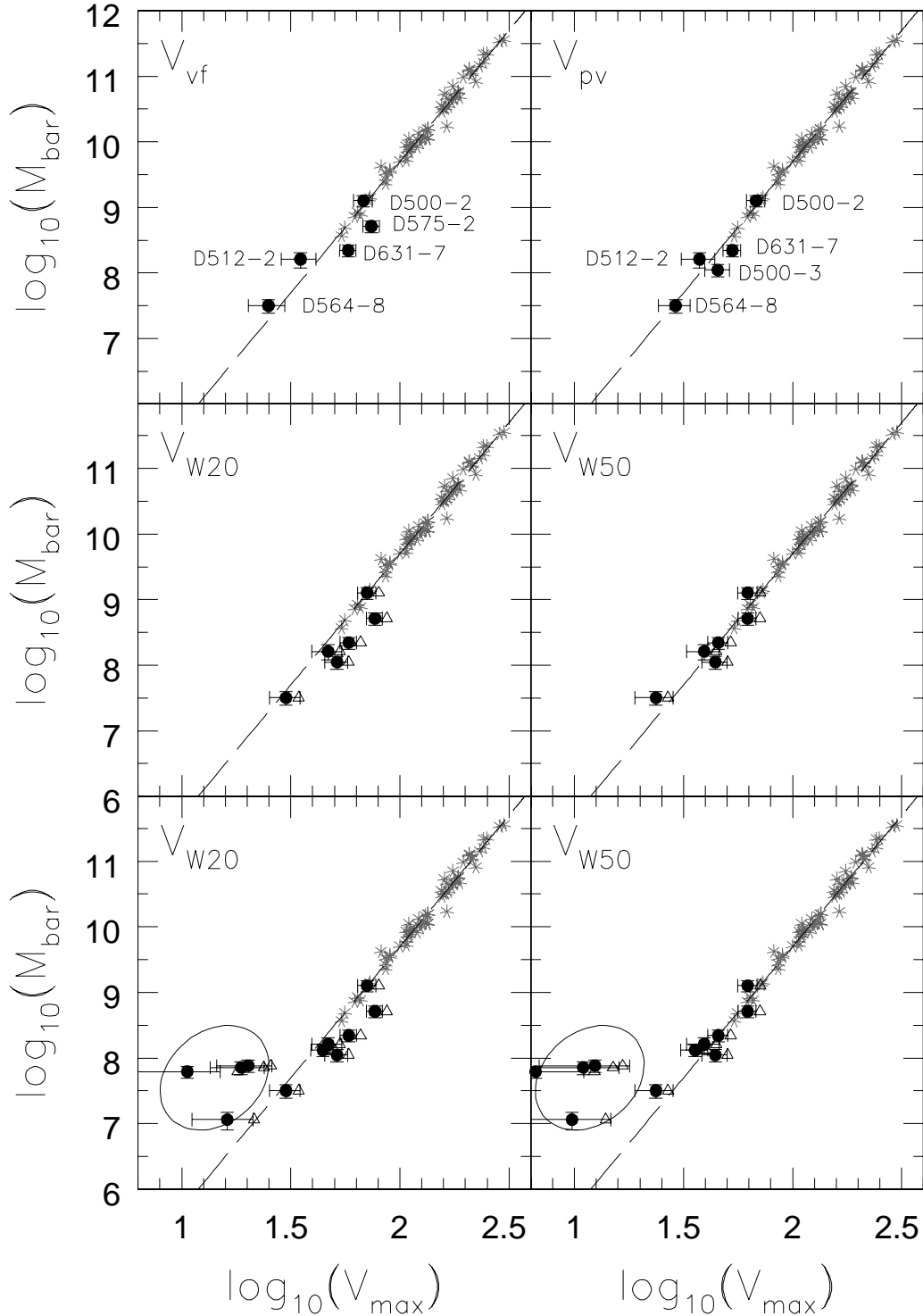


FIG. 4.8: The baryonic Tully-Fisher relation using four different estimates for V_{\max} , namely V_{vf} from the tilted-ring analysis of the velocity fields (top left), V_{pv} from the major-axis position-velocity diagram (top right), V_{W20} , i.e., half the W_{20} (middle and bottom left), and V_{W50} , i.e., half the W_{50} (middle and bottom right). As a reference, we show the BTF relation of the analysis of (McGaugh 2005, dashed line), as well as his individual data points (gray stars). The filled circles in the panels showing a BTF based on W_{20} and W_{50} are based on the turbulence-corrected velocity widths. The open triangles in these panels make use of the corresponding uncorrected velocity widths and are shown merely to illustrate the effect of the turbulence correction. The bottom panels show V_{W20} and V_{W50} for all galaxies in the sample, including those which are either barely resolved or face-on (enclosed by the ellipse). The top and middle panels contain only galaxies having either a V_{vf} or a V_{pv} (the rotation curve sub-sample), i.e., what is referred to in the text as the *clean* BTF.

galaxies for which we use an independent distance estimate (D631-7 and D640-13) and those where we use the Hubble flow distance. For the former, we adopt the uncertainties given in the corresponding source paper (i.e., Karachentsev et al. 2003), and for the latter, we assume a ten percent uncertainty in the distance estimates. The apparent magnitudes of the galaxies in our sample were determined by Pildis et al. (1997), who report a photometric accuracy of 0.05 mag. This is insignificant compared to the influence of the uncertainties in the distance and in the stellar Υ_* , and we therefore ignore the uncertainties of m_V for the uncertainty of the stellar mass.

The second term contributing to the baryonic disk mass is M_{gas} , the mass of the gas, which is given by:

$$M_{\text{gas}} = 1.4M_{\text{HI}} = 1.4 \cdot 2.36 \cdot 10^5 D^2 \int S dv, \quad (4.9)$$

where M_{HI} is the total HI mass, D is the distance in Mpc, S is the total flux in mJy beam^{-1} , and dv is the velocity resolution in km s^{-1} . The constant factor 1.4 corrects the HI mass for the presence of helium and metals. Note that since H_2/HI , the ratio between the molecular and the neutral hydrogen, is much lower in dwarf galaxies compared to luminous spirals (Taylor et al. 1998; Leroy et al. 2005), we do not apply correction terms to account for molecular hydrogen. The uncertainty of the HI mass depends on the uncertainty of the total flux, and quadratically on the distance uncertainty. We focus again on the uncertainty in the distance, which is the dominant source of uncertainty here.

Inserting Eqs. 4.8 and 4.9 into Eq. 4.7, we determine the uncertainty of the baryonic mass by assuming a Gaussian error propagation of the individual uncertainties discussed above.

4.5.4 The baryonic Tully-Fisher relation

In this section we present the baryonic Tully-Fisher relation for the galaxies of our sample, using different estimates for V_{max} . As a reference, we also show the BTF as constructed by McGaugh (2005). He investigated the baryonic Tully-Fisher relation for galaxies with well-determined rotation velocities between 50 km s^{-1} and 300 km s^{-1} , and tested several methods to determine stellar mass-to-light ratios. The one yielding the smallest scatter in the BTF is based on the mass-discrepancy-acceleration relation (MDAcc, see McGaugh 2004). The resulting BTF relation has the following form:

$$M_{\text{bar}} = 50V_{\text{max}}^4, \quad (4.10)$$

with the baryonic mass in M_{\odot} and the maximum rotation velocity in km s^{-1} .

For the construction of a BTF relation, we use four different estimates for V_{max} :

- (a) V_{vf} , obtained from the tilted-ring analysis of the velocity fields
- (b) V_{pv} , estimated with XGAUPROF from the major-axis position-velocity diagrams
- (c) $V_{W20} = \frac{1}{2} W_{20}$, the rotation velocity as derived from half the width of the HI profile at the 20 percent level of the maximum flux
- (d) $V_{W50} = \frac{1}{2} W_{50}$, the rotation velocity as derived from half the width of the HI profile at the 50 percent level of the maximum flux

All estimates are corrected for inclination effects. Additional corrections have been applied to V_{W20} and V_{W50} (as described in Section 4.5.2). In Fig 4.8, we show the baryonic Tully-Fisher relation for the galaxies of our sample. The uncertainties are discussed and quantified in Section 4.5.3. In order to visualize the effect of the turbulence corrections applied to the velocity widths, we also

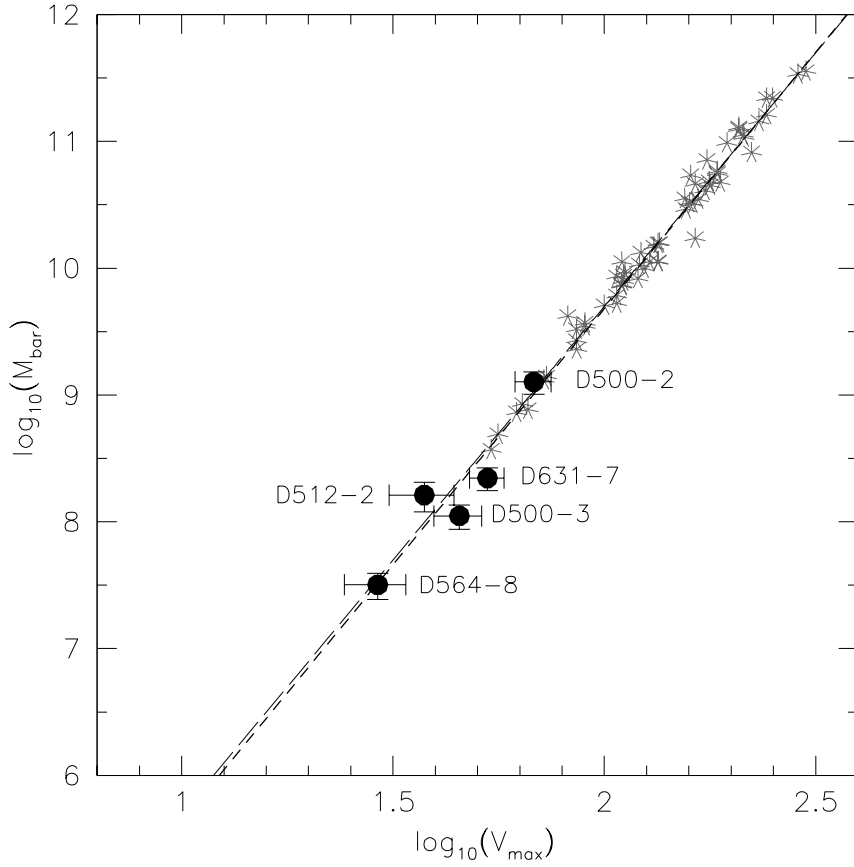


FIG. 4.9: The baryonic Tully-Fisher relation with V_{pv} as an indicator for V_{\max} . The galaxies from McGaugh (2005) are shown as a reference (gray stars), and the long-dashed line is the fit through these data points. Including our data points (filled circles) to the ones from McGaugh (2005) and re-deriving the BTf relation results the fit indicated by the short-dashed line, which is barely distinguishable from the original fit of McGaugh (2005).

include data points based on the uncorrected profile widths (open triangles). As these are shown for illustration purposes only, we do not display uncertainties for these data points. The galaxies in the panels making use of V_{vf} and V_{pv} are labelled. A few galaxies of our sample are located above the BTf relation (indicated in the bottom panels of Fig. 4.8 by an ellipse). However, these are the galaxies with the poorest data quality and are usually only barely resolved (see, e.g., Figs. 4.19 and 4.20 for the moment maps of D640-13 and D646-7). Others like D575-5 are well-resolved, but are almost face-on and therefore not dominated by rotation (cf. 1st moment map shown in Fig. 4.17). Given the known problems with these galaxies, we will disregard them in the further analysis and construct a *clean* BTf including only galaxies from our rotation curve sub-sample (top and middle panels of Fig. 4.8). It is directly apparent that the galaxies from our rotation curve sub-sample agree well with the BTf relation as found by McGaugh (2005), irrespective of whether V_{vf} , V_{pv} , or V_{W50} is used as an estimate for V_{\max} . Using V_{W20} results in a slight overestimate in V_{\max} , as has also been reported by other authors (e.g., Broeils 1992; Verheijen 1997). It is clear that the BTf relation also holds for these extreme dwarf galaxies. In the next section, we will address this in a more quantitative way.

4.5.5 The scatter of the BTF

The panels in Fig. 4.8 clearly show that the new data points from our sample fall almost perfectly on the BTF relation from McGaugh (2005). Based on his sample alone, the BTF is tightly correlated ($\mathcal{R} = 0.99$) and has a mathematical form as given in Eq. 4.10. Increasing his sample by the five galaxies from our sample which have a well-defined V_{pv} , we re-derive the optimum BTF relation by applying a least-square fit. Following McGaugh (2005), we assign each galaxy with equal weight. The resulting BTF has the following form:

$$M_{\text{bar}} = 40V_{\text{max}}^{4.04} \quad (4.11)$$

and is equally well-determined ($\mathcal{R} = 0.99$) as the BTF from McGaugh (2005). The two BTFs (Eq. 4.10 and Eq. 4.11) have an almost identical slope (4 vs. 4.04), but a somewhat different normalization (50 vs. 40). The latter is due to the fact that the low-mass dwarf galaxies constrain the normalization coefficient more strongly than the high-mass galaxies. The overall difference between the two BTF relations is, however, marginal, as can be seen in Fig. 4.9, where we show the BTF relation together with the fit according to Eq. 4.10 (long-dashed line) as well as the fit following Eq. 4.11 (short-dashed line).

We will now come back to the conclusions of Franx & de Zeeuw (1992), who used the scatter of the TF relation to put constraints on the ellipticity of dark matter halos. They argue that if the potential in the plane of the disk is elongated, then the different viewing angles will cause scatter in the TF relation. In return, the scatter of the (B)-TF relation can be used to put an upper limit on the ellipticity of the potential in the plane of the disk. According to Franx & de Zeeuw (1992), a TF relation with a scatter of 0.31 mag (0.46 mag when photometric inclinations are used) constrains the ellipticities of the potentials to be below 0.10. As it is unlikely that all the scatter in the TF relation is due to different viewing angles, they argue that an elongation between 0-0.06 is more reasonable.

Since the work of Franx & de Zeeuw (1992), the quantity and quality of the data has improved significantly and we can now trace the BTF relation over a large range of galaxy masses and rotation velocities. The scatter in the optimum BTF from McGaugh (2005) is $\sigma = 0.098$ dex, or 0.25 mag. Including our galaxies results in a slightly larger scatter ($\sigma = 0.11$ or $\sigma_M = 0.28$ mag) — mainly because the distances to our galaxies are less well-determined. However, the scatter in our BTF relation is still smaller than the scatter on which Franx & de Zeeuw (1992) based their upper limits for the ellipticity of the potentials in the disk plane.

Therefore, their argumentation — based initially on the TF relation of largely high mass galaxies — is also valid for the BTF relation of extreme dwarf galaxies. The fact that even extremely low-mass dwarf galaxies as presented here follow the BTF relation implies that (i) the BTF relation must be a fundamental relation which all rotationally dominated galaxies follow, and (ii) that there is not much room for a large ellipticity of the potentials in the disk plane of the galaxies.

The second point puts important constraints on properties of galaxy halos within the CDM context. It is well-known that CDM models produce density profiles which are too steep to fit the rotation curves of dwarf and low surface brightness galaxies (cf. Moore 1994; Flores & Primack 1994; Navarro et al. 1996; McGaugh & de Blok 1998b). But, as these galaxies are dark matter dominated at all radii (e.g., de Blok & McGaugh 1997; Verheijen 1997; Swaters et al. 2000), one would naturally think that CDM models should work best for them, as the contribution of stars in these galaxies is small. Current and well-motivated attempts to reconcile CDM models and the observations involve halo tri-axiality and the effects of non-circular motions (e.g., Hayashi et al. 2004a; Hayashi & Navarro 2006; Hayashi et al. 2007). As CDM halos are tri-axial (see also Frenk et al. 1988; Dubinski & Carlberg 1991; Capuzzo-Dolcetta et al. 2007), the ellipticity of the potential can

induce large non-circular motions in the central regions of the simulated galaxies, which should then blur the derived rotation velocities, thus letting an intrinsic “cusp” (i.e., a cuspy, steep inner density profile) appear as a constant-density “core” (i.e., a flat, constant inner density profile). Non-circular motions have been measured by several groups (e.g., Schoenmakers et al. 1997; Wong et al. 2004; Gentile et al. 2005; Trachternach et al. 2008a), but none of these authors report large enough non-circular motions to account for the different slopes in the density profiles. In the few cases where relatively large non-circular motions are found, they are generally associated with a bar (cf. Spekkens & Sellwood 2007).

In addition to quantifying non-circular motions, Trachternach et al. (2008a) also put constraints on the elongation of the potential in the plane of the disk. Their results, derived for a sample of 18 spiral and dwarf galaxies from the THINGS survey (Walter et al. 2008; de Blok et al. 2008), show that all galaxies in that sample are consistent with having a round potential and that the average elongation is small (0.017 ± 0.020 , cf. Chapter 2 of this thesis), particularly when compared to what is found in CDM simulations (cf. Frenk et al. 1988; Hayashi & Navarro 2006). Trachternach et al. (2008a) also find that the elongation does not decrease towards the center of the galaxies. The tightly correlated BTF relation constructed here therefore constrains the ellipticity of galaxy potentials independently from the analysis of Trachternach et al. (2008a), but results in consistent limits.

Valenzuela et al. (2007) use a different approach to the cusp/core problem. They reason that non-circular motions, together with projection effects and gas pressure support from hot gas cause a severe underestimate of the central velocities which creates the illusion of a constant-density core. Although these effects might reconcile the different density slopes, they would lead to a (B)TF relation with a much larger scatter than observed.

4.6 Conclusions

We explore the baryonic Tully-Fisher (BTF) relation over a large range of galaxy masses and rotation velocities. We present and discuss several estimates for V_{\max} , the maximum rotation velocity. The different estimates show a good agreement and the BTF relation based on them are equally well-constrained. We discuss the choice of stellar mass-to-light ratio (Υ_*) and show that its choice is not crucial for the extreme dwarf galaxies in our sample, since for them, the stellar mass generally contributes less to the total baryonic mass as it is the case for luminous high-mass galaxies. Our results furthermore show that some of these dwarf galaxies are not rotationally supported, although better spatial resolution might reveal some rotation even for them.

Including the sample of McGaugh (2005), the galaxies presented here show rotation velocities of $25 \text{ km s}^{-1} \leq V_{\max} \leq 300 \text{ km s}^{-1}$. The BTF holds over this large range with a remarkably small scatter of $\sigma_M = 0.28 \text{ mag}$. This small scatter puts strong constraints on the ellipticity of the potential in the plane of the disk of the galaxies. Following the argumentation of Franx & de Zeeuw (1992), we conclude that the ellipticities are likely to be between 0-0.06, which is in contrast to ellipticities from recent theoretical simulations, which predict much higher elongations of the order of 0.1-0.3 (cf. Hayashi & Navarro 2006). Our results confirm those from Franx & de Zeeuw (1992), Franx et al. (1994), and Trachternach et al. (2008a), indicating that, at least in the plane of the disk, galaxy halos are round.

ACKNOWLEDGEMENTS: CT would like to thank Janine van Eymeren and Volker Knierim for many stimulating discussions. The work of CT is supported by the German Ministry for Education and Science (BMBF) through grant 05 AV5PDA/3. The work of WJGdB is based upon research sup-

ported by the South African Research Chairs Initiative of the Department of Science and Technology and National Research Foundation. The Westerbork Synthesis Radio Telescope is operated by the ASTRON (Netherlands Foundation for Research in Astronomy) with support from the Netherlands Foundation for Scientific Research (NWO). This research has made use of the NASA/IPAC Extragalactic Database (NED) which is operated by the Jet Propulsion Laboratory, California Institute of Technology, under contract with the National Aeronautics and Space Administration.

4.A Appendix: Atlas

The Appendix contains summary panels for all galaxies of our sample (Figs. 4.10-4.20) and channel maps for the galaxies from the rotation curve sub-sample (Figs. 4.21-4.26).

The summary panels consist of two rows with three panels each, and contain the following maps:

Top row: *Left panel:* 0th moment map with grayscales. Grayscales run from a column density of $n_{HI} = 1 \cdot 10^{19} \text{ cm}^{-2}$ (white) to $n_{HI} = 2 \cdot 10^{21} \text{ cm}^{-2}$ (black). The 3σ level is indicated by the black contour. *Middle panel:* 1st moment map. The systemic velocity is indicated by the thick contour, the contours are spaced by 10 km s^{-1} (unless mentioned otherwise). The approaching side can be identified by the light grayscales and black contours, and the receding side by dark grayscales and white contours. *Right panel:* 2nd moment map. Grayscales run from 2 to 40 km s^{-1} . Unless mentioned otherwise, the contours levels are given at 5, 10, and 15 km s^{-1} . For all moment maps, the beam size is indicated in the bottom right corner. Additionally, if the center of the galaxy has been derived kinematically with the ROTCUR analysis, the resulting center is indicated in all moment maps by a cross.

Bottom row: *Left panel:* Major axis position-velocity diagram. The position angle of the slice is generally indicated in the top-left corner of the panel. Grayscales run from 2σ to 30σ , and contour levels are given at $2\sigma + n \times 4\sigma$ (i.e., 2,6,10,14,18 σ). The dashed line indicates the systemic velocity. If a V_{pv} has been derived with XGAUPROF, the resulting velocities at either side of the rotation curve are indicated by arrows. *Middle panel:* Minor axis position-velocity diagram. Grayscales and contours are identical to the major axis position-velocity diagram. *Right panel:* Global HI profile of the Hanning smoothed data cube.

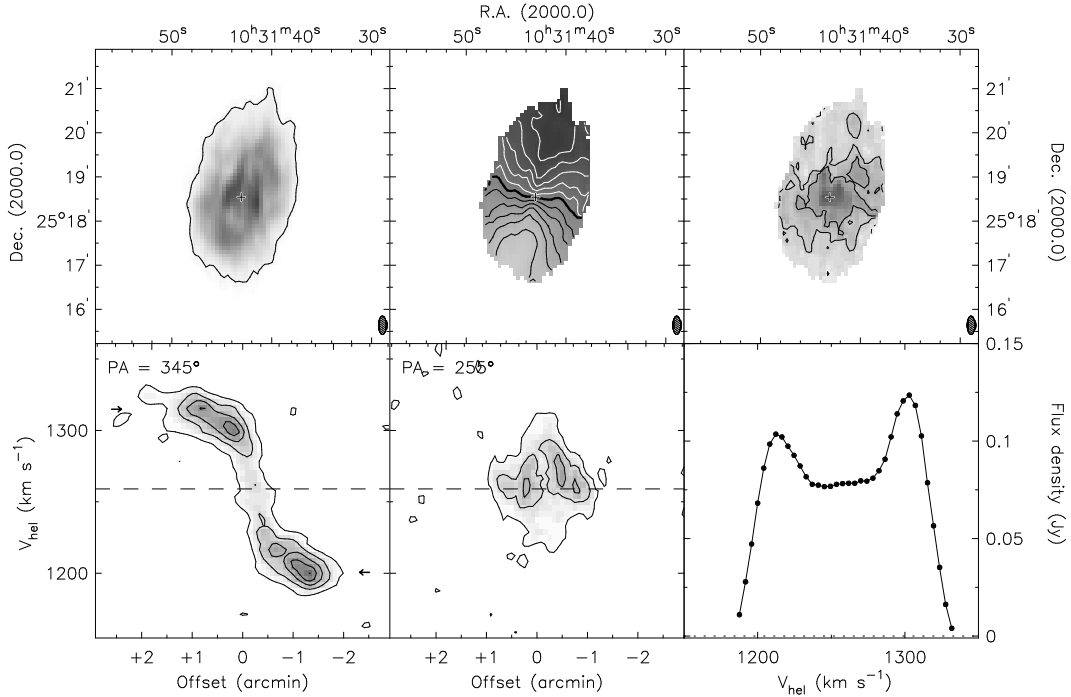


FIG. 4.10: Summary panel for D500-2. A general description of the panels and levels is given at the beginning of the Appendix 4.A. The 3σ contour in the 0th moment map corresponds to a flux of 5.09 mJy, which translates to a column density limit of $n_{HI} = 8.8 \cdot 10^{19} \text{ cm}^{-2}$.

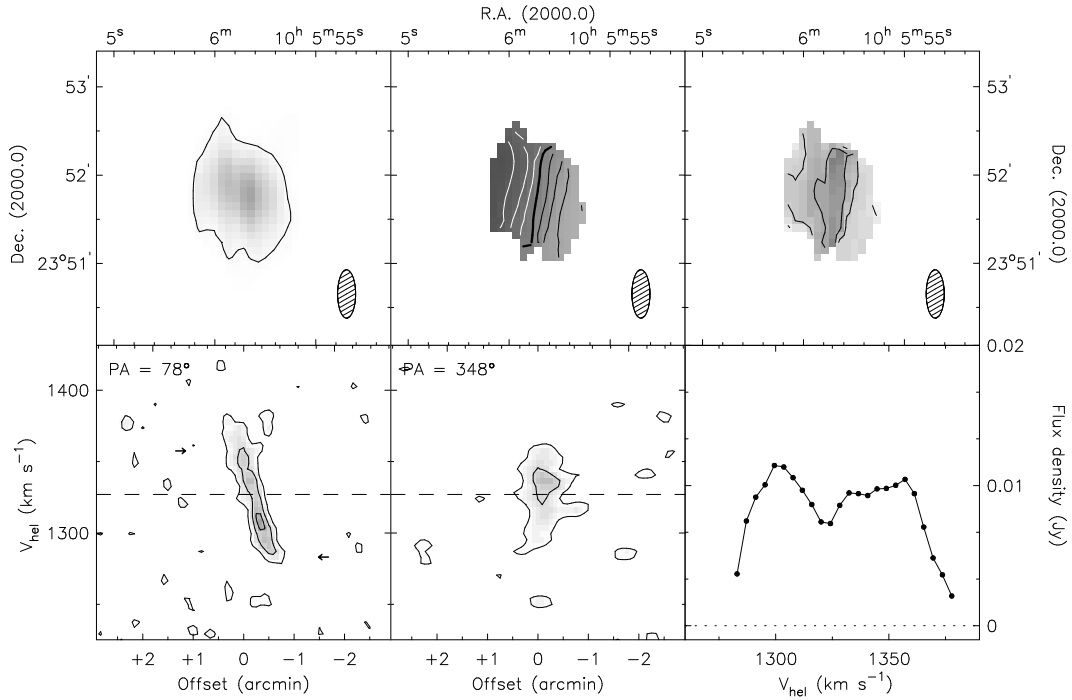


FIG. 4.11: Summary panel for D500-3. A general description of the panels and levels is given at the beginning of the Appendix 4.A. The 3σ contour in the 0th moment map corresponds to a flux of 4.51 mJy, which translates to a column density limit of $n_{HI} = 5.2 \cdot 10^{19} \text{ cm}^{-2}$.

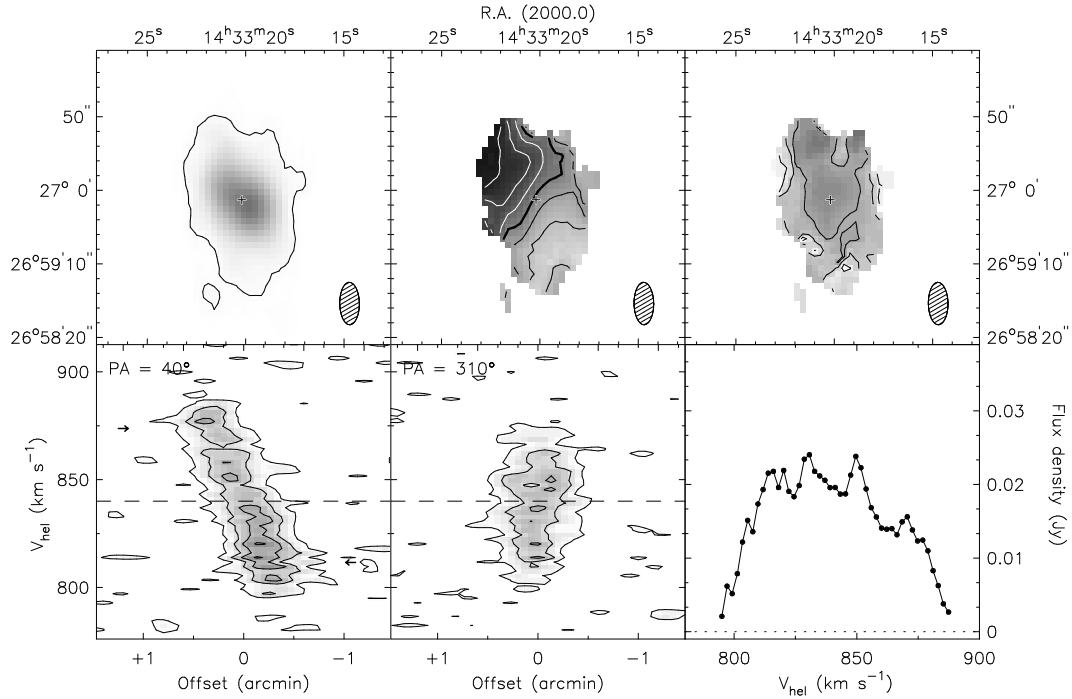


FIG. 4.12: Summary panel for D512-2. A general description of the panels and levels is given at the beginning of the Appendix 4.A. The 3σ contour in the 0th moment map corresponds to a flux of 5.50 mJy, which translates to a column density limit of $n_{HI} = 3.3 \cdot 10^{19} \text{ cm}^{-2}$.

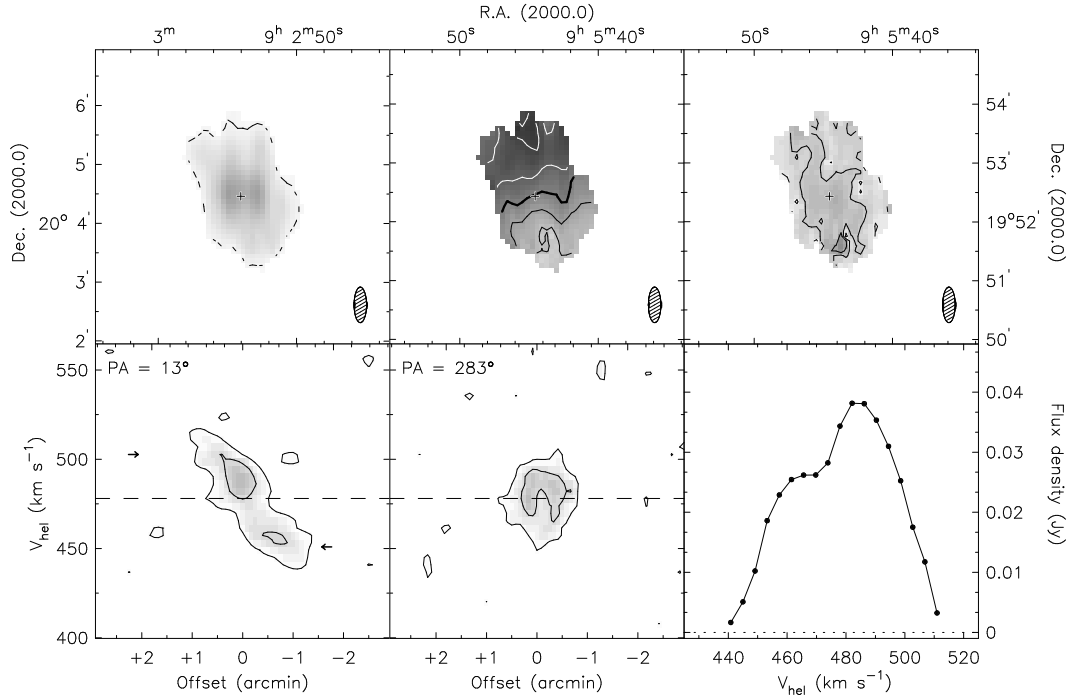


FIG. 4.13: Summary panel for D564-8. A general description of the panels and levels is given at the beginning of the Appendix 4.A. The 3σ contour in the 0th moment map corresponds to a flux of 4.99 mJy, which translates to a column density limit of $n_{\text{HI}} = 4.9 \cdot 10^{19} \text{ cm}^{-2}$.

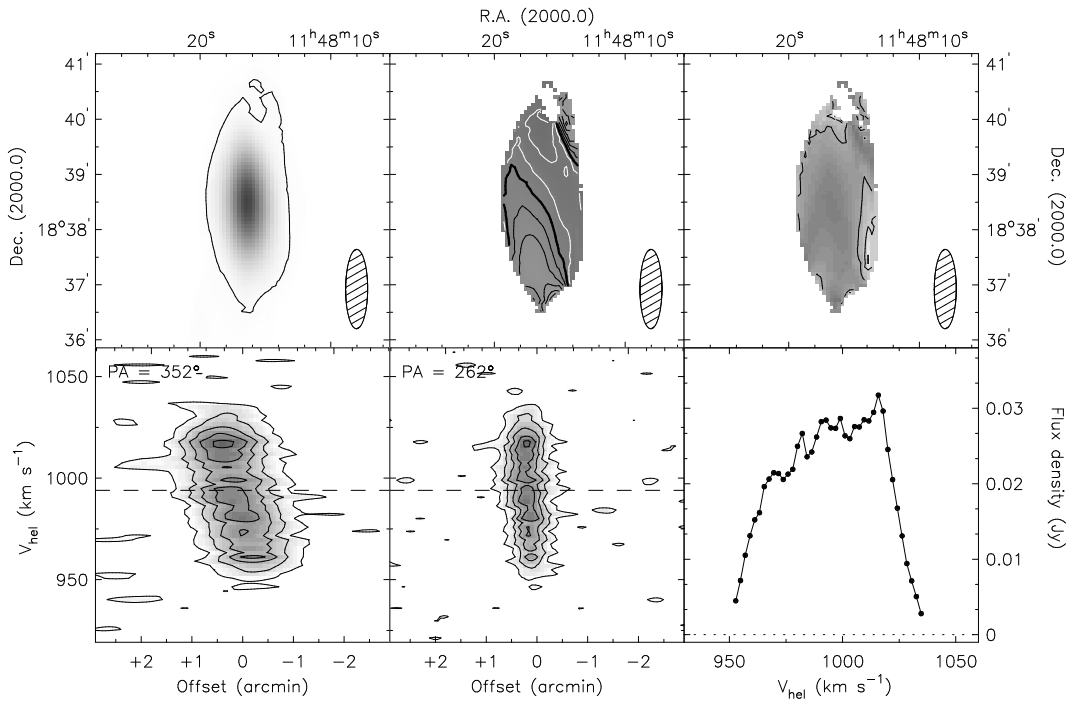


FIG. 4.14: Summary panel for D572-5. A general description of the panels and levels is given at the beginning of the Appendix 4.A. Grayscale in the 0th moment map runs from a column density of $n_{\text{HI}} = 1 \cdot 10^{19} \text{ cm}^{-2}$ (white) to $n_{\text{HI}} = 8 \cdot 10^{20} \text{ cm}^{-2}$ (black). The 3σ contour in the 0th moment map corresponds to a flux of 12.47 mJy, which translates to a column density limit of $n_{\text{HI}} = 1.4 \cdot 10^{19} \text{ cm}^{-2}$. The velocity contours in the 1st moment map are spaced by 5 km s⁻¹.

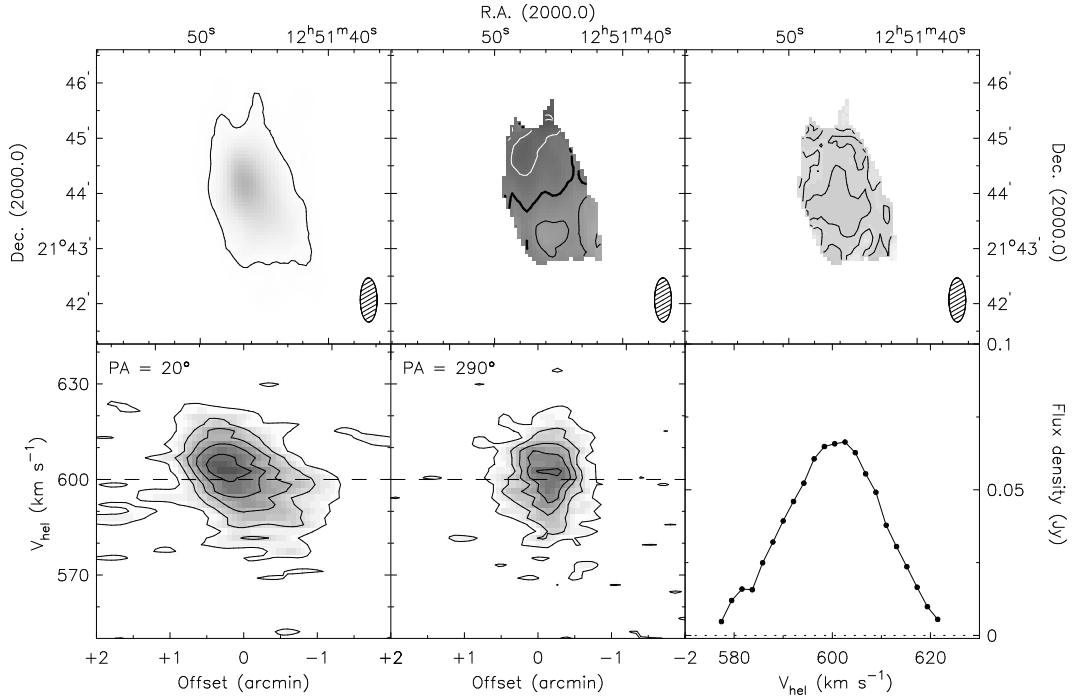


FIG. 4.15: Summary panel for D575-1. A general description of the panels and levels is given at the beginning of the Appendix 4.A. The 3σ contour in the 0th moment map corresponds to a flux of 9.81 mJy, which translates to a column density limit of $n_{HI} = 1.3 \cdot 10^{19} \text{ cm}^{-2}$. The velocity contours in the 1st moment map are spaced by 5 km s^{-1} , and the contours in the 2nd moment map are given at 7.5 km s^{-1} and 9 km s^{-1} .

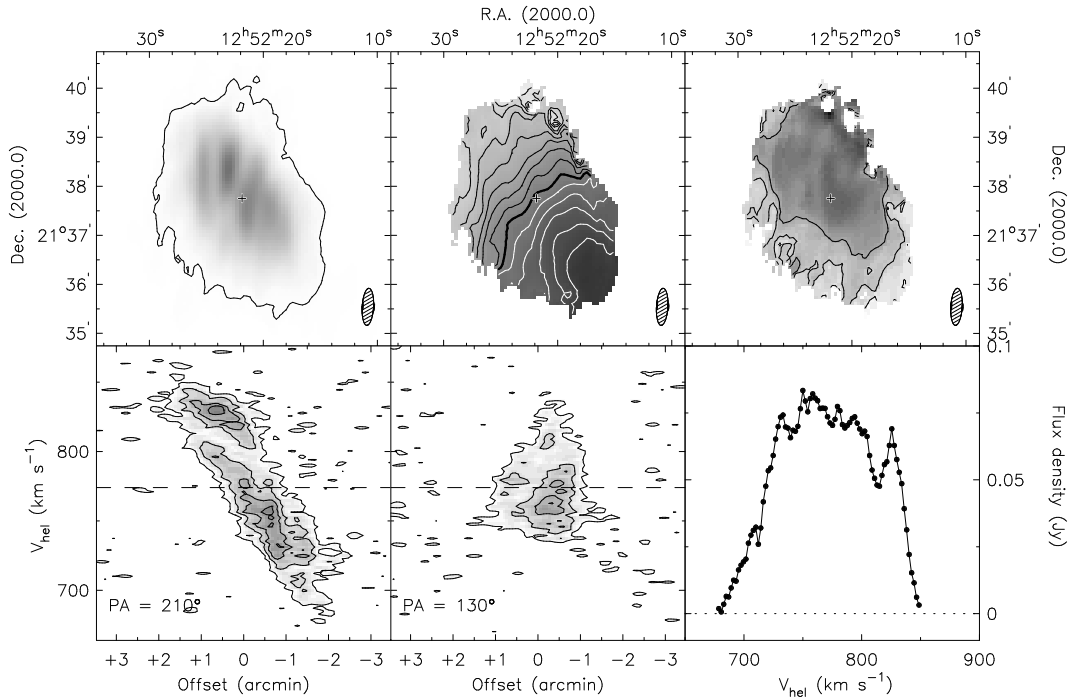


FIG. 4.16: Summary panel for D575-2. A general description of the panels and levels is given at the beginning of the Appendix 4.A. The 3σ contour in the 0th moment map corresponds to a flux of 5.58 mJy, which translates to a column density limit of $n_{HI} = 2.0 \cdot 10^{19} \text{ cm}^{-2}$.

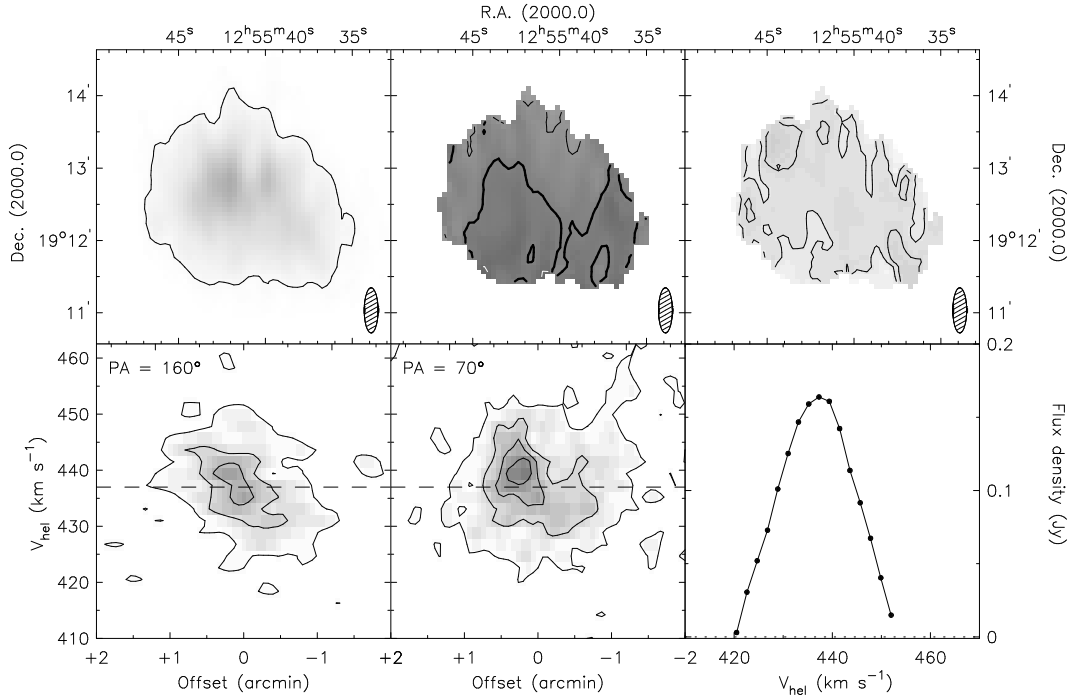


FIG. 4.17: Summary panel for D575-5. A general description of the panels and levels is given at the beginning of the Appendix 4.A. The 3σ contour in the 0th moment map corresponds to a flux of 8.82 mJy, which translates to a column density limit of $n_{\text{HI}} = 0.6 \cdot 10^{19} \text{ cm}^{-2}$. The velocity contours in the 1st moment map are spaced by 5 km s⁻¹, and the contours in the 2nd moment map are given at 6 km s⁻¹ and 7.5 km s⁻¹.

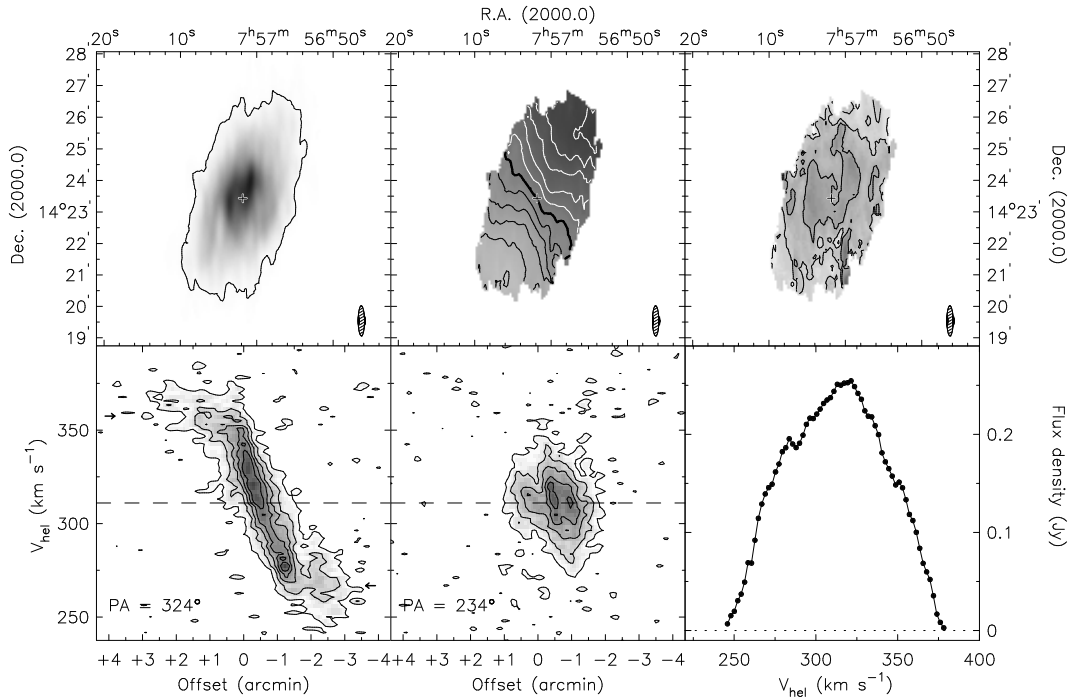


FIG. 4.18: Summary panel for D631-7. A general description of the panels and levels is given at the beginning of the Appendix 4.A. The 3σ contour in the 0th moment map corresponds to a flux of 11.06 mJy, which translates to a column density limit of $n_{\text{HI}} = 3.7 \cdot 10^{19} \text{ cm}^{-2}$.

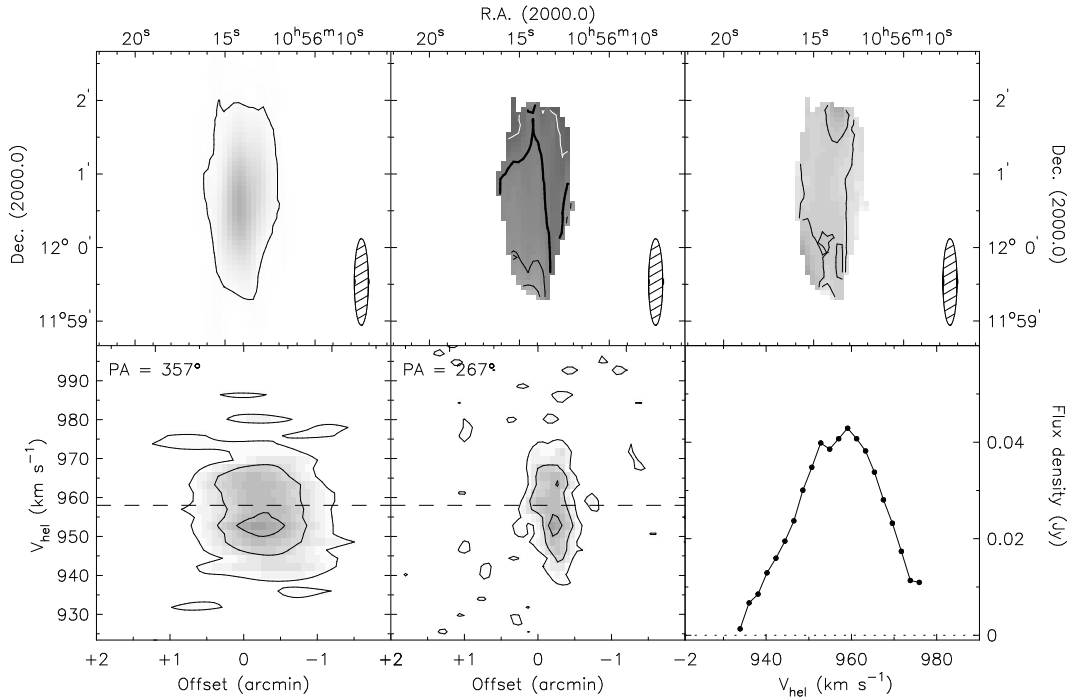


FIG. 4.19: Summary panel for D640-13. A general description of the panels and levels is given at the beginning of the Appendix 4.A. The 3σ contour in the 0th moment map corresponds to a flux of 11.49 mJy, which translates to a column density limit of $n_{HI} = 3.3 \cdot 10^{19} \text{ cm}^{-2}$. The velocity contours in the 1st moment map are spaced by 5 km s^{-1} , and the contours in the 2nd moment map are given at 7.5 km s^{-1} and 10 km s^{-1} .

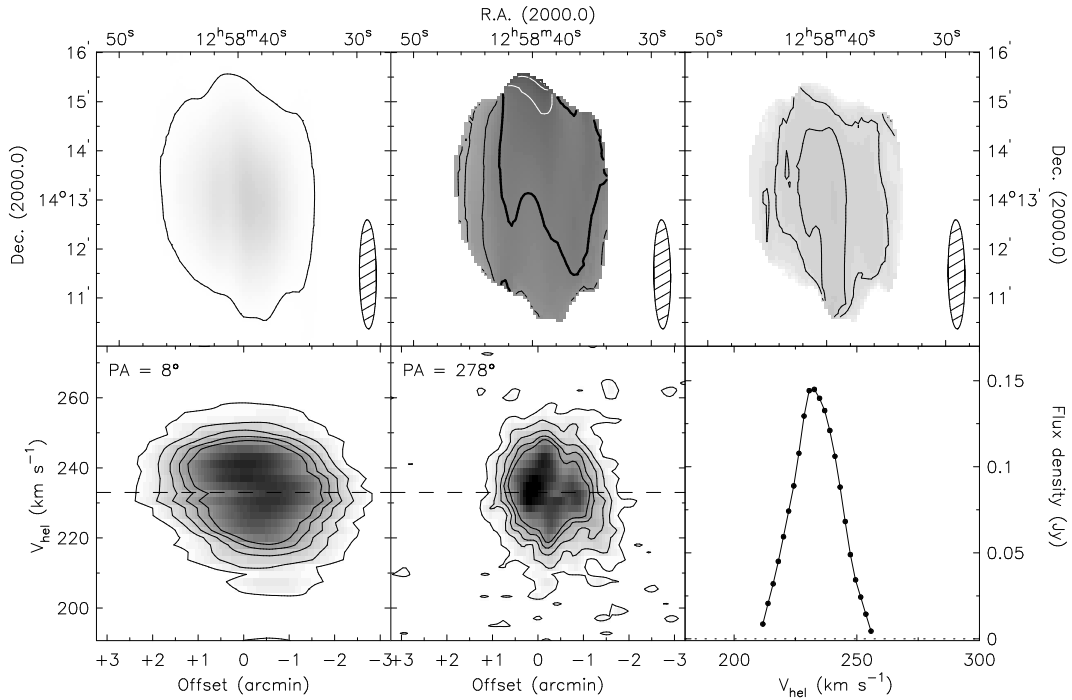


FIG. 4.20: Summary panel for D646-7. A general description of the panels and levels is given at the beginning of the Appendix 4.A. The 3σ contour in the 0th moment map corresponds to a flux of 7.92 mJy, which translates to a column density limit of $n_{HI} = 0.7 \cdot 10^{19} \text{ cm}^{-2}$. The velocity contours in the 1st moment map are spaced by 5 km s^{-1} , and the contours in the 2nd moment map are given at 7.5 km s^{-1} and 9 km s^{-1} .

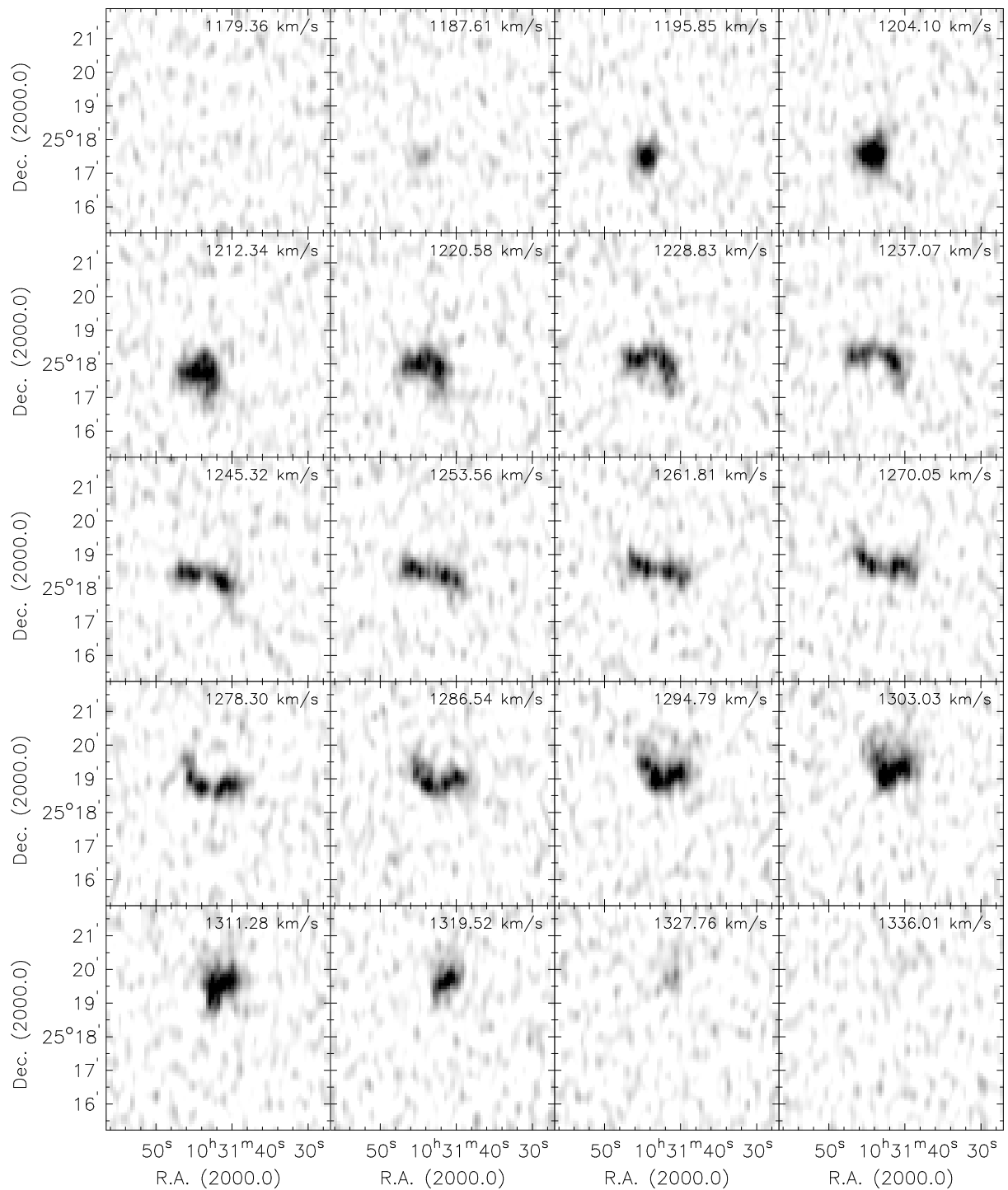


FIG. 4.21: Channel maps of D500-2. Grayscales run from -0.02 to 7 mJy. Every second channel is shown.

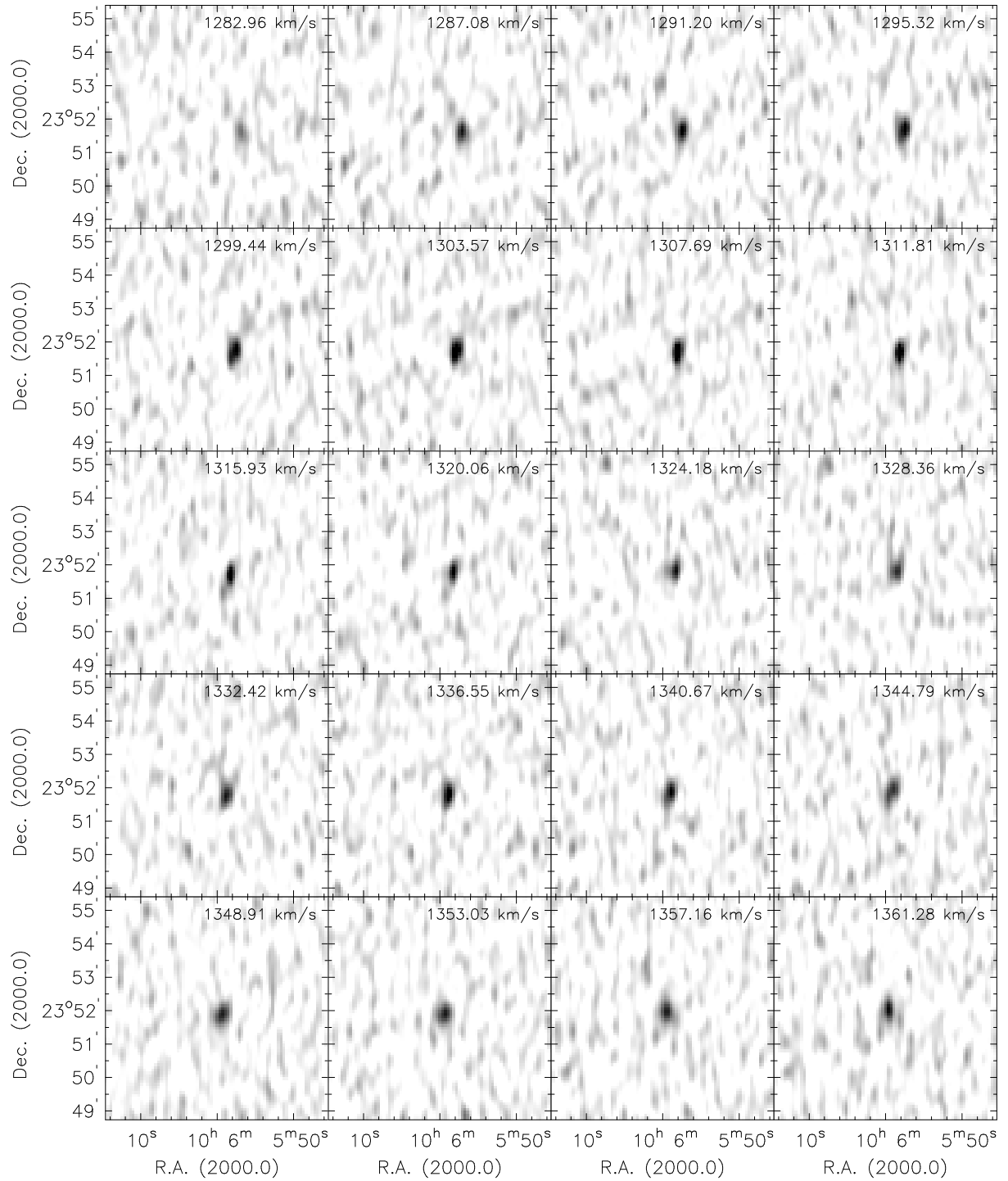


FIG. 4.22: Channel maps of D500-3. Grayscale run from -0.02 to 5 mJy. Every channel is shown.

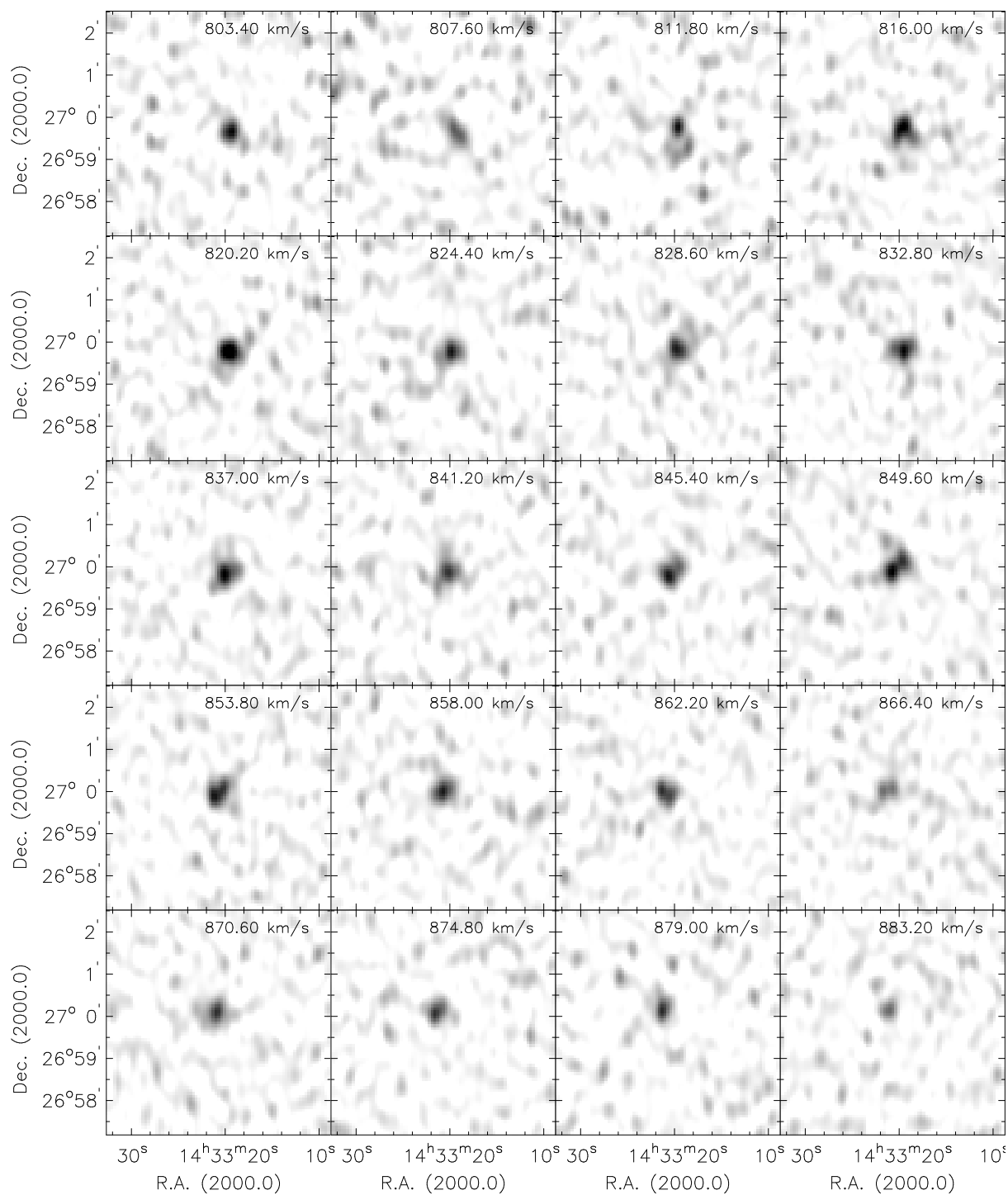


FIG. 4.23: Channel maps of D512-2. Grayscales run from -0.02 to 8 mJy. Every second channel is shown.

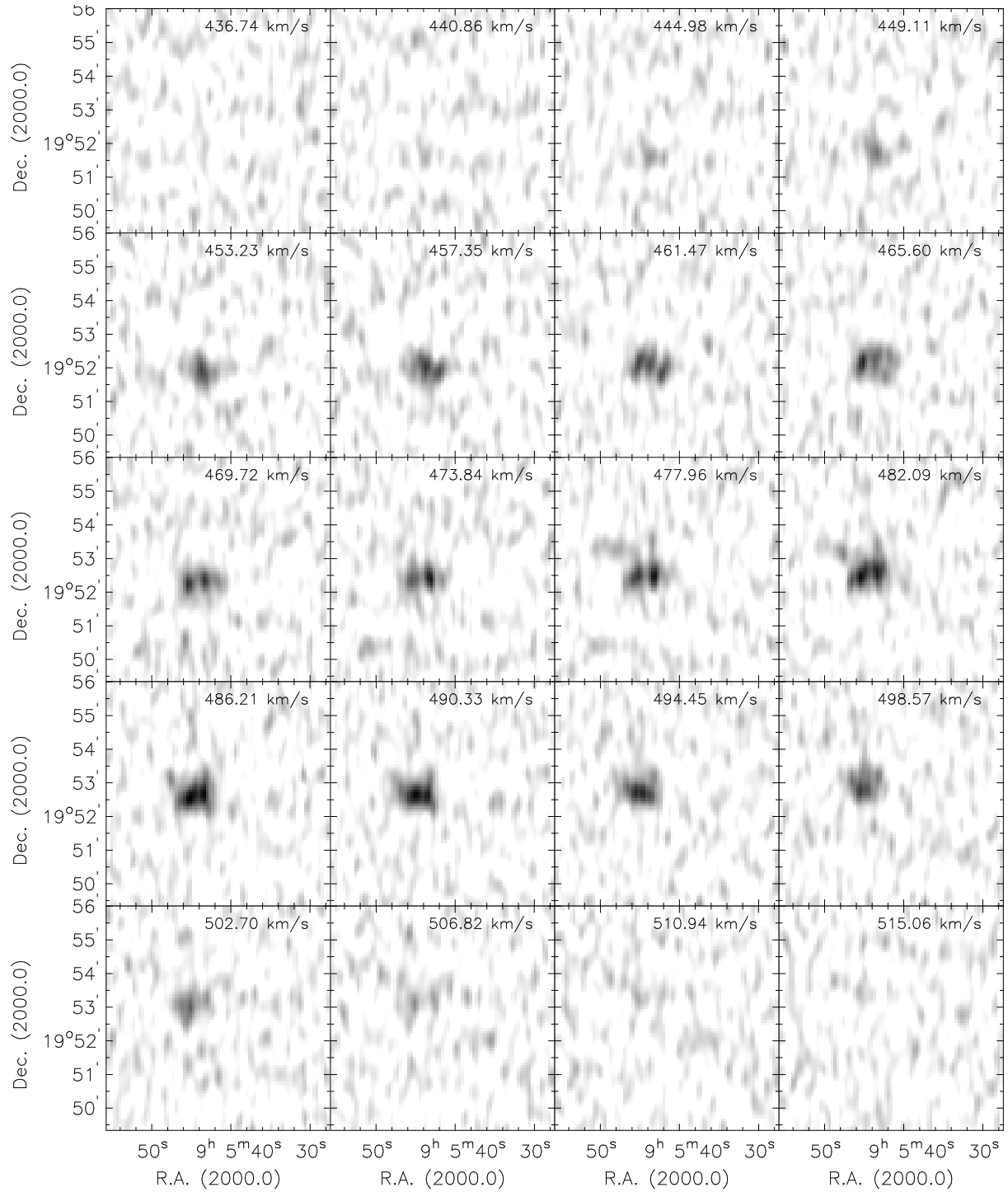


FIG. 4.24: Channel maps of D564-8. Grayscales run from -0.02 to 7 mJy. Every channel is shown.

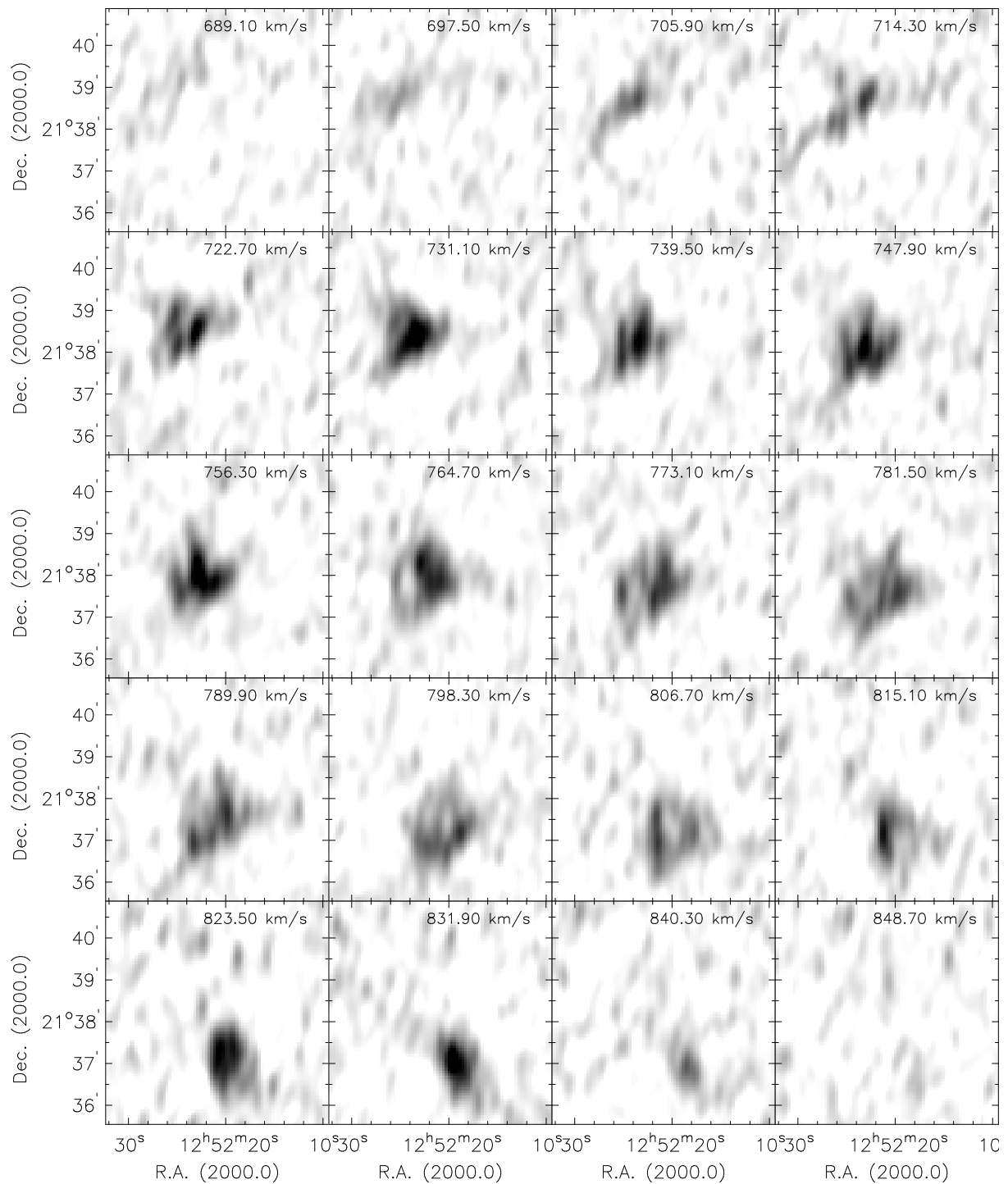


FIG. 4.25: Channel maps of D575-2. Grayscales run from -0.02 to 10 mJy. Every fourth channel is shown.

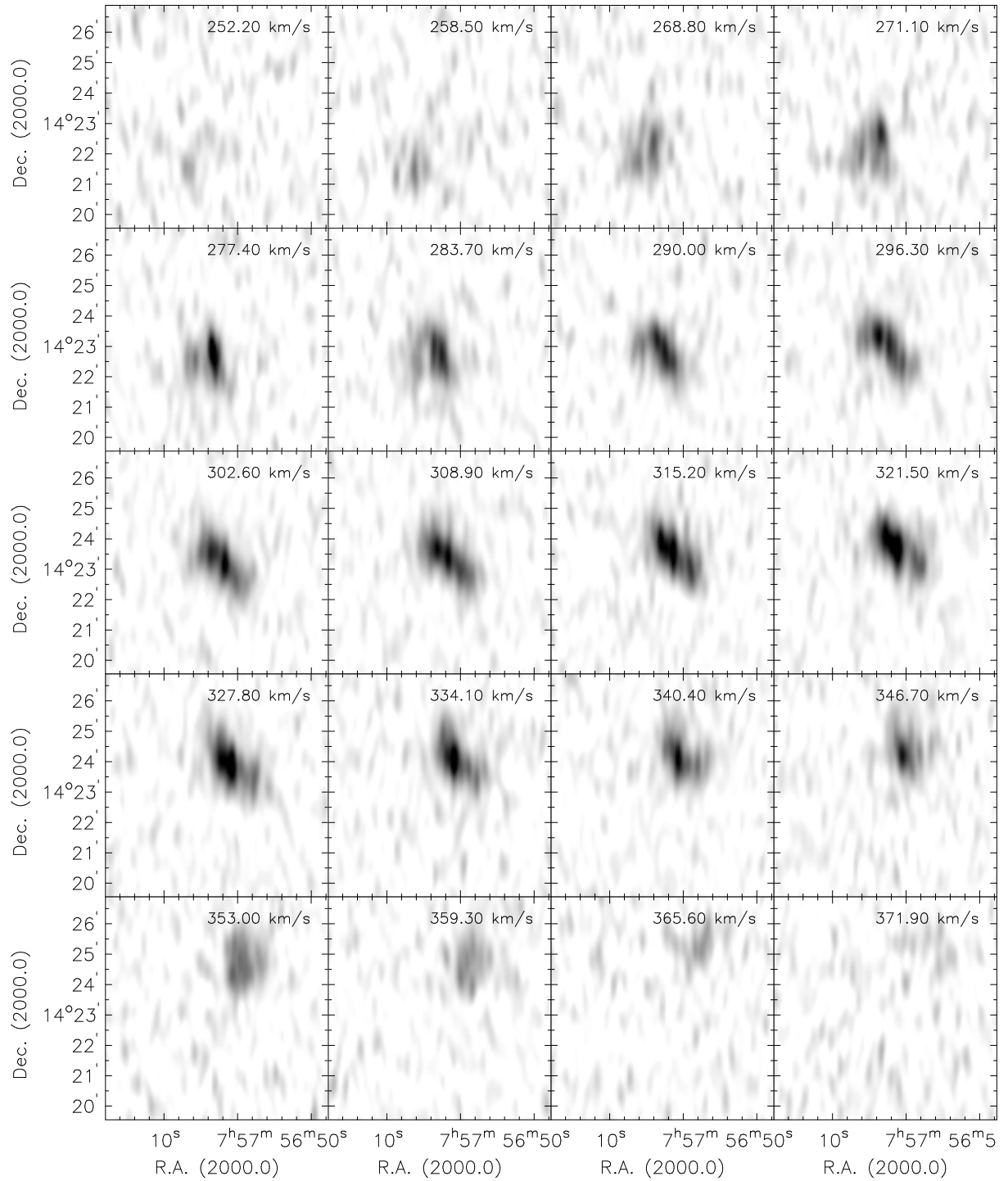


FIG. 4.26: Channel maps of D631-7. Grayscales run from -0.02 to 25 mJy. Every second channel is shown.

Summary and Conclusions

5.1 Summary

The motivation for this thesis is to confront the results from cosmological cold dark matter simulations with new observations. The thesis addresses the cusp/core problem, i.e., the differences between the predicted and observed slopes of the density profiles in the centers of (especially) dwarf galaxies. While the density profiles from CDM simulations show steep central cusps, the observed density profiles of dwarf galaxies show flat inner cores. What causes this discrepancy is still a matter of debate. Recent attempts to explain why observations fail to detect cuspy density profiles often include the effect of non-circular motions (e.g., Rhee et al. 2004; Hayashi et al. 2004a; Hayashi & Navarro 2006; Valenzuela et al. 2007). As the dark matter halos from CDM simulations are tri-axial (e.g., Frenk et al. 1988; Dubinski & Carlberg 1991; Hayashi et al. 2007), the elongation of the potential can cause large deviations from circular rotation, which, according to Hayashi & Navarro (2006) can “hide a cusp in a core”.

The first part of this thesis deals with a sample of 19 galaxies from “The HI Nearby Galaxy Survey” (THINGS, Walter et al. 2008; de Blok et al. 2008). In Chapter 2, various center positions are estimated for these galaxies, including photometric centers as well as kinematic centers. The results discussed in Section 2.6.1 show that for the large majority of the galaxies in the sample, the kinematic and photometric center estimates agree well. No indications for genuine offsets between photometric and kinematic centers are found. The second part of Chapter 2 deals with the harmonic decomposition of the velocity fields of the galaxies in the sample (following the formalism presented in Schoenmakers et al. 1997 and Schoenmakers 1999). The velocity fields are decomposed up to the third harmonic order and the amplitudes of the non-circular motions in the THINGS galaxies are quantified. The results presented in Sections 2.6.2 and 2.6.3 show that the absolute amplitudes of the non-circular motions are smallest in the dwarf galaxies, especially in their inner parts. Large non-circular motions in the centers of the galaxies are preferably found in luminous and/or barred galaxies, which might lead to speculations that the non-circular motions in these galaxies are caused by baryonic features and not the DM halo. Within the sample, the average amplitude of the non-circular motions is $\tilde{A}_r = 4.8 \pm 4.0 \text{ km s}^{-1}$ for the inner 1 kpc and $\tilde{A}_r = 6.7 \pm 5.9 \text{ km s}^{-1}$ when averaged over the entire radial range of the galaxies. However, non-circular motions of the order of 20 km s^{-1} over a large fraction of the disk are needed in order to sufficiently blur a cuspy density profile so that it will look cored (de Blok et al. 2003; Kuzio de Naray et al. 2008). The results presented in this

thesis therefore clearly show that the amount of the non-circular motions is too small to explain the cusp/core problem by invoking non-circular motions.

Although the dwarf galaxies in the sample show the smallest non-circular motions in absolute terms, they also have the smallest rotation velocities. Normalizing the non-circular motions in the central regions of the galaxies by the local rotation velocity therefore enables one to quantify the amount of non-circular motions relative to the circular motions. For the THINGS galaxies, the results show that even though the non-circular motions in the dwarfs are small, the non-circular motions are — in relative terms — not necessarily much smaller than those in galaxies of higher luminosity. At a radius of 1 kpc, Hayashi et al. (2004a) propose non-circular motions as high as 50 percent of the local rotation velocity. The non-circular motions quantified in this thesis are generally far smaller. Averaged over the sample, the median amplitude of the non-circular motions in the inner 1 kpc is 8 ± 3 percent of the local rotation velocity. Only three galaxies out of 18 show non-circular motions which are larger than 20 percent of the local rotation velocity. Two of these galaxies are barred, again suggesting that large non-circular motions are associated with baryonic features. The subsample of THINGS which is studied in this thesis contains four dwarf galaxies (NGC 2366, NGC 2976, IC 2574, and DDO 154); all of them showing a density profile which is inconsistent with an NFW profile, but better approximated with a constant-density core (see de Blok et al. 2008; Oh et al. 2008). Only one dwarf galaxy, IC 2574, shows rather large non-circular motions of 26 percent of the local rotation velocity in its inner 1 kpc. However, Oh et al. (2008) have shown that even after the removal of the non-circular motions by means of creating a so-called bulk velocity field, IC 2574 remains inconsistent with a cuspy density profile. The non-circular motions in the centers of the other three dwarf galaxies in the sample are of the order of 10 percent (or less) of the local rotation velocity. This is far smaller than what Hayashi et al. (2004a) and Hayashi & Navarro (2006) predict in order to reconcile the differences in the density slopes by invoking non-circular motions. The small non-circular motions for these galaxies show that the mass models presented in de Blok et al. (2008) and Oh et al. (2008) are not significantly affected by non-circular motions, and that the density profiles of these galaxies are likely to be truly cored.

The results of the harmonic decomposition can also be used to estimate the ellipticities of the potential in the plane of the disk of the galaxies, apart from an unknown viewing angle φ_2 . The gravitational potential in the simulations of Hayashi & Navarro (2006) is elongated in the inner parts as $\langle \epsilon_{pot} \rangle = 0.2 \pm 0.1$. For the galaxies studied here, the average elongation of the gravitational potential and its scatter, both statistically corrected for the unknown viewing angle φ_2 , is $\langle \epsilon_{pot} \rangle = 0.017 \pm 0.020$. This is significantly lower than the predictions from cosmological simulations. The individual elongation measurements show that the large majority of the galaxies in the sample have elongations which are systematically below the CDM predictions. The elongations of all galaxies in the sample are consistent with a round potential, although some galaxies have large enough uncertainties to make them also (marginally) consistent with the lower end of the predicted range for CDM halos. Furthermore, the results do not suggest that the elongations increase towards the centers of the galaxies. The work presented in this thesis shows therefore no indication for a significant tri-axiality within the HI disks of the THINGS galaxies.

The results from Chapter 2 are double-checked in Chapter 3, where emphasis is placed on non-circular motions not quantified by the previous analysis. This includes non-circular motions of higher harmonic order, as well as the detection efficiency of the fitting routine. The velocity fields of the galaxies from the THINGS survey are decomposed using a fifth, ninth, and fifteenth order harmonic decomposition and the results are compared with those from the third order decomposition presented in Chapter 2. The analysis presented in Section 3.1 shows that though increasing the maximum fit order does result in somewhat larger non-circular motions, the amplitudes are still far too small to

reconcile the different density profiles. Furthermore, the increased number of free parameters for a high-order harmonic decomposition results in a decreased number of galaxies suitable for this kind of analysis. Focussing again on the dwarf galaxies, the increase of the non-circular motions (with respect to the local rotation velocity) is 3.4 percent on average. The non-circular motions in three out of the four dwarfs in the sample are therefore of the order of 13 percent of the local rotation velocity, and thus still far smaller than what is predicted, e.g., by Hayashi et al. (2004a) or Hayashi & Navarro (2006). In Section 3.2, artificial velocity fields with a known amount of non-circular motions have been created and analyzed. The harmonic decomposition of the artificial VFs shows that in 80 percent of the galaxies, the amplitudes of the detected non-circular motions differ by less than ten percent from the ones that have been inserted into the artificial VFs. The so-called recovery-rate (i.e., the ratio between the detected and the inserted non-circular motions) is 95 percent on average. In absolute numbers, the differences between the inserted and the detected non-circular motions are below 1 km s^{-1} for all galaxies in the sample, with an average of 0.2 km s^{-1} . The analysis presented in Chapter 3 therefore shows that RESWRI is able to quantify most non-circular motions within a velocity field of a galaxy and that the contribution of harmonic terms of high order is small. This implies that the velocity fields of the galaxies studied in this thesis do not contain large amount of unquantified non-circular motions and that the conclusions from Chapter 2 remain unchanged.

In the second part of this thesis (Chapter 4), the baryonic Tully-Fisher relation for a sample of 11 extremely low-mass dwarf galaxies is studied. Several different estimates for V_{max} , the maximum rotation velocity are presented and discussed. The different BTF relations generally show good agreement. Furthermore, it is shown that the choice of the stellar mass-to-light ratio has only little effect on the baryonic (gas + stars) mass of these extreme dwarf galaxies. By combining the highest-quality galaxies from sample presented in Section 4.2 (the so-called “rotation-curve sub-sample”) with high-quality data from McGaugh (2005), a BTF relation spanning four orders of magnitude in baryonic mass with rotation velocities of $25 \text{ km s}^{-1} \leq V_{\text{max}} \leq 300 \text{ km s}^{-1}$ is constructed. The dwarf galaxies from the sample presented in this chapter fall almost exactly onto the BTF relation as constructed using the high-mass galaxies from the sample of McGaugh (2005). This indicates that the BTF relation is a fundamental and extremely tight relation which all rotationally supported galaxies seem to follow. The scatter of the (baryonic) Tully-Fisher relation can be used to constrain the ellipticities of the gravitational potential in the plane of the disk. As the halos of CDM simulations are supposed to be tri-axial (e.g., Frenk et al. 1988; Dubinski & Carlberg 1991; Hayashi et al. 2007; Capuzzo-Dolcetta et al. 2007), the mixture of viewing angles will cause some scatter in the (B)-TF relation. Franx & de Zeeuw (1992) analyzed the Tully-Fisher relation for a sample consisting mostly of high-mass galaxies. They conclude that if all the scatter in the TF relation (0.46 mag in their analysis) is due to a mixture of viewing angles, the elongation of the potential is confined to be smaller than 0.1. However, as it is highly unlikely that there is no other source of scatter, they assume that half of the scatter in the TF relation is due to different viewing angles, which then constrains the ellipticity of the gravitational potential to be between 0 and 0.06. While the analysis of Franx & de Zeeuw (1992) was restricted to high-mass galaxies, the data presented in Chapter 4 covers many different galaxies ranging from dwarf galaxies to high-mass spirals. The baryonic Tully-Fisher relation presented in Section 4.5.5 has a scatter of 0.28 mag, which indicates that even with the inclusion of the extreme dwarf galaxies, the ellipticities of the DM halos are likely between 0-0.06, but certainly below 0.1. These limits are consistent with what has been found in Chapter 2, but inconsistent with predictions from CDM simulations.

5.2 Future prospects

Baryonic Tully-Fisher relation

The work on the baryonic Tully-Fisher relation can be continued and improved in several ways. Firstly, the low-mass end of the BTF relation (presented in this thesis) is relatively sparsely populated, future work could focus on increasing the sample. More importantly, however, is to reduce the scatter due to observational/instrumental reasons, e.g., by obtaining HI data of high sensitivity and spatial resolution. For instance, a number of these dwarf galaxies could be observed in the same way as the galaxies from the THINGS survey have been observed (i.e., VLA BCD-arrays). This would result in better resolved velocity fields and thus allow a more detailed modelling of the rotation curves of these galaxies. As an increased spatial resolution would result in better-constrained kinematic inclinations, the scatter which is due to inclination uncertainties would decrease. Work in this direction is done by Hunter et al. (2007) with the so-called “LITTLE THINGS” survey. The largest source of scatter in the BTF relation, however, is the galaxies’ distance. Obtaining independent distance estimates would therefore produce a much cleaner BTF relation. Altogether, it would be desirable to minimize the part of the scatter which is due to observational uncertainties, as this would significantly improve the assessment of the elongation of the gravitational potential.

Non-circular motions in cold dark matter halos

Future work on non-circular motions and cold dark matter halos can be threefold: (i) bigger, better, deeper observations; (ii) additional/other methods of analysis; (iii) modifications of CDM.

The HI data analyzed in Chapters 2 and 3 are of the highest data quality currently available. Nevertheless, a higher resolution would allow to study the non-circular motions in the central parts of the galaxies in an even greater detail. It is currently planned to observe some of the THINGS galaxies with the A-array of the VLA. Combining these data sets with the existing sets of the BCD-array would lead to far smaller beam sizes and thus an improved spatial resolution. It has been already mentioned several times that the cusp/core problem is most apparent for dwarf galaxies. As the sample studied here contains only four dwarfs, increasing their number would put the results on a firmer statistical footing. Work to increase the sample is currently undertaken by observing galaxies from the southern hemisphere with the Australia Telescope Compact Array (ATCA). Once this survey (called THINGS-South) is fully observed and reduced, the harmonic decomposition can be extended to more dwarf galaxies. Furthermore, with the advent of a new generation of radio telescopes like the Square Kilometre Array (SKA), it will be possible to observe galaxies at much larger distances, which also allows to study evolutionary effects.

As a second point, one could think of refining the analysis. It was shown in Chapter 3, that RESWRI is capable of detecting almost all non-circular motions inserted into a *velocity field*. However, a velocity field is already processed data, where each pixel is given a “representative” velocity. The best way to test for the detection efficiency of RESWRI would therefore consist of modelling a data cube with a certain (known) amount of non-circular motions, create a velocity field from the data cube and analyze this. It is also imaginable to work directly on the data cubes, e.g., with the program TiRiFiC (Tilted-Ring-Fitting Code, Józsa et al. 2007). Though this program has great potential, more work on the speed and stability of the fitting routine should show whether it is also applicable to high resolution data cubes as those from the THINGS survey.

Although modifications of the analysis are possible, and improvements on the size of the sample and the data quality are always appreciated, the main focus of the future work lies with the CDM

simulations. The work presented in this thesis clearly shows that the non-circular motions are not large enough to “hide a cusp in a core”. Therefore, the cored density profiles found, e.g., by de Blok et al. (2008) and Oh et al. (2008) are most likely truly cored. This implies that there is a strong need for a modification of CDM simulations.

Bibliography

- Abell, G. O. 1977, *ApJ*, 213, 327
- Adelman-McCarthy, J. K., Agüeros, M. A., & Allam, S.S. et al. 2006, *ApJS*, 162, 38
- Babcock, H. W. 1939, *Lick Observatory Bulletin*, 19, 41
- Battaglia, G., Fraternali, F., Oosterloo, T., & Sancisi, R. 2006, *A&A*, 447, 49
- Begeman, K. G. 1987, PhD thesis, Univ. Groningen
- . 1989, *A&A*, 223, 47
- Bekenstein, J. 2006, *Contemporary Physics*, 47, 387
- Bekenstein, J. D. 2004, *Phys. Rev. D*, 70, 083509
- Bell, E. F., & de Jong, R. S. 2001, *ApJ*, 550, 212
- Benson, A. J., Frenk, C. S., Lacey, C. G., Baugh, C. M., & Cole, S. 2002, *MNRAS*, 333, 177
- Blanton, M. R., Geha, M., & West, A. A. 2007, *ArXiv e-prints*, 707
- Bosma, A. 1978, PhD thesis, Univ. Groningen
- . 1981a, *AJ*, 86, 1791
- . 1981b, *AJ*, 86, 1825
- Braun, R., Walterbos, R. A. M., Kennicutt, Jr., R. C., & Tacconi, L. J. 1994, *ApJ*, 420, 558
- Briggs, D. S. 1995, in *Bulletin of the American Astronomical Society*, Vol. 27, *Bulletin of the American Astronomical Society*, 1444
- Broeils, A. H. 1992, PhD thesis, Univ. Groningen
- Bullock, J. S., Kravtsov, A. V., & Weinberg, D. H. 2000, *ApJ*, 539, 517
- Capuzzo-Dolcetta, R., Leccese, L., Merritt, D., & Vicari, A. 2007, *ApJ*, 666, 165
- Colless, M., & Dunn, A. M. 1996, *ApJ*, 458, 435

- de Blok, E., van der Hulst, T., & McGaugh, S. 1996, *Bulletin of the American Astronomical Society*, 28, 1387
- de Blok, W. J. G. 2004, in *IAU Symposium*, Vol. 220, *Dark Matter in Galaxies*, ed. S. Ryder, D. Pisano, M. Walker, & K. Freeman, 69
- de Blok, W. J. G. 2005, *ApJ*, 634, 227
- de Blok, W. J. G., & Bosma, A. 2002, *A&A*, 385, 816
- de Blok, W. J. G., Bosma, A., & McGaugh, S. 2003, *MNRAS*, 340, 657
- de Blok, W. J. G., & McGaugh, S. S. 1997, *MNRAS*, 290, 533
- de Blok, W. J. G., McGaugh, S. S., Bosma, A., & Rubin, V. C. 2001a, *ApJ*, 552, L23
- de Blok, W. J. G., McGaugh, S. S., & Rubin, V. C. 2001b, *AJ*, 122, 2396
- de Blok, W. J. G., van der Hulst, J. M., & Bothun, G. D. 1995, *MNRAS*, 274, 235
- de Blok, W. J. G., Walter, F., Brinks, E., Trachternach, C., Oh, S.-H., & Kennicutt, Jr., R. C. 2008, submitted to *AJ*
- De Rijcke, S., Zeilinger, W. W., Hau, G. K. T., Prugniel, P., & Dejonghe, H. 2007, *ApJ*, 659, 1172
- Dubinski, J. 1994, *ApJ*, 431, 617
- Dubinski, J., & Carlberg, R. G. 1991, *ApJ*, 378, 496
- Eder, J. A., & Schombert, J. M. 2000, *ApJS*, 131, 47
- Eisenstein, D. J., & Loeb, A. 1996, *ApJ*, 459, 432
- Faber, S. M., & Gallagher, J. S. 1979, *ARA&A*, 17, 135
- Flores, R. A., & Primack, J. R. 1994, *ApJ*, 427, L1
- Franx, M., & de Zeeuw, T. 1992, *ApJ*, 392, L47
- Franx, M., van Gorkom, J. H., & de Zeeuw, T. 1994, *ApJ*, 436, 642
- Frenk, C. S., White, S. D. M., Davis, M., & Efstathiou, G. 1988, *ApJ*, 327, 507
- Geha, M., Blanton, M. R., Masjedi, M., & West, A. A. 2006, *ApJ*, 653, 240
- Gentile, G., Burkert, A., Salucci, P., Klein, U., & Walter, F. 2005, *ApJ*, 634, L145
- Gentile, G., Salucci, P., Klein, U., & Granato, G. L. 2007, *MNRAS*, 375, 199
- Gentile, G., Salucci, P., Klein, U., Vergani, D., & Kalberla, P. 2004, *MNRAS*, 351, 903
- Gurovich, S., McGaugh, S. S., Freeman, K. C., Jerjen, H., Staveley-Smith, L., & De Blok, W. J. G. 2004, *Publications of the Astronomical Society of Australia*, 21, 412
- Habertzettl, L., Bomans, D. J., Dettmar, R.-J., & Pohlen, M. 2007, *A&A*, 465, 95

- Hayashi, E., & Navarro, J. F. 2006, MNRAS, 373, 1117
- Hayashi, E., Navarro, J. F., Jenkins, A., Frenk, C. S., Power, C., White, S. D. M., Springel, V., Stadel, J., Quinn, T., & Wadsley, J. 2004a, ArXiv Astrophysics e-prints
- Hayashi, E., Navarro, J. F., Power, C., Jenkins, A., Frenk, C. S., White, S. D. M., Springel, V., Stadel, J., & Quinn, T. R. 2004b, MNRAS, 355, 794
- Hayashi, E., Navarro, J. F., & Springel, V. 2007, MNRAS, 248
- Hunter, D. A., Brinks, E., Elmegreen, B., Rupen, M., Simpson, C., Walter, F., Westpfahl, D., & Young, L. 2007, in American Astronomical Society Meeting Abstracts, Vol. 211, American Astronomical Society Meeting Abstracts, 95
- Impey, C., Bothun, G., & Malin, D. 1988, ApJ, 330, 634
- Józsa, G. I. G., Kenn, F., Klein, U., & Oosterloo, T. A. 2007, A&A, 468, 731
- Karachentsev, I. D., Makarov, D. I., Sharina, M. E., Dolphin, A. E., Grebel, E. K., Geisler, D., Guhathakurta, P., Hodge, P. W., Karachentseva, V. E., Sarajedini, A., & Seitzer, P. 2003, A&A, 398, 479
- Kasun, S. F., & Evrard, A. E. 2005, ApJ, 629, 781
- Kauffmann, G., White, S. D. M., & Guiderdoni, B. 1993, MNRAS, 264, 201
- Kennicutt, Jr., R. C., Armus, L., Bendo, G., Calzetti, D., Dale, D. A., Draine, B. T., Engelbracht, C. W., Gordon, K. D., Grauer, A. D., Helou, G., Hollenbach, D. J., Jarrett, T. H., Kewley, L. J., Leitherer, C., Li, A., Malhotra, S., Regan, M. W., Rieke, G. H., Rieke, M. J., Roussel, H., Smith, J.-D. T., Thornley, M. D., & Walter, F. 2003, PASP, 115, 928
- Kent, S. M., & Gunn, J. E. 1982, AJ, 87, 945
- Klypin, A., Kravtsov, A. V., Valenzuela, O., & Prada, F. 1999, ApJ, 522, 82
- Kovac, K. 2007, PhD thesis, Univ. Groningen
- Kroupa, P. 1998, in Astronomical Society of the Pacific Conference Series, Vol. 134, Brown Dwarfs and Extrasolar Planets, ed. R. Rebolo, E. L. Martin, & M. R. Zapatero Osorio, 483
- Kuzio de Naray, R. 2007, PhD thesis, Univ. of Maryland
- Kuzio de Naray, R., McGaugh, S. S., & de Blok, W. J. G. 2008, ApJ, 676, 920
- Kuzio de Naray, R., McGaugh, S. S., de Blok, W. J. G., & Bosma, A. 2006, ApJS, 165, 461
- Leroy, A., Bolatto, A. D., Simon, J. D., & Blitz, L. 2005, ApJ, 625, 763
- Lokas, E. L., & Mamon, G. A. 2003, MNRAS, 343, 401
- Maoz, D., Filippenko, A. V., Ho, L. C., Macchetto, F. D., Rix, H.-W., & Schneider, D. P. 1996, ApJS, 107, 215
- Marchesini, D., D'Onghia, E., Chincarini, G., Firmani, C., Conconi, P., Molinari, E., & Zacchei, A. 2002, ApJ, 575, 801

- Matthews, L. D., van Driel, W., & Gallagher, III, J. S. 1998, *AJ*, 116, 2196
- McGaugh, S., & de Blok, E. 1998a, in *Astronomical Society of the Pacific Conference Series*, Vol. 136, *Galactic Halos*, ed. D. Zaritsky, 210
- McGaugh, S. S. 1996, *MNRAS*, 280, 337
- . 2004, *ApJ*, 609, 652
- . 2005, *ApJ*, 632, 859
- McGaugh, S. S., & de Blok, W. J. G. 1998b, *ApJ*, 499, 41
- . 1998c, *ApJ*, 499, 66
- McGaugh, S. S., Rubin, V. C., & de Blok, W. J. G. 2001, *AJ*, 122, 2381
- McGaugh, S. S., Schombert, J. M., Bothun, G. D., & de Blok, W. J. G. 1999, in *Bulletin of the American Astronomical Society*, Vol. 31, *Bulletin of the American Astronomical Society*, 1559
- McGaugh, S. S., Schombert, J. M., Bothun, G. D., & de Blok, W. J. G. 2000, *ApJ*, 533, L99
- Milgrom, M. 1983a, *ApJ*, 270, 371
- . 1983b, *ApJ*, 270, 384
- . 1983c, *ApJ*, 270, 365
- Mo, H. J., Mao, S., & White, S. D. M. 1998, *MNRAS*, 295, 319
- Moore, B. 1994, *Nature*, 370, 629
- Moore, B., Ghigna, S., Governato, F., Lake, G., Quinn, T., Stadel, J., & Tozzi, P. 1999, *ApJ*, 524, L19
- Moore, B., Kazantzidis, S., Diemand, J., & Stadel, J. 2004, *MNRAS*, 354, 522
- Mould, J. R., Huchra, J. P., Freedman, W. L., Kennicutt, Jr., R. C., Ferrarese, L., Ford, H. C., Gibson, B. K., Graham, J. A., Hughes, S. M. G., Illingworth, G. D., Kelson, D. D., Macri, L. M., Madore, B. F., Sakai, S., Sebo, K. M., Silbermann, N. A., & Stetson, P. B. 2000, *ApJ*, 529, 786
- Navarro, J. F., Frenk, C. S., & White, S. D. M. 1996, *ApJ*, 462, 563
- . 1997, *ApJ*, 490, 493
- Noordermeer, E., & Verheijen, M. A. W. 2007, *MNRAS*, 381, 1463
- Oh, S.-H., de Blok, W. J. G., Walter, F., Brinks, E., & Kennicutt, Jr., R. C. 2008, submitted to *AJ*
- Oort, J. H. 1940, *ApJ*, 91, 273
- Persic, M., & Salucci, P. 1992, *MNRAS*, 258, 14P
- Pierce, M. J., & Tully, R. B. 1988, *ApJ*, 330, 579
- Pildis, R. A., Schombert, J. M., & Eder, J. A. 1997, *ApJ*, 481, 157

- Portinari, L., Sommer-Larsen, J., & Tantaló, R. 2004, *MNRAS*, 347, 691
- Rhee, G., Valenzuela, O., Klypin, A., Holtzman, J., & Moorthy, B. 2004, *ApJ*, 617, 1059
- Rubin, V. C., Burstein, D., Ford, Jr., W. K., & Thonnard, N. 1985, *ApJ*, 289, 81
- Rubin, V. C., Ford, Jr., W. K., Thonnard, N., & Burstein, D. 1982, *ApJ*, 261, 439
- Rubin, V. C., Thonnard, N., & Ford, Jr., W. K. 1978, *ApJ*, 225, L107
- Sakai, S., Mould, J. R., Hughes, S. M. G., Huchra, J. P., Macri, L. M., Kennicutt, Jr., R. C., Gibson, B. K., Ferrarese, L., Freedman, W. L., Han, M., Ford, H. C., Graham, J. A., Illingworth, G. D., Kelson, D. D., Madore, B. F., Sebo, K., Silbermann, N. A., & Stetson, P. B. 2000, *ApJ*, 529, 698
- Salpeter, E. E. 1955, *ApJ*, 121, 161
- Sanders, R. H. 1996, *ApJ*, 473, 117
- Sanders, R. H., & McGaugh, S. S. 2002, *ARA&A*, 40, 263
- Sanders, R. H., & Verheijen, M. A. W. 1998, *ApJ*, 503, 97
- Sault, R. J., Teuben, P. J., & Wright, M. C. H. 1995, in *Astronomical Society of the Pacific Conference Series*, Vol. 77, *Astronomical Data Analysis Software and Systems IV*, ed. R. A. Shaw, H. E. Payne, & J. J. E. Hayes, 433
- Schoenmakers, R. H. M. 1999, PhD thesis, Univ. Groningen
- Schoenmakers, R. H. M., Franx, M., & de Zeeuw, P. T. 1997, *MNRAS*, 292, 349
- Schombert, J. M., Pildis, R. A., & Eder, J. A. 1997, *ApJS*, 111, 233
- Simon, J. D., Bolatto, A. D., Leroy, A., & Blitz, L. 2003, *ApJ*, 596, 957
- Simon, J. D., Bolatto, A. D., Leroy, A., Blitz, L., & Gates, E. L. 2005, *ApJ*, 621, 757
- Spano, M., Marcellin, M., Amram, P., Carignan, C., Epinat, B., & Hernandez, O. 2008, *MNRAS*, 383, 297
- Spekkens, K., Giovanelli, R., & Haynes, M. P. 2005, *AJ*, 129, 2119
- Spekkens, K., & Sellwood, J. A. 2007, *ApJ*, 664, 204
- Spergel, D. N., Bean, R., Doré, O., Nolta, M. R., Bennett, C. L., Dunkley, J., Hinshaw, G., Jarosik, N., Komatsu, E., Page, L., Peiris, H. V., Verde, L., Halpern, M., Hill, R. S., Kogut, A., Limon, M., Meyer, S. S., Odegard, N., Tucker, G. S., Weiland, J. L., Wollack, E., & Wright, E. L. 2007, *ApJS*, 170, 377
- Spergel, D. N., Verde, L., Peiris, H. V., Komatsu, E., Nolta, M. R., Bennett, C. L., Halpern, M., Hinshaw, G., Jarosik, N., Kogut, A., Limon, M., Meyer, S. S., Page, L., Tucker, G. S., Weiland, J. L., Wollack, E., & Wright, E. L. 2003, *ApJS*, 148, 175
- Springel, V., White, S. D. M., Jenkins, A., Frenk, C. S., Yoshida, N., Gao, L., Navarro, J., Thacker, R., Croton, D., Helly, J., Peacock, J. A., Cole, S., Thomas, P., Couchman, H., Evrard, A., Colberg, J., & Pearce, F. 2005, *Nature*, 435, 629

- Steinmetz, M., & Navarro, J. F. 1999, *ApJ*, 513, 555
- Stoughton, C., Lupton, R. H., Bernardi, M., & Blanton, M.R. et al. 2002, *AJ*, 123, 485
- Swaters, R. A. 1999, PhD thesis, Univ. Groningen
- Swaters, R. A., Madore, B. F., & Trewhella, M. 2000, *ApJ*, 531, L107
- Swaters, R. A., Madore, B. F., van den Bosch, F. C., & Balcells, M. 2003a, *ApJ*, 583, 732
- Swaters, R. A., Verheijen, M. A. W., Bershady, M. A., & Andersen, D. R. 2003b, *ApJ*, 587, L19
- Taylor, C. L., Kobulnicky, H. A., & Skillman, E. D. 1998, *AJ*, 116, 2746
- Trachternach, C., Bomans, D. J., Habertzettl, L., & Dettmar, R.-J. 2006, *A&A*, 458, 341
- Trachternach, C., de Blok, W. J. G., Brinks, E., Walter, F., & Kennicutt, Jr., R. C. 2008a, submitted to *AJ*
- Trachternach, C., de Blok, W. J. G., McGaugh, S. S., van der Hulst, J. M., & Dettmar, R.-J. 2008b, submitted to *A & A*
- Tully, R. B., & Fisher, J. R. 1977, *A&A*, 54, 661
- Tully, R. B., & Fouque, P. 1985, *ApJS*, 58, 67
- Tully, R. B., & Pierce, M. J. 2000, *ApJ*, 533, 744
- Valenzuela, O., Rhee, G., Klypin, A., Governato, F., Stinson, G., Quinn, T., & Wadsley, J. 2007, *ApJ*, 657, 773
- van Albada, T. S., Bahcall, J. N., Begeman, K., & Sancisi, R. 1985, *ApJ*, 295, 305
- van Albada, T. S., & Sancisi, R. 1986, *Royal Society of London Philosophical Transactions Series A*, 320, 447
- van den Bosch, F. C., Robertson, B. E., Dalcanton, J. J., & de Blok, W. J. G. 2000, *AJ*, 119, 1579
- van der Hulst, J. M., Terlouw, J. P., Begeman, K. G., Zwitter, W., & Roelfsema, P. R. 1992, in *Astronomical Society of the Pacific Conference Series*, Vol. 25, *Astronomical Data Analysis Software and Systems I*, ed. D. M. Worrall, C. Biemesderfer, & J. Barnes, 131
- van der Marel, R. P., & Franx, M. 1993, *ApJ*, 407, 525
- Verheijen, M. A. W. 1997, PhD thesis, Univ. Groningen
- . 2001, *ApJ*, 563, 694
- Walker, T. P., Steigman, G., Kang, H.-S., Schramm, D. M., & Olive, K. A. 1991, *ApJ*, 376, 51
- Walter, F., Brinks, E., de Blok, W. J. G., Bigiel, F., Kennicutt, Jr., R. C., & Thornley, M. 2008, submitted to *AJ*
- Walter, F., Kerp, J., Duric, N., Brinks, E., & Klein, U. 1998, *ApJ*, 502, L143+

Wong, T., Blitz, L., & Bosma, A. 2004, *ApJ*, 605, 183

Zackrisson, E., Bergvall, N., Marquart, T., & Östlin, G. 2006, *A&A*, 452, 857

Zwaan, M. A., van der Hulst, J. M., de Blok, W. J. G., & McGaugh, S. S. 1995, *MNRAS*, 273, L35

Zwicky, F. 1933, *Helvetica Physica Acta*, 6, 110

—. 1937, *ApJ*, 86, 217

Acknowledgements

A PhD thesis is seldom obtained without the support from other people, and I would like to thank all who helped me during that time. First of all, I thank my supervisors, Ralf-Jürgen Dettmar and Erwin de Blok. Without them, this thesis would not have been possible. In particular, I want to thank Erwin for being an excellent supervisor and collaborator, even though this meant (due to different time zones) that he spent lots of his evenings with answering tedious emails from his German student. Thank you also for your hospitality during my visits, for the good time I had in Canberra and Cape Town, and for introducing me to “The Doctor”. I also want to express my gratitude to all members of the THINGS team, especially to Fabian Walter, Elias Brinks and Rob Kennicutt. The meeting in Schloss Hirschhorn was extremely stimulating and I really appreciated your detailed comments on Chapter 2 of this thesis. I am grateful to Stacy McGaugh, who gave valuable comments on the baryonic Tully-Fisher chapter and also calculated the mass-to-light ratios for the different stellar population models. I regret that we have not met in person, yet. During my PhD thesis, I spent several months at the Mount Stromlo Observatory and one month at the Cape Town University. Therefore, I want to thank the staff and the students of both institutes for the hospitality, the nice little chats, and the scientific discussions. I always felt most welcome. I also thank the *old* “Hoher List” team, especially Nicola Bennert, Daniel Brown, Christian Leipski and Olaf Schmithüsen. It is due to their dedication during the astronomical hands-on trainings for students that I decided to concentrate my studies on Astronomy. I am also thankful to all people at the AIRUB who either helped me with one of the many small problems that come up during a PhD or who were just good colleagues that made the days at the AIRUB more enjoyable, though often also less productive. In particular, I thank Volker Knierim for being a good office mate, the many coffees and associated chats, and for all the (scientific) discussions we had. I have also very much appreciated the work of Olaf Schmithüsen and Tim Falkenbach as they helped me quickly and successfully whenever I got any computer or network problems. Furthermore, I want to thank my fellow student and best mate, Janine van Eymeren: for all our lunch-break strolls through the botanical garden, for our many chats and discussions, for putting things back into perspective when I have lost the same, and for (sometimes) being critical with me. Without you, my PhD would indeed have been much harder. Last, but not least, I would like to express my deepest gratitude to Sandra, my companion in life, not only for the everlasting support you gave me, but also for the patient enduring of the limited time I could spend with you.

Curriculum Vitae

Personal details

Name	Clemens Trachternach
Address	Fichtestraße 21a 45739 Oer-Erkenschwick
Nationality	german
Date of birth	11.05.1980 in Datteln

Education

1986-1990	“Astrid-Lindgren Schule” (Primary school) in Recklinghausen
1990-1999	“Willy-Brandt-Gymnasium” (Secondary school) in Oer-Erkenschwick
Jun. 1999	Abitur (A-levels) – University entrance qualification
1999-2004	Study of Physics at the Ruhr-University Bochum
2003-2004	Diploma thesis at the “Astronomisches Institut” of the Ruhr-University Bochum
Dez. 2004	Diploma in Physics
2005-2008	PhD thesis at the “Astronomisches Institut” of the Ruhr-University Bochum

